Stellar Parameters for M dwarfs : the link to exoplanets

Vasco Neves

To cite this version:

Vasco Neves. Stellar Parameters for M dwarfs : the link to exoplanets. Astrophysics [astro-ph]. Université de Grenoble; Universidade do Porto, 2013. English. NNT : 2013GRENY082 . tel-01440510

HAL Id: tel-01440510
https://theses.hal.science/tel-01440510

Submitted on 19 Jan 2017

U.PORTO
FACULDADE DE CIÊNCIAS
UNIVERSIDADE DO PORTO

UNIVERSITÉ
GRENOBLE
ALPES

THÈSE

Pour obtenir le grade de

DOCTEUR DE L'UNIVERSITÉ GRENOBLE ALPES

préparée dans le cadre d'une cotutelle entre l'*Université de Grenoble Alpes* et l'*Universidade do Porto*

Spécialité : **Astrophysique**

Arrêté ministériel : le 6 janvier 2005 -7 août 2006

Présentée par

Vasco NEVES

Thèse dirigée par **Nuno SANTOS**
codirigée par **Xavier DELFOSSE et Xavier BONFILS**

préparée au sein des ***Institut de Planetologie de L'Université de Grenoble*** **et** ***Centro de Astrofísica da Universidade do Porto***

dans **l'*École Doctorale de Physique de Grenoble*** **et** ***Programa Doutoral de Astronomia da Universidade do Porto***

Étude sur les paramétres stellaires des naines M et leur lien à la formation planétaire

Thèse soutenue publiquement le **10 Décembre 2013 à Auditório FC5, Faculdade de Ciências da Universidade do Porto,** devant le jury composé de :

Dr. José LOPES dos SANTOS
Professeur, Faculdade de CIências da Universidade do Porto, Président
Dr. Nuno Miguel Cardoso SANTOS
Chercheur, Centro de Astrofísca da Universidade do Porto, Membre
Dr. Xavier DELFOSSE
Astronome, Institut de Planétologie de L'Université de Grenoble, Membre
Dr. Xavier BONFILS
Astronome, Institut de Planétologie de L'Université de Grenoble, Membre
Dr. Ulrike HEITER
Chercheur, Department of Physics and Astronomy of the Uppsala University, Membre
Dr. Céline REYLÉ
Chercheur, Observatoire des Sciences de l'Univers de Franche-Comté, Rapporteur
Dr. Damien SÉGRANSAN
Chercheur, Observatoire de Genéve, Rapporteur

Acknowledgments

First of all, I would like to thank my supervisors, Nuno Santos and Xavier Delfosse, for all the support and guidance given throughout all these years, full of challenges and pitfalls, but also with unexpected rewards and good surprises.

The completion of this Thesis would not have been possible without the unofficial, but ever present supervision of Xavier Bonfils, during my stay at Grenoble. A sincere and warm acknowledgement of his support is therefore testified here.

I could never forget the companionship and support of Enoe in the most difficult moments when everything seemed to fall apart. Thank you.

I would also like to thank my mates in CAUP for all the good moments and laughter, even in the tensest moments, as well as for giving unexpected insights and new ideas. I will not put here any names, you know who you are!

Last but not least, I would like to thank the eternal and unconditional support of my parents. Without it I would surely not be here writing these words!

Thank you all!

Resumo

No momento em que escrevo esta Tese, o número de planetas anunciados já ultrapassou os 900 e os cerca de 2700 candidatos detectados pelo telescópio espacial Kepler esperam por confirmação. Os espectros e as curvas de luz obtidos nos programas de procura de planetas permitem, também, o estudo em profundidade dos parâmetros das estrelas com planetas e abrem a possibilidade de investigar a relação estrela-planeta. Neste contexto, a determinação com precisão dos parâmetros estelares é crítica na determinação precisa dos parâmetros planetários, nomeadamente, a massa, o raio e a densidade.

No caso das anãs FGK, os métodos de determinação dos parâmetros estelares estão bem estabelecidos e podem ser usados com confiança no estudo da relação estrela-planeta, assim como na obtenção de parâmetros planetários precisos. No entanto, não é esse o caso para as anãs M, as estrelas mais comuns da nossa Galáxia. Ao contrário das suas primas, as estrelas M são mais pequenas, frias e ténues e, assim sendo, mais difíceis de estudar. O grande entrave no estudo das estrelas M está relacionado com a presença de biliões de linhas moleculares que deprimem o contínuo espectral, fazendo com que uma análise espectral clássica se torne quase impossível. A procura de métodos inovadores que possibilitem ultrapassar este obstáculo, tendo em vista a obtenção de parâmetros precisos, é o objectivo desta Tese.

Tendo em conta esse objetivo, foquei os meus esforços em duas linhas principais de pesquisa, baseadas em métodos fotométricos e métodos espectroscópicos. O meu trabalho inicial tinha como objetivo o estabelecimento de uma calibração fotométrica para a metalicidade, mas não me foi possível atingir esse objetivo, pois não tinha sistemas binários FGK+M suficientes com bons dados fotométricos. No entanto, foi possível, com os dados disponíveis, comparar as calibrações fotométricas existentes e refinar ligeiramente a melhor delas, como descrito no Capítulo 3.

Após este trabalho passei a concentrar-me em técnicas espectroscópicas de obtenção de parâmetros estelares em estrelas M. Tendo em mente esse objetivo, usei espectros HARPS de alta resolução para desenvolver um novo método de medição de linhas espectrais independente do contínuo espectral. Seguidamente, usei este método no desenvolvimento de uma nova calibração de metalicidade e temperatura efectiva em estrelas M na região do visível, através da qual consegui atingir uma precisão de 0.08 dex para a [Fe/H] e de 80 K para a temperatura. Este trabalho está descrito no Capítulo 4.

Ao mesmo tempo colaborei na determinação com precisão dos parâmetros da estrela GJ3470 e do seu planeta, onde a minha proficiência na determinação de parâmetros estelares em anâs M teve um papel importante. Os detalhes relacionados com este trabalho de investigação estão descritos no Capítulo 5.

Palavras-chave. estrelas: parâmetros fundamentais – estrelas: tipo tardio – estrelas: baixa massa – estrela: binarias - geral – estrelas: atmosferas – estrelas sistemas planetários – estrelas: individual (GJ 3470) – técnicas: fotometria – técnicas: espectroscopia

Resumé

Au moment d'écrire ma Thèse plus de 900 exoplanètes été annoncées et plus de 2700 planètes détectées par le télescope spatial Kepler sont en attente d'être confirmées. La haute précision des spectres et des courbes de lumière obtenue dans les relevés Doppler et transit, permet l'étude détaillée des paramètres des étoiles hôtes, et ouvre la possibilité d'enquêter sur les corrélations étoile planètes. En outre, la détermination des paramètres stellaires avec précision est un besoin critique pour déterminer les paramètres planétaires, à savoir, la masse, le rayon et la densité.

Dans le cas des naines FGK, la détermination des paramètres stellaires est bien établie et peut être utilisée avec confiance pour étudier la relation planète-étoile ainsi que pour obtenir les paramètres planétaires avec une grande precision. Cependant, ce n'est pas le cas pour les naines M, les étoiles les plus communes de la Galaxie. Par rapport à leurs cousines plus chaudes, les naines M sont plus petites, plus froides, et plus faiblement lumineuses, et donc plus difficile à étudier. Le plus grand défi qui concerne les naines M est lié à la présence de milliards de lignes moléculaires qui gomme le continuum et rend l'analyse spectrale classique presque impossible. Trouver des façons nouvelles et novatrices pour surmonter cet obstacle et obtenir une mesure des paramètres stellaires est l'objectif principal de cette Thèse .

Pour l'atteindre, j'ai concentré mes recherches sur deux approches méthodologiques, photométrique et spectroscopiques. Mon premier travail avait pour objectif d'établir l'étalonnage de métallicité photométrique précis. Par manque de binaires FGK+M avec de bonnes données photométriques je ne pouvais pas atteindre cet objectif. Il m'a cependant était possible, avec les données disponibles, de comparer les étalonnages photométriques déjà établies et légèrement améliorer le meilleur d'entre eux, comme décrit au Chapitre 3.

Puis, je me suis concentré sur les approches spectroscopiques pour obtenir des paramètres stellaires plus précis pour les naines M. À cette fin, j'ai utilisé des spectres HARPS de haute résolution et développé une méthode pour mesurer les lignes spectrales sans tenir compte du continuum . En utilisant cette méthode, je créé un nouvel étalonnage visible avec une précision de 0.08 dex pour [Fe/H] et 80 K pour T_{eff} . Ce travail est dtaill dans le Chapitre 4 .

Finalement , j'ai également participé à l'amélioration des paramètres de l'étoile GJ3470 et de sa planète, où mon expertise dans les paramètres stellaires de naines M avait un rôle important. Les détails concernant cette enquête sont présentés dans le Chapitre 5 .

Mots-clés. étoiles: paramètres fondamentaux – étoiles: type tardif – étoiles: faible masse – étoiles: binaires - général – étoiles: atmosphères – étoiles: systèmes planétaires – étoiles: individuel (GJ 3470) – techniques: photométriques – techniques spectroscopiques

Abstract

At the time of writing of this Thesis more than 900 planets have been announced and about 2700 planets from the Kepler space telescope are waiting to be confirmed. The very precise spectra and light curves obtained in Doppler and transit surveys, allows the in-depth study of the parameters of the host stars, and opens the possibility to investigate the star-plant correlations. Also, determining the stellar parameters with precision is critical for more precise determinations of the planetary parameters, namely, mass, radius, and density.

In the case of the FGK dwarfs, the determination of stellar parameters is well established and can be used with confidence to study the star-planet relation as well as to obtain precise planetary parameters. However, this is not the case for M dwarfs, the most common stars in the Galaxy. Compared to their hotter cousins, M dwarfs are smaller, colder, and fainter, and therefore harder to study. The biggest challenge regarding M dwarfs is related to the presence of billions of molecular lines that depress the continuum making a classical spectral analysis almost impossible. Finding new and innovative ways to overcome this obstacle in order to obtain precise stellar parameters is the goal of this Thesis.

To achieve this goal I focused my research into two main avenues: photometric and spectroscopic methods. My initial work had the objective of establishing a precise photometric metallicity calibration, but I could not reach this goal, as I did not have enough FGK+M binaries with good photometric data. However, it was possible, with the available data, to compare the already established photometric calibrations and slightly improve the best one, as described in Chapter 3.

Then, I focused on spectroscopic approaches with the aim of obtaining precise M dwarf parameters. To this end I used HARPS high-resolution spectra and developed a method to measure the spectral lines disregarding the continuum completely. Using this method I established a new visible calibration with a precision of 0.08 dex for [Fe/H] and 80 K for T_{eff}. This work is detailed in Chapter 4.

Finally, I also participated in the refinement of the parameters of the star GJ3470 and its planet, where my expertise in stellar parameters of M dwarfs had an important role. The details regarding this investigation are shown in Chapter 5.

Keywords. stars: fundamental parameters – stars: late type – stars: low mass – stars: binaries - general – stars: atmospheres – stars: planetary systems – stars: individual (GJ 3470) – techniques: photometric – techniques: spectroscopic

Contents

List of Tables

List of Figures

Chapter 1

Introduction

There are infinite worlds both like and unlike this world of ours...We must believe that in all worlds there are living creatures and plants and other things we see in this world.
Epicurus (ca. 300 BC)

1.1 Since ancient times...

One of the most fundamental questions that has troubled the human mind for untold millennia is its place in the Universe. Looking at the night sky, the stars and the milky way, humanity of times past wandered about the meaning of the dark sky, the heavens and stars, grouped in constellations, inspiring untold stories of the divine and sparking millions of mythologies. These include, for instance, *The Dreaming* oral tales of creation of the Australian Aboriginals, perhaps spanning longer than 50.000 years into the past (Arthur & Morphy 2005), and inscribed in the first known written documents such as the epic Gilgamesh in Sumeria ($\sim$ 2000 BC, Sandars 1960), or the book of the dead in Ancient Egypt ($\sim$ 1500 BC, Tirard & Naville 2004), among many others.

In fact, it was not so long ago that we know that the Earth, and the other planets in the solar system go around the Sun (Copernicus 1543), and that Galileu Galilei, with his newly made telescope, observed that the milky way is in fact composed by many stars (Galilei 1610). We found out even more recently that our Galaxy is just one among billions of others in the Cosmos (Hubble 1929), and less than 25 years separates us from the first discoveries of planets around other stars (Wolszczan & Frail 1992; Mayor & Queloz 1995). But when did humans start to think that other places, other *worlds*, could exist beyond Earth?

The concept of the pluralism of worlds goes back to the atomist school of Ancient Greece. Leucippus (ca. 500BC), quoted by Diogenes Laertius (ca. 300 AD) in his book *"Lives and Opinions of*

Eminent Philosophers" (Laertius & Yonge 1853) states that *"Leucippus holds that the whole is infinite ... part of it is full and part void ... Hence arise innumerable worlds, and are resolved again into these elements."*. Epicurus (341-270BC), the *garden philosopher*, in *Letter to Herodotus* (Laertius & Yonge 1853) writes that *"There are infinite worlds both like and unlike this world of ours ... we must believe that in all worlds there are living creatures and plants and other things we see in this world..."*. Many others held this view that was, however, based on philosophical deduction and subjective intuition and not on experimentation or observations. In fact, the multitude of worlds that the atomists envisioned was inaccessible, much like a parallel universe of contemporary scientific speculative theories, and the stars in the sky were just small lights in a void, with no relation with the Sun.

At the same time there were others, like Plato (428-348 BC), Aristotle (384-322 BC), and later on Ptolemy (100-168) that defended the existence of only one world in the *Kosmos*. This geocentric view became eventually dominant throughout the Middle Ages, as it sat well with the church theology and was therefore adopted. Despite this, there were still scholars, during the Middle ages, who thought that the idea of one Earth or one *Kosmos* would question god's omnipotent powers. Personalities like Albertus Magnus (1193-1280), german bishop and scholar, mused about the possibility of the existence of other worlds, asking himself, *"...do there exist many worlds, or is there but a single world? This is one of the most noble and exalted questions in the study of Nature."*. It was only in 1440 that Nicholas of Cusa (1401-1464) took the bold step to argue, in his work *De docta ignorantia* (Cusa 1440), that *"life, as it exists on Earth, in the form of men, animals and plants, is to be found, let us suppose, in a higher form in the solar and stellar regions(...) Of the inhabitants then of worlds other than our own we can know less, having no standards by which to appraise them. It may be conjectured that in the Sun there exist solar beings, bright and enlightened denizens, and by nature, more spiritual than such as may inhabit the Moon - who are possibly lunatics..."*.

The publication of Copernicus (1473-1543) *De revolutionibus orbium coelestium* (Copernicus 1543) and the change of the Geocentric to the Heliocentric paradigm together with the observations of Galileu Galilei (1564-1642) stimulated new inquiries regarding the possibility of life in other worlds. The Earth was now just a planet like many others, and these new worlds might also have life and inhabitants. One of the most important advocates of pluralism and also the first person that proposed that other worlds exist around other stars, extrapolating from the ideas of Copernicus, was Giordano Bruno (1548-1600). In his book *De l'infinito Universo E Mondi* (Bruno 1584) he affirms without any doubt that *"there are countless suns and countless Earths all rotating around their suns in exactly the same way as the seven planets of our system"*, and that these worlds are *"...no less inhabited than our Earth"*.

The pluralist ideas continued to grow and became very popular by the 17^{th} Century. Christiaan Huygens (1629-1695), one of the most important astronomers and physicist of all times, wrote, in his famous *Kosmotheoros* (Huygens 1698) that *"what we allow'd the Planets, upon the account of our enjoying it, we must likewise grant to all those Planets that surround that prodigious number of Suns. They must have their plants and animals, nay and their rational creatures too, and those as great admirers, and as diligent observers of the heavens as ourselves..."*. Although the ideas regarding pluralism were based on scientific ground, they remained purely speculative until the middle of the 19^{th} century, when science attained enough technological level to start looking for planets around other stars.

1.2 The first attempts

The first attempts began, quite curiously, with a technique that almost didn't bear yet any fruits on its own: Astrometry (see Sect. A.3) . It was in 1855 that Captain William Jacob of the Madras Observatory, in India, claimed that there was a high probability that the binary star system 70 Ophiuchi had a *planetary body in connection with this system* (Jacob 1855). This was later reinforced by Thomas See (See 1896). However, the planet candidate soon falls into oblivion as Forest Moulton demonstrated that the proposed planet, if existed, would by highly unstable (Moulton 1899).

Throughout the best part of the 20^{th} century some exoplanet detection claims of massive planets were made (e.g. Strand 1943; Reuyl & Holmberg 1943; van de Kamp 1963; McCarthy et al. 1985), but all were later dismissed as being spurious signals, due to instrumental systematics.

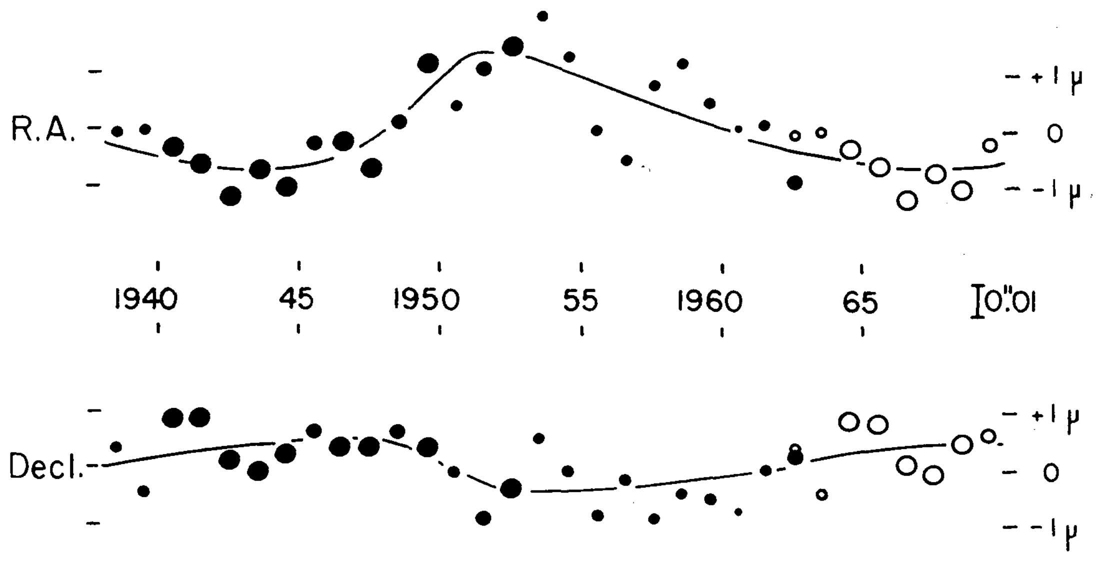

Figure 1.1: Time displacement curves from astrometric measurements of the potential planet discovered by van de Kamp (1963), later shown to be variations of instrumental systematics.

Meanwhile, in 1952, Otto Struve publishes a prescient paper, writing that Jupiter-type planets might exist in orbits as small as 0.02 AU, and that these objects could be found using high-precision radial velocity (Struve 1952). He adds that a close-in 10 Jupiter mass planet could be detected around other stars with 1950's radial velocity technology, estimating that an edge-on orbit of such a planet would have a signal of 2 km/s. With a similar idea, Gordon Walker and Bruce Campbell built the first glass cell of hydrogen fluoride in 1979, and used it as a precise spectral reference against the spectrum of a star. With this technique they achieved the amazing precision of 15 ms^{-1} (Campbell & Walker 1979), and used it to observe 21 stars over 15 years (Campbell et al. 1988). Unfortunately no planets were found, due to the small sample size, and sparse sampling, as they were looking for long-period, Jupiter analogs. It was only in 1989 that another team, lead by David Latham, announced that they found a signal with an amplitude of 600 ms^{-1}, that corresponds to a minimum mass of 11 Jupiter, and a period of 84 days was detected around HD114762 (Latham et al. 1989). The RV signal of this body is shown in Fig. 1.2. However, most posterior studies argue that this object might probably be a brown dwarf or even a low mass M dwarf (e.g. Cochran et al. 1991; Hale 1995; Han et al. 2001).

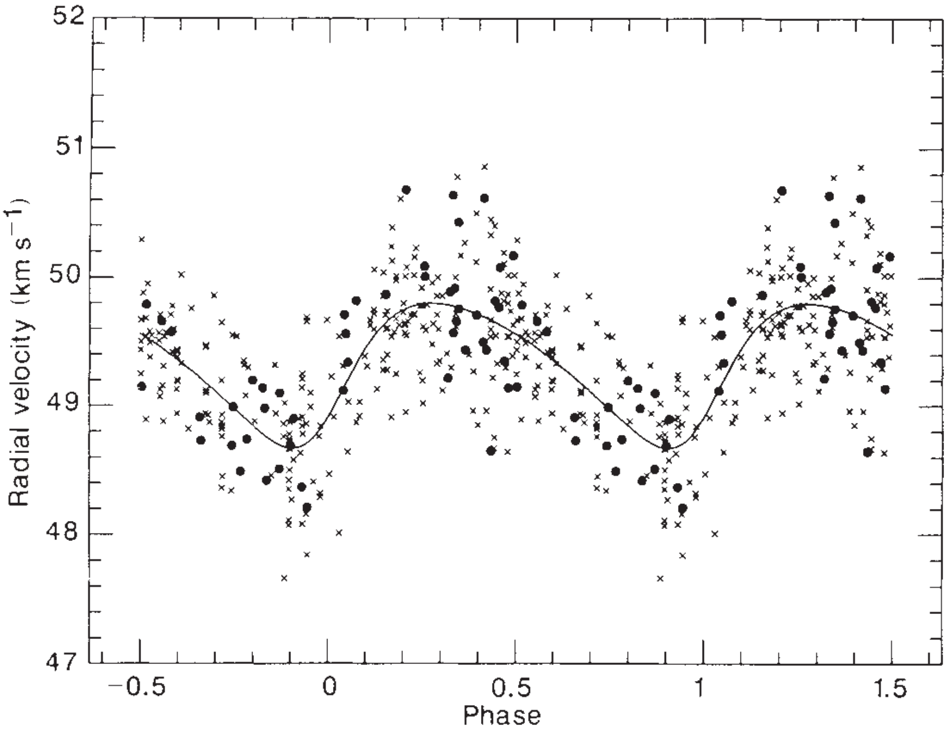

Figure 1.2: Radial velocity curve of the companion of HD114762, with a period of 84 days and a minimum mass of 11 M_J. From Latham et al. (1989).

At the same time that the radial velocity techniques were being developed, another very different technique was concurrently emerging and used towards a very specific type of targets: ultra-precise timing of pulsars at radio wavelengths. Pulsars are neutron stars where the magnetic axis is aligned with Earth. Neutron stars are the remnants of a massive star with a mass in excess of 8 $M_\odot$. The first attempts of detecting planetary bodies around these dead stars (Hills 1970; Bailes et al. 1991) were all retracted as false positives. The first real detection of an extra-solar planet around a pulsar came in 1992 by Wolszczan & Frail (1992). Since then several other pulsar-planets were detected but they don't attract so much popular attention as they are considered dead worlds.

1.3 The first discovery around a main sequence star

Finally, in 1995, an amazing announcement was made. Michel Mayor and Didier Queloz, from the Geneva Observatory, announce that they discovered a 0.5 Jupiter mass planet in a 4.2 day orbit around a solar type star, 51 Peg (Mayor & Queloz 1995). The detection of the first planet was possible due to an unprecedented increase in precision and efficiency made possible by the ELODIE spectrograph (Baranne et al. 1996), commissioned in 1993 at the Observatoire de Haute Provence (OHP), that uses a cross correlation technique. ELODIE used a system with two simultaneous fibre feeds, one for the starlight, and another for the spectrum of a ThAr lamp, used as reference, a technique first described by Griffin & Griffin (1973). Using this new method, a velocity precision of about 13 ms^{-1} was achieved. Fig. 1.3 depicts the radial velocity curve of the extrasolar planet 51 Peg b, from that instrument.

From the first discovery until today 21 years have passed, and the number of confirmed exoplanets

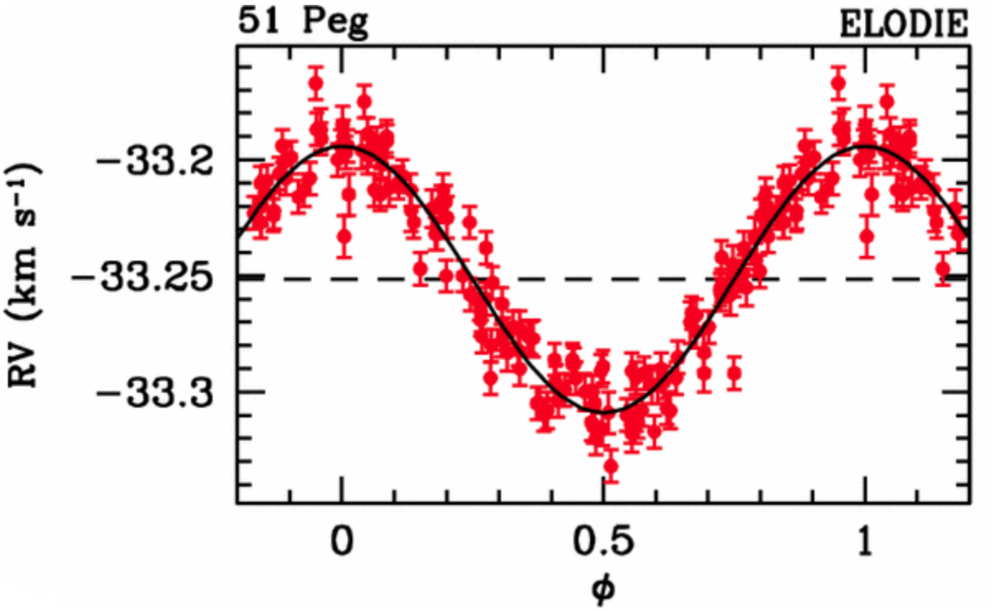

Figure 1.3: Radial velocity curve of the detection of the first extrasolar planet around the star 51 Peg. Taken from Mayor & Queloz (1995).

has grown spectacularly. As of 10/07/2013 the extrasolar planet encyclopaedia (Schneider et al. 2011) counts 908 exoplanets around 700 stars, including 140 multi-planet systems. These planets were detected using a series of different techniques, described in detail in Appendix A.

1.4 Planets around M dwarfs

From the radial velocity and photometric transit programs about $\sim$ 48 planets were found around 28 confirmed M dwarfs. One of the main reasons that led to the growing interest in studying M dwarfs is the fact that, for an equal radial-velocity and transit depth precision, it is easier to detect lower mass planets around these stars. Indeed, the smaller M star mass and radius imply that the reflex velocities induced by planets around them, as well as the transit depths, are considerably larger, when compared to the same effects induced in the more massive, and better studied, FGK stars. For instance, if we consider an Earth-mass planet in a circular, pole-on orbit, with a 1-year period orbiting around two different stars with masses of 1 $M_\odot$ (solar-type) and 0.3 $M_\odot$ (typical M dwarf) we obtain a radial-velocity semi amplitude K of 0.10 and 0.30 ms^{-1} respectively (see Appendix A).

Also, and very important for the current planet-detection programs, is the fact that the habitable zone in these stars are situated in tighter orbits, which makes the detection of planets in this area easier with radial velocity and photometry, as both have their best sensitivity closer to the host star (e.g. Nutzman & Charbonneau 2008), as shown in Fig. 1.4. In this context it is critical to obtain more precise values of stellar mass and radius, as the precision of the planetary mass and radius directly depends on them. But what are M dwarfs?

M dwarfs are the faintest, smallest, and coldest of all stars in the main sequence (MS) and are situated in the bottom right corner of the HR diagram, as shown in Fig. 1.5. M dwarfs are everywhere. Ubiquitous and long lived, M dwarfs comprise $\sim$ 70% of the stars in the galaxy (e.g. Covey et al.

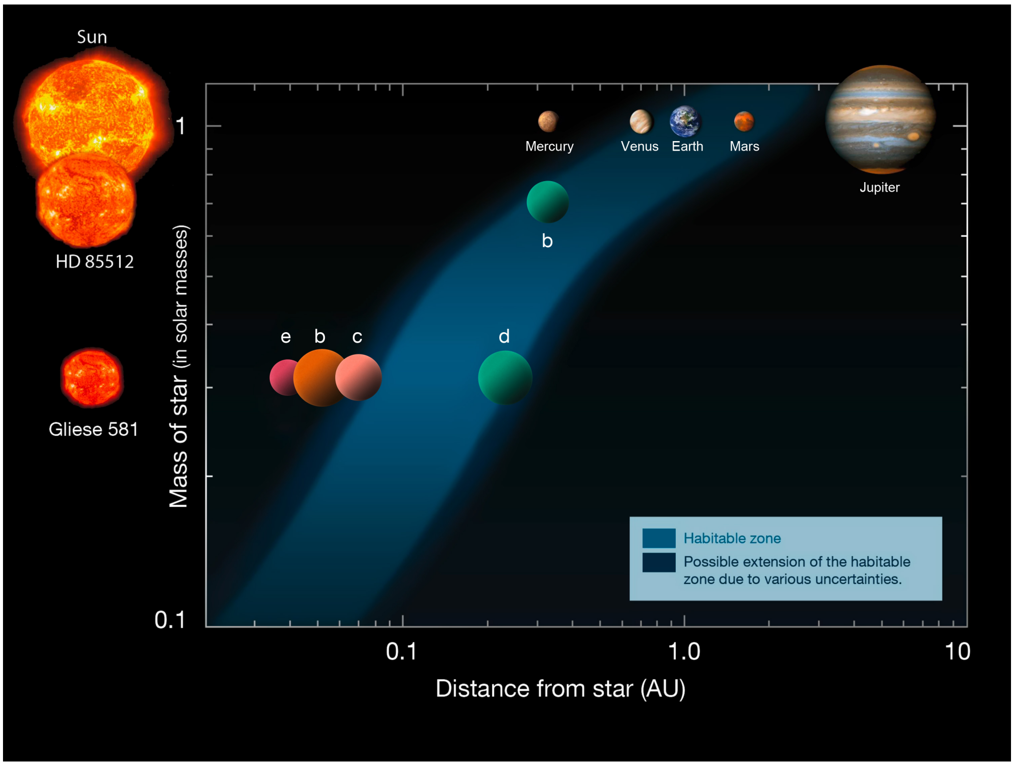

Figure 1.4: The stellar mass versus distance from the star. The habitable zone is depicted as a blue band. From ESO.

2008; Bochanski et al. 2010) and around half of its baryonic mater (Chabrier 2003). Despite being so omnipresent and a lot of them being just around the corner, not a single M dwarf can be seen with the naked eye, due to their very low intrinsic brightness. They have a very small mass and radii, between 0.6 to 0.08 $M_\odot$, and 0.6 to 0.1 $R_\odot$ respectively. Early-type M dwarfs have a large convective envelope and a small radiative core which, however, contains about 90% of the stellar mass, for a M0 0.55 $M_\odot$ star. As the spectral type decreases to M2/M3, the mass fraction drops to 70% for a 0.4 $M_\odot$ star, and when it reaches M4 (and mass $\sim$0.25 $M_\odot$), the star becomes fully convective (Reid & Hawley 2005).

They are also one of the least understood stellar types: M dwarfs are hard to study, not just due to their intrinsic faintness but mostly due to their highly complex spectra, where the continuum regions are impossible to identify, at least in visible wavelengths (e.g. Gustafsson 1989). Fig. 1.6 shows a region of a high-resolution spectrum of a typical G dwarf star (above) and an M-dwarf (below). In the G dwarf star the continuum and the lines are very well defined,while the M dwarf spectrum looks just noise. Surprising as it may be, in this Figure the M dwarf has a higher SNR. The observational spectra of these stars get more and more complex as the stellar subtype increases, due to the increasing presence of billions of weak molecular lines (TiO, VO, H_2O, CO, FeH, etc), that blend with other atomic lines and depress the continuum, making a classical spectral analysis very complicated. For late M dwarfs, the atomic line analysis becomes impossible. One alternative would be to use high-resolution spectral synthesis (e.g. Valenti et al. 1998), but this method does not yet reproduce the fine details of high-resolution spectra of M stars due to incomplete knowledge about the molecular line transitions, and opacities (e.g. Bean et al. 2006b; Önehag et al. 2012).

The study of M stars is also increasingly important in the context of planet formation around very low mass stars. The initial conditions of planet formation (e.g., disk mass, temperature and density

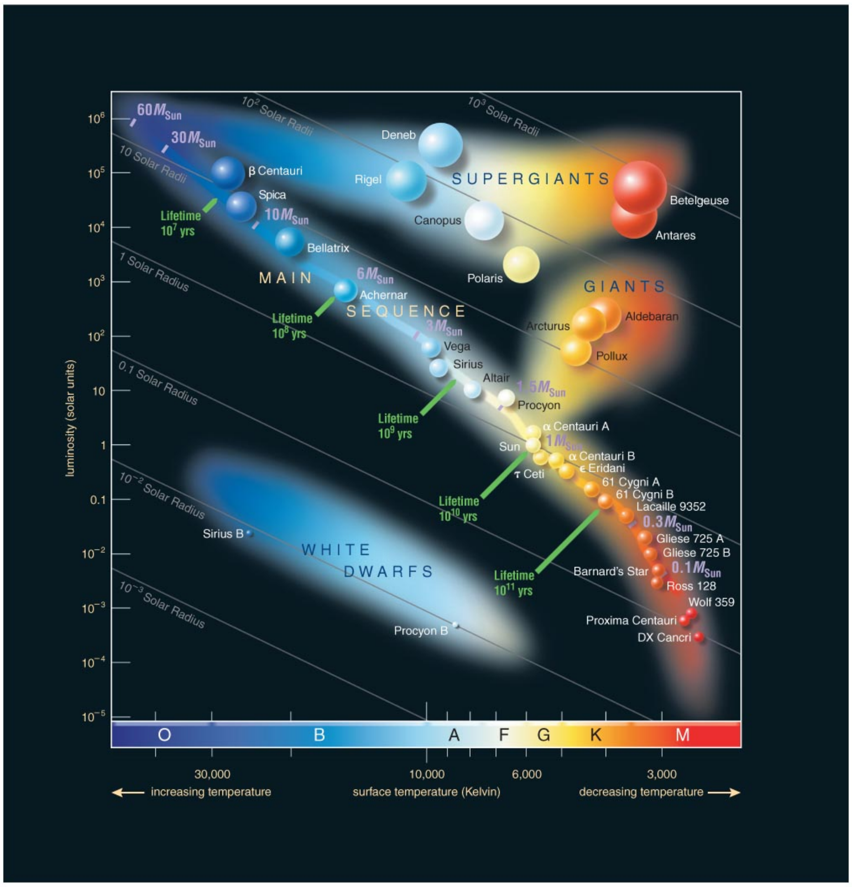

Figure 1.5: The HR Diagram. The M dwarfs are situated at the bottom right corner of the main sequence. From Pearson Education Inc.

profiles, gravity, gas-dissipation and migration timescales) all change with stellar mass (e.g. Ida & Lin 2005; Kornet et al. 2006; Kennedy & Kenyon 2008; Alibert et al. 2011). Some theoretical models on the formation of planets on M dwarfs predict that the formation of giant planets is seriously inhibited around the less massive stars (e.g. Laughlin et al. 2004; Ida & Lin 2005; Kennedy & Kenyon 2008). According to them, the formed rocky or ice cores do not have enough time to get a gas envelope and become super-earths or ice giants instead. Others suggest that the proto-planets may have enough time to grow and to accrete the gas envelope before the disk vanishes, by invoking migration and faster accretion (e.g. Alibert et al. 2005, 2011). Alternatively, Boss (2006a,b) show that the disk instability hypothesis can also play a role in the formation of planets around M dwarfs. Indeed, an increasingly number of planets are being detected around these stars and they show that most planets have, on average, a lower mass than those found on FGK stars, the majority being neptunians and super-earths (e.g. Bonfils et al. 2007; Udry & Santos 2007; Bonfils et al. 2013).

Besides mass, stellar metallicity also plays a major role in the efficiency of the formation of giant planets, as shown by both models (e.g. Ida & Lin 2004b; Mordasini et al. 2009a, 2012) and observational data, for FGK dwarfs, in the form of a giant planet-metallicity correlation (e.g. Gonzalez 1997; Santos et al. 2004b; Fischer & Valenti 2005; Sousa et al. 2011), that seems to partially vanish for Neptunian and smaller planet hosts (Sousa et al. 2008; Ghezzi et al. 2010; Sousa et al. 2011; Mayor et al. 2011; Buchhave et al. 2012). Recent observational works for M dwarfs are in line with a planet-metallicity correlation (e.g. Bonfils et al. 2007; Johnson & Apps 2009; Schlaufman & Laughlin 2010; Rojas-Ayala

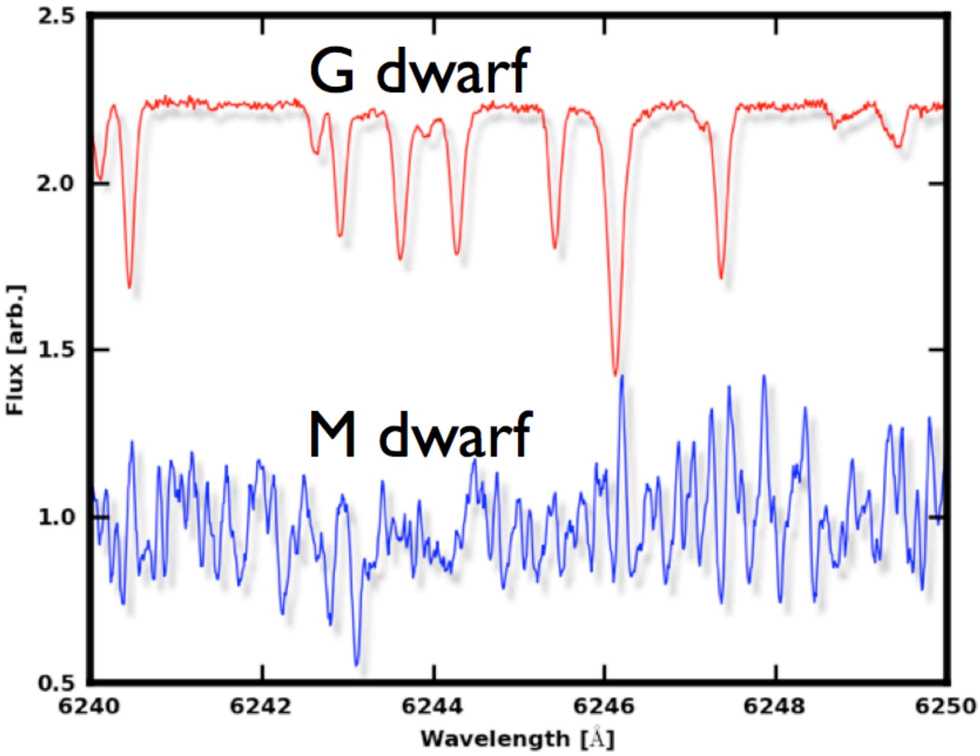

Figure 1.6: Chunk of two HARPS spectra of a typical G dwarf (above) and an M dwarf (below). From Bonfils (2012).

et al. 2012; Terrien et al. 2012). However, more detections of planets around M dwarfs and a more precise metallicity determination are needed to achieve higher confidence levels.

1.5 Planetary system formation

As the number of detected planets increases, one can observe that planetary systems in nature are incredibly diverse in terms of masses and orbital periods, ranging from a fraction of an Earth mass to tens of Jupiter masses, and from a few orbital days to hundreds of years. Most of these systems are very different from our own Solar System, forcing a deep review on the paradigm of core-accretion planetary formation (e.g. Pollack et al. 1996) and opening new possibilities of planetary formation, like the gravitational disk instability (e.g. Boss 1997).

The different planetary systems, including our own, are thought to form as byproducts of the natural evolution of star formation. It is commonly accepted that stars start to form from the gas and dust of a molecular cloud that experiences a gravitational collapse due to an external factor (e.g., supernova shockwave; O, B star stellar winds; other sources of supersonic turbulent flow). This phase corresponds to stage 1 of Fig. 1.7 and lasts approximately 2 Myr. Then, the cloud fragments into tens, hundreds or thousands of fragments, in a process with a timescale of the order of 10^4 yr (stage 2 of Fig 1.7.)

Afterwards, in stage 3, the fragmentation stops and the protostellar embryo continues to grow by accreting more dust and gas. However, the material of and around the protostar carries non zero angular momentum, meaning that the collapsing material will not fall directly into the protostar but onto a flat rotating disk, perpendicular to the angular momentum of the embryo (phase 3 of Fig. 1.7). This prevents

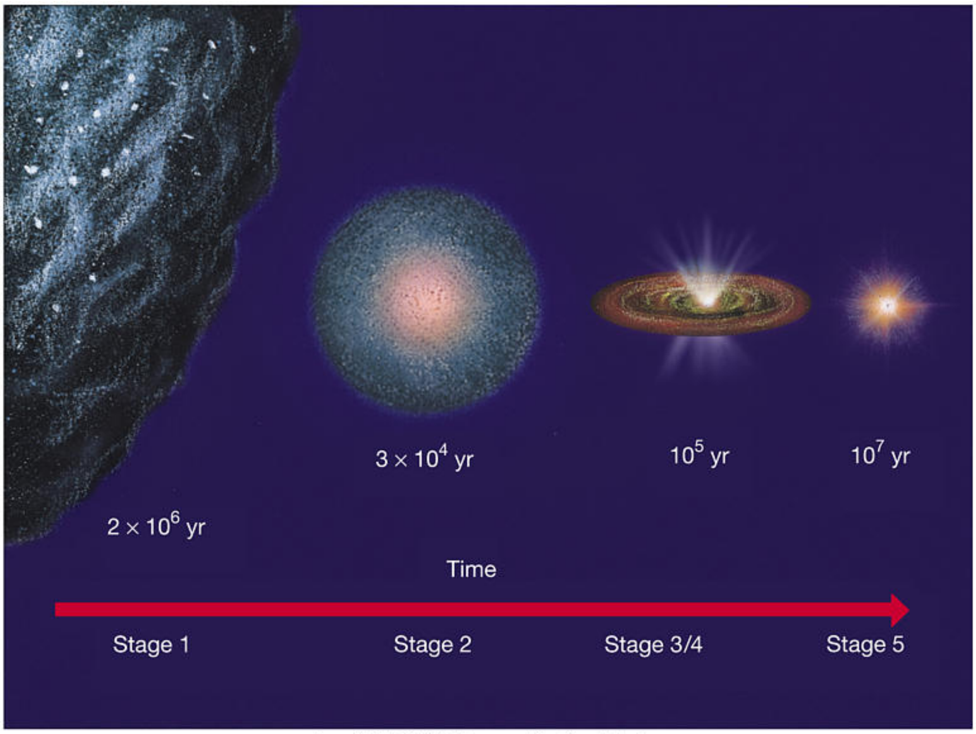

Figure 1.7: Illustration of the process of star formation and evolution, from the primordial cloud of gas and dust to the first sustained thermonuclear reactions inside the stellar core.

the rapid accretion of the disk dust and gas, which makes planet formation possible.

Viscosity, accretion, grain coagulation and photoevaporation all contribute to the evolution from a massive accretion disk to a less dense protoplanetary disk (phase 4 of Fig. 1.7). After this phase, the protostar enters in its last evolution phase to the main sequence as a class III object, where the initial disk has been largely cleared (phase 5 of Fig. 1.7). For a complete review, see for example, McKee & Ostriker (2007).

Fig. 1.8 shows a possible evolution for planet formation and evolution, from the initial molecular cloud to the formation of planets. Most massive accretion disks do not survive more than 1 Myr, that then evolve to protoplanetary disks with little or no accretion and last for 1 to 10 million years. Later on debris disk form due to collisional processes between protoplanetary bodies.

Planets are thought to form mainly through core-accretion processes (e.g. Safronov 1972; Pollack et al. 1996), that consists in the progressive agglomeration of material, from dust settling to the build up of planetesimals with sizes of the order of $\sim$ km caused by collisional processes or gravitational instabilities. From here, planetesimals collide and agglomerate together forming, in most cases, rocky planets in the inner disk, within the ice line or form, in general, a mixture of icy and rocky cores of giant planets, beyond the ice line. Finally, when the cores that mostly form in the outer disk reach a critical size, typically estimated to be of the order of ten earth masses, a runaway process of gas accretion start, enabling the rapid formation of gas giant planets within the typical timescale of 10 Myr of the protoplanetary disk existence (e.g. Haisch et al. 2001; Thommes et al. 2008; Youdin 2010).

However, the formation of some giant planets (and brown dwarfs) may also be caused by gravitational disk instability. This alternative scenario is similar to the one of stellar formation and is based

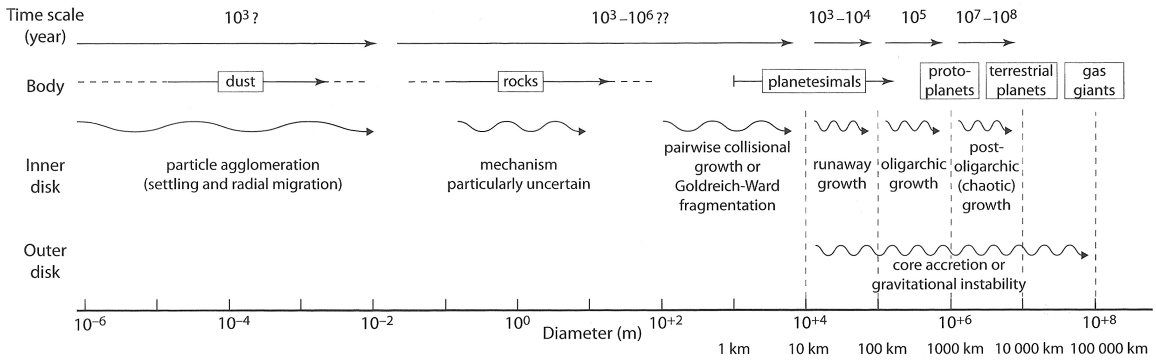

Figure 1.8: Schematic of the growth of planets, starting with sub-micron dust up to terrestrial and Jovian-type planets. The timescale of each process is given, along with the uncertainties still associated to the understanding of the planet formation process. From Perryman (2011).

on the hypothesis that parts of the protoplanetary disk may become gravitationally unstable during their evolution and growth. Then, they may fragment, forming giant protoplanets in relatively fast timescales, as short as 1000 years (e.g. Boss 1997).

Before the protoplanetary disk disappears completely, the gas viscosity, as well as the planet-planet gravitational interaction, allow the planetary system bodies to migrate inwards or outwards (see e.g. Trilling et al. 1998; Armitage 2010). After around $\sim$ 100 Myr the planet formation process is complete.

From the huge diversity of planetary system configurations one can analyze the distribution of the different planet and stellar parameters, such as mass, period, eccentricity, metallicity, and interpret them as a kind of fossil record of the processes of planet formation and evolution (e.g. Udry & Santos 2007).

1.6 Host star properties

The formation and evolution of extrasolar planets and their host stars are intrinsically connected. Therefore it is logical to expect that some of the properties of the star, such as metallicity, mass, effective temperature and abundances correlate with the parameters of their planets.

1.6.1 Planet-metallicity correlation

At the time the first extrasolar planets were being discovered, studies regarding their host stars properties found that planet host stars were systematically metal-rich compared to the field stars (Gonzalez 1997; Santos et al. 2001). A few years later, with the availability of larger uniform samples, it was confirmed that the giant planet frequency for FGK dwarfs rises exponentially with the host star metallicity (e.g. Santos et al. 2004b; Fischer & Valenti 2005), as shown in Fig 1.9. The exact slope of the metallicity dependence is still debated however (e.g. Johnson et al. 2010a; Mortier et al. 2013).

Three hypothesis were formulated to explain this correlation: 1) the primordial hypothesis, that proposes that the enhanced metallicity of the primordial disk increases the probability of planet formation (Pinsonneault et al. 2001; Santos et al. 2003); 2) the pollution scenario, where the infall of planetary

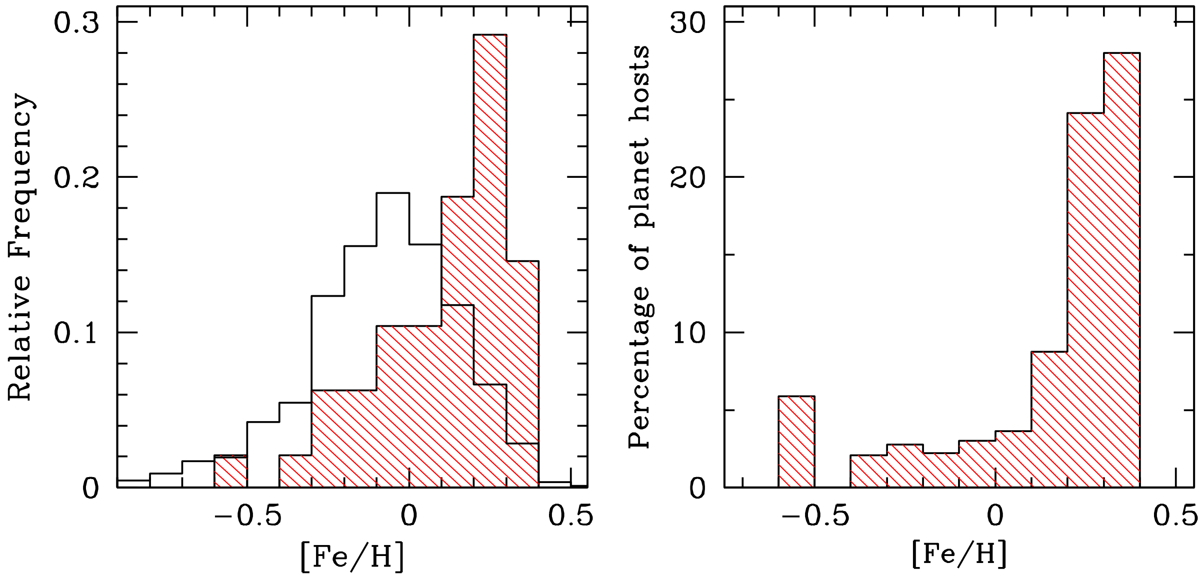

Figure 1.9: *Left panel:*[Fe/H] distributions for 98 planet host stars (hashed red histogram) of the CORALIE sample and for the 875 star CORALIE sample (solid line histogram). *Right panel:* Planet frequency of the CORALIE planet-search program. From Santos et al. (2004b).

material have enriched the outer layers of the star, making them metal-rich (e.g Gonzalez 1998; Pasquini et al. 2007), and 3) the existence of an orbital period bias due to the dependence of migration rates on metallicity (Livio & Pringle 2003).

Except for some punctual cases where an excess of some elements in a few stars has been discussed (e.g. Israelian et al. 2003; Laws et al. 2003), the quantities of engulfed planetary material could not significantly change the average metal content of the host star (e.g. Montalbán & Rebolo 2002; Santos et al. 2003). In fact, in the pollution scenario, we should expect a trend of metallicity with the length of the convective zones on FGK dwarfs (e.g. Pinsonneault et al. 2001; Santos et al. 2003), but the trend is not detected.

Regarding the last hypothesis, a weak trend of metallicity with orbital period was found (Gonzalez 1998; Sozzetti 2004), but not confirmed. Moreover, in theoretical studies, the effect of [Fe/H] on the migration rate may not be strong enough to have any discernible effect (Livio & Pringle 2003).

Most results suggest that the higher content of metals is primordial and therefore reflects the metal content of the molecular cloud where the star was formed (e.g. Pinsonneault et al. 2001; Livio & Pringle 2003; Santos et al. 2004b; Fischer & Valenti 2005). Several core accretion models can reproduce the observed correlation thus corroborating the observational results (e.g. Ida & Lin 2004a; Benz et al. 2006; Mordasini et al. 2009b, 2012).

For lower mass planets, the so-called Neptunians and Super-Earths, the planet metallicity-relation simply vanishes (e.g. Udry et al. 2006; Sousa et al. 2008, 2011; Buchhave et al. 2012, see Fig. 1.10). The flat relation is supported by core-accretion models, as several works (e.g. Ida & Lin 2004a; Benz et al. 2006; Mordasini et al. 2012) show that planets with masses lower than 30 $M_{\oplus}$ should be evenly distributed across all [Fe/H] ranges, or even exist preferentially around metal-poor stars (e.g. Benz et al. 2006; Mordasini et al. 2012). This result is easily explained by the fact that the relative lack of metals in the protostellar disk will increase the time of formation of the protoplanet cores, that may not have time to accrete enough gas to become giant planets.

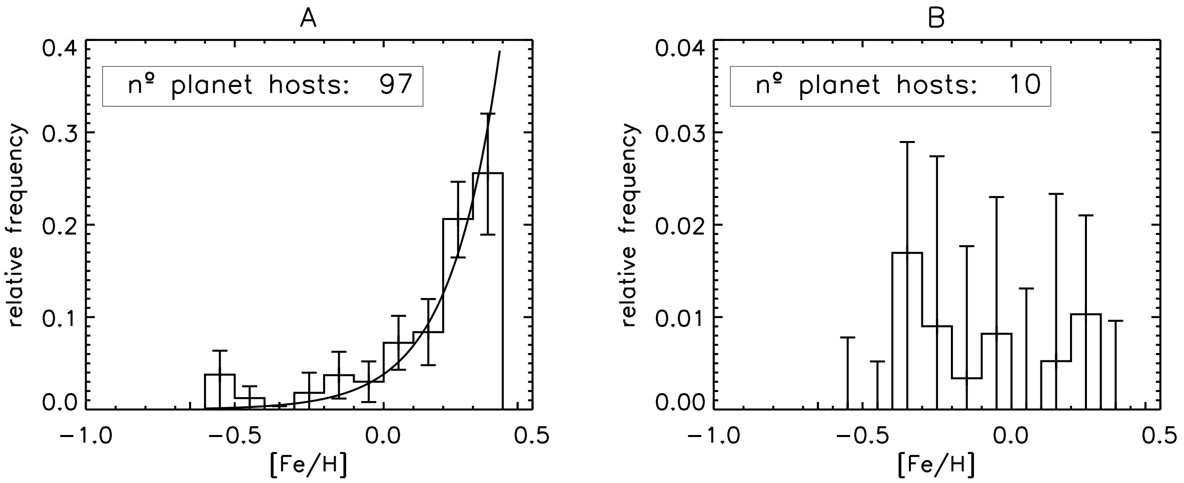

Figure 1.10: Frequency of planet-hosts as a function of [Fe/H] for the all planet hosts (*left panel*), and for planet-hosts with only Neptunian planets (*right panel*), of the volume-limited 582 FGK HARPS star sample (Sousa et al. 2011).

Regarding more massive stars, like intermediate mass subgiants ($1.3 < M_{\odot} < 1.9$) and giants, the [Fe/H] trend seems to be weaker or non-existent (e.g. Pasquini et al. 2007; Takeda et al. 2008), but other works reach the opposite conclusion (e.g. Hekker & Meléndez 2007). Nevertheless, the frequency of giant planets around these stars is higher than their lower mass counterparts (Johnson et al. 2007; Lovis & Mayor 2007; Johnson et al. 2010a), meaning that, on average, the stellar mass may have a greater importance in higher mass stars.

These results have significant implications in constraining models of planet formation. In Sect. 1.5 we saw that we have two main models of planet formation: core-accretion and disk instability. The first one predicts a metallicity-giant planet correlation, the second one does not, in general. Therefore, the fact that the percentage of planets around metal-rich star is higher favours the core-accretion model as the dominant mechanism for planet formation.

1.6.2 Planet-stellar mass correlation

The evidence of a planet-stellar mass correlation is not as easy to establish as its metallicity counterpart. The detection biases are harder to correct, as the RV sensitivity changes both with brightness and stellar mass.

Early works on the planet-stellar mass link have shown a weak correlation of giant planets with increasing mass, with hints that higher mass stars, up to 1.5 $M_{\odot}$ may have a higher giant planet frequency (e.g. Laws et al. 2003). This hint was reinforced by works on M dwarfs, where giant planets are scarce (Endl et al. 2006; Butler et al. 2006; Bonfils et al. 2007) and more frequent at intermediate mass subgiants and giants (Johnson et al. 2007; Lovis & Mayor 2007). At the same time it seems that there are indications that planets around more massive stars tend to have higher masses (e.g. Lovis & Mayor 2007). Core-accretion models support these results as it is predicted that planet formation efficiency should increase with stellar mass (e.g. Laughlin et al. 2004; Ida & Lin 2005; Kennedy & Kenyon 2008; Alibert et al. 2011). Another mechanism that may come into play is the ‘compensation effect’ (e.g.

Thommes et al. 2008; Mordasini et al. 2012), where a lower metallicity can be compensated by a higher disk mass to allow giant planet formation (and vice-versa). Moreover, the existence of both a planet-metallicity and planet-stellar mass relation suggests that the surface density of dust is very important in the planet formation process (e.g. Laughlin et al. 2004; Ida & Lin 2004b; Robinson et al. 2006).

More recently, a study of Johnson et al. (2010a) quantifies a mass-metallicity-planet function, where the frequency of giant planets is defined by the functional form $f_p = C.(M_\star/M_\odot)^\alpha.10^{\beta.[Fe/H]}$. C, α, and β have the best fit values of 0.07, 1.0, and 1.2 respectively. They reach the conclusion that this function has a much higher significance than a similar one with only the [Fe/H] dependence. Quantitatively, this translates into an Bayesian evidence 2400 times higher for f_p than for the metallicity only model, according to Kass & Raftery (1995). However, a recent work by Mortier et al. (2013) has tested different functional forms using a HARPS+CORALIE sample of 1798 stars, and did not find any difference between different functional forms (metallicity & mass dependence, only metallicity dependence, only mass dependence, and a combination of different functions, including cutoff or a constant for lower [Fe/H] values) with stellar mass and [Fe/H] or with only metallicity (see Fig. 1.11). The Bayesian evidence ratio between the different functions sits between 1.0 and 4.12 meaning a very low preference between models. They also predict that it will only be possible to disentangle between the different functional forms with a sample of about 5000 stars.

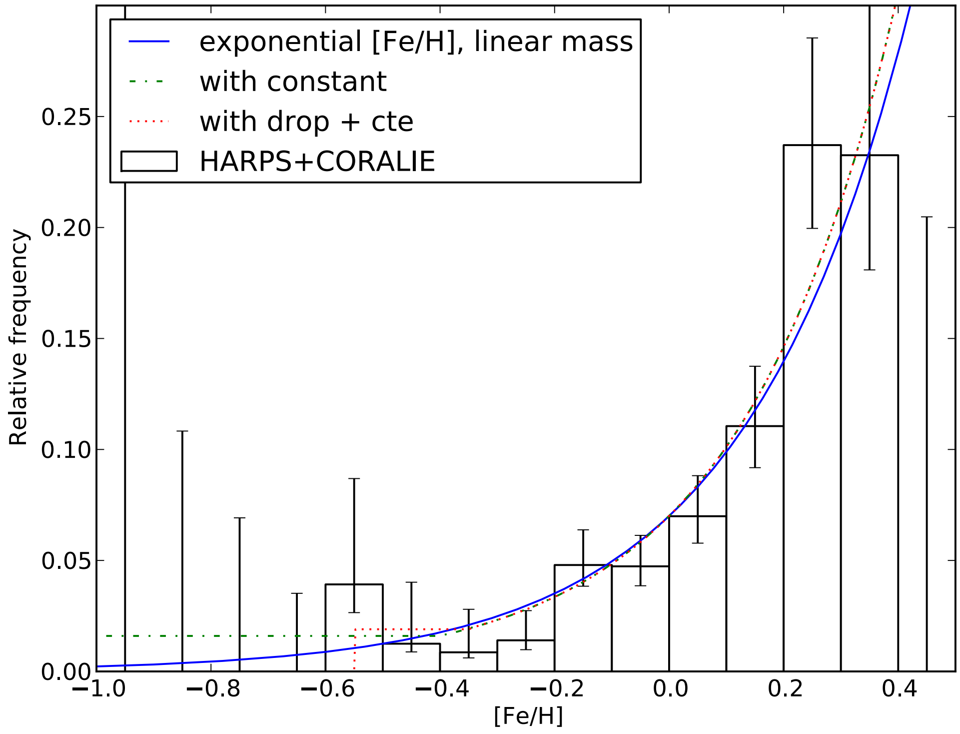

Figure 1.11: Frequency of giant planets as a function of stellar mass and metallicity, using the CORALIE+HARPS 1798 star sample. Three functional forms are plotted. The solid blue line corresponds to an exponential fit of [Fe/H] considering a linear increase with mass, the green dashed line depicts an exponential form with [Fe/H] and a constant, and the red dotted line an exponential form with [Fe/H] plus a constant and a drop. From Mortier et al. (2013).

Finally, the results on stellar mass and metallicity show that core accretion seems to be the primary formation mechanism for planet formation, supported by the existence of planet-mass and planet-metallicity correlations, at least for closer in planets. Disk instability may be more important in massive planets with very wide orbits (Dodson-Robinson et al. 2009) like the ones observed by direct imaging (e.g. Kalas et al. 2008; Marois et al. 2010).

1.6.3 Evidence from chemical abundances

The study of elements other than iron, usually used as a metallicity proxy, can be of great importance. The measurement of abundances, from light elements up to alpha (synthesised in part in the massive stellar cores but mostly in Supernova explosions by means of alpha particle capture, e.g., Si, Ca, Ti, Sc) and iron group elements (mostly formed in Supernovae type Ia, like Cr, Va, Co, Ni, Mn), can give a more detailed insight into the process of planetary formation and evolution. If the planet-metallicity correlation holds, all elements, in general and on average, should be overabundant in planet host stars. However, if the overabundance of refractory elements is caused by pollution, then we should see, on average, an increased abundance of refractory elements only due to more effective evaporation of the volatile elements (e.g. Smith et al. 2001).

For instance, the ratio of $^6Li/^7Li$ may give us clues regarding the pollution of a star by a falling exoplanet, because it is expected that ^7Li will survive longer inside the lower mass sequence dwarfs and is thus thought to be much more abundant that the lighter lithium isotope, that is readily destroyed during the pre-main sequence lifetime of the star (e.g. Forestini 1994; Montalbán & Rebolo 2002). Therefore, any positive ratio may signal a planetary ingestion. A ratio of 0.05 dex was found by Israelian et al. (2001, 2003) in the host star HD82943 that could explain the accretion of a planet with about 1 M_J. However, other works did not confirm this result (Reddy et al. 2002; Ghezzi et al. 2009).

The abundance of ^7Li itself may also be lower for planet host stars, as shown by numerous works, but only for a very limited temperature range (5600-5850 K) (Israelian et al. 2004; Chen & Zhao 2006; Takeda et al. 2007; Gonzalez 2008; Israelian et al. 2009, see Fig. 1.12), but other authors did not observe any difference (e.g. Luck & Heiter 2006). This difference of ^7Li, if it exists, may be caused by planet migration within the disk (Israelian et al. 2004; Chen & Zhao 2006; Israelian et al. 2009), or a sudden transfer of angular momentum from the disk to the star. Both processes cause a spin-up of the stellar rotation, thus preserving the lithium content longer.

Another light element that may give us highlights about the formation process is beryllium. Be is destroyed inside the stars at a higher temperature than Li, and it is therefore expected that the Be will survive in late G and K stars but Li not. The measurement of both elements can give us clues regarding the mixing and the variation of the angular moment of the system (Santos et al. 2002). No significative differences were found between host and non-host stars (e.g. Santos et al. 2004a,c; Delgado Mena et al. 2011; Gálvez-Ortiz et al. 2011; Takeda et al. 2011; Delgado Mena et al. 2012).

For other volatile elements, such as C,O, S, and others, the general conclusion is that the abundance of those elements follows the same trend as [Fe/H], while the abundance relative to iron does not differ between planet and non-planet hosts (e.g. Bond et al. 2008; Delgado Mena et al. 2010; González Hernández et al. 2010; Brugamyer et al. 2011).

Some refractory elements (e.g., Al, Ca, Ti, Mg, Ni, Si...) were also studied, and it was confirmed that, in general, they would follow the same trends as iron. The same studies also show that, in general,

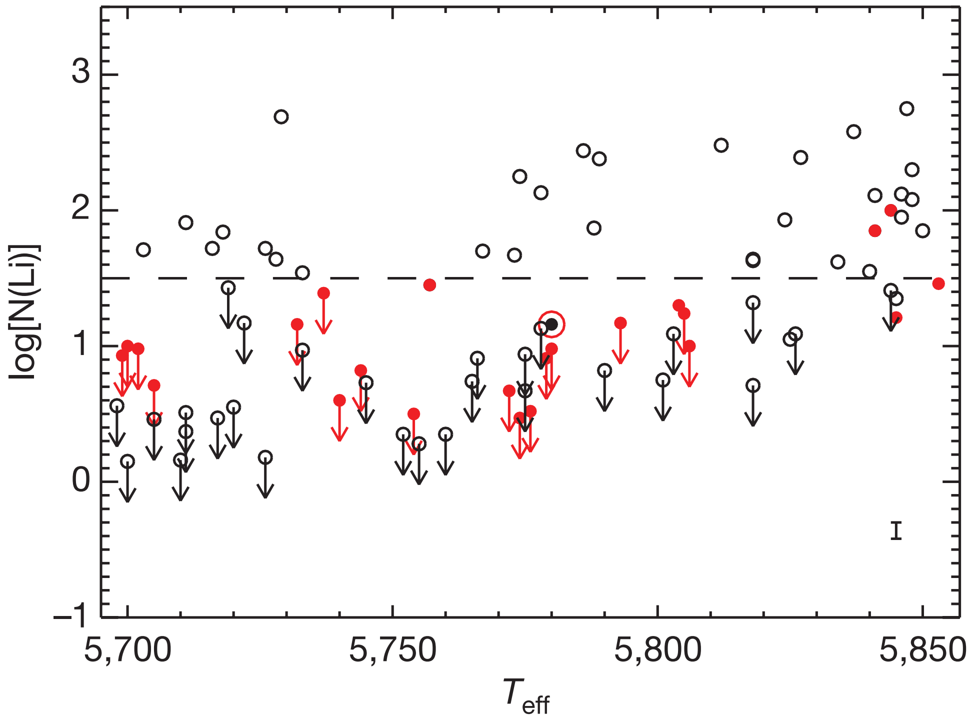

Figure 1.12: Lithium abundances as a function of effective temperatures for solar-analogs with (red circles) and without (open circles) planets. The symbols with down arrows indicate upper limits. From Israelian et al. (2009).

there is not a significant difference between the abundance of refractory elements relative to iron between planet hosts and non-hosts (e.g. Bodaghee et al. 2003; Beirão et al. 2005; Gilli et al. 2006; Bond et al. 2006; Takeda 2007; Neves et al. 2009; Adibekyan et al. 2012b). However, Adibekyan et al. (2012a) found that, for lower metallicity planet-hosts, some alpha elements are overabundant, implying that they also have an important role in planet formation. The trends seem to be also the same for heavy elements, beyond the iron peak (e.g. Bond et al. 2008).

Finally, several works investigated the trends of the abundances, from light elements to refractories, with the element's condensation temperature (T_C). An increasing trend with the condensation temperature must be expected if the overabundance of the heavier elements is caused by pollution . On the other hand, if the origin of the overabundance is primordial, no trend with condensation temperature should be observed. In this regard the results are contradictory. For instance Ecuvillon et al. (2006) does not find any trend with T_C. However, Meléndez et al. (2009) in his work about solar twins (stars with a temperature, [Fe/H] and surface gravity very similar to the Sun) finds that the Sun is overabundant in volatile elements, but under-abundant in refractories compared to the solar twins with giant planets, while having a very similar trend to the solar twins without giant planets. They put forward the hypothesis that the "missing" refractory elements have been used to form terrestrial planets. This result was later confirmed by Gonzalez et al. (2010).

However, González Hernández et al. (2010) investigated the same trends as Meléndez et al. (2009) and found that there were no conclusive trends with T_C. Afterwards, Ramírez et al. (2010) again confirmed the results of Meléndez et al. (2009), using a wider sample, and found that the differences were bigger for $T_C > 900$ K. They also showed that the under-abundance of volatiles in solar twins with planets found by González Hernández et al. (2010) were biased due to Galactic chemical evolution, as these stars were, on average, metal rich. Later on, González Hernández et al. (2011) reanalysed his data and removed the Galactic chemical evolution trend from his results, but didn't find any trend with T_C.

Taking all results of the different elements into account, the dominating opinion among researchers is that the cause of the metal enrichment in planet-host stars is primordial, and that these stars have formed in metal-rich molecular clouds.

1.7 The Thesis

During my thesis I set out to answer some of the outstanding questions regarding M dwarfs and the star-planet connection. The main goal of my Ph.D. is the study of the relation between stellar parameters of M dwarfs and extrasolar planets, aiming to find statistical clues to the processes of planet formation and evolution. In order to reach this goal it is necessary to find more precise methods of determination of stellar parameters of M dwarfs, in special metallicity and effective temperature, when compared with present state-of-the-art studies. To achieve this, different strategies were developed, using high-resolution spectra, as well as photometric and astrometric data.

The drive for higher precision is important in two ways. First, it allows the search for new statistical clues for planet formation and evolution. Second, a higher precision of the stellar mass and radius enables the obtention of more precise measurements of the planetary mass and radius, as shown in Eq. A.1 and A.2, for the radial velocity technique, and in Eq. A.3 and A.4 for the transits. During this work I investigated both avenues.

In my first year of PhD, I pursued a way to upgrade the metallicity calibration of Bonfils et al. (2005) (see Sect. 2.4.1). The original goal was to use FGK+M binaries to get a precise measurement of [Fe/H] from the primaries, using classical spectroscopic analysis, and then use high-precision and homogeneous visible and infrared photometry of the M dwarf secondary to establish a new [Fe/H] calibration. I could not get enough FGK+M binaries with precise V photometry to put forward a competitive photometric calibration. I ended up using our sample of 23 binaries to test the available M dwarf photometric calibrations of Bonfils et al. (2005), Johnson & Apps (2009), and Schlaufman & Laughlin (2010), that have similar dispersion, around 0.2 dex, but suffer from systematics at the ± 0.1 dex level. I found that the Schlaufman & Laughlin (2010) calibration has the lowest offsets and dispersion against our sample and marginally refined that calibration. This work culminated with a publication, Neves et al. (2012), shown in Chapter 3.

During the second and third year of my PhD I investigated spectroscopic methods that could potentially be more precise than photometric methods to obtain metallicities and effective temperatures of M dwarfs. I concluded, from our previous work (Neves et al. 2012), that the photometric methods were reaching their limit. I assumed that, at the time, the available photospheric models were not complete enough to use synthetic spectra derived from them. Therefore, I used available HARPS M dwarf spectra from our group (Bonfils et al. 2013) to establish an empirical spectroscopic calibration anchored on the [Fe/H] values from our previous work (Neves et al. 2012) and T_{eff} values from Casagrande et al. (2008). I achieved a precision for [Fe/H] and T_{eff} of 0.08 dex and 100 K respectively. From here I quantified the frequency of Jovian and Neptunian planet hosts as a function of [Fe/H], confirming the trend of the presence of giant planets around metal-rich stars, as in FGK dwarfs, as well as the non-relation of Neptunians and smaller planets with metallicity (e.g. Sousa et al. 2011). A hint of an anti-correlation of [Fe/H] with the presence of Neptunian and smaller planets was found but it was not possible to statistically distinguish it from the simpler flat relation. Fig 1.13 illustrates, in the upper panels the histograms of [Fe/H] for stars with Giant planets (a) and stars with Neptunians and smaller planets (b). The lower panels show the frequency of stars with planets for each case. Regarding stellar mass, I found a hypothetical correlation with planets, but was found to be the result of a detection bias. The paper describing this work is shown in Chapter 4.

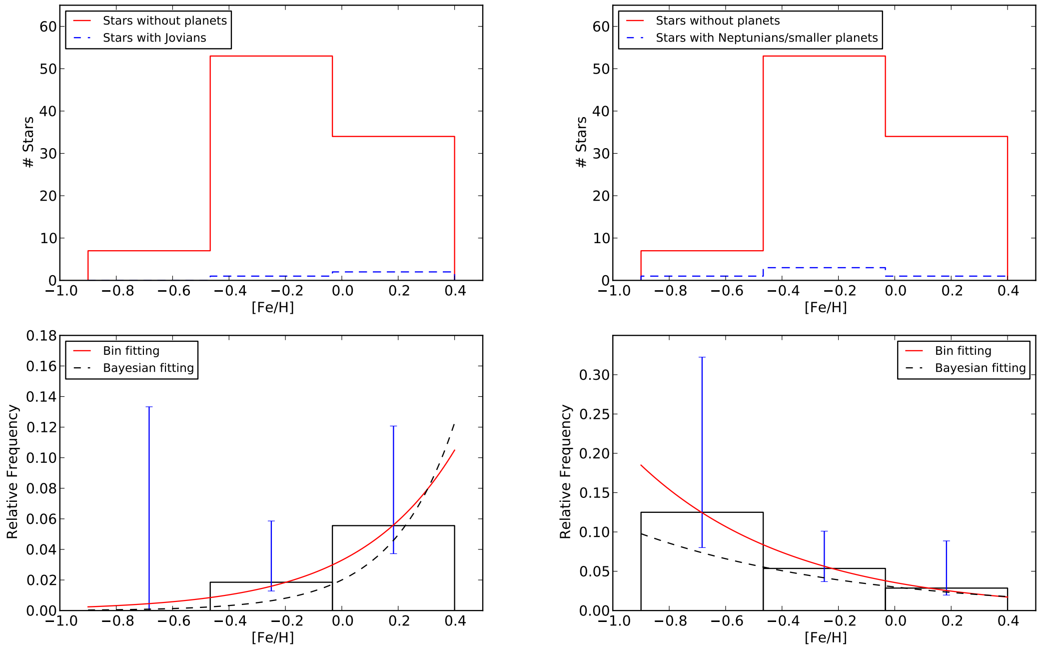

(a) (b)

Figure 1.13: (a) Upper panel: Histogram of metallicity with 3 bins for stars without planets (solid red) and stars with Giant planets (dashed blue); Lower panel: Frequency of stars with Giant planets; (b) Upper panel: Histogram of metallicity with 3 bins for stars without planets (solid red) and stars with Neptunians and smaller planets only (dashed blue); Lower panel: Frequency of stars with Neptunians and smaller planets only. From Neves et al. (2013).

In the last part of my Ph.D. me and some of my collaborators were also involved in the observation of the M dwarf GJ3470, using the radial velocity and photometric techniques, that resulted in the detection and characterisation of a new transiting planet, GJ3470 b, a low-density ‘Hot Uranus’ exoplanet (Bonfils et al. 2012). GJ3470 b is one of the few confirmed lower-mass planets that transit its star, and its host star is bright enough to allow detailed follow-up studies, that may give hints to its formation and evolution process. GJ3470 was later observed with the Spitzer telescope (Demory et al. 2012), with the aim of refining the stellar parameters of the system. After analysing the data, we derived a stellar mass of $M_\star = 0.539^{+0.047}_{-0.030} M_\odot$ and a radius of $R_\star = 0.568^{+0.037}_{-0.031} R_\odot$. Also, we determined that the host star of GJ 3470 b is metal-rich, with a metallicity of [Fe/H] = $+0.20 \pm 0.10$ and an effective temperature of $T_{eff} = 3600 \pm 100$ K. The revised stellar parameters yield a planetary radius $R_p = 4.83^{+0.22}_{-0.21} R_\oplus$ that is

13% larger than our own previous value reported in Bonfils et al. (2012). Finally, we found a planetary mass $M_p = 13.9^{+1.5}_{-1.4} M_\oplus$ that translates to a very low planetary density, $\rho_p = 0.72^{+0.13}_{-0.12} g cm^{-3}$, which is 33% smaller than the original value. The details of this work as well as the published paper are described in detail in Chapter 5.

My thesis is structured as follows. First, in Chapter 2 I describe in some detail the techniques to obtain stellar parameters in FGK stars, the challenges facing the determinations of M dwarf parameters, and its state of the art. Then, in chapters 3, 4, and 5 I present the work done in the last four years, along with three published papers. Finally, in chapter 6, I draw the conclusions and show the future prospects.

Chapter 2

Fundamental parameters of M dwarfs

Measuring accurate stellar parameters from the optical spectra of M dwarfs is a very challenging task. As the abundances of diatomic and triatomic molecules (e.g. TiO, VO, H_2O, CO) in the photospheric layers increases with spectral subtype, their forest of weak lines eventually erases the spectral continuum and makes a line-by-line spectroscopic analysis difficult for all but the earlier M subtypes (e.g. Gustafsson 1989; Woolf & Wallerstein 2005). As already shown before, Fig. 1.6 shows a good example of a high-resolution spectrum where a G dwarf star (above) and a M dwarf (below) are compared. Despite the spectra of the M dwarf looking just like noise, it has a higher signal-to-noise ratio.

In the following Section I will make a brief outlook regarding the classical derivation of stellar parameters of FGK stars, adding some details regarding M dwarfs. Afterwards, I will discuss the difficulties of the continuum determination for M dwarfs (Sec. 2.2), as well as an explanation regarding the need for spectral synthesis, in Sect 2.3. Finally, the state of the art regarding the determination of M dwarf parameters will be discussed in Sec. 2.4.

2.1 Classic spectroscopic analysis

This section follows Gray (2005); Reid & Hawley (2005), and Bonfils (2012) closely, where I will present a brief outlook on the determination of stellar parameters for a FGK dwarf star. Me and my collaborators applied this procedure to calculate the parameters of the FGK primaries in binaries systems with a M dwarf secondary in order to infer the [Fe/H] of both stars, as detailed in Chapter 3. This work culminated in the publication of the first paper of my Ph.D.

If we take a good look at a regular stellar spectra (Fig. 1.6) we can easily identify the presence of many absorption lines. These lines correspond to electronic transitions among the different levels of atoms and molecules (bound-bound transitions). This is especially true for cooler stars of the FGKM end of the HR diagram, where the atoms and molecules of many species are not fully ionised. The elements other than hydrogen and helium, referred as 'metals' (e.g., C, O, Mg, Si, Fe, Ti, etc), only account for a tiny percentage of the abundance ($\sim 2\%$). However, most spectral lines have origin in these metal species.

These lines show different shapes and strengths that derive directly from the conditions in the photosphere of the star (temperature, pressure, radiation, magnetic and velocity fields). The most important aspect in the determination of the stellar parameters is the strength of the line absorption, that depends on the number of absorbers that correspond to a certain electronic transition.

2.1.1 Local thermodynamic equilibrium

If we consider that collisions (rather that radiation) dominate the excitation of the atoms (as a good approximation in the case of FGKM stars), then local thermodynamic equilibrium (LTE) will apply and we can express the ratio between the number of atoms in an energy level n and the total number of the atoms of that species as

$$\frac{N_n}{N} = \frac{g_n}{u(T)} 10^{-\theta(T)\chi_n}, \tag{2.1}$$

where N_n is the population of energy level n, N is the total number of atoms, g_n is the degeneracy of level n, χ_n is the excitation energy of the same level, $\theta(T) = 5040/T$, $u(T) = \Sigma g_i e^{-\chi_i/kT}$ is the partition function, k is the Boltzmann's constant and T is the temperature. This is one formulation of the well known Boltzmann equation.

Similarly, the ionisation for the collision dominated gas can be calculated using Saha's Equation,

$$\frac{N_1}{N_0} = \frac{\Phi(T)}{P_e}, \tag{2.2}$$

where

$$\Phi(T) = \frac{(\pi m_e)^{3/2}(2kT)^{5/2}}{h^3} \frac{u_1(T)}{u_0(T)} e^{-I/kT}. \tag{2.3}$$

The N_1/N_0 is the ratio of ions in a given ionisation state to the number of neutral atoms, u_1/u_0 is the ratio of ionic to neutral partition functions, m_e is the electron mass, h is the Plank's constant, P_e is the electron pressure and I is the ionisation potential. The transition from neutral to first ion, and upwards occurs fairly rapidly with T_{eff}, as shown in Fig. 2.1, for Iron.

Thermodynamic equilibrium is achieved when the temperature, pressure and chemical potential of a system are constant. In LTE, these thermodynamic parameters are varying in space and time but this variation is slow enough for us to assume that, in some neighbourhood about each point, thermodynamic equilibrium exists (hence the 'local'). When the LTE is valid, each point will behave like a black body of temperature T. This is, of course, an approximation, but it is acceptable for the cases when the ratio of collision to radiation induced transitions is large, as it is the case for photospheres of FGKM stars. In the outer photospheric layers, LTE performs poorly due to the proximity of the open space boundary, where the radiation can escape freely. This boundary is responsible for the formation of the absorption lines. We cannot use strong lines calculated by LTE because their cores form in these upper layers.

In the photospheres of M dwarfs, the temperature is lower and surface gravity is higher, leading to higher matter densities. Both low temperature and high density will increase the opacity of the photosphere. This effect is due to the increase of many low-energy transitions from neutral atoms (the now dominant form in the cooler atmosphere) and molecules, and to the increased density of atoms and molecules, that augment the probability of interaction with the radiation. This combination of factors

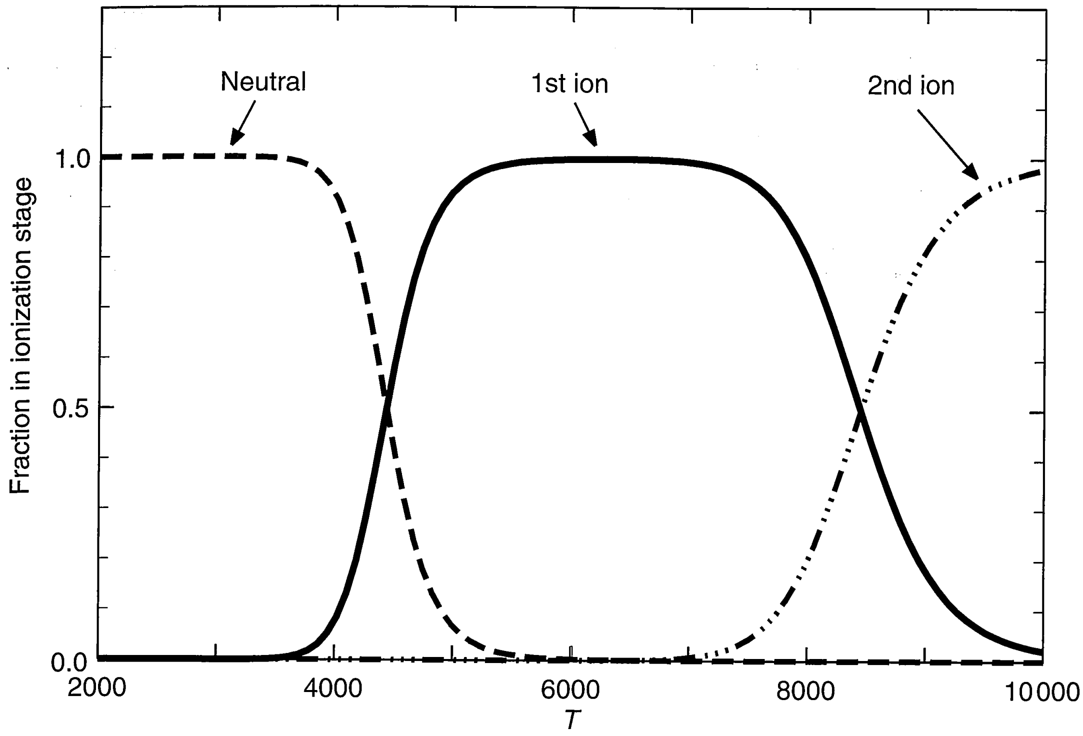

Figure 2.1: Plot showing the fraction of the ionisation stage of Iron as a function of T_{eff}, in a model photosphere. From Gray (2005).

move the atmosphere towards LTE. Therefore LTE is also valid when modelling M dwarf atmospheres.

As we will see in the following sections, LTE will be used to calculate our model atmosphere and help us find the stellar parameters. We must recall that the temperature in the LTE approximation is the same for all physical processes: thermal velocity distributions, ionisation equilibrium, excitation of atomic populations. It's a simplification over the real problem but it is very practical.

2.1.2 The behaviour of line strength

The strength or equivalent width (EW) of a spectral line depends on the absorption coefficient (the fraction of incident radiant energy absorbed per unit mass or thickness of an absorber) and on the number of absorbers, derived from Eqs. (2.1) and (2.2). This implies that the line strength depends on temperature, electron pressure and the atomic constants. This is valid only as a good approximation for weak lines (i.e., lines with typical EW $\lesssim$ 200 mÅ). Stronger lines may depend on other factors.

From the accurate measurement of the EW of weak lines, and using the correct atmospheric models we can calculate the stellar parameters (metallicity, temperature, surface gravity, microturbulence, and others), and also chemical abundances.

The Measurement of the EW

Equivalent width is a measure of the intensity of a spectral line. It is defined as the width of a rectangle with height between the level of the continuum, normalised to unity, and the reference zero, having a surface equal to the profile of the spectral line, as shown on Fig. 2.2.

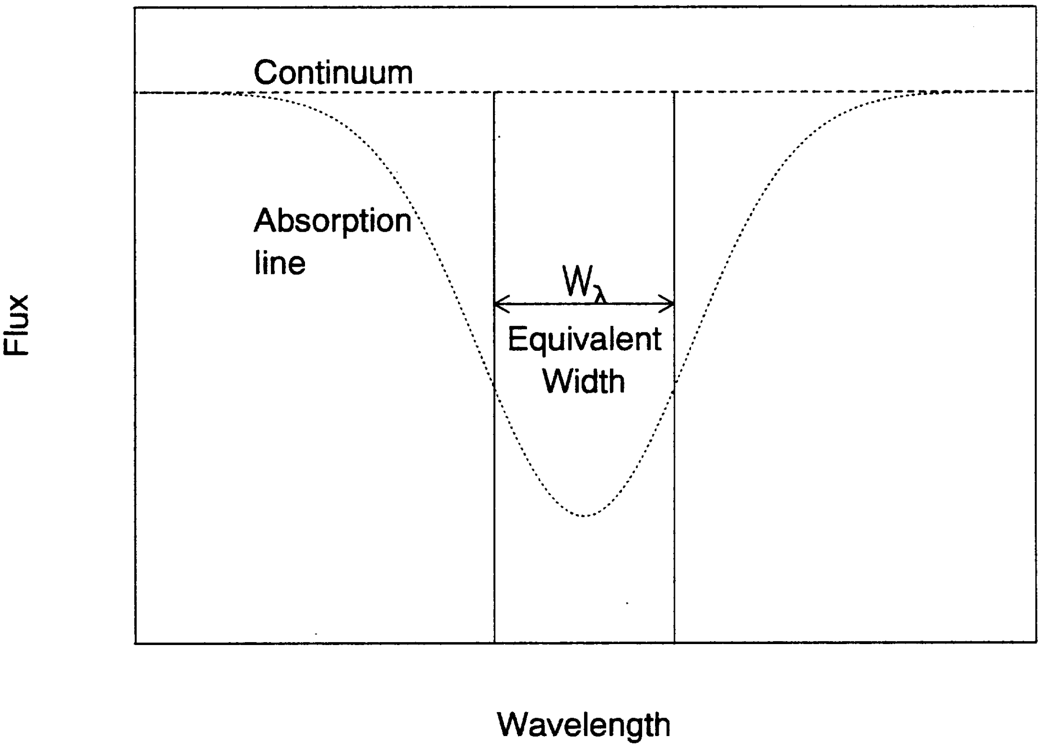

Figure 2.2: Illustration of a spectral line and its equivalent width, W_λ. Taken from Reid & Hawley (2005).

The EW is thus measured in wavelength units (Å or mÅ). Mathematically we have

$$W = \int_{-\infty}^{\infty} \frac{I_c - I_\lambda}{I_c} d\lambda, \tag{2.4}$$

where I_c is the intensity of the continuum and I_λ is the intensity of the wavelength at each $d\lambda$. Usually, the EWs are measured by fitting a gaussian function to the spectral line and to the local continuum. We must note that, in some of the following plots, the equivalent width will be represented by W.

2.1.3 The temperature dependence

Temperature is the most important variable in determining the line strength. This results from transition probabilities of the excitation and ionisation process equations (section 2.1.1). We can appreciate the behaviour of the EW of a typical weak line (e.g., Iron) with T_{eff} depicted by Fig. (2.3). Four different cases are shown:

1. weak line of a neutral species with the element mostly neutral.
2. weak line of a neutral species with the element mostly ionised.
3. weak line of an ion with the element mostly neutral.
4. weak line of an ion with the element mostly ionised.

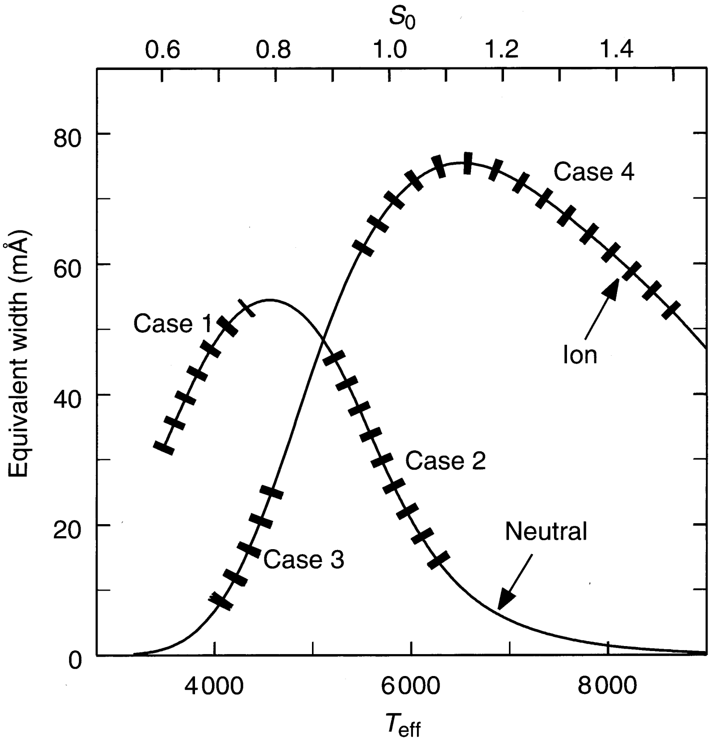

Figure 2.3: Plot of the behaviour of the EW of typical weak metal lines (e.g., Iron) with T_{eff}. The cases discussed in the text are shown. From Gray (2005).

The four highlighted cases can be expressed into equations, following Gray (2005). For case 1 (neutral line, element neutral) we have,

$$\frac{1}{R}\frac{dR}{dT} = \frac{2.5}{T} + \frac{\chi + 0.75}{kT^2} - \Omega \tag{2.5}$$

as the fractional change of line strength as a function of T, where $R = \frac{l_v}{k_v}$, the ratio of line to continuous absorption, T is the temperature, χ is the excitation potential, k the Boltzmann constant, I the ionisation potential, and Ω is a variable related to the electronic pressure of cooler stars ($P_e = const.e^{\Omega T}$). For case 2 (neutral line, element ionised),

$$\frac{1}{R}\frac{dR}{dT} = \frac{\chi + 0.75 - I}{kT^2}, \tag{2.6}$$

case 3 (ionic line, element neutral),

$$\frac{1}{R}\frac{dR}{dT} = \frac{5}{T} + \frac{\chi + 0.75}{kT^2} - 2\Omega, \tag{2.7}$$

and case 4 (ionic line, element ionised),

$$\frac{1}{R}\frac{dR}{dT} = \frac{2.5}{T} + \frac{\chi + 0.75}{kT^2} - \Omega. \tag{2.8}$$

For the four cases above, and for a given T and Ω, the ratio R is only dependent of the excitation potential χ. From Boltzmann and Saha equations (Eq. 2.1, and Eq. 2.2 respectively), for a given T, we can also determine the number of electrons in each excitation and ionisation level. Using this information we can calculate the abundance of each spectral line. As the abundance should be the same independently of the excitation potential we can use multiple lines of the same element to refine the calculation of the temperature. The parameter calculation steps are shown in Sect. 2.1.7.

In cases 1 and 3 an increase in T_{eff} leads to an increase in the line strength. This also happens in case 4 up to a maximum value of EW. We can observe, for these cases, that the electron pressure term, Ω, goes against the increase of the strength, reflecting an increased continuous absorption.

The decrease of the line strength with T_{eff} in case 4 is caused by the increase in the continuum absorption from the negative hydrogen ion, whereas the decrease in case 2 is due to the ionisation of the absorbing species. In any case, we can predict how a certain line will grow or weaken by considering the ratio of the line absorption coefficient with the continuum absorption coefficient.

Note that the weakening of the line due to an increase of the continuum absorption also affects the lines in case 1 and 3. However, this effect is weak compared to the excitation one.

The direction and strength of change will depend on the temperature and on the excitation potential (the minimum energy that an electron of a certain atom needs to make a successful transition between the ground state and an excited state) of the line. For stars similar to the Sun, cases 2 and 4 apply because most elements are ionised. Solar lines of neutral species almost always decrease in strength with T_{eff}, but ionised species have the opposite behaviour. In the case of cooler M dwarfs, where the atmosphere is composed mostly of neutral species, cases 1 and 3 are the ones of interest. However, as shown in Section 2.2, the existence of hundreds of millions of molecular lines makes a EW-based analysis next to impossible.

2.1.4 The abundance dependence

The abundance is also an important factor in the line strength variation. As the abundance increases, line strength also increases, as expected. However, the EW does not change linearly with abundance, as we can see in Fig. 2.4(a).

There are three different regimes. The first one corresponds to the weaker line behaviour, where the doppler core dominates and the EW is proportional to the abundance A. The second phase begins when the central depth approaches the maximum value and the line saturates and grows asymptotically towards a constant value. The third one starts as the optical depth of the line wings becomes significant compared to the absorption of the continuum. We are only interested in the first phase, where the behaviour of the curve is linear.

Every spectral line shows a similar behaviour. A plot like Fig. 2.4(a) is called a curve of growth. Fig. 2.4(b) shows the line profile change with the chemical abundance of the absorbing species.

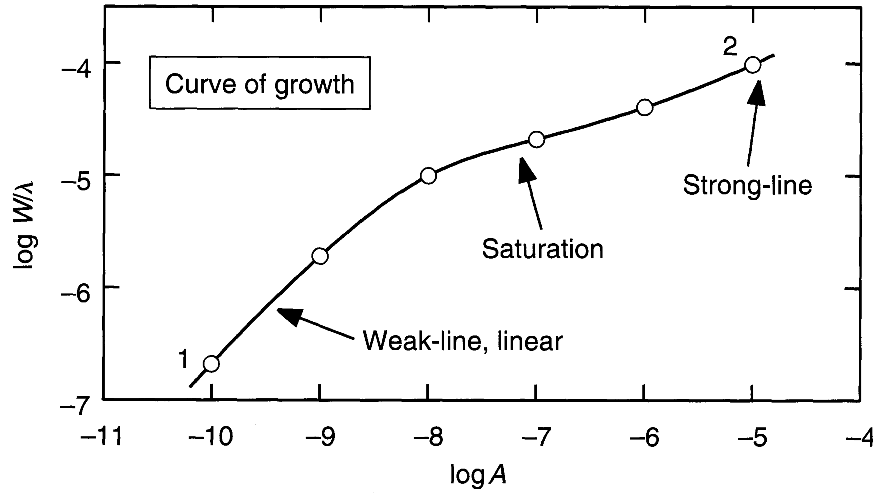

(a)

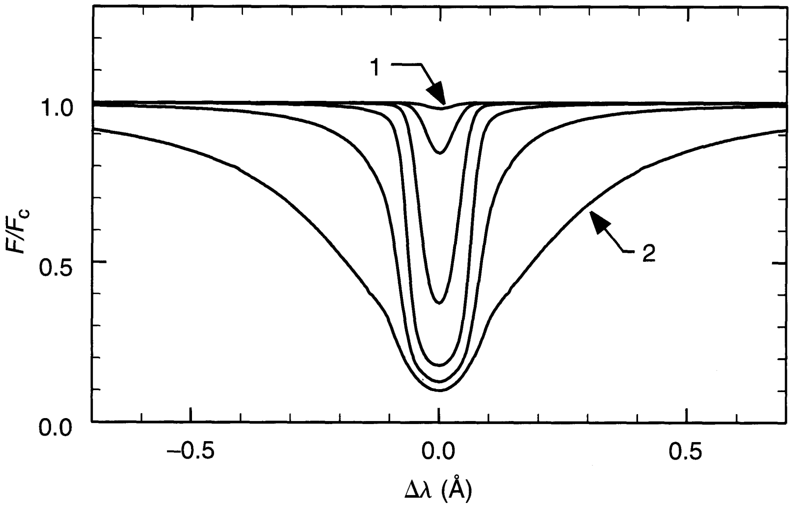

(b)

Figure 2.4: a) Typical curve of growth from a model photosphere: log-log plot of the reduced EW (W/λ) with abundance (A).; b) Line profile change with chemical abundance of the absorption species. The dots in (a) correspond to the different lines in (b). Taken from Gray (2005).

2.1.5 The pressure dependence

The pressure effects are visible in different ways. The dominant effect in weak lines is the change in the ratio of line absorbers to the continuum absorption (due to the H$^-$ ion in solar type stars). This effect translates into a $k_\nu \approx constP_e$. To account for pressure effects we must consider gas pressure (P_g) and electron pressure (P_e). In cool stars, the pressure can be approximated by $P_g \approx Cg^{2/3}$ and $P_e \approx C'g^{1/3}$, where C and C' are constants and g is the stellar surface gravity. In this case, pressure changes can be translated into approximate gravity dependences for the F, G and K stars. We can see such dependence illustrated in Fig. 2.5.

It is important to emphasise that pressure effects in stellar spectra are much weaker than temperature effects. For weak metal lines in cool stars, we can enumerate the following rules, based on Eq. 2.2:

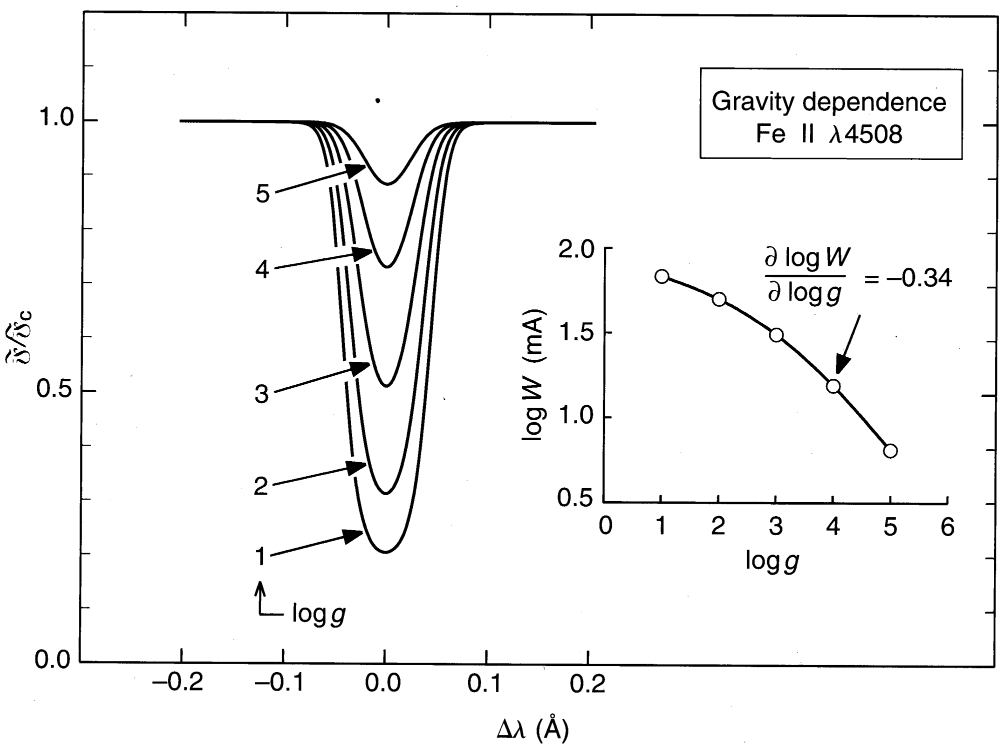

Figure 2.5: Profiles of FeII λ4508 shown for several values of surface gravity (in cm/s^2). The inset is shown in shows a log-log plot of EW with surface gravity. The values of $\log g$ correspond to the white dots in the inset. From Gray (2005).

1. weak lines formed where most of the element is in the next higher ionisation stage are insensitive to pressure changes.

2. weak lines formed where most of the element is in that same ionisation stage are pressure sensitive: lower pressure cause greater line strength.

3. weak lines formed where most of the element is in the next lower ionisation stage are very pressure sensitive. Lower pressure enhances the lines.

For the first case, the N_{r+1} is approximately equal to the total number of the element. Therefore, for constant T_{eff}, $N_{r+1} \approx N \approx const$. Hence, $N_r \approx const P_e$, and $l_\nu \approx const.P_e$. We can then write that

$$R = \frac{l_\nu}{k_\nu} \approx const \frac{P_e}{P_e} \approx const, \tag{2.9}$$

meaning that for case 1, the lines are quasi-insensitive to pressure effects. For case 2 we have $N_r \approx N \approx const$. Therefore,

$$R = \frac{l_\nu}{k_\nu} = \frac{const}{P_e} \approx const g^{-1/3}, \tag{2.10}$$

meaning a lower line strength with increasing pressure. For case 3 we can show that $N_r \approx N \approx const$, and $N_{r+2} \approx const/P_e^2$. We can write

$$R = \frac{l_v}{k_v} = \frac{const}{P_e^3} \approx const\, g^{-1}. \tag{2.11}$$

Regarding solar type stars, where most metals are ionised, cases 1 and 2 are more common (neutral and first ion species, respectively). For the cooler M dwarfs, cases 1 and 2 are also the most common ones, but it is more complicated as we have to take into account the line absorbers that depress the continuum (see Sect. 2.2).

If the surface gravity ($\log g$) is unknown, it can be determined by forcing the ion and neutral solutions to give the same abundance (spectroscopic surface gravity), since the former are pressure dependent and the latter are insensitive to pressure changes.

2.1.6 Microturbulence and velocity fields

In the analysis of line profiles we should be aware that photospheric velocity fields (the turbulence) introduce Doppler shifts, that will be reflected in the spectra: the small scale motion ($<<$ mean free path of photons), microturbulence, can affect the radiation transfer and the large scale motions, macroturbulence and rotation, introduce a broad distribution of Doppler shifts that reshapes the line profile, but does not change its EW.

Microturbulence is an *ad-hoc* broadening parameter and is almost always incorporated into stellar parameter analysis because it adjusts the EW of saturated lines when they are smaller or greater than predicted. Fig. 2.6 shows the effect of microturbulence on the curve of growth. As we can see, changes in microturbulence can change the shape of the curve of growth and consequently the measured abundance.

To obtain the correct value of microturbulence one has to simply change its value in the atmospheric models until all spectral lines of an element, namely iron, give the same abundance, independently of the EWs.

In M dwarfs, microturbulence is not a very important parameter, amounting only to 1-2 km s^{-1} and is usually computed around these values or simply neglected on stellar modelling (Reid & Hawley 2005).

2.1.7 Method

The classical determination of spectroscopic parameters ([Fe/H], T_{eff}, $\log g$, and microturbulence) of solar-type stars follows a very precise methodology. Here we refer to Bonfils (2012). First of all, we need four things:

- A stellar atmospheric model (e.g. ATLAS9 (Kurucz 1993) or PHOENIX (Allard & Hauschildt 1995) models)
- A list of lines of an element that has several neutral and ionised lines, in the wavelength region of interest, with a good excitation potential range (e.g., iron, titanium). The elemental lines and its properties can be extracted in a line list database, like VALD (Piskunov et al. 1995).

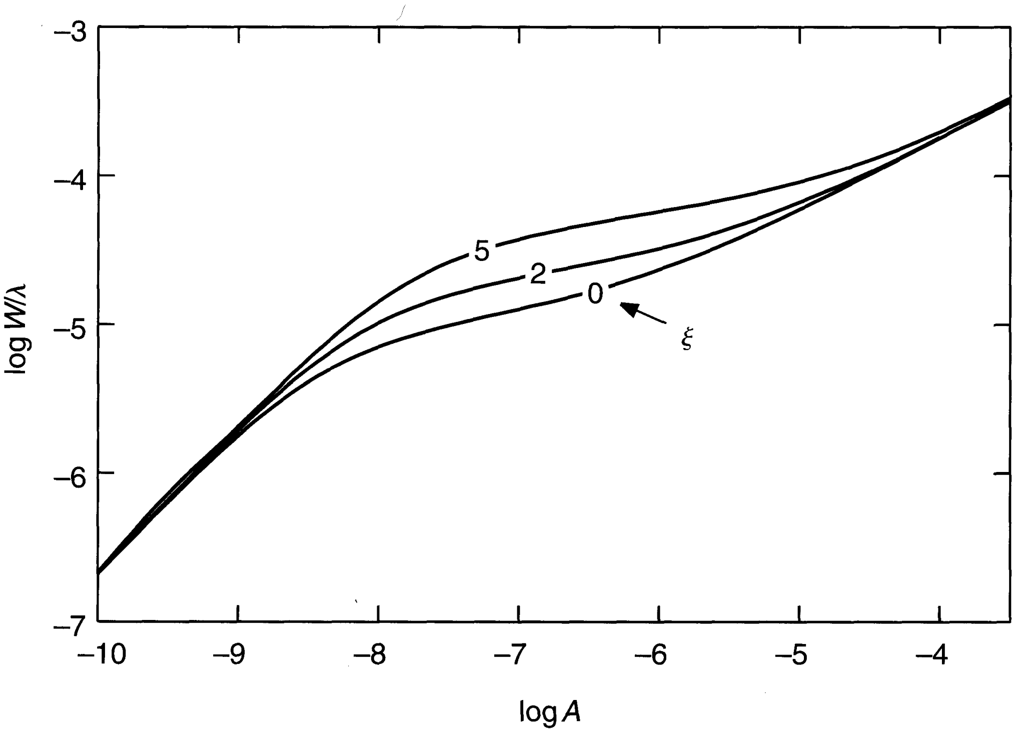

Figure 2.6: Curves of growth with different values of microturbulence. From Gray (2005).

- A code to compute abundances from a given atmospheric model, and measured EWs (e.g., MOOG (Sneden 1973)).

From here the procedure is as follows. Some of the steps are illustrated in Fig. 2.7 of the MOOG program:

1. Measure of the EWs for the list of lines of the chosen element.
2. Compute a stellar atmosphere from pertinent values of [Fe/H], $\log g$, T_{eff}, and microturbulence (normally the initial values are the solar values, or from other reference star) by interpolating on a grid of model atmospheres (e.g. ATLAS9 - Kurucz 1993).
3. Use both the measured EWs and the computed stellar atmosphere to calculate the abundance ε of the element.
4. Determine microturbulence by computing the slope of the abundance of neutral iron ($\log \varepsilon(FeI)$) versus the reduced EW ($\log EW/\lambda$). If the slope is not very close to zero, the process goes back to step 2, until the slope is ~ 0 (as shown in the middle panel of Fig. 2.7).
5. Determine the T_{eff}, computing the slope of $\log \varepsilon(FeI)$ versus the excitation potential (ξ). If the slope is not zero, the process starts again from step 2, until the slope is ~ 0 (Top panel of Fig. 2.7).
6. Determine the $\log(g)$, by comparing the abundance derived from the neutral and ionised elements of the specie. If the abundances are not the same, the process starts again from step 2.

At this stage, the value of [Fe/H] has already converged. In practice, to speed up the process, the iterations are made by changing all the parameters at the same time, using an algorithm like the downhill

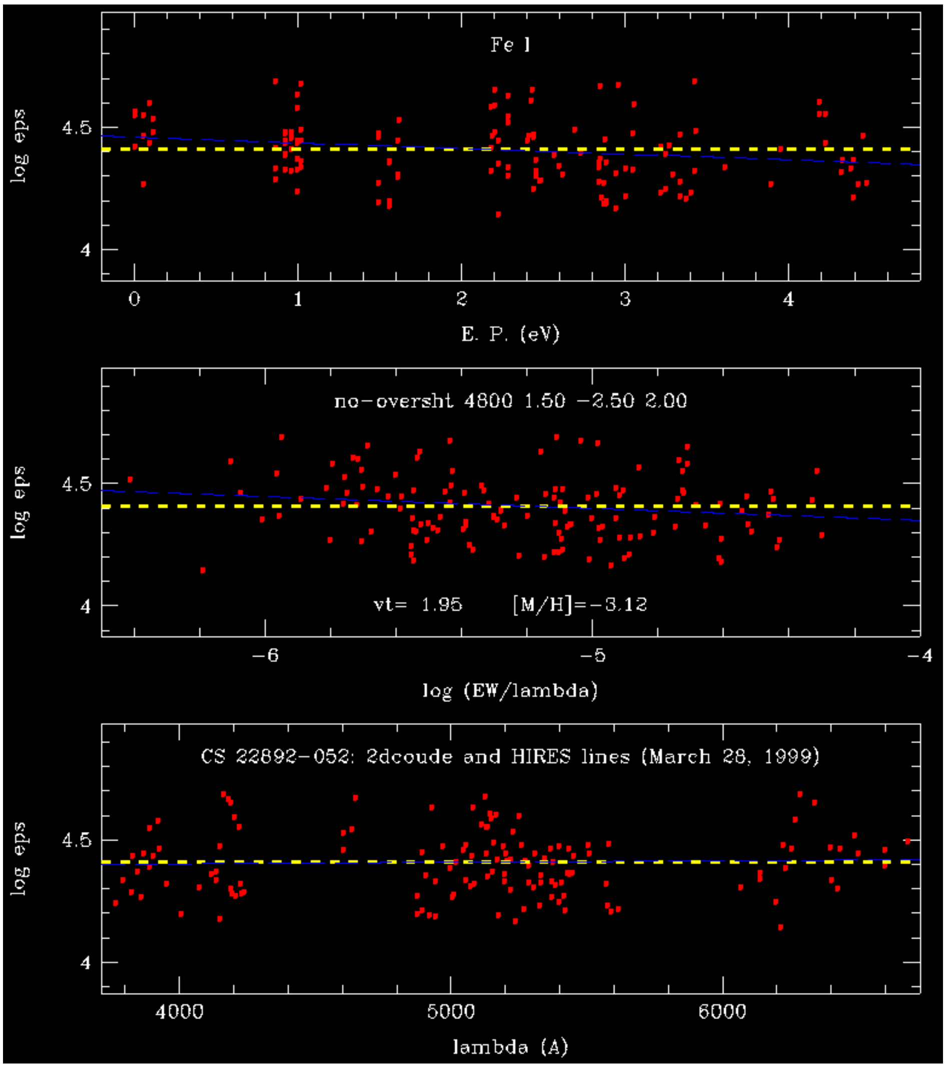

Figure 2.7: Output plots from MOOG. The red dots are the calculated values of the abundance of each line. *Top panel*: Abundance versus excitation potencial. *Middle panel*: Abundance versus reduced equivalent width. *Bottom panel*: Abundance versus wavelength.

simplex method (Press et al. 1992). The typical dispersions obtained using this method are of the order of 50 K for T_{eff}, 0.12 dex for $\log g$, 0.08 dex for microturbulence, and 0.05 dex for [Fe/H] (e.g. Santos et al. 2004b).

2.2 The continuum problem in M dwarfs

The continuum estimation requires a very good knowledge of the continuum opacity. For FGK dwarfs, this is relatively well-known, as the source of continuum opacity is mainly dominated by the H^- ion (Gray 2005). However the case for M dwarfs is more complicated due to the presence of strong molecular line absorption.

Fig. 2.8 shows a spectrum of an M8 dwarf (solid line) together with a model fit, from Allard & Hauschildt (1995) (dotted line), as well as the plot of the H^- continuum (dashed line), the Blackbody spectrum with the same temperature (dashed-dotted line) and the location of molecular line absorption bands. In the same plot we can observe the H^- continuum and the blackbody spectra at the same effective temperature. It is straightforward that a H^- continuum approximation is insufficient, and that it is necessary to take into account the most important transitions of elements like TiO, VO, FeH, H_2O, and CO into the models.

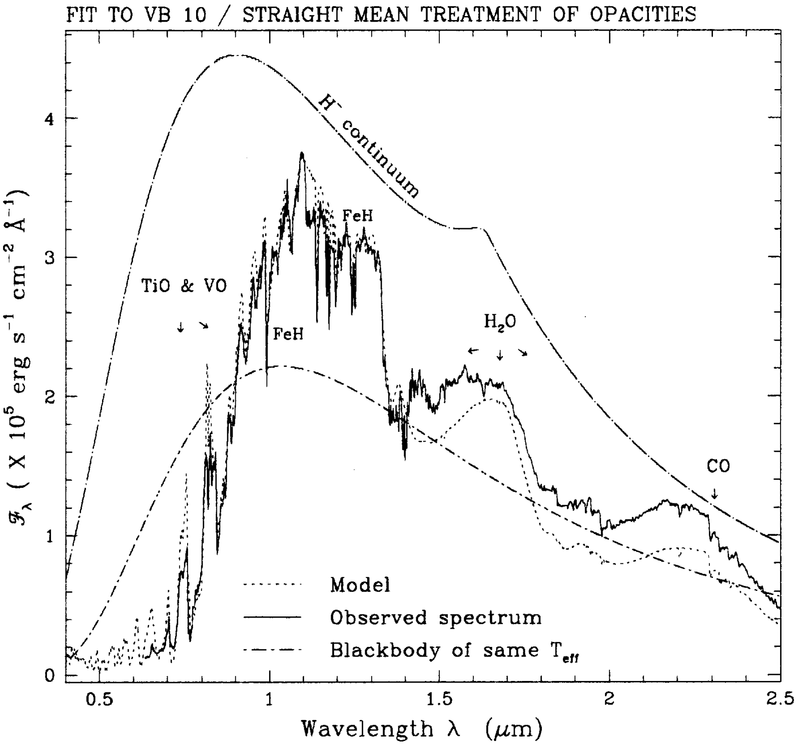

Figure 2.8: Observed spectrum of the M8 dwarf VB 10, shown as the solid line. The model fit is shown as the dashed line, the H^- continuum as a dashed line and a blackbody with the same temperature as the star is depicted with a dash-dotted line. The location of the molecular line absorption bands are also shown. From Allard & Hauschildt (1995).

The processes responsible for line formation (bound-bound) include transitions between bound levels within atoms and molecules, including the low-energy vibrational and rotational transitions of molecules. In M dwarfs, hydride and oxide molecules dominate the line opacity in the visible and infrared. These transitions are responsible for the incredible increase of the complexity of the models of M dwarfs, due to the sheer number of possible transitions, numbering in the hundreds of millions for each molecule. They are also the reason why we cannot yet calculate stellar parameters and abundances in a precise way with the classical method, using the radiative transfer models, due to the uncertainties of the placement of the true continuum. Indeed, overcoming this difficulty is the main motivation of this Thesis. In contrast, the bound-free and free-free transitions, responsible for the continuum opacity, are easy to compute but none has a significant impact in the cool M dwarf atmospheres (Reid & Hawley 2005).

Fig. 2.9 shows the most important opacity contributors for a M6 dwarf with $T_{eff} = 2800K$ and solar metallicity. From the figure we can see that the opacity is dominated by the TiO molecule in the visible and the water molecule in the infrared. The H^- opacity continues to be important, followed by collision-induced (or pressure induced) absorption of molecular hydrogen with itself and other molecules. The collision-induced absorption is caused by the interaction of a photon with the temporary electric dipole induced during a collision of two molecules. Further details can be consulted in Reid & Hawley (2005).

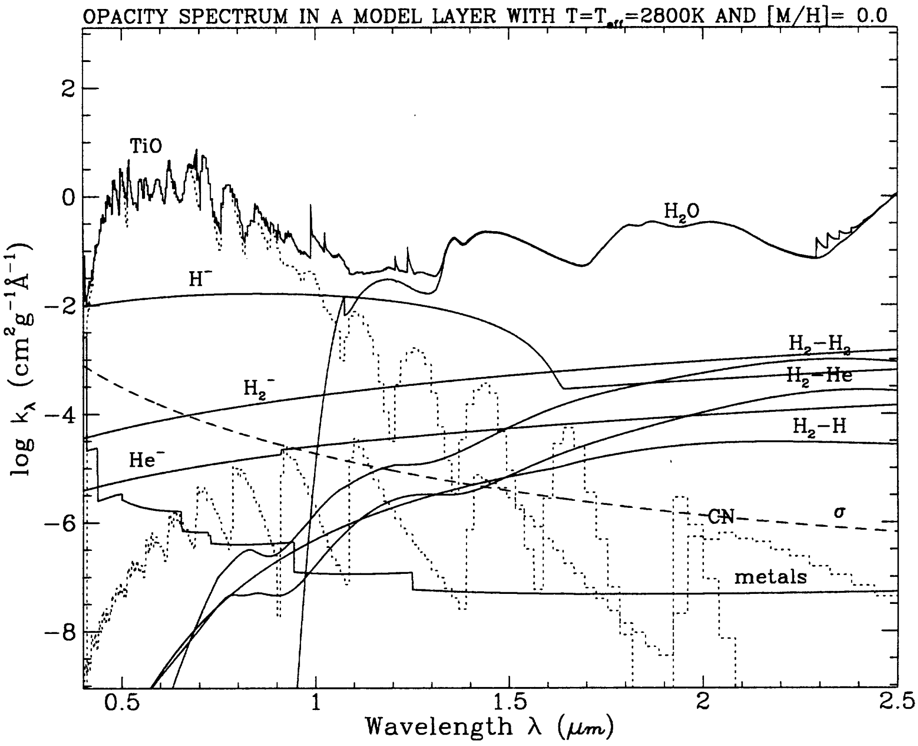

Figure 2.9: Opacity spectrum of a model photosphere with T_{eff} = 2800 K and [M/H] = 0.0. The different opacity contributors are shown in the Figure. From Allard & Hauschildt (1995).

Also, the line broadening effect known as pressure or collisional broadening is very important in the high-pressure atmospheres of M dwarfs. The van der Waals forces originating mainly from atomic and molecular hydrogen increase the energy levels of atomic and molecular species, causing significant line-broadening. This effect contributes mostly to the Lorenz damping profile of a line, having a significant contribution on the stronger absorption lines. Increasing the energy width of the transition increases also the scattering effects, contributing to move the photosphere away from LTE. (Reid & Hawley 2005)

Other broadening effects exist, such as microturbulence and stark broadening, but they have a much smaller effect when comparing to collisional broadening.

2.3 Spectral synthesis

The spectroscopic method described above becomes more and more difficult as one goes towards lower temperatures, into the M dwarf domain. In the cool atmosphere of M dwarfs, the temperature is low enough to enable the formation of molecules like TiO, VO, FeH, H_2O, CO, among other oxides and hydrides. These molecules have hundreds of millions of vibrational and rotational transitions each, and become the most important sources of opacity in the photosphere, replacing the H^- ion (Sect. 2.2). The presence of a forest of molecular lines in the typical M dwarf spectrum depresses the continuum in the visible and, in a lesser extent, in the infrared, making the measurement of the EWs and the classical spectroscopic analysis challenging. The continuum problem in M dwarfs is clearly illustrated in Fig 1.6, where we can compare the high-resolution spectra of two stars, a G star, in red, and a M dwarf, in blue.

At a first glance, the M dwarf spectrum seems to be only noise, but all features in the spectra correspond to line transitions. Actually, the M dwarf spectrum has a SNR higher than the G star! In this context one may resort to full spectral synthesis to measure the stellar parameters as well as elemental abundances.

In order to obtain a synthetic spectrum one has to use an adequate model atmosphere, such as the PHOENIX (Allard & Hauschildt 1995) and MARCS (Brett 1995a,b), as well as a program that can produce the desired spectra like MOOG Sneden (1973), SYNTH (Piskunov 1992), SME (Valenti & Piskunov 1996). The first attempts of modelling the atmospheres of M dwarfs were made by Gingerich & Kumar (1964), who used continuum opacities only and assumed radiative equilibrium (without convection); Tsuji (1966), who was the first to include a few molecules (CaH, H_2O, and CO) and introduced convection; and Auman (1969), who also used convection and a better treatment of water opacity. The biggest improvements came with Mould (1976); Mould & Hyland (1976); Mould & Wyckoff (1978), who modified the Kurucz (1970) ATLAS code, by including convection and a much bigger list of atomic and molecular lines, including the TiO molecule, that he found temperature sensitive. The Mould models persisted for 20 years until significant improvements were made in the early 1990s by Allard (1990) and Kui (1991), that a few years later originated the famous PHOENIX (Allard & Hauschildt 1995) and MARCS (e.g. Brett 1995a,b) models. Again, bigger line lists of water and TiO were added. The next improvement was made with the NextGen models with even more line lists and opacity treatment for all molecules and all atmospheres above 3000 K (Hauschildt et al. 1999), that are still used today for M dwarfs, with small improvements (e.g. Allard et al. 2010). From the models we can extract synthetic spectra. These spectra are convolved with instrumental and filter profiles to provide spectra at specific resolutions and photometry, respectively.

To compare the synthetic spectra to the observed ones, one should normally create a library of synthetic spectra[1] ranging all spectral parameters and then find the best fit among them using, for instance, a simple χ^2 fitting procedure. The uncertainties will be proportional to the parametric interval of the synthetic spectra as well as the goodness of the fit.

Despite all efforts, the model atmospheres used to make the synthesis still lack the appropriate opacities and molecular transitions in order to reproduce the finer details of high resolution spectra (e.g. Valenti et al. 1998; Bean et al. 2006b), as shown in Fig. 2.10. However, models are evolving very fast and they now incorporate several hundred millions of atomic and molecular line opacities, allowing the extraction of the stellar parameters, like effective temperature, surface gravity, microturbulence and metallicity with reasonable precision (e.g. Önehag et al. 2012). It might be possible that this technique can be used to reach a similar precision to classical spectral analysis used in FGK dwarfs in the next few years, in particular in the near-IR. The latest progress in obtaining spectral parameters using spectral synthesis is detailed in the following Section.

2.4 State of the art

Measuring accurate stellar parameters from the optical spectra of M dwarfs is not an easy task, as we have seen in the previous Sections. In this section we will make a brief description of the state of the art regarding the stellar parameters for M dwarfs.

---

[1] For instance: `http://phoenix.ens-lyon.fr/simulator/`

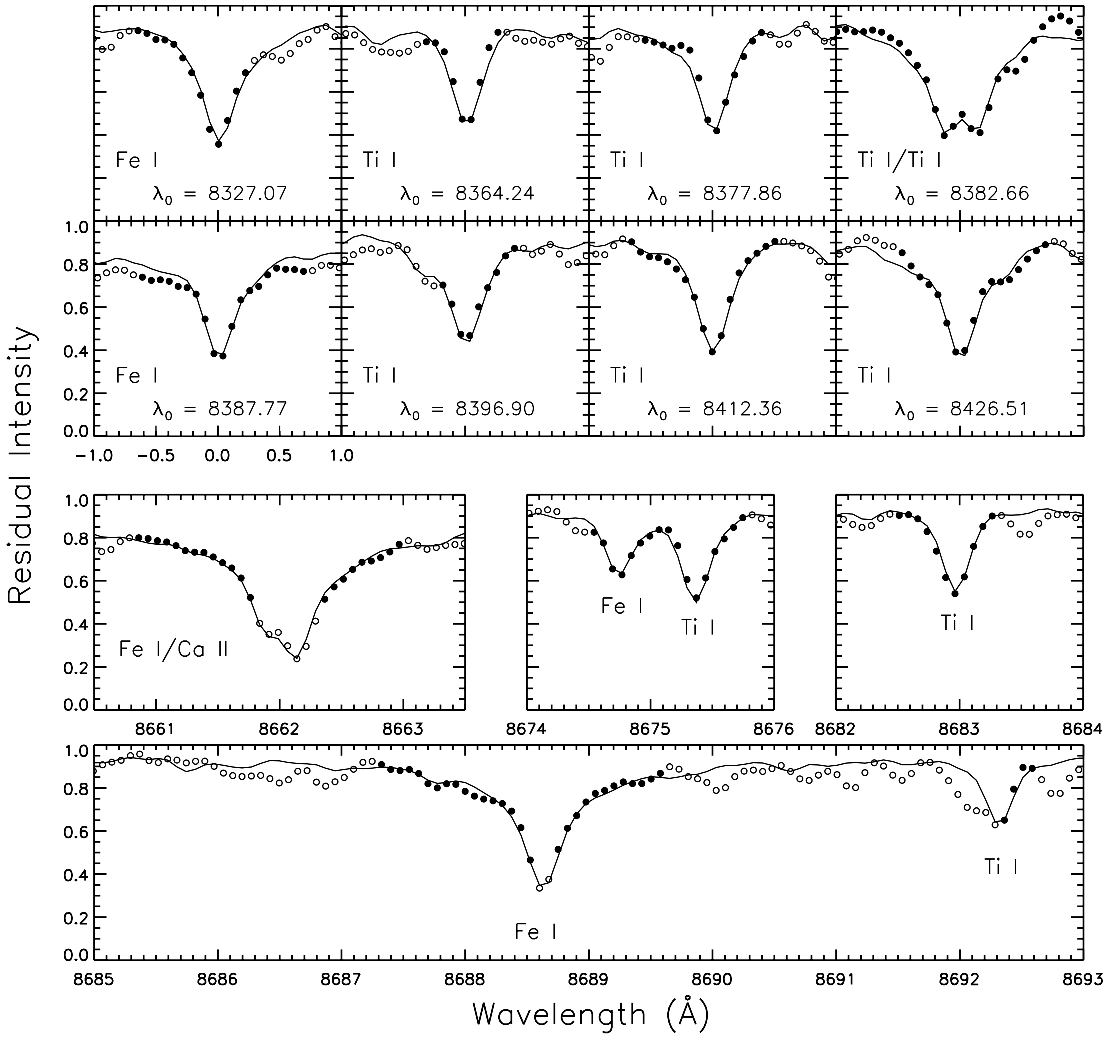

Figure 2.10: Fit of synthetic spectra (solid lines) to atomic line profiles (circles) for HIP12114B. From Bean et al. (2006b).

2.4.1 Metallicity

The metallicity determination of M dwarfs follows essentially two avenues: photometric and spectroscopic based methods. The former techniques use M dwarf photometry in the visible and infrared bands to create [Fe/H] calibrations (e.g. Bonfils et al. 2005; Johnson & Apps 2009; Schlaufman & Laughlin 2010), while the latter ones rely on low to high-resolution spectra to measure indices and lines in order to establish spectroscopic calibrations (e.g. Woolf & Wallerstein 2005; Rojas-Ayala et al. 2010) or compare them to synthetic spectra, made from M dwarf atmospheric models (e.g. Valenti et al. 1998). In this section we will explore the progress made in the last few years for metallicity, using both approaches.

The general effect of the decrease of the metallicity in the photosphere of M dwarfs is the reduction of the opacity. This effect explain that, for instance, low metallicity M dwarfs appear hotter, and have a stronger brightness in the blue, compared to similar stars with the same mass and luminosity, but with solar metallicity. Moreover, in low metallicity stars, the hydrogen opacity sources become comparatively stronger, especially in the infrared, which leads to a redistribution of the flux from the infrared towards the visible (Reid & Hawley 2005). On the contrary, the increased TiO and VO abundances in metal-rich M dwarfs shift radiative flux from the visible range, where these species dominate the opacities, to the near infrared. At the same time, for a fixed mass, an increased metallicity reduces the bolometric luminosity. The shift of the radiative flux from the visible to the infrared, on the one hand, and the reduction of the bolometric luminosity, on the other hand, work together in the visible, but, in the [Fe/H] and T_{eff} range of interest here, they largely cancel out in the near-infrared. As a result, the absolute V magnitude on an M dwarf is very sensitive to its metallicity, while its near infrared magnitudes are not (Chabrier & Baraffe 2000; Delfosse et al. 2000). Position in a color/absolute magnitude diagram that combines visible and near-infrared bands is therefore a sensitive metallicity probe, but one that needs external calibration.

The photometric approach

Following the photometric avenue, Bonfils et al. (2005) pioneered a photometric calibration based on the metallicity effect of the $V-K$ color in a M_k vs. $(V-K)$ color-absolute magnitude diagram. This metallicity effect was based in the Delfosse et al. (2000) work, where the higher dispersion of the mass-luminosity relationship in the V-band, compared to the same relationships in the J, H, and K bands, was interpreted as being due to metallicity. Then, in order to use this [Fe/H] probe, Bonfils et al. (2005) used 20 FGK+M binary systems as calibrators, where the metallicity from the primary, calculated via a classical spectroscopic analysis (see Sect. 2.1), was assumed to be the same for the M dwarf secondary. Twenty nine spectroscopic measurements of stars of the M dwarf sample of early-type, metal-poor M dwarfs of Woolf & Wallerstein (2005) were also used as calibrators. The proposed calibration, illustrated in the M_K vs. $V-K$ diagram of Fig 2.11, and defined as

$$[Fe/H] = 0.196 - 1.527M_K + 0.091M_K^2 + 1.886(V-K) - 0.142(V-K)^2, \qquad (2.12)$$

has a dispersion of 0.20 dex. The M_K, V, and K are the absolute magnitude in the K band, and the V- and K-band photometry respectively. This calibration is valid for M_k between 4 and 7.5 mag, $V-K$ between 2.5 and 6 mag, and [Fe/H] between -1.5 and 0.2 dex.

The results of the metallicity of M dwarfs are intriguing since there is an offset of 0.07 dex towards lower metallicities when compared with a 1000 star sample from the FGK CORALIE program (Queloz et al. 2000a; Udry et al. 2000) with a modest significance of 2.7σ, that might imply that the decreased frequency of Jovians around M dwarfs is a reflection of their lower metallicities rather than their lower masses. Afterwards, Bonfils et al. (2007) used that calibration to compare M dwarfs with and without planets, and found, using a Kolmogorov-Smirnov test, that planet hosts had a probability of $\sim 11\%$ of being drawn from the same distribution. The main disadvantage of this calibration comes from its reliance on absolute magnitudes, that require very precise parallaxes, limiting the usefulness of the calibration for stars closer to 50 pc.

Several studies were published to try to improve the Bonfils et al. (2005) calibration. Johnson & Apps (2009) argue that local M and FGK dwarfs should have the same metallicity distribution, and accordingly chose to fix their mean M dwarf metallicity to the value of a volume-limited sample of FGK dwarfs from the Valenti & Fischer (2005) SPOCS sample (-0.05 dex). They defined a sequence representative of average M dwarfs in the $\{(V-K_s)-M_{K_s}\}$ color-magnitude diagram, and used the

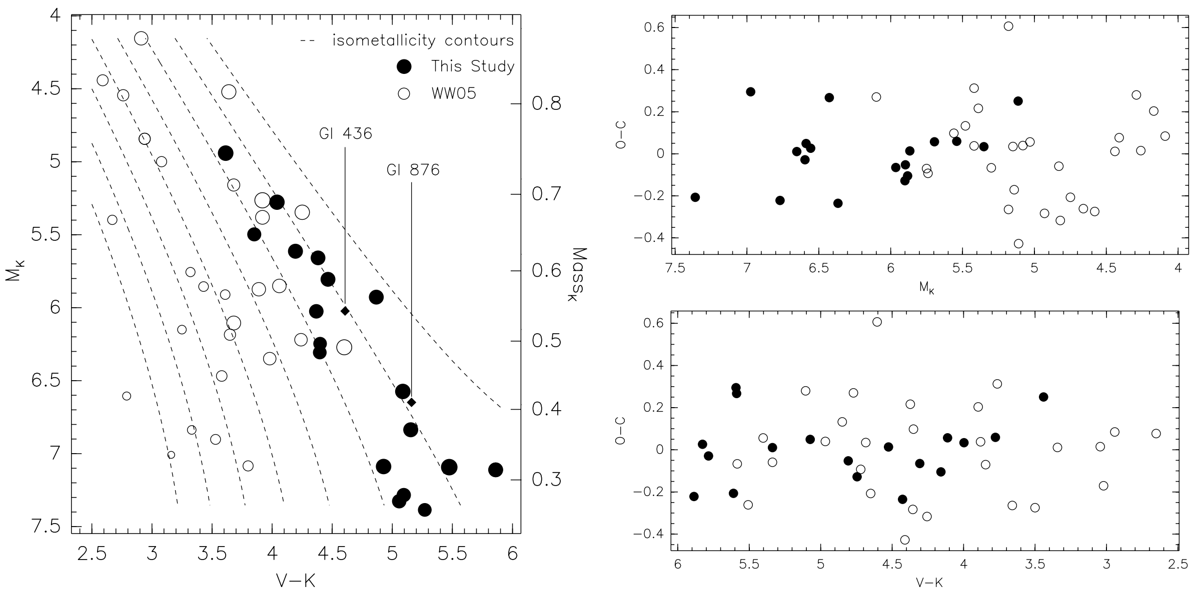

Figure 2.11: *Left panel.* M_K vs. $V-K$ color-magnitude diagram. The circles correspond to metallicity determinations, where the filled circles represent the [Fe/H] values calculated by Bonfils et al. (2005), while the open circles correspond to determinations taken from Woolf & Wallerstein (2005). The symbol size is proportional to [Fe/H]. The dashed lines represent isometallicity contours for Eq. 2.12 spaced by 0.25 dex from -1.50 (left) to +0.25 dex (right). *Right panels.* Residuals of the calibration. From Bonfils et al. (2005).

distance to that main sequence along M_{K_s} as a metallicity diagnostic. They note that the inhomogeneous calibration sample of Bonfils et al. (2005) is a potential source of systematics, and consequently chose to calibrate their scale from the metallicities of just six metal-rich M dwarfs in multiple systems with FGK primary components. Their calibration can be written as

$$[Fe/H] = 0.56\Delta M_K - 0.05, \tag{2.13}$$

where ΔM_K, assumed to be proportional to [Fe/H], is the difference between the M_{Ks} value in the isometallicity curve corresponding to the mean value of [Fe/H] of the main sequence GK stars from a volume-limited sample from the Valenti & Fischer (2005) catalog (as defined by a fifth-order polynomial $MS = \sum a_i(V-K_s)^i$, where a = $\{-9.58933, 17.3952, -8.88365, 2.22598, -0.258854, 0.0113399\}$), and the absolute magnitude in the K_s band of the M dwarf. The calibration is depicted in Fig 2.12.

Johnson & Apps (2009) present two observational arguments for fixing the mean M dwarf metallicity. They first measured [Fe/H] for 109 G0-K2 stars ($4900 < T_{eff} < 5900$ K) and found no significant metallicity gradient over this temperature range, from which they conclude that no difference is to be expected for the cooler M dwarfs. We note, however, that a linear fit to their G0-K2 data set ([Fe/H]= $9.74 \times 10^{-5}(T_{eff} - 5777) - 0.04$) allows for a wide metallicity range when extrapolated to the cooler M dwarfs ($2700 < T_{eff} < 3750$), for M7 to M0 spectral type, with [Fe/H] = -0.24 allowed at the 1 σ level for an M0 dwarf and significantly lower than the [Fe/H] offset in B05 (Neves et al. 2012). More importantly, they measured a large (0.32 dex) offset between the B05 metallicities of six metal-rich M dwarfs in multiple systems and the spectroscopic metallicities which they measured for their primaries. This robustly points to a systematic offset in the B05 calibration for metal-rich M dwarfs, but does not directly probe the rest of the (T_{eff}, [Fe/H]) space. They conclude that M dwarf planet hosts follow the same trend as FGK stars, that is, they are preferentially metal rich. They also suggest that the lack of

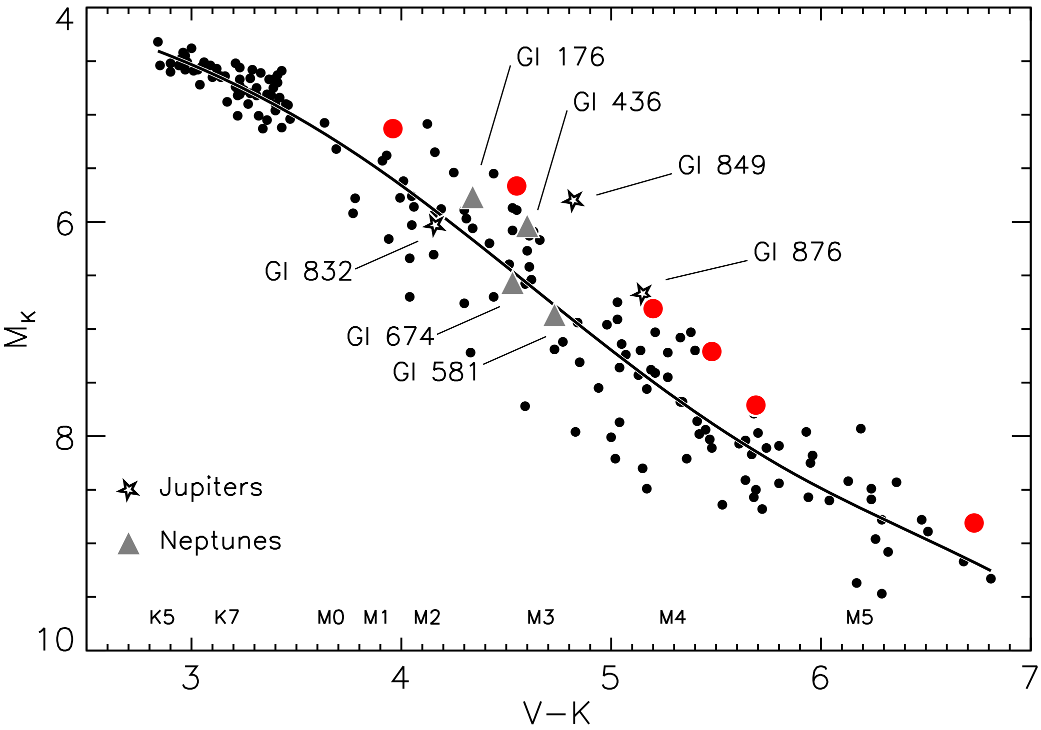

Figure 2.12: M_K vs. $V-K$ color-magnitude diagram from Johnson & Apps (2009). The nearby low-mass K and M stars are shown as black dots. The solid line is a fifth order polinomial fit to the mean Main Sequence. The large red circles depict 5 high-[Fe/H] red dwarf secondaries with a FGK primary that were used in the calibration (Eq. 2.13). The stars represent M dwarfs with at least one Jovian planet, while the triangles represent stars with at least one Neptune-type planet.

Jovian planets around M dwarfs is mostly correlated to a lower stellar mass and not to a lower value of [Fe/H], consistent with the works of planetary formation around M stars (e.g. Laughlin et al. 2004; Ida & Lin 2005). The calibration of Johnson & Apps (2009) is valid for $V-K$ values between 3.9 and 6.6 mag.

Schlaufman & Laughlin (2010) improved upon Bonfils et al. (2005) and Johnson & Apps (2009) in two ways. They first point out that, for M and FGK dwarfs to share the same mean metallicity, matched kinematics is as important as volume completeness. Since the various kinematic populations of our Galaxy have very different mean metallicities, the mean metallicity of small samples fluctuates very significantly with their small number of stars from the metal-poor populations. To overcome this statistical noise, they draw from the Geneva-Copenhagen Survey a volume-limited sample of F and G stars (GCS - Nordström et al. 2004) a subsample that kinematically matches the volume limited sample of M dwarfs used by Johnson & Apps (2009). They find a $\simeq -0.14 \pm 0.06$ dex mean metallicity for that sample, 0.09 dex lower than adopted by Johnson & Apps (2009). However, they only used that sample to verify that the mean metallicity of M dwarfs in the solar neighbourhood is well defined. In the end, the M dwarfs within a sample of binaries with an FGK primary that they used to fix their calibration are not volume-limited or kinematically-matched, but their mean metallicity ([Fe/H] = -0.17 ± 0.07) is statistically indistinguishable from the mean metallicity of the volume-limited and kinematically-matched sample.

Second, they use stellar evolution models to guide their parametrization of the color-magnitude space. Using [Fe/H] isocontours for the Baraffe et al. (1998) models, they show that in a $\{(V-K_s)-$

$M_{K_s}\}$ diagram, changing the [Fe/H] affects $(V-K_s)$ at an essentially constant M_{K_s}. The metallicity is therefore best parametrized by $(V-K_s)$, and their calibration uses a linear function of the $(V-K_s)$ distance from a nominal sequence in the $\{(V-K_s)-M_{K_s}\}$ diagram. They do not force any specific mean metallicity, but verify *a posteriori* that it matches expectations. The new calibration is then

$$[Fe/H] = 0.79\Delta(V-K_s) - 0.17, \tag{2.14}$$

where $\Delta(V-K_s) = (V-K_s)_{obs} - (V-K_s)_{iso}$. The $(V-K_s)_{obs}$ is the difference between the observed V and K_s magnitudes, and the $(V-K_s)_{iso}$ is the same isometallicity curve as in Johnson & Apps (2009), but with $(V-K)$ as a function of M_k with the 5^{th} order polynomial coefficients, 51.1413, -39.3756, 12.2862, -1.83916, 0.134266, and -0.00382023, in increasing order. Fig. 2.13 shows a Color-Magnitude calibration illustrating the new calibration.

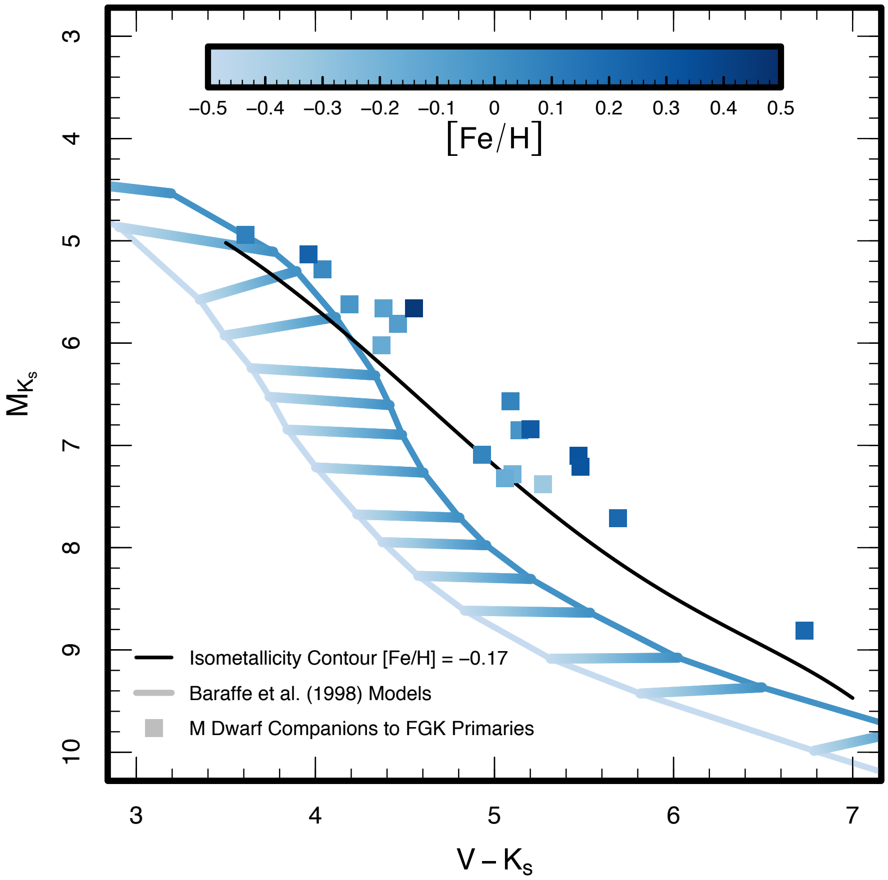

Figure 2.13: M_{K_S} vs. $V-K$ color-magnitude diagram from Schlaufman & Laughlin (2010). The solid line is the isometallicity contour closely following the GK Main Sequence stars, as described in Johnson & Apps (2009). The two blue lines depict two isochrones taken from Baraffe et al. (1998) models, with the same age (5 Gyr) but with different metallicity (-0.5 dex on the left and 0.0 dex on the right). The horizontal lines connect the points with the same stellar mass. The models indicate that differences in [Fe/H] best correlate with horizontal shifts in this color-magnitude diagram.

They conclude that the previous empirical photometric calibrations systematically underestimate (Bonfils et al. 2005) or overestimate (Johnson & Apps 2009) metallicity at the low- and high-end of their range, respectively. The uncertainty of the calibration is not mentioned, but we measure a 0.14 dex dispersion from their sample. Instead, they compute a multiple correlation coefficient, R, claiming that their model is one order of magnitude better in explaining the variance in the calibration sample than previous studies (i.e., $R \sim 0.49$ for their model, 0.06 for Johnson & Apps 2009, and 0.05 for Bonfils et al. 2005). In the end, they conclude that their results suggest that metal rich M dwarfs are more likely to host planets, as in FGK stars, and they claim that there is a hint that this correlation might extend to low-mass planets as well. This latter result is in opposition to results obtained for low-mass planets orbiting FGKM stars, which state that there is no significative relation between metallicity and the existence of low-mass planets (e.g. Sousa et al. 2008). However, the Schlaufman & Laughlin (2010) sample only has 5 Neptunian hosts and the calibration they use has a precision around 0.17 dex (Neves et al. 2012). Also, in Neves et al. (2012), me and my collaborators proposed a refinement of this calibration with a new sample, as detailed in Chapter 3. Moreover, in our latest study regarding metallicity, Neves et al. (2013), detailed in Chapter 4, shows that there is no correlation between Neptunian hosts and metallicity and there is a hint that there might even exist an anti-correlation instead.

Casagrande et al. (2008) devised an alternative technique, based on their previous study of FGK stars using the infrared flux method (Casagrande et al. 2006), to determine effective temperatures and metallicities. The infrared flux method (IRFM) uses multiple photometry bands to derive effective temperatures, bolometric luminosities, and angular diameters. The basic idea of IRFM (Blackwell & Shallis 1977) is based on the comparison of the ratio between the bolometric flux $F_{Bol}(Earth)$ and the infrared monochromatic flux $F_{\lambda}(Earth)$, both measured on Earth, to the ratio between the surface bolometric flux ($\propto \sigma T_{eff}^4$) and the surface infrared monochromatic flux for a model of the star, $F_{\lambda}(model)$, based on PHOENIX models (Brott & Hauschildt 2005). The T_{eff} can then be calculated iteratively as

$$T_{eff(n)} = \left[\frac{F_{\lambda}(model)_{(n-1)} F_{Bol}(Earth)_{(n-1)}}{\sigma F_{\lambda}(Earth)_{(n-1)}} \right]^{1/4}. \tag{2.15}$$

To adapt this method to M dwarfs, Casagrande et al. (2008) added optical bands, creating the so-called MOITE, Multiple Optical and Infrared TEchnique. This method provides sensitive indicators of both temperature and metallicity. The proposed effective temperature scale extends down to 2100-2200 K, into the L-dwarf limit, and is supported by interferometric angular diameters above $\sim$ 3000K. Casagrande et al. (2008) obtain metallicities by computing the effective temperature of the star for each color band $(V(RI)_c JHK_s)$ for several trial metallicities, between -2.1 and 0.4 in 0.1 dex steps, and by selecting the metallicity that minimizes the scatter among the six trial effective temperatures. Casagrande et al. (2008) estimate that their total metallicity uncertainty is 0.2 to 0.3 dex. The MOITE method does not reduce into a closed form that can be readily applied by others but Neves et al. (2012) used data given by their first author to test this calibration against high-resolution spectroscopic measurements of FGK stars in FGK+M binaries and found a dispersion of 0.33 dex and an offset of -0.11 dex, which makes this a poor calibration of the [Fe/H] (for details see the Appendix of my paper in Section 3.5). Despite that, this technique has a good future potential and its T_{eff} calibration is still a reference today (see Sect. 2.4.2).

Recently, Johnson et al. (2012) published a new infrared photometric calibration, described in their Appendix, in which they claim a precision of 0.15 dex. The argument used is that higher metallicity preferentially suppresses the flux in the J band when compared with the K_s band, that is relatively featureless. The difference between the two bands is mostly likely due to changes in the continuous opacity of molecular species, such as H_2^-, H^-, He^-, H_2^+, and C^- (Allard & Hauschildt 1995), and also many more line absorption in the J band. Then, they fit a two-part function to $(J-K_s)_0$ versus $(V-K_s)$ diagram, where $(J-K_s)_0 = 0.835$ for $3.8 < (V-K)_0 < 5.5$, and for $(V-K) \geq 5.5$, $(J-K_s)_0 = \sum_i a_i (V-K_s)^i$, where $a = (1.637, -0.2910, 0.02557)$. Here they assume that this fit corresponds to the isometallicity contour equal to the mean value of the Solar Neighbourhood, that Johnson & Apps (2009) found to be -0.05 dex, based on an 18 pc volume-limited sample of stars in the SPOCS catalogue (Valenti & Fischer 2005).

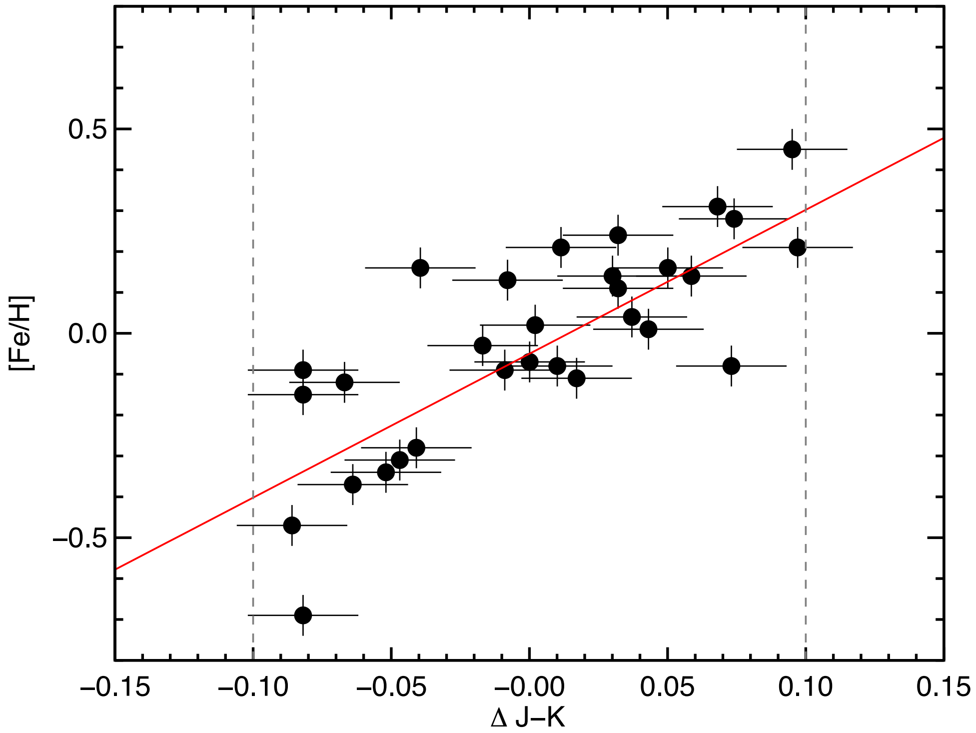

Figure 2.14: Plot of [Fe/H] as a function of $\Delta(V-K_S$, taken from Johnson et al. (2012). The calibrators are shown as black dots. The red line is the fit of the calibrations, and the dashed lines are the calibration limits.

Finally, they use 30 FGK+M wide binary systems as calibrators, from the SPOCS catalogue, inferring the value of the metallicity of the secondary as the same as the primary, from which there are high precision measurements from Valenti & Fischer (2005). The calibration, shown in Fig. 2.14, is then

$$[Fe/H] = -0.050 + 3.520\Delta(V-K_s), \tag{2.16}$$

where $\Delta(V-K_s) = (J-K_s)_{obs} - (J-K_s)_0$, and $(J-K_s)_{obs}$ is the difference of the J and K_s magnitudes, and is valid in an $J-K_s$ interval between -0.1 and 0.1 mag, and between -0.4 and 0.2 dex in metallicity.

The spectroscopic approach

The techniques used to obtain the metallicity of M dwarfs based on spectroscopic measurements were pioneered by Mould (1976); Mould & Hyland (1976); Mould & Wyckoff (1978), who were the first to make a systematic effort to compare M dwarf spectral features to their models. These models, based on the ATLAS code (Kurucz 1970) already included convection and atomic and molecular line opacities

(TiO, CaH, and H_2O). They found that TiO bands were sensitive to metallicity and temperature, and CaH bands to surface gravity. From these early works rough indices were created that enabled the spectroscopic identification of M subdwarfs (i.e., metal-poor M dwarfs kinematically associated with the halo) (e.g. Stauffer & Hartmann 1986; Ruiz & Anguita 1993) and stimulated the development of more detailed models of M dwarf photospheres (e.g. Allard & Hauschildt 1995; Brett 1995a,b), that eventually brought the development of low-resolution spectroscopic indices based on the molecular bands of TiO and CaH that are used today to identify metal-poor subdwarfs (e.g. Gizis 1997; Woolf & Wallerstein 2006; Lépine et al. 2007, 2013).

On the spectroscopic high-resolution avenue, a very interesting technique was developed by Woolf & Wallerstein (2005). They measured atomic abundances from the high-resolution spectra of 37 K and M dwarfs through a classical line-by-line analysis (see Sect. 2.1), but they fixed the $\log g$ with parallaxes and available models (Hauschildt et al. 1999; Ségransan et al. 2003a) when available (else $\log g$ was fixed to 5.0 dex). The T_{eff} was also determined with models, using observed V, H, and K_s photometry. From here, the microturbulence was calculated by making sure that there was no slope of titanium abundances with the reduced EWs. Then, they used an iterative procedure to get [Fe/H] similar to the one in Sect. 2.1.7), until it converged. They claim a precision of [Fe/H] between 0.05 and 0.10 dex. However, because of restrictions in models, mainly due to a lack of complete molecular line lists, they had to restrict their work to the earliest M subtypes ($T_{eff} > 3500$ K) and to mostly metal-poor stars(median [Fe/H]$= -0.89$ dex). The technique is extended in Woolf & Wallerstein (2006) to 32 additional stars, and they find that metallicity correlates with CaH and TiO band strengths, but do not offer a quantitative calibration. They give, however, a grid of values with [Fe/H] between 0.05 and -1.5 dex, with a cited uncertainty of ± 0.30 dex. Woolf et al. (2009), following previous works, gives a quantitative expression for metallicity,

$$[Fe/H] = a + b\zeta_{TiO/CaH}, \tag{2.17}$$

where $a = -1.685 \pm 0.079$, $b = 1.632 \pm 0.096$, and

$$\begin{aligned} &\zeta_{TiO/CaH} = \frac{1 - TiO5}{1 - [TiO5]_{Z_\odot}}, \text{where} \\ &[TiO5]_{Z_\odot} = -0.164(CaH2 + CaH3)^3 + 0.670(CaH2 + CaH3)^2 - \\ &- 0.118(CaH2 + CaH3) - 0.050, \end{aligned}$$

as illustrated in Fig. 2.15. The TiO5, CaH2, and CaH3 are spectral indices, and the calibration has estimated uncertainties of ± 0.3 dex. However, it has the same limitations as the previous studies that it was based on (Woolf & Wallerstein 2005, 2006). Also, it is suggested by Mann et al. (2013) that this calibration may be sensitive to stellar characteristics other than effective temperature and metallicity, namely stellar activity and gravity, as it may wrongly overestimate the [Fe/H] of some stars.

An alternative formulation of this technique was used just for Kapteyn's star (Woolf & Wallerstein 2004), where the $\log g$ and T_{eff} was fixed directly from precise parallax and interferometric measurements. Using this approach they got a precision for the [Fe/H] of 0.01 dex. The big limitation here is the lack of measurements of the radius of M dwarfs with interferometry, but it holds promise for the

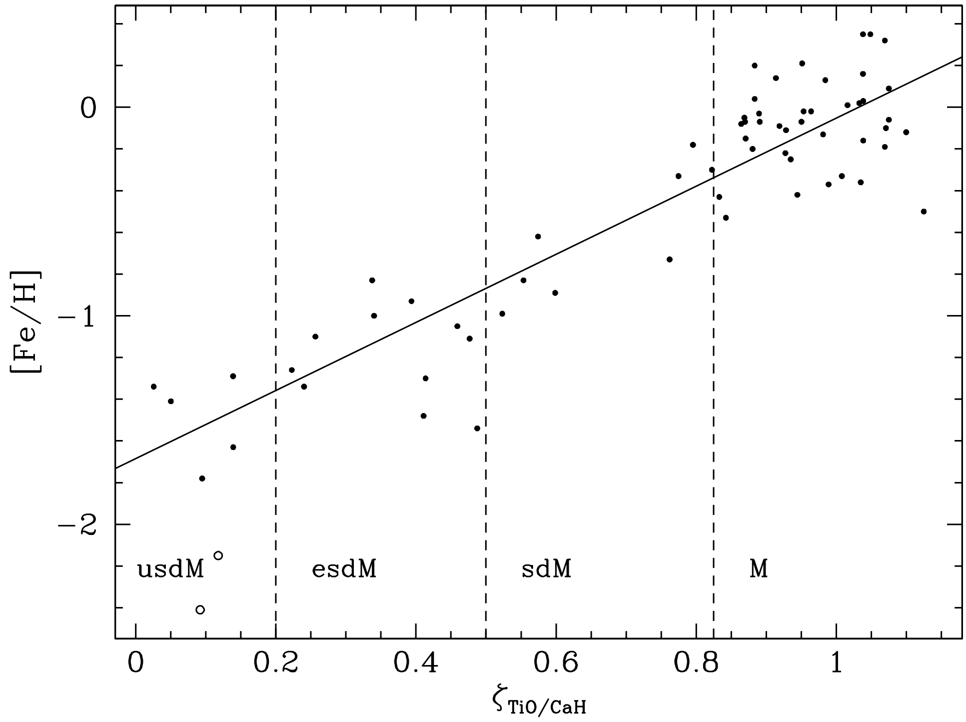

Figure 2.15: Plot of [Fe/H] versus the metallicity index $\zeta_{Tio/CaH}$ from Woolf et al. (2009). The black line depicts the calibration fit.

near future, with the increase of interferometric measurements of M dwarfs (e.g. Boyajian et al. 2012). Alternatively, the transits can also provide a good estimation of the stellar radius, as the transit duration is function of R_*/a, where R_* is the stellar radius and a the semi-major axis of the orbit of the planet. Using Kepler's third law and a mass-radius relation from models, it is possible to change R_*/a into a function of R_* only (Seager & Mallén-Ornelas 2003).

The development of techniques to measure solar to super-solar metallicities of M dwarfs has been slow. The increasing line opacities towards metal-rich stars make the model atmospheres calculations highly complex and uncertain. It is only in the last few years that important progress has been made, driven by increasing interest in exoplanet research and to the fact that it is easier to find (giant) planets around metal-rich stars - the well-know planet-metallicity correlation (e.g. Gonzalez 1997; Santos et al. 2001; Fischer & Valenti 2005).

In the meantime, Rojas-Ayala et al. (2010) have recently published a novel and potentially very precise technique for measuring M dwarf metallicities. Their technique is based on spectral indices measured from low-dispersion ($R \sim 2700$) K-band spectra, and it needs neither photometric magnitudes nor parallaxes, allowing measurements of fainter (or/and farther away) stars. They analysed 17 M dwarf secondaries with an FGK primary, which also served as metallicity calibrators, and measured the equivalent widths of the NaI doublet (2.206 and 2.209 μm), and the CaI triplet (2.261,2.263 and 2.265 μm). With these measurements and a water absorption spectral index sensitive to stellar temperatures they constructed a metallicity scale with an adjusted multiple correlation coefficient greater than the one of Schlaufman & Laughlin (2010) ($R^2_{ap} = 0.63$), and also with a tighter RMS$_p$ of 0.02 when compared to other studies (0.05, 0.04, and 0.02 for Bonfils et al. (2005); Johnson & Apps (2009); Schlaufman & Laughlin (2010). The metallicity calibration is valid over -0.5 to +0.5 dex, with an estimated uncertainty of ±0.15 dex. This technique has been improved in a recent paper Rojas-Ayala et al. (2012) where they re-calibrate the [Fe/H] and [M/H] relations using a new water index, H_2O-K2. They also compared their measurements with BT-Settl-2010 models (Allard et al. 2010), where they could confirm the [Fe/H] sensitivity of the Na and Ca indexes, for $T_{eff} > 3000K$, as well as the independence of the water index from metallicity (Fig. 2.16). They also demonstrate that the chosen indexes are weakly dependent of surface gravity (see Sect. 2.4.4).

The new relations,

$$\begin{aligned} &[Fe/H] = A + B\frac{NaI_{EW}}{H_2O-K2} + C\frac{CaI_{EW}}{H_2O-K2} \\ &A = -1.039 \pm 0.170 \\ &B = 0.092 \pm 0.023 \\ &C = 0.119 \pm 0.033 \end{aligned} \tag{2.18}$$

and

$$\begin{aligned} &[M/H] = A + B\frac{NaI_{EW}}{H_2O-K2} + C\frac{CaI_{EW}}{H_2O-K2} \\ &A = -0.731 \pm 0.120 \\ &B = 0.066 \pm 0.016 \\ &C = 0.083 \pm 0.023 \end{aligned} \tag{2.19}$$

where the H_2O-K2 water index is defined as

$$H_2O-K2 = \frac{F(2.070-2.090)/F(2.235-2.255)}{F(2.235-2.255)/F(2.360-2.380)}, \tag{2.20}$$

and the $F(X-Y)$ is the median of the flux in the range $(X-Y)$ μm. The two metallicity calibrations have a residual mean square error (similar to rms) of, respectively, 0.141 dex and 0.100 dex. The residual mean square error (RMSE) is defined as

$$RMSE = \sqrt{RMS_p} = \sqrt{\sum \frac{(y-y_i)^2}{n-p}}, \tag{2.21}$$

where RMS_p is the residual mean square, $(y-y_i)$ is the value of the residuals, n is the number of data points, and p the number of parameters.

The infrared calibrations in the H and K_s band of Terrien et al. (2012) follows the method of Rojas-Ayala et al. (2012) closely, using 22 calibrations from FGK+M pairs. From here they derive two expressions for metallicity,

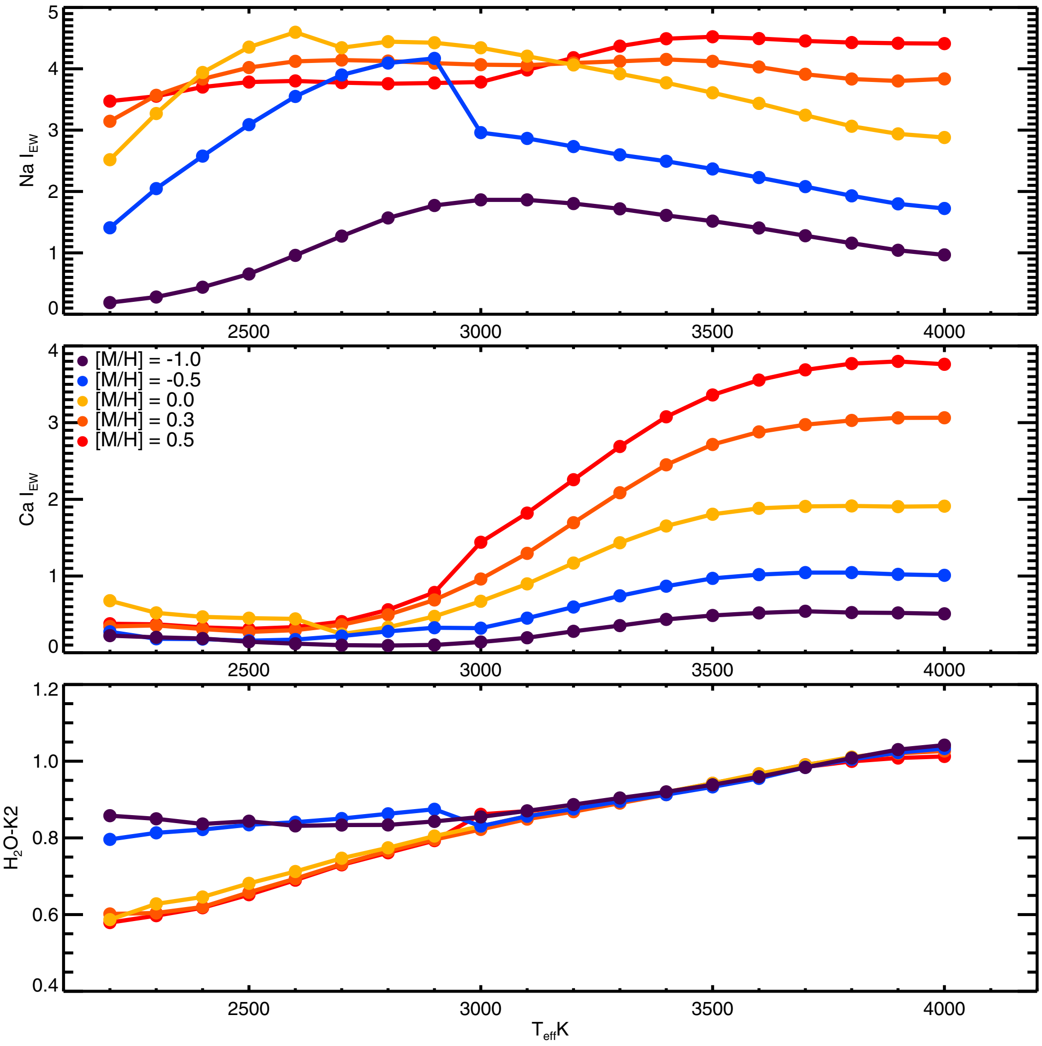

Figure 2.16: Plots of the equivalent widths of the NaI doublet (top), the CaI triplet (middle) and the water index (bottom), measured from the BT-Settl-2010 synthetic spectra (Allard et al. 2010) as a function of T_{eff}. The different colours correspond to different metallicities. From Rojas-Ayala et al. (2012).

$$[Fe/H]_K = 0.132EW_{Na} + 0.083EW_{Ca_H} - 0.403(H_2O - K) - 0.616, \tag{2.22}$$

and

$$[Fe/H]_H = 0.340EW_{Ca_K} + 0.407EW_K + 0.436(H_2O - H) - 1.485, \tag{2.23}$$

where EW_X is the EW measurement of a respective metallicity feature, and $H_2O - X$ is a water index, similar to the one in Rojas-Ayala et al. (2012), measured in the H or K band respectively. The dispersion of both calibrations is 0.12 dex, being similar in precision to Rojas-Ayala et al. (2012). Fig. 2.17 shows the residuals of the H and K band calibrations.

The latest publication based on spectroscopic indices, Mann et al. (2013), follows a similar approach to Rojas-Ayala et al. (2012) and Terrien et al. (2012), using low resolution visible and infrared spectra ($1300 < R < 2000$) of M dwarf secondaries with an FGK primary as calibrator. Their calibration sample is much larger than the one of Rojas-Ayala et al. (2012), with 112 calibration pairs, and they use many more spectroscopic features, 120, that they found sensitive to metallicity, using a purely empirical

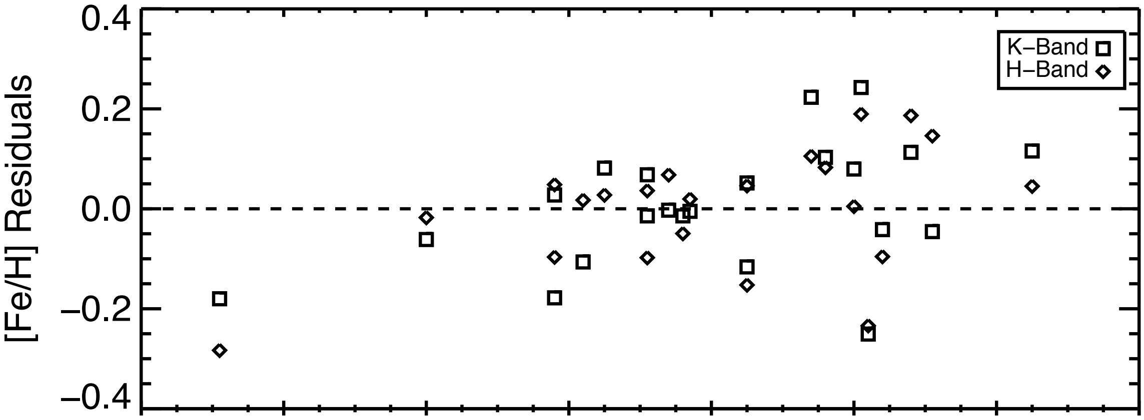

Figure 2.17: Residuals of the two [Fe/H] calibrations in the H and K-band, taken from Terrien et al. (2012).

Table 2.1: Metallicity calibration statistics from Mann et al. (2013).

Equation #	Band	Wavelength Range	SpT range	Metal Type	R^2_{ap}	$RMSE$	σ	χ^2_{Red}
8	Optical	$0.35 < \lambda \leq 1.00$	K5.0 - M2.0	[Fe/H]	0.84	0.07	0.13	8.8
9	Optical	$0.35 < \lambda \leq 1.00$	K5.0 - M2.0	[M/H]	0.80	0.06	0.11	6.4
10	Optical	$0.35 < \lambda \leq 1.00$	M2.0 - M6	[Fe/H]	0.68	0.06	0.14	7.1
11	Optical	$0.35 < \lambda \leq 1.00$	M2.0 - M6	[M/H]	0.65	0.06	0.11	7.8
12	J	$1.00 < \lambda \leq 1.44$	K5.0 - M5.0	[Fe/H]	0.71	0.07	0.16	11.4
13	J	$1.00 < \lambda \leq 1.44$	K5.0 - M5.0	[M/H]	0.55	0.08	0.15	9.4
14	H	$1.44 < \lambda \leq 1.80$	K5.0 - M5.0	[Fe/H]	0.77	0.07	0.14	3.7
15	H	$1.44 < \lambda \leq 1.80$	K5.0 - M5.0	[M/H]	0.73	0.06	0.12	4.2
16	K	$1.80 < \lambda \leq 2.45$	K5.0 - M5.0	[Fe/H]	0.86	0.06	0.11	4.7
17	K	$1.80 < \lambda \leq 2.45$	K5.0 - M5.0	[M/H]	0.77	0.05	0.10	3.8

blind method (blind here means without *a priori* knowledge of line lists or line sizes). From here they established five sets of [Fe/H] and [M/H] calibrations in the optical and infrared (Eq. 8 through 17 in their paper), using a linear combination of the features with colours (in the visible) or water indexes (in the infrared). The water indexes are taken from Terrien et al. (2012) and Rojas-Ayala et al. (2012) for the H- and the K-band respectively. Table 2.1 shows the results of each calibration, taken from their paper, where we can observe that the RMSE varies from 0.05 to 0.07 dex and the dispersion, calculated using a Monte-Carlo technique, ranges from 0.10 to 0.16 dex. It is worth noting that the calibrations cover a wide range of spectral types and wavelength ranges, from K5 to M6 and from the visible to the infrared K-band. The most important conclusion from this work is that, at this resolution (R $\sim$ 2000) it may not be possible to improve the technique further, because there is no benefit of adding more spectral features to the calibrations nor it helps having higher SN spectra or more binary calibrators. The possible improvements may be achieved going to higher resolutions (see our work in Chapter 4), and to lower metallicities.

The high-resolution spectral synthesis technique is also starting to produce its first important results for M dwarfs (e.g. Valenti et al. 1998; Bean et al. 2006b,a). As explained in Sect 2.3, the technique is based on the use of model atmosphere programs like PHOENIX (e.g. Hauschildt et al. 1999)) with a stellar analysis program that is able to synthesise spectra, like SYNTH (Piskunov 1992), SME (Valenti & Piskunov 1996) or MOOG (Sneden 1973). Although the recent revision of the solar oxygen abundance (Asplund et al. 2009; Caffau et al. 2011) has greatly improved the agreement between model atmosphere prediction and spectra of M dwarfs observed at low-to-medium resolution (Allard et al. 2010), many visual-to-red spectral features still correspond to molecular bands that are missing or incompletely described in the opacity databases that underly the atmospheric models. At high spectral resolution, many individual molecular lines in synthetic spectra are additionally displaced from their actual position. In the end, the synthetic spectra atomic or/and molecular lines are fitted to the observed ones and selected with a χ^2 fitting or similar procedure. The stellar parameters are then taken from the model that correspond to the best fit to the observed spectra (see Fig. 2.18).

In the last few years several studies were made regarding spectral synthesis and fit matching to high-resolution spectra. For instance, Bean et al. (2006b) used this technique to determine with precision the stellar parameters of M dwarfs secondaries with an FGK primary, where the measurements were made with high-precision classical spectroscopic analysis. First, they found that a similar approach made by Valenti et al. (1998) was giving, on average, a value 0.56 dex lower than the measures on the primaries. Then, they changed their approach using a modified MOOG version with updated species and new atomic and molecular line lists from PHOENIX models. From here they fitted synthetic spectra for 16 atomic lines in the 8326-8427 and 8660-8639 Å region, as well as a TiO band centred at 7088 Å to high-resolution spectra of the M dwarf secondaries. They found that their results were consistent to 0.11 dex with techniques applied to solar-type stars, with uncertainties of 48 K and 0.12 dex for effective temperature and metallicity, respectively. These uncertainties do not include any kind of systematic errors, and the used models do not reproduce all the features of the complex M dwarf spectra. This technique was applied later on by Bean et al. (2006a) to determine the metallicities of three planet host stars. It was found that all stars have subsolar metallicities, which contrasts strongly with the observed trend seen in FGK hosts, and have even lower, however compatible, values than those of Bonfils et al. (2005).

The latest contribution from high-resolution [Fe/H] determinations comes from Önehag et al. (2012). They analysed 11 high-resolution J-band spectra of M dwarfs from CRIRES (Kaeufl et al. 2004), with synthetic spectra using SME based on MARCS model atmospheres (Gustafsson et al. 2008). The big advantage of using the J-band is that there are much less molecular bands than in the visible ranges, allowing a precise continuum placement. 13 lines were used to calculate the [Fe/H], and the values of T_{eff} and $\log g$ (from Casagrande et al. (2008) and Bean et al. (2006b) respectively) were fixed for each star, while the microturbulence was set to 1 kms^{-1}. The [Fe/H] and macroturbulence were set as free parameters and were fit simultaneously. An illustration of the procedure is shown in Fig 2.18, where the observed spectrum is depicted with open squares. The thick solid line represents the best fit of the calculated spectra. The upper and lower thin lines represent two calculated spectra where the temperature is 200 K higher and lower, respectively. The uncertainties in metallicity vary from 0.01 to 0.15 dex. When compared with other studies, the Önehag et al. (2012) values are systematically higher than the ones of Bean et al. (2006b) and Bonfils et al. (2005) (with average differences of 0.20 and 0.17 dex respectively) but agrees reasonably with Johnson & Apps (2009) and even better with Schlaufman & Laughlin (2010) (average differences of 0.13 and 0.09 dex respectively). Three M dwarfs from this study are within a binary system with a hotter primary with established [Fe/H] values from spectroscopic analysis. The [Fe/H] values agree within 0.02 dex, except for HD101930A/B with a 0.11 dex difference, but within the uncertainties of the method. This work is limited in range of both spectral type and metallicity but holds great promise in the future.

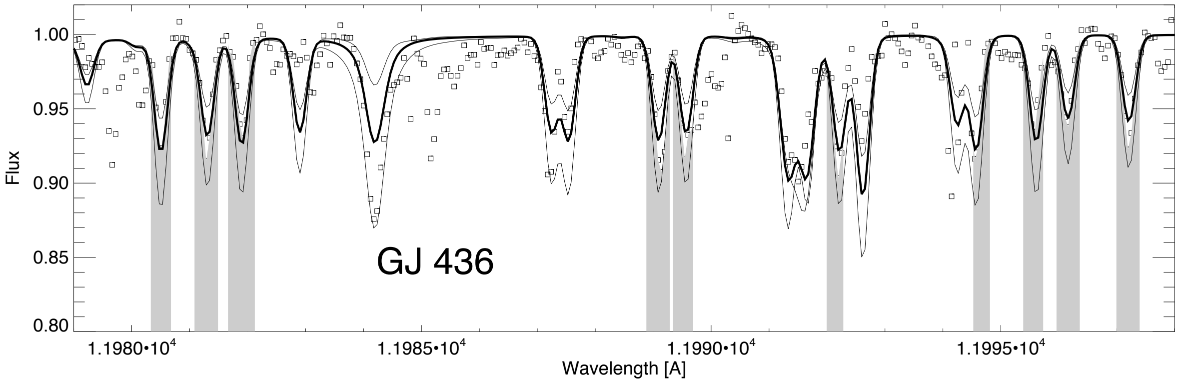

Figure 2.18: Observed (open squares) and synthetic spectra (solid lines) for GJ 436, from Önehag et al. (2012). The thick line correspond to the best-fit synthetic spectra, while the two thin lines correspond to calculated spectra 200 K above and below the best-fit spectra.

2.4.2 Effective temperature

The determination of precise temperatures is still one of the biggest challenges in M dwarf parameter determination. The $\log g$ of most nearby M dwarfs is around ~ 5 dex, and [Fe/H] near the solar abundance, making temperature a challenging parameter to determine with precision. Moreover, the T_{eff} is the parameter that has the most impact in the variation of line strength (Sect. 2.1).

Like metallicity, the determination of effective temperature follows two main avenues: the photometric methods and the spectroscopic ones. In most cases, methods that are applied to determine metallicity (Sect. 2.4.1) are also applied to effective temperature at the same time, in order to disentangle both effects. There are now tens of references for T_{eff} calculation using several different techniques. It is not in the scope of this work to analyze them all in detail. Therefore, we will only show here a few selected works published in the last few years.

Photometric methods

One of the most interesting studies concerning photometry is the Casagrande et al. (2008) calibration, based on IFRM, and already described in Sect. 2.4.1. They present a set of 25 calibrations based on color-temperature relations, using the same functional form, expressed as

$$\theta_{eff} = a_0 + a_1 X + a_2 X^2 + a_3 X^3 \tag{2.24}$$

where $\theta_{eff} = 5040/T_{eff}$, X represent the colour (e.g., $V-J, V-H, V-K$, etc), and a_x the fit coefficients. The calibrations have an internal precision ranging from 17 K (V-J colour) to 85 K ($I_C - H$). However the total error budget amounts to 100 K, and external comparison shows systematics between 100-200 K. It is still widely used today. Fig 2.19 shows, as example, three calibrations of this work.

The latest study regarding effective temperatures (and other parameters, such as radii and luminosity), from Boyajian et al. (2012), is regarded as the new reference. This study is based on interferometric diameter measurements of 54 K and M dwarfs, that can be converted to stellar radii with HIPPARCOS distances (van Leeuwen 2007), with typical errors below 5%. Then, they calculate the bolometric flux

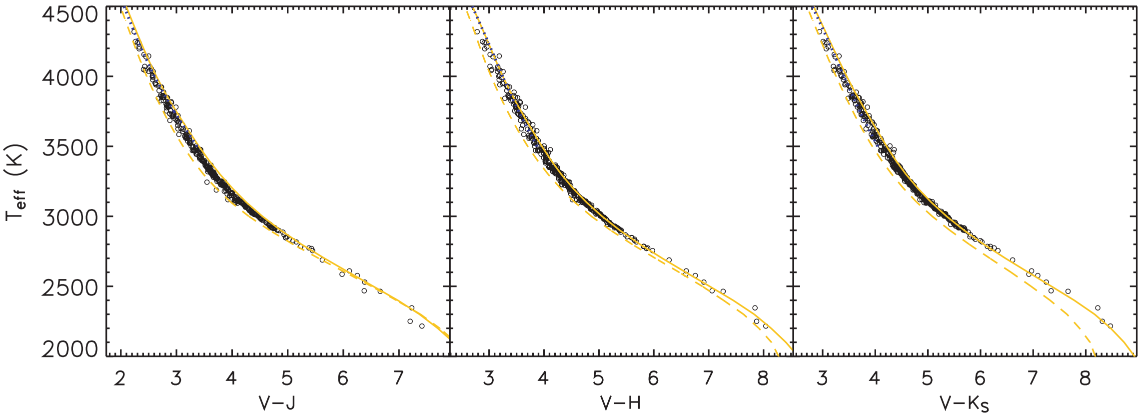

Figure 2.19: T_{eff} versus colour plots from Casagrande et al. (2008). The solid and dashed lines are calculated with a PHOENIX model (Brott & Hauschildt 2005), closely following the empirical calibration, and correspond to -1.0 and 0.0 dex metallicity, respectively.

(F_{BOL}) of each star, by producing stellar energy distributions done with available $BRVIJHK_s$ photometry fitted to spectral templates of Pickles (1998), following a procedure similar to the one of van Belle et al. (2008). The typical uncertainty associated with F_{BOL} is 1.3%.

It is then possible to directly calculate the effective temperature of each star via the rewritten Stefan-Boltzmann Law,

$$T_{eff} = 2341 \left(\frac{F_{BOL}}{D^2} \right)^{1/4}, \tag{2.25}$$

where D is the measured diameter from interferometry. From here they have established a set of 6 new temperature calibrations as a function of colour and metallicity with the following functional form

$$T_{eff} = a_0 + a_1 X + a_2 X^2 + a_3 X [Fe/H] + a_4 [Fe/H] + a_5 [Fe/H]^2, \tag{2.26}$$

where X is the colour index ($B-V, V-R, V-I, V-J, V-H$, or $V-K_s$). Four of the T_{eff} relations are shown in Fig 2.20. The median absolute deviation of the calibrations ranges from 43 to 70 K (corresponding to a dispersion between 64 and 104K). However, including metallicity only improves the uncertainties by 30%. These relations are valid in a range of colours (e.g., $1.5 < V-K < 5.0$) and [Fe/H] between -0.68 and 0.35 dex. An external comparison with the latest BT-Settl PHOENIX model atmosphere color-temperature curves (Allard et al. 2012) shows excellent agreement with the calibration. A qualitative comparison with other works also shows a good agreement.

Spectroscopic methods

On the spectroscopic side, it is worth mentioning, for instance, the works of Woolf & Wallerstein (2005, 2006); Woolf et al. (2009), already described in Sect. 2.4.1, where T_{eff} is first obtained with synthetic photometry from NEXTGEN models (Hauschildt et al. 1999) and then used as initial values into an iterative procedure similar to classical spectroscopic analysis (Sect. 2.1). However, this technique is limited to metal poor and early-type M dwarfs. These authors achieve typical precisions on T_{eff} between 20-50 K, but they refer systematics may be as large as 100-200 K. Woolf et al. (2009) also offers a T_{eff}

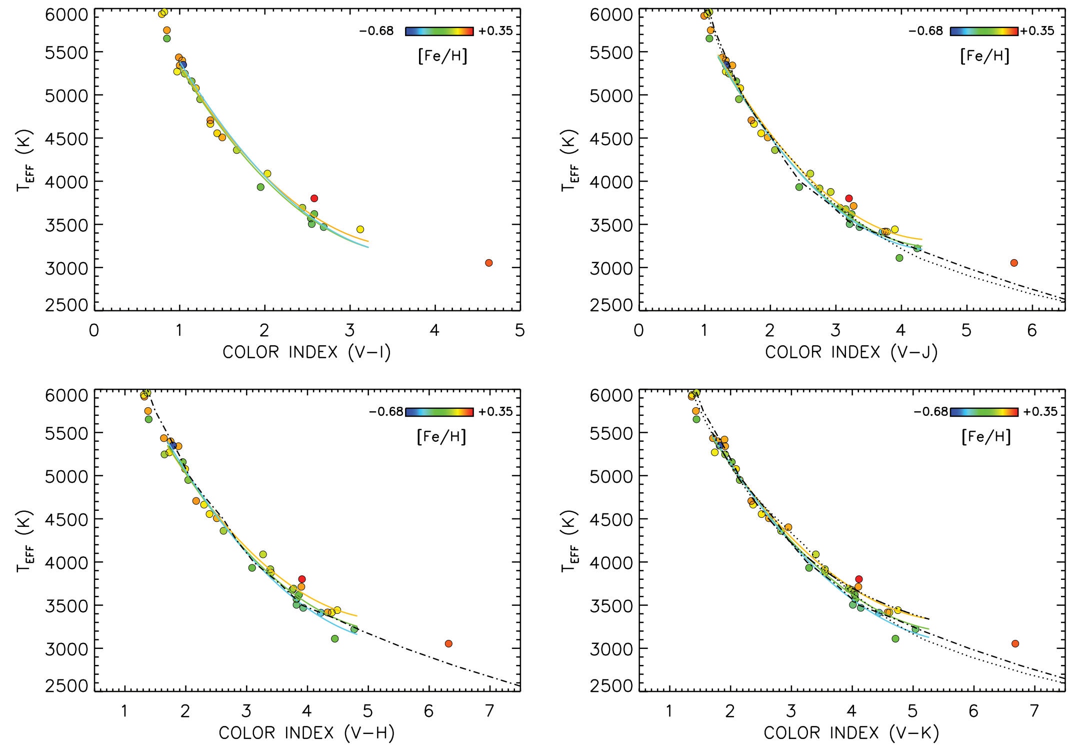

Figure 2.20: Four Colour-Temperature plots from Boyajian et al. (2012). The data points colour reflect the stellar metallicity, as shown in the legend. The coloured lines are solutions to the [Fe/H] dependent fits of the empirical relations of Eq. 2.26.

calibration based on a spectroscopic EW ratio, using the Ca II triplet lines EWs at 8498, 8542, and 8622 Å, and the K I line at 7699 Å. The best fit configures a linear relation, shown in Fig 2.21, and can be written as

$$T_{eff} = a + b(CaII/KI), \tag{2.27}$$

where $a = 3222 \pm 62$, and $b = 83.0 \pm 9.6$. This calibration is valid between 3500 and 4100 K, and the authors report an accuracy of $\pm 100K$ for this calibration.

As explained in Sect 2.4.1, Rojas-Ayala et al. (2010, 2012) used low-resolution spectra of M dwarfs to establish an empirical calibration of metallicity for M dwarfs, and used Allard et al. (2010) atmospheric models to validate this calibration. Based on the observed correlation of the water index with T_{eff} in Allard et al. (2010) synthetic spectra, and its independence of [Fe/H], as illustrated in the bottom panel of Fig. 2.16, they measured the effective temperature of the M dwarfs by comparing the EWs of their water index (Eq. 2.20) from Allard et al. (2010) synthetic spectra to the EWs of M dwarf spectra. According to Rojas-Ayala et al. (2012), systematics of the order of ±100 K are expected.

In order to explore later-type M dwarfs using high-resolution spectroscopic methods it is necessary to use full spectral synthesis. The examples already given in Sect. 2.4.1 include the works of, for instance, Bean et al. (2006b) and Önehag et al. (2012), where such a method is used to obtain a range of parameters, including temperature. Using such methods Bean et al. (2006b) analyses 5 M dwarfs with a FGK primary, and obtains a dispersion of 48 K, but systematics are not accounted for in their assessment. The sample is also very small to attest the technique reliability and range.

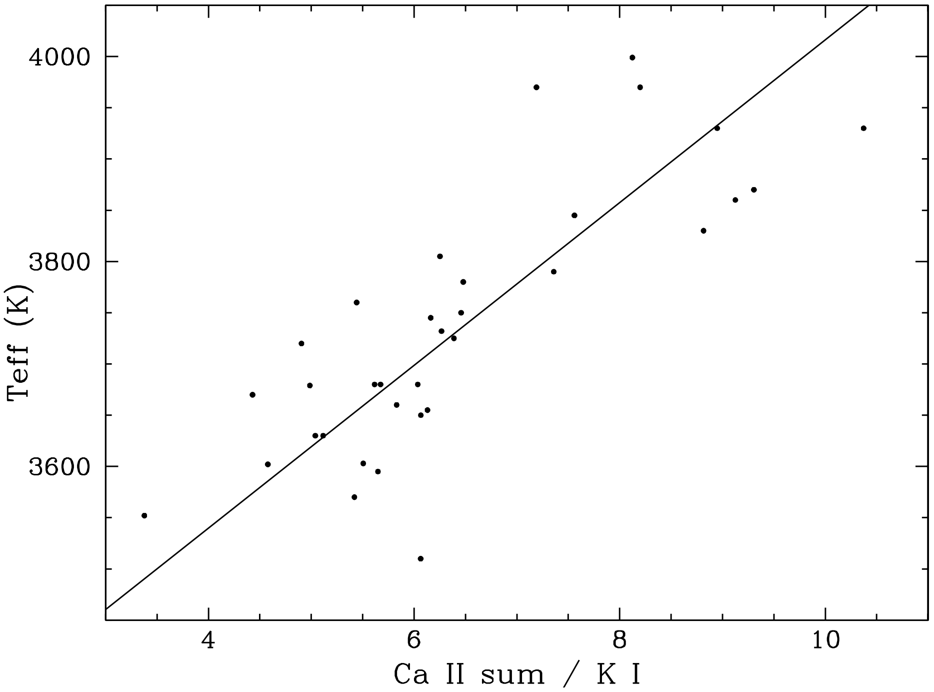

Figure 2.21: T_{eff} versus CaII/KI index from Woolf et al. (2009). The linear fit to the data is shown by a solid line.

Önehag et al. (2012) builds on the fast progress of model atmospheres in the last few years. Their sample is composed of 11 M dwarfs, of which three are secondaries in a binary system with a FGK-type companion. They fit synthetic to observed high-resolution spectra in the J band (1100-1400 nm), that is relatively free of molecular lines. Regarding T_{eff} they used the Casagrande et al. (2008) calibration to get an input value to evaluate the fit to the synthetic spectra created by SME and based on MARCS model atmospheres (Gustafsson et al. 2008). Uncertainties in the temperature are assumed to be $\sim$ 150 K.

2.4.3 Mass & radius

The determination of precise stellar mass and radius is very important in the context of extrasolar planets. The precision of these quantities is directly connected to the precision that we can obtain for the mass and radius of the planets, as seen in Eq. A.1,A.2 in the case of the RV technique and in Eq. A.3,A.4 in the case of transits.

The determination of mass and radius follows two main avenues. On the one hand we have the indirect methods, that are based in theoretical evolutionary models (e.g. Baraffe et al. 1998; Demarque et al. 2004; Dotter et al. 2008) that use observational data, such as luminosity and/or colour as input. On the other hand there are direct methods of obtaining precise measurements of these parameters, such as the observation of double-line eclipsing binaries (e.g. Delfosse et al. 1999; Torres et al. 2010), for stellar mass, as well as direct radii measurements with interferometry (e.g. Ségransan et al. 2003b; Demory et al. 2009; Boyajian et al. 2012), but these measurements are difficult to obtain and are thus limited to a handful of observations. The typical uncertainties are of the order of 5% for both the stellar mass and radius.

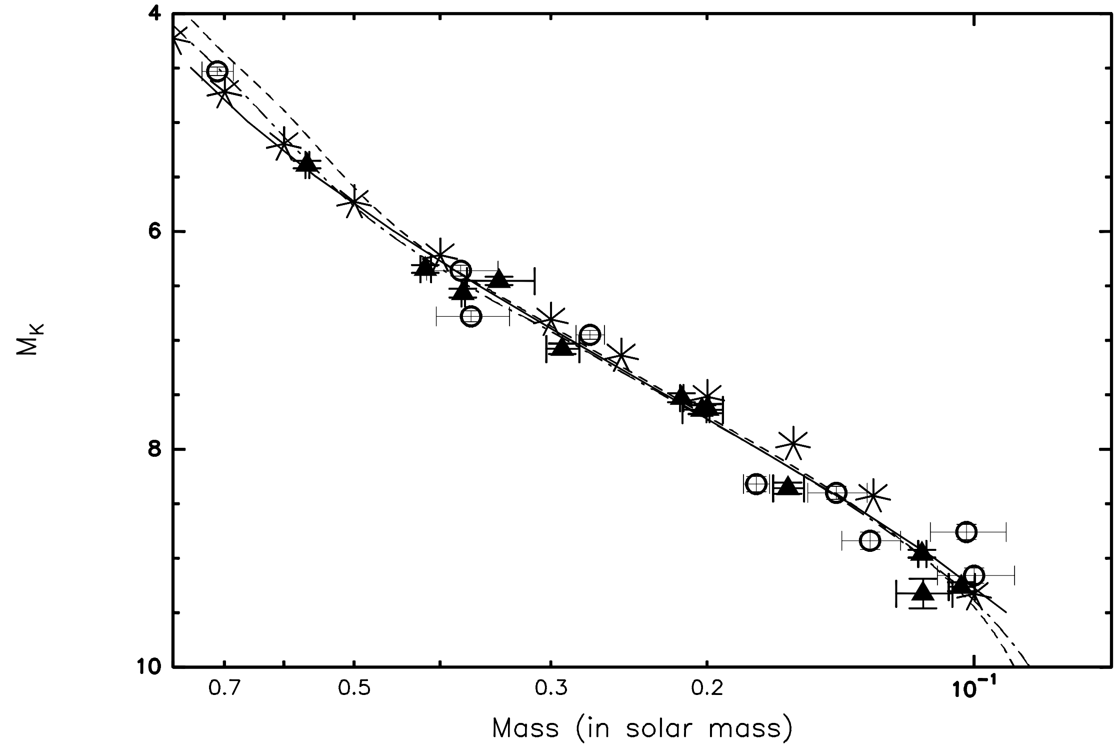

Figure 2.22: K-band mass-luminosity relation from Delfosse et al. (2000). The data points correspond to data taken from different sources. The dashed and dash-dotted lines correspond to 5 Gyr curves from Baraffe et al. (1998) models, with a metallicity of -0.5 and 0.0 dex respectively. The solid line correspond to the polynomial fit of the data points.

By compiling a list of accurate direct measurements, from different techniques, it is also possible to establish empirical mass-luminosity relations, such as the one of Delfosse et al. (2000) or mass-radius (shown in Fig 2.23) and radius-temperature-metallicity calibrations (Boyajian et al. 2012).

We used the relations of Delfosse et al. (2000) in two of our works, detailed in Chapters 4 and 5, to calculate the stellar mass of M dwarfs. These calibrations are based in empirical mass-luminosity relationships, where the relation between infrared absolute magnitude and mass is very tight, beyond measurement errors, as shown in Fig. 2.22 for the case of M_K. For instance, we can write the K-band relation, defined as

$$\log M/M_{\odot} = 10^{-3}(1.8 + 6.12 M_K + 13.205 M_K^2 - 6.2315 M_K^3 + 0.37529 M_K^4), \tag{2.28}$$

where M is the stellar mass and M_K the K-band absolute magnitude. The calibrations are magnitude limited (for instance, M_k is between 4.5 and 9.5), and the agreement with the evolutionary models of Baraffe et al. (1998) is excellent. The individual measurements that originate the calibrations have an accuracy between 0.2 to 10% (with most of the error due to uncertainties in the parallaxes), and it is assumed that the calibration has uncertainties of the order of 10%.

The mass-radius relations of Boyajian et al. (2012) are the most recent attempt aimed at obtaining a precise calibration for mass and radii of K and M dwarfs. They compiled data from double-line spectroscopic eclipsing binaries, from Torres et al. (2010) and López-Morales (2007), where the mass and radius is measured to better than 3 and 5% respectively. For single stars they used the calibration of

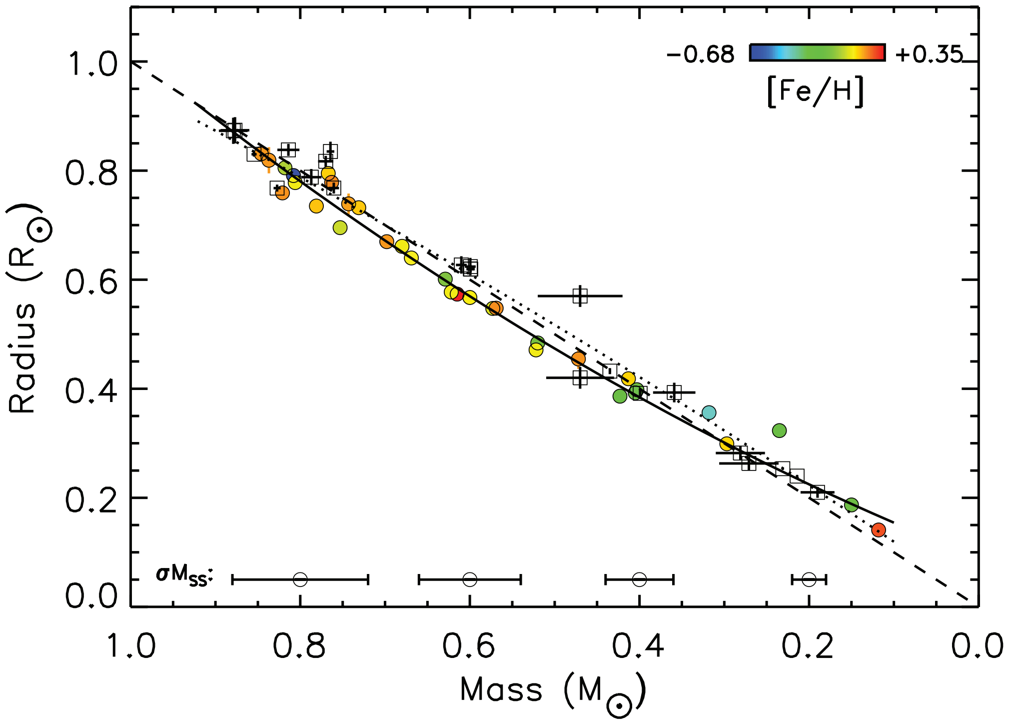

Figure 2.23: Mass-radius relations for single and EB stars. The filled circles and solid line are the data and solution for single stars. The open squares and dotted line are for the EB stars. The typical single star mass error bar is shown at the bottom of the figure. From Boyajian et al. (2012).

Henry & McCarthy (1993) to obtain the stellar mass, assumed to have uncertainties of the order of 10%, and interferometric radii measurements with uncertainties lower than 5%. From here they established two mass-radius calibrations, one for single stars,

$$R_{SS}(R_\odot) = 0.0906(\pm 0.0027) + 0.6063(\pm 0.0153)M + 0.3200(\pm 0.0165)M^2, \tag{2.29}$$

and another for eclipsing binaries,

$$R_{EB}(R_\odot) = 0.0135(\pm 0.0070) + 1.0718(\pm 0.0373)M - 0.1297(\pm 0.0367)M^2, \tag{2.30}$$

where M is the stellar mass for both equations. Both relations are illustrated in Fig. 2.23, where the filled circles and solid line are the data and solution for single stars, while the open squares and dotted line are for the EB stars. Although the mass errors for single stars are large, there is not any discernible metallicity dependence on the mass-radius relation.

The mass-radius anomaly

It is known for some time that the observational measurements of radii are typically 5-10% larger than the ones obtained with evolutionary models of low mass stars (e.g. López-Morales 2007). It was also found that almost all of the systems where a bigger discrepancy was found are members of short-period binaries, with $P < 3$ days. The leading explanation for this effect is that the tidal forces in these binaries tend to synchronise the stellar spins with the orbital period, resulting in a faster rotation and thus higher activity levels. Activity is known to suppress convective transport, meaning that the radius of the star will inflate and T_{eff} will be lower. The impact of metallicity on this effect seems less likely (Torres 2013). However, radii observations of long-period binary systems, LSPMJ1112-7626, from the MEARTH project (Nutzman & Charbonneau 2008; Irwin et al. 2009), where both stars are inflated (Irwin et al. 2011), and the secondary of the double system Kepler-16 (Doyle et al. 2011; Winn et al. 2011), which is also inflated contradict this argument. Using a sample with low star masses and radius having uncertainties lower than 3%, Ribas (2006) showed that the discrepancies are present throughout the whole mass range, and are not above the convective boundary ($\sim$0.35 $M_{\odot}$) only.

Boyajian et al. (2012) also investigated whether the observed discrepancy between observed and predicted radii was also present for single stars. They found that, on average, observations overestimate the radius by 5%, and that this discrepancy is more evident for stars with stellar mass lower than 0.42 $M_{\odot}$. They also find a slight dependence on [Fe/H], where 4 out of 5 stars with radius deviations of more than 1σ, and with masses lower than 0.42 $M_{\odot}$ have a metallicity lower than -0.35 dex. This result has the opposite [Fe/H] trend of the one of Berger et al. (2006), that shows that stars with bloated radius have higher metallicities, and does not agree with Demory et al. (2009) as well, that concludes that the radii of single stars are consistent with models. However, both Berger et al. (2006) and Demory et al. (2009) used radii with precisions better than 10% only. Lastly, Boyajian et al. (2012) concludes that taking into account metallicity is important when using colour indexes, but it does not have a measurable impact on the stellar parameters, and wrote that *'throwing a bucketful of metals in a star does not make it expand in size or cool its surface temperature, it simply morphs the observed colour index'*.

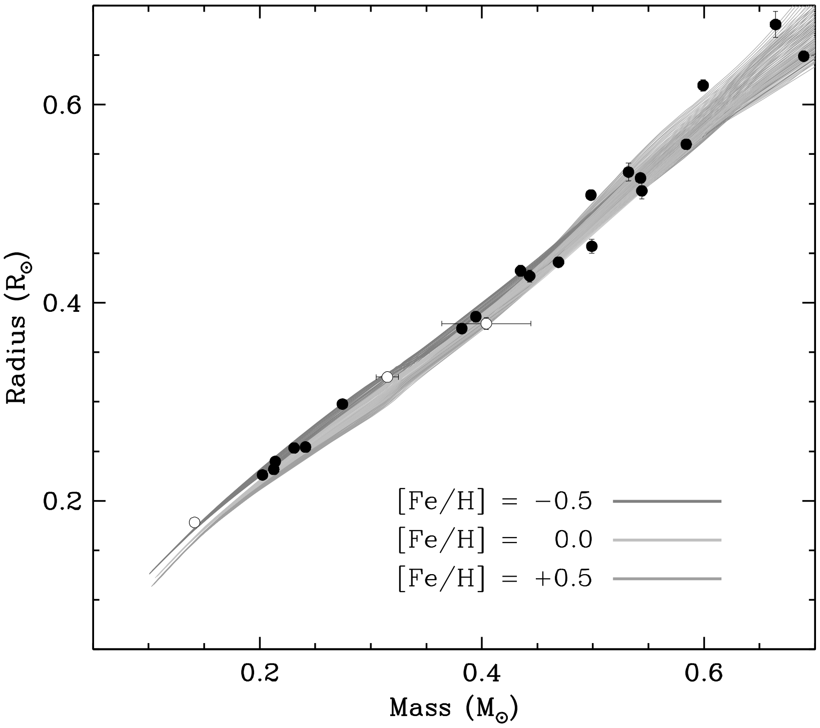

Figure 2.24: Mass-radius diagram for low mass stars, including measurements from double-lined eclipsing binaries (filled symbols) and single line EBs and single stars (open symbols). Three bands depicting Dartmouth models (with ages between 1-13 Gyr) with three different metallicities are also shown.

Recently, Torres (2013) selected a sample with an even narrower criteria, including M dwarfs with mass and radius uncertainties lower than 2%, as shown in Fig. 2.24. The plot also shows three bands depicting three Dotter et al. (2008) evolutionary models with three different metallicities (-0.5, 0.0, and 0.5 dex) and with ages spanning from 1 to 13 Gyr. We now observe that, due to the dramatic decrease of the observational uncertainties, there is hardly any systematic differences between the models and the observations. However, we should be careful when analysing active stars, as high-rotating active stars may provoke an overestimation of the radius of the order of 3 to 6 % (Morales et al. 2010). The effect of activity on stellar mass is thought to be much smaller, and lower than 1%.

2.4.4 Surface gravity & velocity fields

Surface gravity is calculated with precision in studies of high resolution spectral analysis, either directly or by means of synthetic to observational spectra fitting (e.g., Woolf & Wallerstein 2005; Bean et al. 2006b, respectively). However, it seems to be disregarded in the majority of other studies, where they input it as a fixed value, usually 5.0 dex, arguing that the effect of varying it ± 0.5 dex implies only minor differences to the other parameters (e.g. Casagrande et al. 2008), as illustrated in Fig. 2.25, for the water index of Rojas-Ayala et al. (2012).

Regarding velocity fields (micro/macro turbulence), they are generally used as an *ad-hoc* broadening parameter, used in stellar parameter analysis in a similar way as in FGK dwarfs, as explained in Sect. 2.1.6. However, it is not considered a critical parameter as is often neglected (Reid & Hawley 2005).

Alternatively, one can also calculate $\log g$ using the classical law of gravitation (Newton 1760) with the values obtained from measurements, calibrations or models of stellar mass and radius.

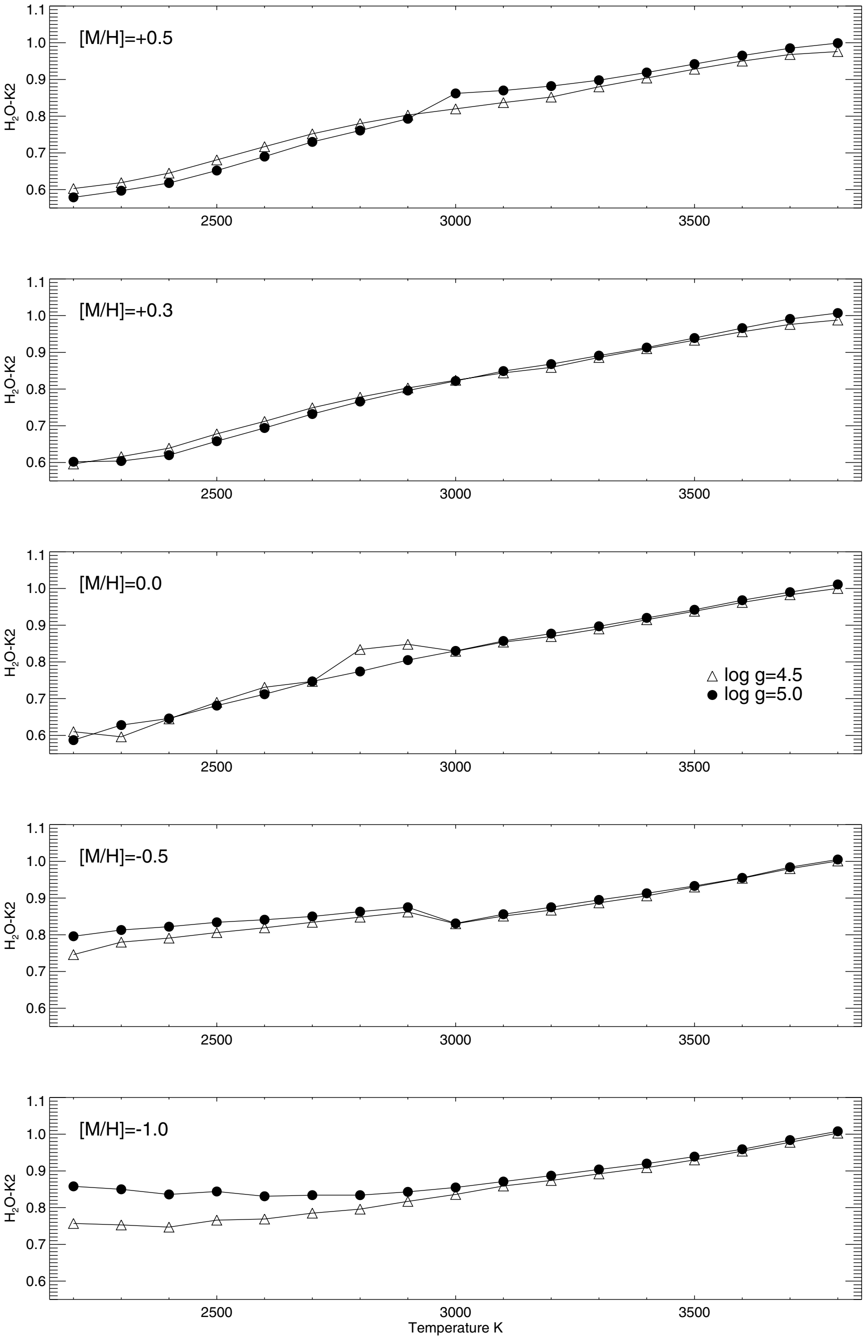

Figure 2.25: H_2O-K2 index measured from Allard et al. (2010) synthetic spectra as a function of T_{eff} for [Fe/H] between -1.0 to 0.5 dex. The triangles represent models with $\log g = 4.5$ and black dots depict models with $\log g = 5.0$. The water index shows negligible sensitivity to surface gravity for $T_{eff} > 3000$ K. From Rojas-Ayala et al. (2012).

Chapter 3

A Comparative study of photometric metallicity scales

3.1 Introduction

As shown in Chapter 2, high-precision stellar parameters of M dwarfs are not easy to obtain. This limitation surfaces mainly due to a lack of understanding of the photospheres of M dwarfs, that in turn mainly derives from incomplete lists of molecular absorption lines, that are numbered in the hundreds of millions but also originates from incomplete physics in the modelling of the photosphere. The ‘missing’ lines from photospheric models lead to an incorrect overestimation of the continuum in synthetic spectra, making any measurement of atomic or molecular lines prone to significant errors, that propagate to stellar parameters.

In my first year of PhD, I pursued a way to upgrade the metallicity calibration of Bonfils et al. (2005) (see Sect. 2.4.1). This calibration is based on the observed difference between the mass-luminosity relation of the V-band, that has a large intrinsic scatter (±0.1 dex), and of the infrared bands (J, H, and K) that has very little scatter (Delfosse et al. 2000). Using [Fe/H] measurements from FGK primaries with M dwarf secondaries as well as direct M dwarf measurements from Woolf & Wallerstein (2005), they obtained a calibration with a dispersion of 0.20 dex.

The original idea was to get as many FGK+M binaries as possible, in order to get a precise measurement of [Fe/H] from the primaries and use high-precision and homogeneous visible and infrared photometry of the M dwarf secondary to establish a new calibration. Unfortunately, at the time, me and my collaborators could not get enough FGK+M binaries with precise V photometry to put forward a photometric calibration that could increase the precision towards 0.10 dex or lower. Instead, we opted to use our limited sample of 23 binaries to test the available M dwarf photometric calibrations of Bonfils et al. (2005), Johnson & Apps (2009), and Schlaufman & Laughlin (2010), all described in Sect. 2.4.1. The motivation to test the three different calibrations comes from the fact that, despite having similar precision, they suffer from systematics at the ±0.1 dex level.

The FGK+M binaries were taken from the third edition of the catalog of nearby stars (Gliese &

Jahreiß 1991), the catalog of nearby wide binary and multiple systems (Poveda et al. 1994), the catalog of common proper-motion companions to HIPPARCOS stars (Gould & Chanamé 2004), and the catalog of disk and halo binaries from the revised Luyten catalog (Chanamé & Gould 2004). We selected only the binaries with a separation of at least 5 arcsec and removed all fast rotators and spectroscopic primaries, as well as all pairs without common proper motion, and systems where the primary star is not in the HIPPARCOS catalog (van Leeuwen 2007), from which we obtain the parallax of the binaries. Most of the precise (< 0.03 dex) V-band photometry was taken from Mermilliod et al. (1997) and most of the infrared JHK-band photometry comes from Skrutskie et al. (2006).

This work culminated with the publication of an article in Astronomy & Astrophysics entitled "Metallicity of M dwarfs II. A comparative study of photometric metallicity scales". This article is attached to the Thesis in Section 3.5. In this Chapter we will first explain the method we use to evaluate the photometric calibrations, in Section 3.2. Then, in Section 3.3, we describe each one of the three calibrations and we apply our methodology to all of them. We also refine the calibration we found best (the Schlaufman & Laughlin (2010) calibration) with our sample, in Section 3.3.4. Finally, in Section 3.4, we discuss our results.

3.2 Evaluating the photometric calibrations

To assess the three alternative photometric calibrations, we evaluated the mean and the dispersion of the difference between the spectroscopic metallicities of the primaries and the metallicities that each calibration predicts for the M dwarf components. As in previous works (Schlaufman & Laughlin 2010; Rojas-Ayala et al. 2010), we also computed the residual mean square RMS_p and the squared multiple correlation coefficient R^2_{ap} (Hocking 1976). The residual mean square RMS_p is defined as

$$RMS_p = \frac{SSE_p}{n-p}, SSE_p = \sum (y_{i,model} - y_i)^2, \tag{3.1}$$

where SSE_p is the sum of squared residuals for a p-term model, n the number of data points, and p the number of free parameters of the model. The squared multiple correlation coefficient R^2_{ap} is defined as

$$R^2_{ap} = 1 - (n-1)\frac{RMS_p}{SST}, SST = \sum (y_i - \bar{y})^2. \tag{3.2}$$

A low RMS_p means that the model describes the data well, while R^2_{ap} close to 1 signifies that the tested model explains most of the variance of the data. The R^2_{ap} can take negative values, when the model under test increases the variance over a null model.

We recall that p should be set to the number of adjusted parameters when a model is adjusted, but instead is zero when a preexisting model is evaluated against independent data. We are, somewhat uncomfortably, in an intermediate situation, with 11, 2, and 12 binary systems in common with the samples that define the calibrations of Bonfils et al. (2005), Johnson & Apps (2009), and Schlaufman & Laughlin (2010) hereafter B05, JA09, and SL10, respectively), and some measurements for those systems in common. Our sample therefore is not fully independent, and in full rigour p should take some effective value between zero and the number of parameters in the model. Fortunately, that number, 2 for

Table 3.1: The equations of the different calibrations, along with their calculated evaluation parameters. Taken from Neves et al. (2012).

Calibration Source + equation	offset [dex]	rms [dex]	RMS$_P$ [dex]	R$^2_{ap}$
B05 : $[Fe/H] = 0.196 - 1.527M_K + 0.091M_K^2 + 1.886(V - K_s) - 0.142(V - K_s)^2$	-0.04 ± 0.04	0.20 ± 0.02	0.04 ± 0.01	0.31 ± 0.22
B05(2) : $[Fe/H] = -0.149 - 6.508\Delta M, \Delta M = Mass_V - Mass_K$	-0.05 ± 0.04	0.22 ± 0.02	0.05 ± 0.01	0.21 ± 0.34
JA09 : $[Fe/H] = 0.56\Delta M_K - 0.05, \Delta M_K = MS - M_K$	0.14 ± 0.04	0.24 ± 0.04	0.06 ± 0.02	0.03 ± 0.51
SL10 : $[Fe/H] = 0.79\Delta(V - K_s) - 0.17, \Delta(V - K_s) = (V - K_s)_{obs} - (V - K_s)_{iso}$	0.02 ± 0.04	0.19 ± 0.03	0.04 ± 0.01	0.41 ± 0.29
This work : $[Fe/H] = 0.57\Delta(V - K_s) - 0.17$	0.00 ± 0.04	0.17 ± 0.03	0.03 ± 0.01	0.43 ± 0.23

all three calibrations, is a small fraction of the sample size, 23. The choice of any effective p between 0 and 2 therefore has little impact on the outcome. We present results for $p = 0$, except when adjusting an update of the Schlaufman & Laughlin (2010) calibration to the full sample, where we use $p = 2$ as we should.

We evaluate the uncertainties on the offset, dispersion, RMS$_p$, and R$^2_{ap}$ through bootstrap resampling. We generated 100,000 virtual samples with the size of our observed sample by random drawing elements of our sample, with repetition. We computed the described parameters for each virtual sample, and used their standard deviation to estimate the uncertainties.

Table 3.1 displays the defining equations of the various calibrations, their mean offset for our sample, the dispersion around the mean value (*rms*), the residual mean square (RMS_p), the square of the multiple correlation coefficient (R^2_{ap}), as well as their uncertainties. The M_K from the B05 calibration is the absolute magnitude calculated with K_s photometric magnitudes and *Hipparcos* parallaxes. The ΔM from the B05(2) calibration is the difference between the V- and the K-band mass-luminosity relations of Delfosse et al. (2000). In the JA09 calibration, the ΔM_K is the difference between the M_{Ks} value in the isometallicity curve corresponding to the mean value of [Fe/H] of the main sequence GK stars from the Valenti & Fischer (2005) catalog (as defined by a fifth-order polynomial $MS = \sum a_i (V - K_s)^i$, where a = $\{-9.58933, 17.3952, -8.88365, 2.22598, -0.258854, 0.0113399\}$), and the absolute magnitude in the K_s band. The $\Delta(V - K_s)$ in the SL10 and 'This work' calibrations is the difference between the observed $V - K_s$ colour and the fifth-order polynomial function of M_{K_s} adapted from the previously mentioned formula from Johnson & Apps (2009). In this case, the coefficients of the polynomial are, in increasing order: (51.1413, −39.3756, 12.2862, −1.83916, 0.134266, −0.00382023).

3.3 The three photometric [Fe/H] calibrations

In this section we discuss the results found for the three photometric metallicity calibrations in turn, and examine their agreement with our spectroscopic sample. Figure 3.1 plots the [Fe/H] obtained from each calibration against the spectroscopic [Fe/H], and it guides us through that discussion.

3.3.1 Bonfils et al. (2005) calibration

As recalled in Sect. 2.4.1, B05 first calibrated the position in a $\{(V - K_s) - M_{K_s}\}$ colour-magnitude diagram into a useful metallicity indicator. That calibration is anchored, on the one hand, in spectroscopic

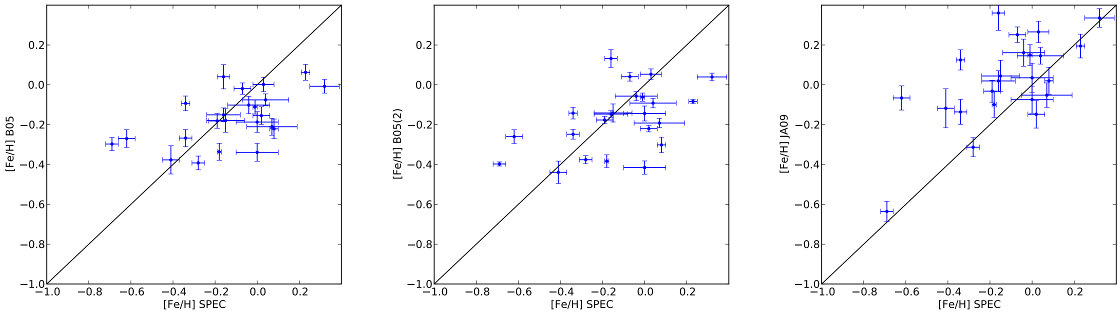

(a) B05 Calibration (b) B05(2) Calibration (c) JA09 Calibration

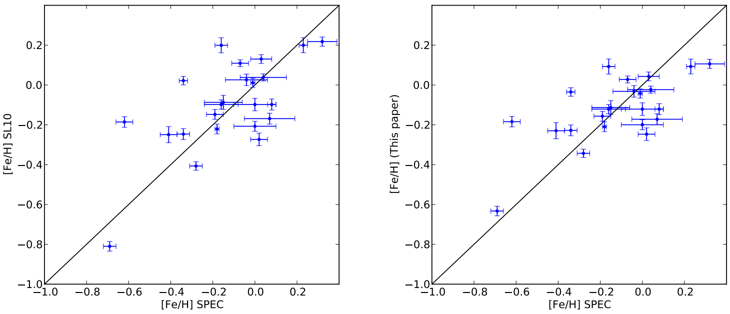

(d) SL10 Calibration (e) This work

Figure 3.1: [Fe/H] estimated from the the calibrations versus spectroscopic metallicity.The blue dots with error bars represent the data points. The black line depicts a one-to-one relationship. Taken from Neves et al. (2012).

metallicity measurements of early metal-poor M-dwarfs by Woolf & Wallerstein (2005), and on the other hand, in later and more metal-rich M dwarfs which belong in multiple systems for which B05 measured the metallicity of a hotter component. The B05 calibration has a ∼0.2 dex dispersion.

For our sample, the B05 calibration is offset by -0.04 ± 0.04 dex and has a dispersion of 0.20 ± 0.02 dex. The negative offset is in line with SL10 finding (see Sect. 3.3.3) that B05 generally underestimates the true [Fe/H]. Correcting from this -0.04 offset almost eliminates the metallicity difference between local M dwarfs and FGK stars.

SL10 also report that the B05 calibration has a very poor R^2_{ap}, under 0.05 (contrasting with our 0.31 result), and that their own model explains almost an order of magnitude more of the variance of their calibration sample. In Table 3.1, we observe, however, that R^2_{ap} is a noisy diagnostic for small samples, as the uncertainties calculated by bootstrapping are high.

In addition to their more commonly used calibration, B05 provide an alternative formulation for [Fe/H]. That second expression, labeled B05(2) in Table 3.1, works from the difference between the V- and K_s-band mass-luminosity relations of Delfosse et al. (2000). The two B05 formulations perform essentially equally for our sample, with B05(2) having a marginally higher dispersion. In the remainder of this Chapter we therefore no longer discuss B05(2).

3.3.2 Johnson & Apps (2009) calibration

Johnson & Apps (2009) derived an alternative calibration, anchored in FGK+M binaries that partly overlap the Bonfils et al. (2005) sample, which forces the agreement of the mean metallicities of local samples of M and FGK dwarfs, as detailed in Sect. 2.4.1.

From Table 3.1, we observe that the JA09 calibration is a good metallicity predictor for our sample at high metallicities, where its calibrator was chosen. With decreasing metallicity, that calibration increasingly overestimates the metallicity, however, as previously pointed out by SL10(see below). Quantitatively, we measure a $+0.14 \pm 0.04$ dex offset for our sample and a dispersion of 0.24 ± 0.04 dex.

3.3.3 Schlaufman & Laughlin (2010) calibration

More recently, Schlaufman & Laughlin (2010) have pointed out the importance of kinematically matching the M and GK samples before comparing their metallicity distributions, and used stellar structure models of M dwarfs to guide their choice of a more effective parametrization of position in the M_{K_s} vs $V-K_s$ diagram. A detailed description of their technique and results is shown in Sect. 2.4.1.

We measure a 0.14 ± 0.02 dex dispersion for the SL10 sample against their calibration, but that calibration has a significantly higher dispersion of 0.19 ± 0.03 for our validation sample. That increased dispersion reflects our sample probing a wider metallicity range than SL10, as verified by computing the dispersion of an 18 star subsample that matches the metallicity range of the SL10 sample. That dispersion is 0.15 ± 0.03 dex, and indistinguishable from 0.14 ± 0.02 dex for the SL10 sample. The increased dispersion for a wider metallicity range suggests that a linear function of $(V-K_s)$ does not fully describe metallicity. We also measure an offset of 0.02 ± 0.04 dex. Offset and *rms* both improve over either the B05 and JA09 calibrations.

3.3.4 Refining the Schlaufman & Laughlin (2010) calibration

We produced updated coefficients for the SL10 prescription, using the RMS_p free parameter $p = 2$ (see Sect. 3.2). The expression for the new metallicity calibration is

$$
\begin{aligned}
[Fe/H] &= 0.57\Delta(V-K_s) - 0.17, \qquad (3.3)\\
\Delta(V-K_s) &= (V-K_s)_{obs} - (V-K_s)_{iso},
\end{aligned}
$$

where $(V-K_s)_{obs}$ is the observed $V-K_s$ color and $(V-K_s)_{iso}$ is a fifth-order polynomial function of M_{K_s} that describes the mean main sequence of the solar neighbourhood from the Valenti & Fischer (2005) catalog. This expression is adopted from Schlaufman & Laughlin (2010), who adapted an M_{K_s} vs $(V-K_s)$ formula from Johnson & Apps (2009).

Table 3.1 shows limited differences between this new fit and the original SL10 calibration. The dispersion of the new fit is tighter by just 0.02 dex (0.17 ± 0.03 dex instead of 0.19 ± 0.03), and the offset is now 0.00 ± 0.04, as expected. The R^2_{ap} value is similar (0.43 ± 0.23 vs 0.41 ± 0.29) and uncertain. Readjusting the coefficients therefore produces a marginal improvement at best.

The dispersion, shown in Table 3.1, is well above the measurement uncertainties. Those therefore contribute negligibly to the overall dispersion, which must be dominated by other sources.

As can be seen in Fig. 3.1, B05 or B05(2) tend to underestimate [Fe/H], while the JA09 calibration clearly overestimates [Fe/H] except at the highest metallicities.

3.4 Discussion

We have assembled a sample of M dwarf companions to hotter FGK stars, where the system has an accurate parallax and the M dwarf component has accurate V and K_s-band photometry. Using the metallicities of the primaries, newly measured or retrieved from the literature, and the assumption that the two components have identical initial compositions, we compared the dispersions of the Bonfils et al. (2005), Johnson & Apps (2009), and Schlaufman & Laughlin (2010) photometric metallicity calibrations. We find that the Schlaufman & Laughlin (2010) scale, which is intermediate between Bonfils et al. (2005) and Johnson & Apps (2009), has the lowest dispersion. We slightly refine that relation, by readjusting its coefficients on our sample.

We find that our tight selection of binaries with accurate parallaxes and photometry sample has insignificantly reduced the dispersion of the measurements around the calibration compared to looser criteria. This suggests that the dispersion, hence the random errors of the calibration, is not defined by measurement uncertainties but instead reflects intrinsic astrophysical dispersion. Nonlinearities in the metallicity dependence of the $V - K_s$ colour are likely to contribute, as suggested both by atmospheric models (Allard, private communication) and by the increased dispersion that we measure over a wider metallicity range. They are, however, unlikely to be the sole explanation, since we see dispersion even in narrow areas of the colour-magnitude diagram. Stellar evolution cannot significantly contribute, since early M dwarfs evolve rapidly to the main sequence and they remain there for much longer than a Hubble time, but rotation and magnetic activity could play a role. Unless, or until, we develop a quantitative understanding of this astrophysical dispersion, the photometric calibration approach may therefore have reached an intrinsic limit. Those calibrations also have the very practical inconvenience of needing an accurate parallax. This limits their use to the close solar neighbourhood, at least until the GAIA catalog becomes available in a decade.

Alternative probes of the metallicities of M dwarfs are therefore obviously desirable. One obvious avenue is to work from higher spectral resolution information and to identify spectral elements that are most sensitive to metallicity and others that are most sensitive to effective temperature. We pursued this approach at visible wavelengths, with HARPS spectra, and the results are shown in detail in Chapter 4.

3.5 Paper: A comparative study of photometric metallicity scales

Abstract.

Stellar parameters are not easily derived from M dwarf spectra, which are dominated by complex bands of diatomic and triatomic molecules and do not agree well with the individual line predictions of atmospheric models. M dwarf metallicities are therefore most commonly derived through less direct techniques. Several recent publications propose calibrations that provide the metallicity of an M dwarf from its K_s band absolute magnitude and its $V - K_s$ colour, but disagree at the ± 0.1 dex level. We compared these calibrations using a sample of 23 M dwarfs, which we selected as wide (> 5 arcsec) companions of F-, G-, or K- dwarfs with metallicities measured on a homogeneous scale and which we require to have V band photometry measured to better than $\sim$0.03 magnitude.

We find that the Schlaufman & Laughlin (2010) calibration has the lowest offsets and residuals against our sample, and used our improved statistics to marginally refine that calibration. With more strictly selected photometry than in previous studies, the dispersion around the calibration is well in excess of the [Fe/H] and photometric uncertainties. This suggests that the origin of the remaining dispersion is astrophysical rather than observational.

Contribution. Here I wrote the totality of the paper and did almost all the work. My co-authors contributed with observations, important ideas and suggestions and helped in the revision of the paper making relevant remarks and corrections.

A&A 538, A25 (2012)
DOI: 10.1051/0004-6361/201118115

Astronomy & Astrophysics

Metallicity of M dwarfs

II. A comparative study of photometric metallicity scales*

V. Neves[1,2,3], X. Bonfils[2], N. C. Santos[1,3], X. Delfosse[2], T. Forveille[2], F. Allard[4], C. Natário[5,6], C. S. Fernandes[5], and S. Udry[7]

[1] Centro de Astrofísica, Universidade do Porto, Rua das Estrelas, 4150-762 Porto, Portugal
email: `vasco.neves@astro.ua.pt`
[2] UJF-Grenoble 1 / CNRS-INSU, Institut de Planétologie et d'Astrophysique de Grenoble (IPAG) UMR 5274, 38041 Grenoble, France
[3] Departamento de Física e Astronomia, Faculdade de Ciências, Universidade do Porto, Rua do Campo Alegre, 4169-007 Porto, Portugal
[4] Centre de Recherche Astrophysique de Lyon, UMR 5574: CNRS, Université de Lyon, École Normale Supérieure de Lyon, 46 Allée d'Italie, 69364 Lyon Cedex 07, France
[5] Centro de Astronomia e Astrofísica da Universidade de Lisboa, Campo Grande, Ed. C8 1749-016 Lisboa, Portugal
[6] Leiden Observatory, Leiden University, The Netherlands
[7] Observatoire de Genève, Université de Genève, 51 Chemin des Maillettes, 1290 Sauverny, Switzerland

Received 16 September 2011 / Accepted 12 October 2011

ABSTRACT

Stellar parameters are not easily derived from M dwarf spectra, which are dominated by complex bands of diatomic and triatomic molecules and do not agree well with the individual line predictions of atmospheric models. M dwarf metallicities are therefore most commonly derived through less direct techniques. Several recent publications propose calibrations that provide the metallicity of an M dwarf from its K_s band absolute magnitude and its $V - K_s$ color, but disagree at the ±0.1 dex level. We compared these calibrations using a sample of 23 M dwarfs, which we selected as wide (>5 arcsec) companions of F-, G-, or K-dwarfs with metallicities measured on a homogeneous scale and which we require to have V band photometry measured to better than ~0.03 mag. We find that the Schlaufman & Laughlin (2010, A&A, 519, A105) calibration has the lowest offsets and residuals against our sample, and used our improved statistics to marginally refine that calibration. With more strictly selected photometry than in previous studies, the dispersion around the calibration is well in excess of the [Fe/H] and photometric uncertainties. This suggests that the origin of the remaining dispersion is astrophysical rather than observational.

Key words. stars: late-type – stars: fundamental parameters – binaries: general – planetary systems – stars: atmospheres

1. Introduction

M dwarfs are the smallest and coldest stars of the main sequence. Long lived and ubiquitous, M dwarfs are of interest in many astrophysical contexts, from stellar evolution to the structure of our Galaxy. Most recently, interest in M dwarfs has been increased further by planet search programs. Planets induce higher reflex velocities and deeper transits when they orbit and transit M dwarfs rather than larger FGK stars, and the habitable zone of the less luminous M dwarfs are closer in. Lower mass, smaller, and possibly habitable planets are therefore easier to find around M dwarfs, and are indeed detected at an increasing pace (e.g. Udry et al. 2007; Mayor et al. 2009).

Interesting statistical correlations between the characteristics of exoplanets and the properties of their host stars have emerged from the growing sample of exoplanetary systems (e.g. Endl et al. 2006; Johnson et al. 2007; Udry & Santos 2007; Bonfils et al., in prep.). Of those, the planet-metallicity correlation was first identified and remains the best established: a higher metal content increases, on average, the probability that a star hosts Jovian planets (Gonzalez 1997; Santos et al. 2001, 2004; Fischer & Valenti 2005). Within the core-accretion paradigm for planetary formation, that correlation reflects the higher mass of solid material available to form protoplanetary cores in the protoplanetary disks of higher metallicity stars. The correlation is then expected to extend to, and perhaps be reinforced in, the cooler M dwarfs. To counterbalance the lower overall mass of their protoplanetary disks, those disks need a higher fraction of refractory material to form similar populations of the protoplanetary core. Whether the planet-metallicity correlation that seems to vanish for Neptunes and lower mass planets around FGK stars (Sousa et al. 2008; Bouchy et al. 2009) persists for Neptune-mass planets around M dwarfs is still an open question.

Our derivation of the first photometric metallicity calibration for M dwarfs (Bonfils et al. 2005) was largely motivated by probing their planet-metallicity correlation, though only two M-dwarf planetary systems were known at the time. A few planet detections later, a Kolmogorov-Smirnov test of the metallicity distributions of M dwarfs *with* and *without* known planets indicated that they only had a ~11% probability of being drawn from a single parent distribution (Bonfils et al. 2007). With an improved metallicity calibration and a larger sample of

---

* Based on observations collected with the FEROS spectrograph at la Silla observatory under ESO programs 073.D-0802(A), 074.D-0670(A), 078.D-0760(A), and with the ELODIE and SOPHIE spectrographs at the Observatoire de Haute Provence.

M dwarf planets, Schlaufman & Laughlin (2010) lower the probability that M-dwarf planetary hosts have the same metallicity distribution as the general M dwarf population to ∼6%. This result is in line with expectations for the core accretion paradigm, but is only significant at the $\sim 2\sigma$ level. Both finding planets around additional M dwarfs and measuring metallicity more precisely will help characterize this correlation and the possible lack thereof. Here we explore the second avenue.

Measuring accurate stellar parameters from the optical spectra of M dwarfs unfortunately is not easy. As the abundances of diatomic and triatomic molecules (e.g. TiO, VO, H_2O, CO) in the photospheric layers increases with spectral subtype, their forest of weak lines eventually erases the spectral continuum and makes a line-by-line spectroscopic analysis difficult for all but the earlier M subtypes. Woolf & Wallerstein (2005, 2006) measured atomic abundances from the high-resolution spectra of 67 K and M dwarfs through a classical line-by-line analysis, but had to restrict their work to the earliest M subtypes ($T_{\rm eff} > 3500$ K) and to mostly metal-poor stars (median [Fe/H] = −0.89 dex). They find that metallicity correlates with CaH and TiO band strengths, but do not offer a quantitative calibration.

Although the recent revision of the solar oxygen abundance (Asplund et al. 2009; Caffau et al. 2011) has greatly improved the agreement between model atmosphere prediction and spectra of M dwarfs observed at low-to-medium resolution (Allard et al. 2010), many visual-to-red spectral features still correspond to molecular bands that are missing or incompletely described in the opacity databases that underly the atmospheric models. At high spectral resolution, many individual molecular lines in synthetic spectra are additionally displaced from their actual position. Spectral synthesis, as well, has therefore had limited success in analyzing M dwarf spectra (e.g. Valenti et al. 1998; Bean et al. 2006). In this context, less direct techniques have been developed to evaluate the metal content of M dwarfs. Of those, the most successful leverage the photometric effects of the very molecular bands that complicate spectroscopic analyses. Increased TiO and VO abundances in metal-rich M dwarfs shift radiative flux from the visible range, where these species dominate the opacities, to the near infrared. For a fixed mass, an increased metallicity also reduces the bolometric luminosity. Those two effects of metallicity work together in the visible, but, in the [Fe/H] and $T_{\rm eff}$ range of interest here, they largely cancel out in the near-infrared. As a result, the absolute V magnitude on an M dwarf is very sensitive to its metallicity, while its near infrared magnitudes are not (Chabrier & Baraffe 2000; Delfosse et al. 2000). Position in a color/absolute magnitude diagram that combines visible and near-infrared bands is therefore a sensitive metallicity probe, but one that needs external calibration.

We pioneered that approach in Bonfils et al. (2005), where we anchored the relation on a combination spectroscopic metallicities of early-M dwarfs from Woolf & Wallerstein (2005) and metallicities, which we measured for the FGK primaries of binary systems containing a widely separated M dwarf component. That calibration, in terms of the K_s-band absolute magnitude and the $V - K_s$ color, results in a modestly significant disagreement between the mean metallicity of solar-neighborhood early/mid-M dwarfs and FGK dwarfs. Johnson & Apps (2009) correctly points out that M and (at least) K dwarfs have the same age distribution, since both live longer than the age of the universe, and that they are therefore expected to have identical metallicity distributions. They derived an alternative calibration, anchored in FGK+M binaries that partly overlap the Bonfils et al. (2005) sample, which forces the agreement of the mean metallicities of local samples of M and FGK dwarfs. Most recently, Schlaufman & Laughlin (2010) have pointed out the importance of kinematically matching the M and GK samples before comparing their metallicity distributions, and used stellar structure models of M dwarfs to guide their choice of a more effective parametrization of position in the M_{K_s} vs. $V - K_s$ diagram. The difference between the three calibrations varies slightly across the Hertzsprung-Russell diagram but, on average, the Johnson & Apps (2009) calibration is 0.2 dex more metal-rich than Bonfils et al. (2005), and Schlaufman & Laughlin (2010) is half-way between those two extremes. Those discrepancies are largely irrelevant when comparing M dwarfs with metallicities consistently measured on any of these three scales, but they are uncomfortably large in any comparison with external information.

We set out here to test those three calibrations. For that purpose, we have assembled a sample of 23 M dwarfs with accurate photometry, parallaxes, and metallicity measured from a hotter companion (Sect. 2). We then perform statistical tests of the three calibrations in Sect. 3, and in Sect. 4 we discuss those results and slightly refine the Schlaufman & Laughlin (2010) calibration, which we find works best. Section 5 presents our conclusions, and an appendix compares our preferred calibration against metallicities obtained with independent techniques.

2. Sample and observations

We adopt the now well-established route of measuring the metal content of the primaries of FGK+M binaries through classical spectroscopic methods, by assuming that it applies to the M secondaries. We searched for such binaries in the third edition of the catalog of nearby stars (Gliese & Jahreiß 1991), the catalog of nearby wide binary and multiple systems (Poveda et al. 1994), the catalog of common proper-motion companions to *Hipparcos* stars (Gould & Chanamé 2004), and the catalog of disk and halo binaries from the revised Luyten catalog (Chanamé & Gould 2004). To ensure uncontaminated measurements of the fainter M secondaries, we required separations of at least 5 arcsec. That initial selection identified almost 300 binaries. We eliminated known fast rotators, spectroscopic binaries, pairs without a demonstrated common proper motion, as well as systems that do not figure in the revised *Hipparcos* catalog (van Leeuwen 2007) from which we obtained the parallaxes of the primaries, and the precise parallax of the secondary, in the case of GI 551. With very few exceptions, the secondaries have good JHK_s photometry in the 2MASS catalog (Skrutskie et al. 2006), which we therefore adopt as our source of near-infrared photometry. The only exception is Gl 551 (Proxima Centauri), which has saturated K_s 2MASS measurements and for which we use the Bessell (1991) measurements that we transform into K_s photometry using the equations of Carpenter (2001).

Precise optical photometry of the secondaries, to our initial surprise, has been less forthcoming, and we suspected noise in their V-band photometry to contribute much of the dispersion seen in previous photometric metallicity calibrations. We therefore applied a strict threshold in our literature search and only retained pairs in which the V-band magnitude of the secondary is measured to better than 0.03 mag. This criterion turned out to severely restrict our sample, and we plan to obtain V-band photometry for the many systems that meet all our other requirements, including the availability of a good high-resolution spectrum of the primary. Mermilliod et al. (1997) has been our main source of Johnson-Cousins VRI photometry. For ten sources RI photometry was in Weistrop and Kron systems instead of Johnson-Cousins. We therefore applied transformations

Table 1. Stellar parameters measured from the primaries, with the [Fe/H] of the M dwarf secondary inferred from the primary.

Primary	Secondary	$T_{\rm eff}$ [K]	log g [cm s^{-2}]	ξ_t [km s^{-1}]	[Fe/H]	[Fe/H] source	$T_{\rm eff}$ source
Gl53.1A	Gl53.1B	4705 ± 131	4.33 ± 0.26	0.76 ± 0.25	0.07 ± 0.12	B05	
Gl56.3A	Gl56.3B	5394 ± 47	–	–	0.00 ± 0.10	COR	S08CAL
Gl81.1A	Gl81.1B	5332 ± 22	3.90 ± 0.03	0.99 ± 0.02	0.08 ± 0.02	S08	
Gl100A	Gl100C	4804 ± 81	4.82 ± 0.24	1.25 ± 0.24	–0.28 ± 0.03	New	
Gl105A	Gl105B	4910 ± 65	4.55 ± 0.14	0.77 ± 0.18	–0.19 ± 0.04	New	
Gl140.1A	Gl140.1B	4671 ± 65	4.31 ± 0.15	0.54 ± 0.31	–0.41 ± 0.04	S08	
Gl157A	Gl157B	4854 ± 71	4.75 ± 0.19	1.31 ± 0.20	–0.16 ± 0.03	New	
Gl173.1A	Gl173.1B	4888 ± 72	4.72 ± 0.16	0.97 ± 0.21	–0.34 ± 0.03	New	
Gl211	Gl212	5293 ± 109	4.50 ± 0.21	0.79 ± 0.17	0.04 ± 0.11	B05	
Gl231.1A	Gl231.1B	5951 ± 14	4.40 ± 0.03	1.19 ± 0.01	–0.01 ± 0.01	New	
Gl250A	Gl250B	4670 ± 80	4.41 ± 0.16	0.70 ± 0.19	–0.15 ± 0.09	B05	
Gl297.2A	Gl297.2B	6461 ± 14	4.65 ± 0.02	1.74 ± 0.01	0.03 ± 0.05	New	
Gl324A	Gl324B	5283 ± 59	4.36 ± 0.11	0.87 ± 0.08	0.32 ± 0.07	B05	
Gl559A	Gl551	5857 ± 24	4.38 ± 0.04	1.19 ± 0.03	0.23 ± 0.02	New	
Gl611A	Gl611B	5214 ± 44	4.71 ± 0.06	–	–0.69 ± 0.03	SPO	
Gl653	Gl654	4723 ± 89	4.41 ± 0.24	0.52 ± 0.31	–0.62 ± 0.04	S08	
Gl666A	Gl666B	5274 ± 26	4.47 ± 0.04	0.74 ± 0.05	–0.34 ± 0.02	New	
Gl783.2A	Gl783.2B	5094 ± 66	4.31 ± 0.13	0.30 ± 0.19	–0.16 ± 0.08	B05	
Gl797A	Gl797B	5889 ± 32	4.59 ± 0.06	1.01 ± 0.06	–0.07 ± 0.04	B05	
GJ3091A	GJ3092B	4971 ± 79	4.48 ± 0.15	0.81 ± 0.22	0.02 ± 0.04	S08	
GJ3194A	GJ3195B	5860 ± 47	–	–	0.00 ± 0.10	SOP	S08CAL
GJ3627A	GJ3628B	5013 ± 47	–	–	–0.04 ± 0.10	SOP	S08CAL
NLTT34353	NLTT34357	5489 ± 19	4.46 ± 0.03	0.91 ± 0.03	–0.18 ± 0.01	New	

References. [B05] Bonfils et al. (2005); [COR] CCF [Fe/H] derived from spectra of the CORALIE Spectrograph; [S08CAL] $T_{\rm eff}$ calibration from Sousa et al. (2008); [S08] Sousa et al. (2008); [New] This paper; [SPO] Valenti & Fischer (2005); [SOP] CCF [Fe/H] taken from spectra of the SOPHIE Spectrograph (Bouchy & The Sophie Team 2006).

following Weistrop (1975) and Leggett (1992), respectively. The $RIJH$ photometry was used to calculate metallicity from the Casagrande et al. (2008) calibration, as discussed in the Appendix. Our final sample contains 23 systems, of which 19 have M-dwarf secondaries and four have K7/K8 secondaries.

We either measured the metallicity of the primaries from high-resolution spectra or adopted measurements from the literature which are on the same metallicity scale. We obtained spectra for nine stars with the FEROS spectrograph (Kaufer & Pasquini 1998) on the 2.2 m ESO/MPI telescope at La Silla. We used the ARES program (Sousa et al. 2007) to automatically measure the equivalent widths of the Fe 1 and Fe 2 weak lines (<200 mÅ) in the Fe line list of Sousa et al. (2008). This list is comprised of 263 Fe 1 and 36 Fe 2 stable lines, ranging, in wavelength, from 4500 to 6890 Å. Then, we followed the procedure described in Santos et al. (2004): [Fe/H] and the stellar parameters are determined by imposing excitation and ionization equilibrium, using the 2002 version of the MOOG (Sneden 1973) spectral synthesis program with a grid of ATLAS9 plane-parallel model atmospheres (Kurucz 1993).

For three stars, we used spectra gathered with the CORALIE (Queloz et al. 2000) spectrograph, on the Swiss Euler 1.2 m telescope at la Silla, and SOPHIE (Bouchy & The Sophie Team 2006) spectrograph, on the Observatoire de Haute Provence 1.93 m telescope. For those three stars, we use metallicities derived from a calibration of the equivalent width of the cross correlation function (CCF) of their spectra with numerical templates (Santos et al. 2002). We adopted that approach, rather than a standard spectroscopic analysis, because those observations were obtained with a ThAr lamp illuminating the second fiber of the spectrographs for highest radial velocity precision. The contamination of the stellar spectra by scattered ThAr light would affect stellar parameters measured through a classical spectral analysis, but is absorbed (to first order) into the calibration of the CCF equivalent width to a metallicity. That calibration is anchored onto abundances derived with the Santos et al. (2004) procedures, and has been verified to be on the same scale to within 0.01 dex (Sousa et al. 2011).

We adopt 10 [Fe/H] determinations from previous publications of our group (Bonfils et al. 2005; Sousa et al. 2008), which also used the Santos et al. (2004) methods. Finally, we take one metallicity value from Valenti & Fischer (2005). That reference derived its metallicities through full spectral synthesis, and Sousa et al. (2008) found that they are on the same scale as Santos et al. (2004).

Table 1 lists the adopted stellar parameters (effective temperature, surface gravity, micro-turbulence, and metallicity) from high-resolution spectra of the primaries. Table 2 lists parallaxes and photometry for the full sample, along with their respective references. Columns 1 and 3 display the names of the primary and secondary stars, while Cols. 2 and 4 display their respective spectral types. Column 5 lists the *Hipparcos* parallaxes of the primaries with their associated standard errors. Columns 6 to 11 contain the $V(RI)_{\rm c}JHK_{\rm s}$ photometry of the secondary and their associated errors. Column 12 contains the bibliographic references for the photometry.

3. Evaluating the photometric metallicity calibrations

To assess the three alternative photometric calibrations, we evaluated the mean and the dispersion of the difference between the spectroscopic metallicities of the primaries and the metallicities that each calibration predicts for the M dwarf components. As in previous works (Schlaufman & Laughlin 2010; Rojas-Ayala et al. 2010), we also computed the residual mean square rms$_p$

Table 2. Sample of wide binaries with an FGK primary and an M dwarf secondary, listing the parallaxes of the primary and photometry of the secondary, along with their respective references.

Primary	Sp. Type. primary	Secondary	Sp. Type secondary	π [mas]	V [mag]	R [mag]	I [mag]	J [mag]	H [mag]	K_s [mag]	$V/RI/JHK$ source
Gl53.1A	K4	Gl53.1B	M3	48.20 ± 1.06	13.60 ± 0.02	12.48 ± 0.05	11.01 ± 0.05	9.533 ± 0.039	8.927 ± 0.023	8.673 ± 0.024	W93 / W93 / 2MASS
Gl56.3A	K1	Gl56.3B	K7	37.75 ± 0.95	10.70 ± 0.02	09.84 ± 0.03	9.01 ± 0.03	8.012 ± 0.021	7.369 ± 0.029	7.190 ± 0.020	B90 / B90 / 2MASS
Gl81.1A	G9	Gl81.1B	K7	30.44 ± 0.60	11.20 ± 0.01	10.30 ± 0.01	9.41 ± 0.01	8.413 ± 0.023	7.763 ± 0.021	7.597 ± 0.027	C84 / C84 / 2MASS
Gl100A	K4.5	Gl100C	M2.5	51.16 ± 1.33	12.85 ± 0.01	11.79 ± 0.01	10.43 ± 0.01	9.181 ± 0.027	8.571 ± 0.029	8.347 ± 0.021	C84 / C84 / 2MASS
Gl105A	K3	Gl105B	M4	139.27 ± 0.45	11.66 ± 0.02	10.45 ± 0.05	8.87 ± 0.05	7.333 ± 0.018	6.793 ± 0.038	6.574 ± 0.020	W93 / W93 / 2MASS
Gl140.1A	K3.5	Gl140.1B	K8	51.95 ± 1.16	10.17 ± 0.01	– ± –	– ± –	7.436 ± 0.023	6.828 ± 0.023	6.620 ± 0.040	S96 / – / 2MASS
Gl157A	K4	Gl157B	M2	64.40 ± 1.06	11.61 ± 0.03	– ± –	– ± –	7.773 ± 0.024	7.162 ± 0.033	6.927 ± 0.031	U74 / – / 2MASS
Gl173.1A	K3	Gl173.1B	M3	32.69 ± 1.51	14.19 ± 0.02	13.05 ± 0.05	11.65 ± 0.05	10.263 ± 0.022	9.715 ± 0.028	9.421 ± 0.024	W93 / W93 / 2MASS
Gl211	K1	Gl212	M0	81.44 ± 0.54	09.76 ± 0.01	8.81 ± 0.05	7.76 ± 0.05	6.586 ± 0.021	5.963 ± 0.016	5.759 ± 0.016	HIP / W93 / 2MASS
Gl231.1A	G0	Gl231.1B	M3.5	51.95 ± 0.40	13.27 ± 0.02	12.15 ± 0.05	10.62 ± 0.05	9.088 ± 0.023	8.559 ± 0.042	8.267 ± 0.018	WT81 / WT81 / 2MASS
Gl250A	K3	Gl250B	M2	114.94 ± 0.86	10.08 ± 0.01	09.04 ± 0.01	7.80 ± 0.01	6.579 ± 0.034	5.976 ± 0.055	5.723 ± 0.036	L89 / L89 / 2MASS
Gl297.2A	F6.5	Gl297.2B	M2	44.68 ± 0.30	11.80 ± 0.02	– ± –	– ± –	8.276 ± 0.019	7.672 ± 0.027	7.418 ± 0.016	R04 / – / 2MASS
Gl324A	G8	Gl324B	M4	81.03 ± 0.75	13.16 ± 0.01	11.94 ± 0.05	10.27 ± 0.05	8.560 ± 0.027	7.933 ± 0.040	7.666 ± 0.023	D88 / WT77 / 2MASS
Gl559A	G2	Gl551	M6	772.33 ± 2.42	11.05 ± 0.02	9.43 ± 0.03	7.43 ± 0.03	5.357 ± 0.023	4.835 ± 0.057	4.31 ± 0.03	B90 / B90 / 2MASS+B91
Gl611A	G8	Gl611B	M4	68.87 ± 0.33	14.23 ± 0.02	13.00 ± 0.05	11.38 ± 0.05	9.903 ± 0.021	9.453 ± 0.021	9.159 ± 0.017	W96 / W96 / 2MASS
Gl653	K5	Gl654	M2	93.40 ± 0.94	10.07 ± 0.01	9.10 ± 0.01	7.95 ± 0.01	6.780 ± 0.029	6.193 ± 0.021	5.975 ± 0.026	K02 / K02 / 2MASS
Gl666A	G8	Gl666B	M0	113.61 ± 0.69	08.70 ± 0.01	– ± –	– ± –	7.237 ± 9.999	5.112 ± 0.023	4.856 ± 0.020	E79 / – / 2MASS
Gl783.2A	K1	Gl783.2B	M4	49.04 ± 0.65	14.06 ± 0.02	12.81 ± 0.03	11.20 ± 0.03	9.627 ± 0.018	9.108 ± 0.015	8.883 ± 0.018	DS92 / DS92 / 2MASS
Gl797A	G5	Gl797B	M2.5	47.65 ± 0.76	11.87 ± 0.01	– ± –	– ± –	8.160 ± 0.020	7.645 ± 0.023	7.416 ± 0.016	D82 / – / 2MASS
GJ3091A	K2	GJ3092B	M	33.83 ± 1.00	15.64 ± 0.03	13.81 ± 0.05	11.97 ± 0.05	11.092 ± 0.023	10.540 ± 0.026	10.266 ± 0.021	P82 / E76 / 2MASS
GJ3194A	G4	GJ3195B	M3	41.27 ± 0.58	12.55 ± 0.02	11.49 ± 0.05	10.15 ± 0.05	8.877 ± 0.021	8.328 ± 0.023	8.103 ± 0.029	W96 / W96 / 2MASS
GJ3627A	G5	GJ3628B	M3.5	38.58 ± 2.17	14.10 ± 0.03	12.88 ± 0.05	11.31 ± 0.05	9.828 ± 0.022	9.247 ± 0.021	9.015 ± 0.018	W88 / W88 / 2MASS
NLTT34353	G5	NLTT34357	K7	20.73 ± 1.05	12.41 ± 0.02	11.51 ± 0.03	10.59 ± 0.03	9.595 ± 0.026	8.910 ± 0.026	8.734 ± 0.019	R89 / R89 / 2MASS

References. [2MASS] Skrutskie et al. (2006); [B90] Bessell (1990); [B91] Bessell (1991); [C84] Caldwell et al. (1984); [D82] Dahn et al. (1982); [D88] Dahn et al. (1988); [DS92] – Dawson & Forbes (1992); [E76] Eggen (1976); [E79] – Eggen (1979); [HIP] van Leeuwen (2007); [K02] Koen et al. (2002); [L89] Laing (1989); [P82] Pesch (1982); [R04] Reid et al. (2004); [R89] Ryan (1989); [S96] Sinachopoulos & van Dessel (1996); [U74] Upgren (1974); [W88] Weis (1988); [W93] Weis (1993); [W96] Weis (1996); [WT77] Weistrop (1977); [WT81] Weistrop (1981).

Table 3. Equations of the different calibrations, along with their calculated evaluation parameters.

Calibration Source + equation	Offset [dex]	rms [dex]	rms_P [dex]	R^2_{ap}
B05 : $[\mathrm{Fe/H}] = 0.196 - 1.527 M_K + 0.091 M_K^2 + 1.886(V - K_\mathrm{s}) - 0.142(V - K_\mathrm{s})^2$	-0.04 ± 0.04	0.20 ± 0.02	0.04 ± 0.01	0.31 ± 0.22
B05(2) : $[\mathrm{Fe/H}] = -0.149 - 6.508\Delta M, \Delta M = Mass_V - Mass_K$	-0.05 ± 0.04	0.22 ± 0.02	0.05 ± 0.01	0.21 ± 0.34
JA09 : $[\mathrm{Fe/H}] = 0.56\Delta M_K - 0.05, \Delta M_K = MS - M_K$	0.14 ± 0.04	0.24 ± 0.04	0.06 ± 0.02	0.03 ± 0.51
SL10 : $[\mathrm{Fe/H}] = 0.79\Delta(V - K_\mathrm{s}) - 0.17, \Delta(V - K_\mathrm{s}) = (V - K_\mathrm{s})_\mathrm{obs} - (V - K_\mathrm{s})_\mathrm{iso}$	0.02 ± 0.04	0.19 ± 0.03	0.04 ± 0.01	0.41 ± 0.29
This paper : $[\mathrm{Fe/H}] = 0.57\Delta(V - K_\mathrm{s}) - 0.17$	0.00 ± 0.04	0.17 ± 0.03	0.03 ± 0.01	0.43 ± 0.23

and the squared multiple correlation coefficient R^2_{ap} (Hocking 1976).

The residual mean square rms_p is defined as

$$\mathrm{rms}_p = \frac{SSE_p}{n - p}, \qquad SSE_p = \sum (y_{i,\mathrm{model}} - y_i)^2, \tag{1}$$

where SSE_p is the sum of squared residuals for a p-term model, n the number of data points, and p the number of free parameters of the model. The squared multiple correlation coefficient R^2_{ap} is defined as

$$R^2_{ap} = 1 - (n - 1)\frac{\mathrm{rms}_p}{SST}, \qquad SST = \sum (y_i - \bar{y})^2. \tag{2}$$

A low rms_p means that the model describes the data well, while R^2_{ap} close to 1 signifies that the tested model explains most of the variance of the data. The R^2_{ap} can take negative values, when the model under test increases the variance over a null model.

We recall that p should be set to the number of adjusted parameters when a model is adjusted, but instead is zero when a preexisting model is evaluated against independent data. We are, somewhat uncomfortably, in an intermediate situation, with 11, 2, and 12 binary systems in common with the samples that define the calibrations of Bonfils et al. (2005), Johnson & Apps (2009), and Schlaufman & Laughlin (2010), and some measurements for those systems in common. Our sample therefore is not fully independent, and in full rigor p should take some effective value between zero and the number of parameters in the model. Fortunately, that number, 2 for all three calibrations, is a small fraction of the sample size, 23. The choice of any effective p between 0 and 2 therefore has little impact on the outcome. We present results for $p = 0$, except when adjusting an update of the Schlaufman & Laughlin (2010) calibration to the full sample, where we use $p = 2$ as we should.

We evaluate the uncertainties on the offset, dispersion, rms_p, and R^2_{ap} through bootstrap resampling. We generated 100 000 virtual samples with the size of our observed sample by random drawing elements of our sample, with repetition. We computed the described parameters for each virtual sample, and used their standard deviation to estimate the uncertainties.

Table 3 displays the defining equations of the various calibrations, their mean offset for our sample, the dispersion around the mean value (rms), the residual mean square (rms_p), the square of the multiple correlation coefficient (R^2_{ap}), as well as their uncertainties. The M_K from the B05 calibration is the absolute magnitude calculated with the K_s photometric magnitudes and the *Hipparcos* parallaxes. The ΔM from the B05(2) calibration is the difference between the V- and the K-band mass-luminosity relations of Delfosse et al. (2000). In the JA09 calibration, the ΔM_K is the difference between the mean value of [Fe/H] of the main sequence FGK stars from the Valenti & Fischer (2005) catalog (as defined by a fifth-order polynomial $MS = \sum a_i (V - K_\mathrm{s})^i$, where $a = \{-9.58933, 17.3952, -8.88365, 2.22598, -0.258854, 0.0113399\}$), and the absolute magnitude in the K_s band. The $\Delta(V - K_\mathrm{s})$ in the SL10 and "This paper" calibrations is the difference between the observed $V - K_\mathrm{s}$ color and the fifth-order polynomial function of M_{K_s} adapted from the previously mentioned formula from Johnson & Apps (2009). In this case, the coefficients of the polynomial are, in increasing order: (51.1413, −39.3756, 12.2862, −1.83916, 0.134266, −0.00382023).

Figure 1 depicts the different [Fe/H] calibrations from Bonfils et al. (2005) (a and b), Johnson & Apps (2009) (c), Schlaufman & Laughlin (2010) (d), and the calibration determined in this paper (e). Table 4 displays the metallicity values from spectroscopy and the different calibrations, where the individual values for each star can be compared directly.

The bootstrap uncertainties of the parameters (Table 3) show that the rms values are the most robust. The R^2_{ap} parameter, in contrast, has large uncertainties. With our small sample size, it therefore does not provide an effective diagnostic of the alternative models.

4. The latest metallicity measurements and calibrations

In this section we discuss the three photometric metallicity calibrations in turn, and examine their agreement with our spectroscopic sample. Figure 2 plots the [Fe/H] obtained from each calibration against the spectroscopic [Fe/H], and it guides us through that discussion.

4.1. Bonfils et al. (2005) calibration

As recalled in the introduction, B05 first calibrated position in a $\{(V - K_\mathrm{s}) - M_{K_\mathrm{s}}\}$ color–magnitude diagram into a useful metallicity indicator. That calibration is anchored, on the one hand, in spectroscopic metallicity measurements of early metal-poor M-dwarfs by Woolf & Wallerstein (2005), and on the other hand, in later and more metal-rich M dwarfs which belong in multiple systems for which B05 measured the metallicity of a hotter component. The B05 calibration has a ~0.2 dex dispersion. Then, they used the calibration to measure the metallicity distribution of a volume-limited sample of 47 M dwarfs, which they found to be more metal-poor (by 0.07 dex[1]) than 1000 FGK stars, with a modest significance of 2.6σ. As mentioned above, Bonfils et al. (2007) used that calibration to compare M dwarfs with and without planets, and found that planet hosts are marginally metal-rich.

For our sample, the B05 calibration is offset by -0.04 ± 0.04 dex and has a dispersion of 0.20 ± 0.02 dex. The negative offset is in line with SL10 finding (see Sect. 4.3) that B05 generally underestimates the true [Fe/H]. Correcting from this −0.04 offset almost eliminates the metallicity difference between local M dwarfs and FGK stars.

---

[1] erroneously quoted as a 0.09 dex difference in Johnson & Apps (2009).

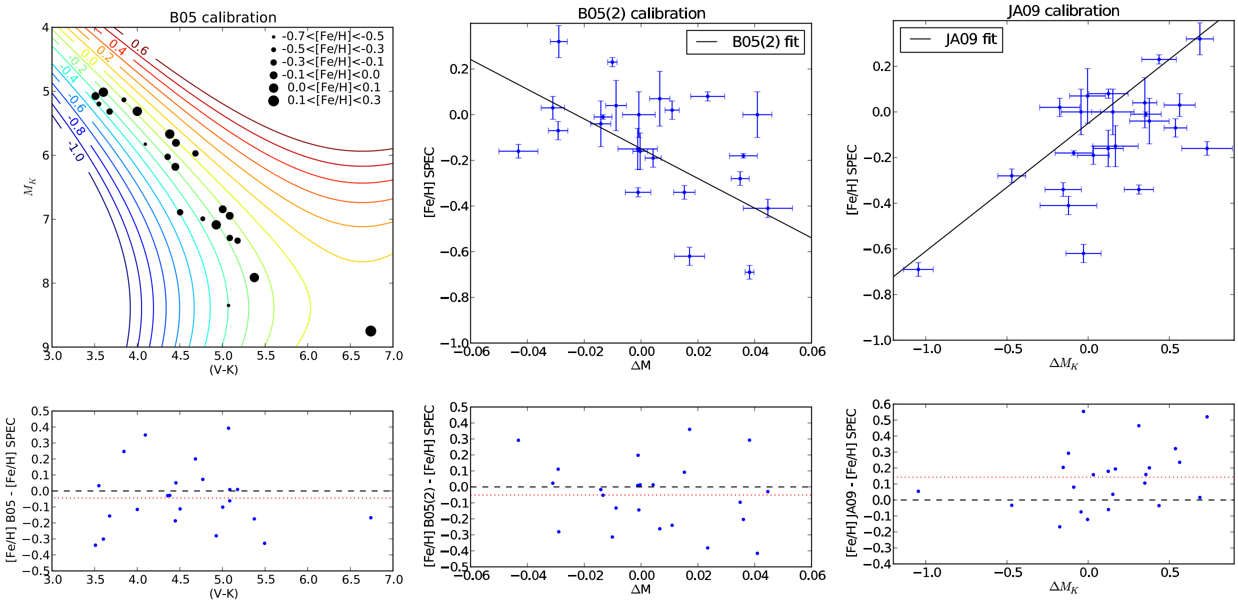

(a) B05 Calibration (b) B05(2) Calibration (c) JA09 Calibration

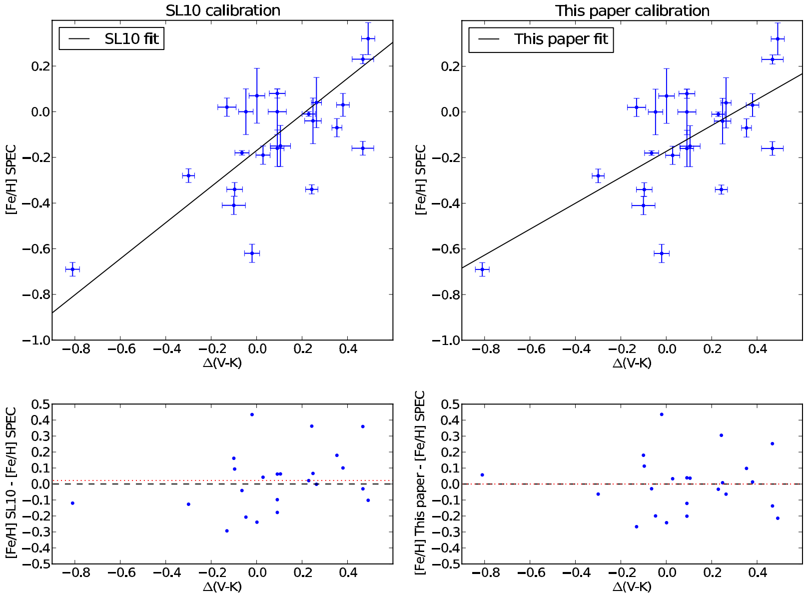

(d) SL10 Calibration (e) This paper

Fig. 1. The different [Fe/H] calibrations from Bonfils et al. (2005) **a**, **b**), Johnson & Apps (2009) **c**), Schlaufman & Laughlin (2010) **d**), and the calibration determined in this paper **e**). In each upper panel, the blue/black dots represent the data points. The black line depicts a fit to the data except in panel **a**), where the calibrated [Fe/H] is shown as isometallicity contours. The lower subpanels show the difference between the calibrated and the spectroscopic metallicity. The black dashed lines represent the null value, and the red dotted line represents the mean difference for that calibration.

SL10 also report that the B05 calibration has a very poor R^2_{ap}, under 0.05, and that their own model explains almost an order of magnitude more of the variance of their calibration sample. In Sect. 3, we noted, however, that R^2_{ap} is a noisy diagnostic for small samples.

In addition to their more commonly used calibration, B05 provide an alternative formulation for [Fe/H]. That second expression, labeled B05(2) in Table 3, works from the difference between the V- and K_s-band mass-luminosity relations of Delfosse et al. (2000). The two B05 formulations perform essentially equally for our sample, with B05(2) having a marginally higher dispersion. In the remainder of this paper we therefore no longer discuss B05(2).

4.2. *Johnson & Apps (2009) calibration*

Johnson & Apps (2009) argue that local M and FGK dwarfs should have the same metallicity distribution, and accordingly chose to fix their mean M dwarf metallicity to the value (−0.05 dex) for a volume-limited sample of FGK dwarfs from the Valenti & Fischer (2005) sample. They defined a sequence representative of average M dwarfs in the $\{(V-K_s)-M_{K_s}\}$ color–magnitude diagram, and used the distance to that main sequence

Table 4. Spectroscopic metallicity of the primaries and metallicities predicted for the secondary by the different calibrations.

Primary	Secondary	[Fe/H] [dex]					
		Spectroscopic	B05	B05(2)	JA09	SL10	This paper
Gl53.1A	Gl53.1B	0.07	–0.21	–0.19	–0.05	–0.17	–0.17
Gl56.3A	Gl56.3B	0.00	–0.34	–0.42	–0.07	–0.21	–0.20
Gl81.1A	Gl81.1B	0.08	–0.22	–0.30	0.02	–0.10	–0.12
Gl100A	Gl100C	–0.28	–0.39	–0.38	–0.31	–0.41	–0.34
Gl105A	Gl105B	–0.19	–0.18	–0.18	–0.03	–0.15	–0.15
Gl140.1A	Gl140.1B	–0.41	–0.38	–0.44	–0.12	–0.25	–0.23
Gl157A	Gl157B	–0.16	0.04	0.13	0.36	0.20	0.10
Gl173.1A	Gl173.1B	–0.34	–0.27	–0.25	–0.14	–0.25	–0.23
Gl211	Gl212	0.04	–0.08	–0.09	0.15	0.04	–0.02
Gl231.1A	Gl231.1B	–0.01	–0.11	–0.06	0.15	0.01	–0.04
Gl250A	Gl250B	–0.15	–0.18	–0.14	0.04	–0.09	–0.11
Gl297.2A	Gl297.2B	0.03	0.00	0.05	0.27	0.13	0.05
Gl324A	Gl324B	0.32	–0.01	0.04	0.34	0.22	0.11
Gl559A	Gl551	0.23	0.06	–0.08	0.19	0.20	0.10
Gl611A	Gl611B	–0.69	–0.30	–0.40	–0.64	–0.81	–0.64
Gl653	Gl654	–0.62	–0.27	–0.26	–0.07	–0.19	–0.18
Gl666A	Gl666B	–0.34	–0.09	–0.14	0.12	0.02	–0.03
Gl783.2A	Gl783.2B	–0.16	–0.15	–0.15	0.02	–0.10	–0.12
Gl797A	Gl797B	–0.07	–0.02	0.04	0.25	0.11	0.03
GJ3091A	GJ3092B	0.02	–0.15	–0.22	–0.15	–0.27	–0.25
GJ3194A	GJ3195B	0.00	–0.19	–0.14	0.04	–0.10	–0.12
GJ3627A	GJ3628B	–0.04	–0.10	–0.06	0.16	0.03	–0.03
NLTT34353	NLTT34357	–0.18	–0.34	–0.38	–0.10	–0.22	–0.21

along M_{K_s} as a metallicity diagnostic. They note that the inhomogeneous calibration sample of B05 is a potential source of systematics, and consequently chose to calibrate their scale from the metallicities of just six metal-rich M dwarfs in multiple systems with FGK primary components.

JA09 present two observational arguments for fixing the mean M dwarf metallicity. They first measured [Fe/H] for 109 G0-K2 stars ($4900 < T_\mathrm{eff} < 5900$ K) and found no significant metallicity gradient over this temperature range, from which they conclude that no difference is to be expected for the cooler M dwarfs. We note, however, that a linear fit to their G0-K2 data set ($[\mathrm{Fe/H}] = 9.74 \times 10^{-5}(T_\mathrm{eff} - 5777) - 0.04$) allows for a wide metallicity range when extrapolated to the cooler M dwarfs ($2700 < T_\mathrm{eff} < 3750$, for M7 to M0 spectral type, with $[\mathrm{Fe/H}] = -0.24$ allowed at the 1σ level for an M0 dwarf and significantly lower than the [Fe/H] offset in B05. More importantly, they measured a large (0.32 dex) offset between the B05 metallicities of six metal-rich M dwarfs in multiple systems and the spectroscopic metallicities which they measured for their primaries. This robustly points to a systematic offset in the B05 calibration for metal-rich M dwarfs, but does not directly probe the rest of the (T_eff, [Fe/H]) space. We do find that the JA09 calibration is a good metallicity predictor for our sample at high metallicities, where its calibrator was chosen. With decreasing metallicity, that calibration increasingly overestimates the metallicity, however, as previously pointed out by SL10 (see below). Quantitatively, we measure a +0.14 ± 0.04 dex offset for our sample and a dispersion of 0.24 ± 0.04.

4.3. *Schlaufman & Laughlin (2010) calibration*

Schlaufman & Laughlin (2010) improve upon B05 and JA09 in two ways. They first point out that, for M and FGK dwarfs to share the same mean metallicity, matched kinematics is as important as volume completeness. Since the various kinematic populations of our Galaxy have very different mean metallicities, the mean metallicity of small samples fluctuates very significantly with their small number of stars from the metal-poor populations. To overcome this statistical noise, they draw from the Geneva-Copenhagen Survey volume-limited sample of F and G stars (Holmberg et al. 2009) a subsample that kinematically matches the volume limited sample of M dwarfs used by JA09. They find a ≃−0.14 ± 0.06 dex mean metallicity for that sample, 0.09 dex lower than adopted by JA09. However, they only used that sample to verify that the mean metallicity of M dwarfs in the solar neighborhood is well defined. In the end, the M dwarfs within a sample of binaries with an FGK primary that they used to fix their calibration are not volume-limited or kinematically-matched, but their mean metallicity ($[\mathrm{Fe/H}] = -0.17 \pm 0.07$) is statistically indistinguishable from the mean metallicity of the volume-limited and kinematically-matched sample.

Second, they use stellar evolution models to guide their parametrization of the color-magnitude space. Using [Fe/H] iso-contours for the Baraffe et al. (1998) models, they show that in a $\{(V - K_\mathrm{s}) - M_{K_\mathrm{s}}\}$ diagram, changing [Fe/H] affects $(V - K_\mathrm{s})$ at an essentially constant M_{K_s}. The metallicity is therefore best parametrized by $(V - K_\mathrm{s})$, and their calibration uses a linear function of the $(V - K_\mathrm{s})$ distance from a nominal sequence in the $\{(V - K_\mathrm{s}) - M_{K_\mathrm{s}}\}$ diagram. They do not force any specific mean metallicity, but verify a posteriori that it matches expectations.

We measure a 0.14 ± 0.02 dex dispersion for the SL10 sample against their calibration, but that calibration has a significantly higher dispersion of 0.19 ± 0.03 for our validation sample. That increased dispersion reflects our sample probing a wider metallicity range than SL10, as verified by computing the dispersion of an 18 star subsample that matches the metallicity range of the SL10 sample. That dispersion is 0.15 ± 0.03 dex, and indistinguishable from 0.14 ± 0.02 dex for the SL10 sample. The increased dispersion for a wider metallicity range suggests that a linear function of $(V - K_\mathrm{s})$ does not fully describe metallicity. We also measure an offset of 0.02 ± 0.04 dex. Offset and rms both improve over either of the B05 and JA10 calibrations.

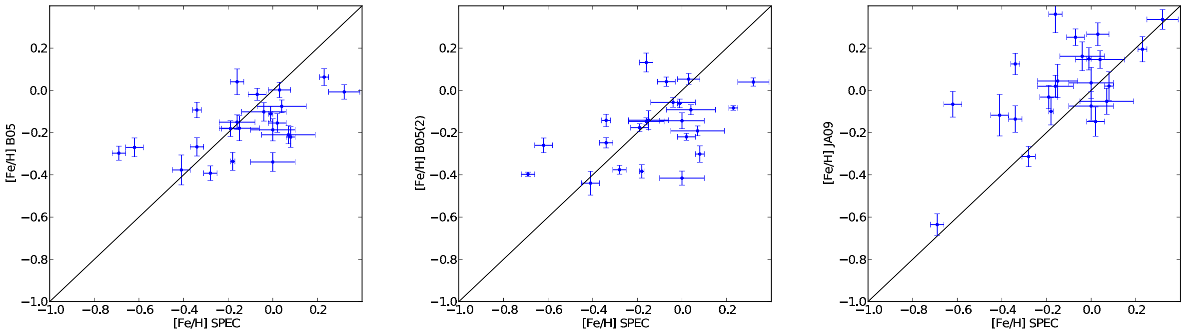

(a) B05 Calibration (b) B05(2) Calibration (c) JA09 Calibration

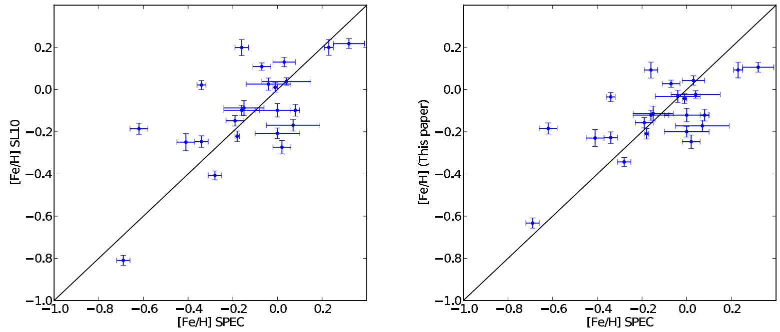

(d) SL10 Calibration (e) This paper

Fig. 2. [Fe/H] estimated from the the calibrations versus spectroscopic metallicity. The blue dots with error bars represent the data points. The black line depicts a one-to-one relationship.

4.4. Refining the Schlaufman & Laughlin (2010) calibration

We produced updated coefficients for the SL10 prescription, using the rms$_p$ free parameter $p = 2$ (see Sect. 3). The expression for the new metallicity calibration is

$$\begin{aligned} [\mathrm{Fe/H}] &= 0.57\Delta(V - K_\mathrm{s}) - 0.17, \\ \Delta(V - K_\mathrm{s}) &= (V - K_\mathrm{s})_\mathrm{obs} - (V - K_\mathrm{s})_\mathrm{iso}, \end{aligned} \tag{3}$$

where $(V - K_\mathrm{s})_\mathrm{obs}$ is the observed $V - K_\mathrm{s}$ color and $(V - K_\mathrm{s})_\mathrm{iso}$ is a fifth-order polynomial function of M_{K_s} that describes the mean main sequence of the solar neighborhood from the Valenti & Fischer (2005) catalog. This expression is adopted from Schlaufman & Laughlin (2010), who adapted an M_{K_s} vs. $(V-K_\mathrm{s})$ formula from Johnson & Apps (2009).

Table 3 shows limited differences between this new fit and the original SL10 calibration. The dispersion of the new fit is tighter by just 0.02 dex (0.17 ± 0.03 dex instead of 0.19 ± 0.03), and the offset is now 0.00 ± 0.04, as expected. The R^2_ap value is similar (0.43 ± 0.23 vs. 0.41 ± 0.29) and uncertain. Readjusting the coefficients therefore produces a marginal improvement at best.

The dispersion, in all panels of Fig. 1, is well above the measurement uncertainties. Those therefore contribute negligibly to the overall dispersion, which must be dominated by other sources.

As can be seen in Fig. 2, B05 or B05(2) tend to underestimate [Fe/H], while the JA09 calibration clearly overestimates [Fe/H] except at the highest metallicities.

5. Summary

We have assembled a sample of M dwarf companions to hotter FGK stars, where the system has an accurate parallax and the M dwarf component has accurate V and K_s-band photometry. Using the metallicities of the primaries, newly measured or retrieved from the literature, and the assumption that the two components have identical initial compositions, we compared the dispersions of the Bonfils et al. (2005), Johnson & Apps (2009), and Schlaufman & Laughlin (2010) photometric metallicity calibrations. We find that the Schlaufman & Laughlin (2010) scale, which is intermediate between Bonfils et al. (2005) and Johnson & Apps (2009), has the lowest dispersion. We slightly refine that relation, by readjusting its coefficients on our sample.

We find that our tight selection of binaries with accurate parallaxes and photometry sample has insignificantly reduced the dispersion of the measurements around the calibration compared to looser criteria. This suggests that the dispersion, hence the random errors of the calibration, is not defined by measurement uncertainties but instead reflects intrinsic astrophysical dispersion. Nonlinearities in the metallicity dependence of the $V - K_\mathrm{s}$ color are likely to contribute, as suggested both by atmospheric models (Allard, priv. comm.) and by the increased dispersion that we measure over a wider metallicity range. They are, however, unlikely to be the sole explanation, since we see dispersion even in narrow areas of the color–magnitude diagram. Stellar evolution cannot significantly contribute, since early-M dwarfs evolve rapidly to the main sequence and they remain there for much longer than a Hubble time, but rotation and magnetic activity could play a role. Unless, or until, we develop a quantitative understanding of this astrophysical dispersion, the photometric calibration approach may therefore have reached an intrinsic limit. Those calibrations also have the very practical inconvenience of needing an accurate parallax. This limits their use to the close solar neighborhood, at least until the GAIA catalog becomes available in a decade.

Alternative probes of the metallicities of M dwarfs are therefore obviously desirable. One obvious avenue is to work from higher spectral resolution information and to identify spectral elements that are most sensitive to metallicity and others that are most sensitive to effective temperature. We are pursuing this approach at visible wavelengths (Neves et al., in prep.), as do Rojas-Ayala et al. (2010, see Appendix A.2) in the near infrared, with encouraging results in both cases.

Acknowledgements. We would like to thank Luca Casagrande for kindly providing the metallicities calculated from his calibration. We also would like to thank Barbara Rojas-Ayala for finding an error in the text regarding the absolute magnitudes. We acknowledge the support by the European Research Council/European Community under the FP7 through Starting Grant agreement number 239953. N.C.S. also acknowledges the support from Fundação para a Ciência e a Tecnologia (FCT) through program Ciência 2007 funded by FCT/MCTES (Portugal) and POPH/FSE (EC), and in the form of grant reference PTDC/CTE-AST/098528/2008. V.N. would also like to acknowledge the support from the FCT in the form of the fellowship SFRH/BD/60688/2009.

Appendix A: Other methods

A.1. Calibration of Casagrande et al. (2008)

In Sect. 4 we described the photometric metallicity calibrations in detail. Casagrande et al. (2008) devised a completely different technique, based on their previous study of FGK stars using the infrared flux method (Casagrande et al. 2006), to determine effective temperatures and metallicities. The infrared flux method uses multiple photometry bands to derive effective temperatures, bolometric luminosities, and angular diameters. The basic idea of IRFM (Blackwell & Shallis 1977) is to compare the ratio between the bolometric flux and the infrared monochromatic flux, both measured on Earth, to the ratio between the surface bolometric flux ($\propto \sigma T_{\rm eff}^4$) and the surface infrared monochromatic flux for a model of the star. To adapt this method to M dwarfs, Casagrande et al. (2008) added optical bands, creating the so-called MOITE, Multiple Optical and Infrared TEchnique. This method provides sensitive indicators of both temperature and metallicity. The proposed effective temperature scale extends down to 2100–2200 K, into the L-dwarf limit, and is supported by interferometric angular diameters above ~3000 K. Casagrande et al. (2008) obtain metallicities by computing the effective temperature of the star for each color band ($V(RI)_{\rm C}JHK_{\rm s}$) for several trial metallicities, between −2.1 and 0.4 in 0.1 dex steps, and by selecting the metallicity that minimizes the scatter among the six trial effective temperatures. Casagrande et al. (2008) estimate that their total metallicity uncertainty is 0.2 to 0.3 dex.

The MOITE method does not reduce into a closed form that can be readily applied by others, but Luca Casagrande kindly computed MOITE [Fe/H] values for our sample (Table A.1). We evaluated the calibration in the same manner as in Sect. 3 and obtained a value of −0.11 ± 0.07 dex for the offset, 0.32 ± 0.06 dex for the rms, 0.10 ± 0.04 dex for the rms$_P$, and −1.09 ± 1.45 for the R^2_{ap}. From these values and from Fig. A.1, we can observe that the Casagrande et al. (2008) calibration has a higher rms and rms$_p$ and a poorer R^2_{ap} than the three photometric calibrations, consistently with the high metallicity uncertainty referred by Casagrande et al. (2008). The negative R^2_{ap} value formally means that this model increases the variance over a constant metallicity model, but as usual R^2_{ap} is a noisy diagnostic.

Table A.1. Metallicity values from spectroscopy and obtained using the method of Casagrande et al. (2008, C08 in this table).

Primary	Secondary	[Fe/H] [dex]	
		Spectroscopic	C08
Gl53.1A	Gl53.1B	0.07	–0.07
Gl56.3A	Gl56.3B	0.00	–0.21
Gl81.1A	Gl81.1B	0.08	–0.08
Gl100A	Gl100C	–0.28	–0.10
Gl105A	Gl105B	–0.19	–0.30
Gl140.1A	Gl140.1B	–0.41	–0.30
Gl157A	Gl157B	–0.16	–0.10
Gl173.1A	Gl173.1B	–0.34	–0.20
Gl211	Gl212	0.04	–0.21
Gl231.1A	Gl231.1B	–0.01	–0.28
Gl250A	Gl250B	–0.15	–
Gl297.2A	Gl297.2B	0.03	0.00
Gl324A	Gl324B	0.32	–0.20
Gl559A	Gl551	0.23	–
Gl611A	Gl611B	–0.69	–0.40
Gl653	Gl654	–0.62	–0.30
Gl666A	Gl666B	–0.34	–
Gl783.2A	Gl783.2B	–0.16	–0.30
Gl797A	Gl797B	–0.07	–0.90
GJ3091A	GJ3092B	0.02	–0.30
GJ3194A	GJ3195B	0.00	–0.60
GJ3627A	GJ3628B	–0.04	–0.20
NLTT34353	NLTT34357	–0.18	0.19

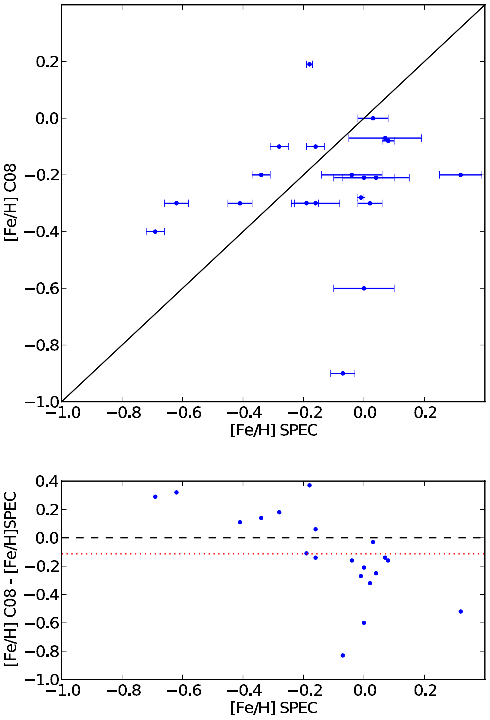

Fig. A.1. [Fe/H] obtained with the Casagrande et al. (2008) method versus the spectroscopic metallicity. The blue dots with error bars represent the data points. The black line depicts a one-to-one relationship. The metallicity difference between the values of the calibrations and the spectroscopic measurements is shown below each [Fe/H]–[Fe/H] plot. The black dashed line is the zero point of the difference, and the red dotted line represents the average of the metallicity difference.

A.2. Rojas-Ayala et al. (2010) calibration

Rojas-Ayala et al. (2010) have recently published a novel and potentially very precise technique for measuring M dwarf metallicities. Their technique is based on spectral indices measured from moderate-dispersion ($R \sim 2700$) K-band spectra, and it needs neither a V magnitude nor a parallax, allowing measurement of fainter (or/and farther) stars. They analyzed 17 M dwarf secondaries with an FGK primary, which also served as metallicity calibrators, and measured the equivalent widths of the NaI doublet (2.206 and 2.209 μm), and the CaI triplet (2.261, 2.263 and 2.265 μm). With these measurements and a water absorption spectral index sensitive to stellar temperatures, they constructed a metallicity scale with an adjusted multiple correlation coefficient greater than the one of Schlaufman & Laughlin (2010) ($R^2_{ap} = 0.63$), and also with a tighter rms$_p$ of 0.02 when compared to other studies (0.05, 0.04, and 0.02 for Bonfils et al. 2005; Johnson & Apps 2009; and Schlaufman & Laughlin 2010 respectively). The metallicity calibration is valid over −0.5 to +0.5 dex, with an estimated uncertainty of ±0.15 dex.

A test of the Rojas-Ayala et al. (2010) calibration for our full sample would be very interesting, but is not currently possible for lack of near-infrared spectra for most of the stars. Seven of our stars, however, have their metallicities measured in Rojas-Ayala et al. (2010) (Gl 212, Gl 231.1B, Gl 250B, Gl 324B, Gl611B, Gl783.2B, and Gl 797B with predicted [Fe/H] of 0.09, −0.05, −0.04, 0.30, −0.49, −0.19, and −0.06 dex, respectively). We find a dispersion of only 0.08 dex and an offset of 0.04 dex between our spectroscopic measurements of the primaries and the Rojas-Ayala et al. (2010) metallicities of the secondaries. These numbers are extremely encouraging, but still have little statistical significance. They will need to be bolstered by testing against a larger sample and over a wider range of both metallicity and effective temperature.

Note added in proof At the conference "Extreme Solar Systems II" (September 2011), E. Newton and collaborators presented a poster entitled "Investigating M Dwarf Metallicity calibrations". The authors compared the same three photometric calibrations tested in the present paper against the NIR spectroscopic calibration of Rojas-Ayala et al. (2010). They found that the Bonfils et al. (2005) calibration has the lowest rms (0.153), compared with the metallicity determination of Rojas-Ayala et al. (2010), while the Schlaufman & Laughlin (2010) and the Johnson & Apps (2009) calibrations have rms values of 0.218 and 0.305, respectively.

References

Allard, F., Homeier, D., & Freytag, B. 2010, To appear in the proceedings of Cool Stars 16 [arXiv:1011.5405]
Asplund, M., Grevesse, N., Sauval, A. J., & Scott, P. 2009, ARA&A, 47, 481
Baraffe, I., Chabrier, G., Allard, F., & Hauschildt, P. H. 1998, A&A, 337, 403
Bean, J. L., Benedict, G. F., & Endl, M. 2006, ApJ, 653, L65
Bessell, M. S. 1990, AAPS, 83, 357
Bessell, M. S. 1991, AJ, 101, 662
Blackwell, D. E., & Shallis, M. J. 1977, MNRAS, 180, 177
Bonfils, X., Delfosse, X., Udry, S., et al. 2005, A&A, 442, 635
Bonfils, X., Mayor, M., Delfosse, X., et al. 2007, A&A, 474, 293
Bouchy, F., & The Sophie Team 2006, in Tenth Anniversary of 51 Peg-b: Status of and prospects for hot Jupiter studies, ed. L. Arnold, F. Bouchy, & C. Moutou, 319
Bouchy, F., Mayor, M., Lovis, C., et al. 2009, A&A, 496, 527
Caffau, E., Ludwig, H.-G., Steffen, M., Freytag, B., & Bonifacio, P. 2011, SOLPHYS, 268, 255
Caldwell, J. A. R., Spencer Jones, J. H., & Menzies, J. W. 1984, MNRAS, 209, 51
Carpenter, J. M. 2001, AJ, 121, 2851
Casagrande, L., Portinari, L., & Flynn, C. 2006, MNRAS, 373, 13
Casagrande, L., Flynn, C., & Bessell, M. 2008, MNRAS, 389, 585
Chabrier, G., & Baraffe, I. 2000, ARA&A, 38, 337
Chanamé, J., & Gould, A. 2004, ApJ, 601, 289
Dahn, C. C., Harrington, R. S., Riepe, B. Y., et al. 1982, AJ, 87, 419
Dahn, C. C., Harrington, R. S., Kallarakal, V. V., et al. 1988, AJ, 95, 237
Dawson, P. C., & Forbes, D. 1992, AJ, 103, 2063
Delfosse, X., Forveille, T., Ségransan, D., et al. 2000, A&A, 364, 217
Eggen, O. J. 1976, ApJS, 30, 351
Eggen, O. J. 1979, ApJS, 39, 89
Endl, M., Cochran, W. D., Kürster, M., et al. 2006, ApJ, 649, 436
Fischer, D. A., & Valenti, J. 2005, ApJ, 622, 1102
Gliese, W., & Jahreiß, H. 1991, Preliminary Version of the Third Catalogue of Nearby Stars, Tech. Rep.
Gonzalez, G. 1997, MNRAS, 285, 403
Gould, A., & Chanamé, J. 2004, ApJS, 150, 455
Hocking, R. R. 1976, Biometrics, 32, 1
Holmberg, J., Nordström, B., & Andersen, J. 2009, A&A, 501, 941
Johnson, J. A., & Apps, K. 2009, ApJ, 699, 933
Johnson, J. A., Butler, R. P., Marcy, G. W., et al. 2007, ApJ, 670, 833
Kaufer, A., & Pasquini, L. 1998, in SPIE Conf. Ser., 3355, ed. S. D'Odorico, 844
Koen, C., Kilkenny, D., van Wyk, F., Cooper, D., & Marang, F. 2002, MNRAS, 334, 20
Kurucz, R. 1993, ATLAS9 Stellar Atmosphere Programs and 2 km s^{-1} grid, Kurucz CD-ROM No. 13, Cambridge, Mass.: Smithsonian Astrophysical Observatory, 13
Laing, J. D. 1989, South African Astronomical Observatory Circular, 13, 29
Leggett, S. K. 1992, ApJS, 82, 351
Mayor, M., Bonfils, X., Forveille, T., et al. 2009, A&A, 507, 487
Mermilliod, J., Mermilliod, M., & Hauck, B. 1997, A&AS, 124, 349
Pesch, P. 1982, PASP, 94, 345
Poveda, A., Herrera, M. A., Allen, C., Cordero, G., & Lavalley, C. 1994, Rev. Mex. Astron. Astrofis., 28, 43
Queloz, D., Mayor, M., Weber, L., et al. 2000, A&A, 354, 99
Reid, I. N., Cruz, K. L., Allen, P., et al. 2004, AJ, 128, 463
Rojas-Ayala, B., Covey, K. R., Muirhead, P. S., & Lloyd, J. P. 2010, ApJ, 720, L113
Ryan, S. G. 1989, AJ, 98, 1693
Santos, N. C., Israelian, G., & Mayor, M. 2001, A&A, 373, 1019
Santos, N. C., Mayor, M., Naef, D., et al. 2002, A&A, 392, 215
Santos, N. C., Israelian, G., & Mayor, M. 2004, A&A, 415, 1153
Schlaufman, K. C., & Laughlin, G. 2010, A&A, 519, A105
Sinachopoulos, D., & van Dessel, E. L. 1996, AAPS, 119, 483
Skrutskie, M. F., Cutri, R. M., Stiening, R., et al. 2006, AJ, 131, 1163
Sneden, C. 1973, Ph.D. Thesis, Univ. of Texas
Sousa, S. G., Santos, N. C., Israelian, G., Mayor, M., & Monteiro, M. J. P. F. G. 2007, A&A, 469, 783
Sousa, S. G., Santos, N. C., Mayor, M., et al. 2008, A&A, 487, 373
Sousa, S. G., Santos, N. C., Israelian, G., et al. 2011, A&A, 526, A99
Udry, S., & Santos, N. 2007, ARA&A, 45, 397
Udry, S., Bonfils, X., Delfosse, X., et al. 2007, A&A, 469, L43
Upgren, A. R. 1974, PASP, 86, 294
Valenti, J. A., & Fischer, D. A. 2005, VizieR Online Data Catalog, 215, 90141
Valenti, J. A., Piskunov, N., & Johns-Krull, C. M. 1998, ApJ, 498, 851
van Leeuwen, F. 2007, A&A, 474, 653
Weis, E. W. 1988, AJ, 96, 1710
Weis, E. W. 1993, AJ, 105, 1962
Weis, E. W. 1996, AJ, 112, 2300
Weistrop, D. 1975, PASP, 87, 367
Weistrop, D. 1977, ApJ, 215, 845
Weistrop, D. 1981, AJ, 86, 1220
Woolf, V. M., & Wallerstein, G. 2005, MNRAS, 356, 963
Woolf, V. M., & Wallerstein, G. 2006, PASP, 118, 218

Chapter 4

Planet-metalllicity and planet-stellar mass correlations of the HARPS GTO M dwarf sample

4.1 Introduction

During the second and third year of my PhD I investigated spectroscopic methods that could be potentially more precise than photometric methods to obtain metallicities and effective temperatures of M dwarfs. I concluded, from my previous work (Neves et al. 2012), that the photometric methods were reaching their limit. Therefore, I considered several research alternatives, including working with medium or/and high-resolution spectra of FGK and M dwarfs in FGK+M dwarf binaries, in order to anchor the metallicity of the M dwarf using the established determination from the FGK primary, and also obtaining the values of the parameters by comparing high-resolution spectra of M dwarfs with synthetic spectra (e.g. Allard et al. 2010).

Finally, I assumed that, at that time, the photospheric models of M dwarfs that were being used to create synthetic spectra were not complete enough to reach the precision that we sought. Therefore, I concluded that the most practical approach to obtain high-precision values for metallicity and effective temperature was to establish an empirical calibration, using already available high-resolution HARPS M dwarf spectra from our group (Bonfils et al. 2013), and use the [Fe/H] values obtained from our previous work (Neves et al. 2012) and T_{eff} values from Casagrande et al. (2008) as initial values.

With the development of the technique to calculate, with precision, the [Fe/H] and T_{eff}, using high-resolution spectra, described in Sect. 4.2, me and my collaborators explored the planet-metallicity correlation of the HARPS 102 star M dwarf sample, detailed in Sect. 4.3. In Sect. 4.4 we added the California Planet survey sample to our own, with the aim of improving our statistic in order to explore the planet-[Fe/H] connection in more detail. We also investigated the planet-mass correlation, detailed in Sect. 4.5, using the established mass-luminosity relations of Delfosse et al. (2000), but confirmed that it was biased. Finally, in Sect. 4.6 we discuss our results.

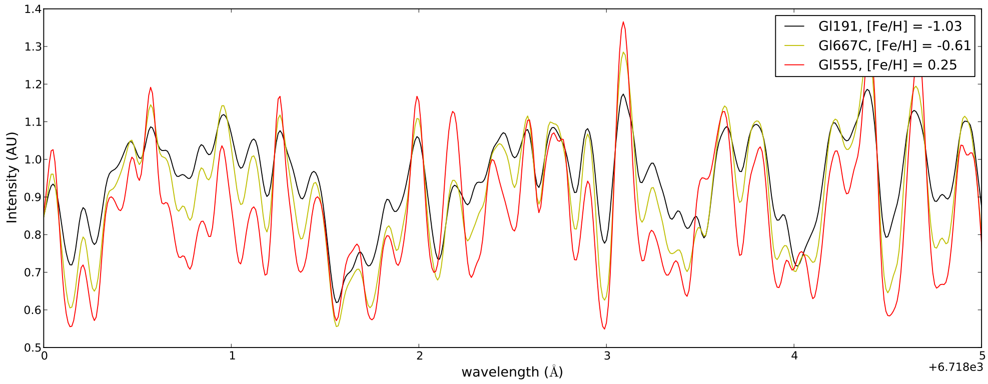

Figure 4.1: A small region of the high-resolution spectra of the M-dwarfs Gl191, Gl667C, and Gl555 (with [Fe/H] = -1.03, -0.61, and 0.25 dex, respectively) from the HARPS GTO program. We note that the metallicity is determined indirectly, with the Neves et al. (2012) calibration. It is possible to see by eye that, in general, the line strength changes with metallicity.

4.2 A new M dwarf metallicity and effective temperature calibration

Here we briefly explain the method that we developed to estimate the metallicity and effective temperature of M dwarfs. Fig 4.1 shows an illustration of the effect of [Fe/H] in a small wavelength region in three of our spectra. From the observation of the effect of [Fe/H] and T_{eff} on our spectra we investigated the possible correlations of the strength of the lines with these parameters, with the aim of developing a new calibration for M dwarfs.

The method is based on the measurement of ‘peak-to-peak’ equivalent widths (EW) of lines and features from the spectra of our volume-limited M dwarf HARPS sample and uses existing photometric calibrations for metallicity (Neves et al. 2012) and effective temperature (Casagrande et al. 2008), as starting values (Eq. 3.4 and 2.24 respectively). Our method achieves an increase in precision of the metallicity and effective temperature but the accuracy of the new scale is tied to the accuracy of the photometric calibrations.

4.2.1 Calibration sample

From the initial 102 M dwarf star spectra of the Bonfils et al. (2011) sample we initially chose 62 stars with S/N greater than 100. Seven stars (Gl191, Gl285, Gl388, Gl699, Gl729, Gl803, GJ1125) were then discarded *a posteriori*, due to a bad correlation of the line measurements with either the reference metallicity or temperature scales, that can be attributed to high activity/rotation (Gl191, Gl285, Gl388, Gl729, Gl803) or to a bad value of the radial velocity (GJ1125). We ended up with a sample of 55 stars, shown in the Appendix of Neves et al. (2013), and presented in Sect. 4.7.

4.2.2 Method

With our calibration sample we first measured ‘peak-to-peak’ equivalent widths (EWs) of lines and features using the 26 redder orders of median normalised HARPS spectra, in the region between 530 to

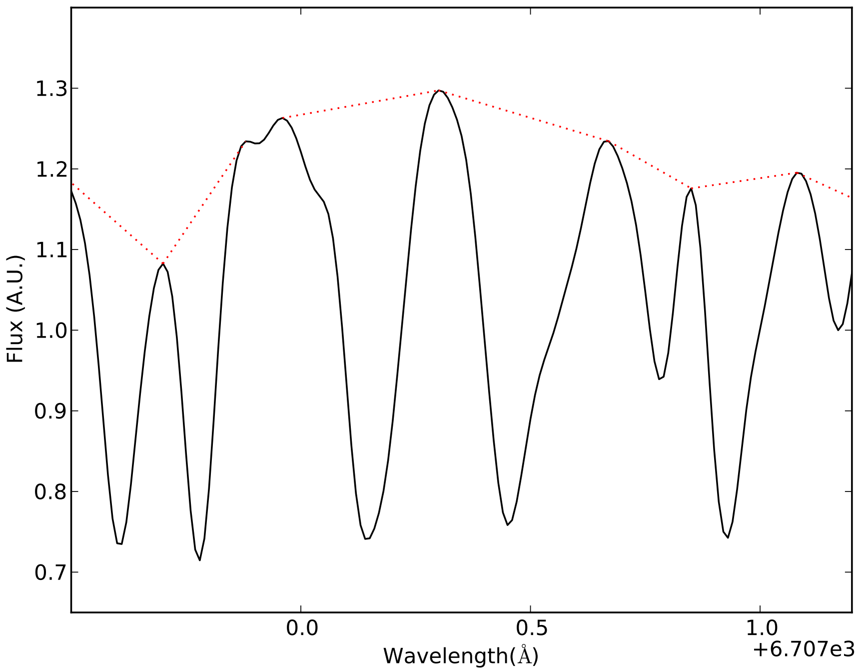

Figure 4.2: Small region of the Gl 205 spectra illustrating the ṕeak to peak' equivalent width line measurement. The red dotted line represents the 'peak-to-peak' flux.

690 nm. Here we consider features as blended lines. We define the 'peak-to-peak' equivalent widths as

$$W = \sum \frac{F_{pp} - F_\lambda}{F_{pp}} \Delta\lambda, \tag{4.1}$$

where F_{pp} is the value of the flux between the peaks of the line/feature at each integration step and F_λ the flux of the line/feature. The measurement of the EWs is illustrated in Fig. 4.2, where the 'peak-to-peak' flux corresponds to the red dotted lines, and the black line is the flux of the reference spectra. The EW is thus measured between the red dotted line and the solid black line. We used the very high S/N (~1430 @ 550nm) spectral orders of the star Gl 205 as a reference from where the line/feature regions are going to be measured for all other stars. We rejected lines/features with EW $< 8\ m\AA$ and very steep lines/features.

We investigated the correlations and partial correlations of [Fe/H] and T_{eff}, previously calculated with the photometric calibrations mentioned in Sect. 4.1 with the line/feature EWs. Fig. 4.3 shows the histograms of the partial correlation values of [Fe/H] with T_{eff} kept constant(solid blue histogram) and the partial correlation values of T_{eff} with [Fe/H] kept constant (dashed green histogram). We observe that a significant number of lines have a good correlation with the parameters.

Then we calculated a linear fit of the EWs with the metallicity (taken from Neves et al. 2012) and effective temperature (taken from Casagrande et al. 2008), using a least squares approach. For each EW i and for each star m we have,

$$W_{i,m} = \alpha_i [Fe/H]^T_m + \beta_i T^T_{eff m} + \gamma_i, \tag{4.2}$$

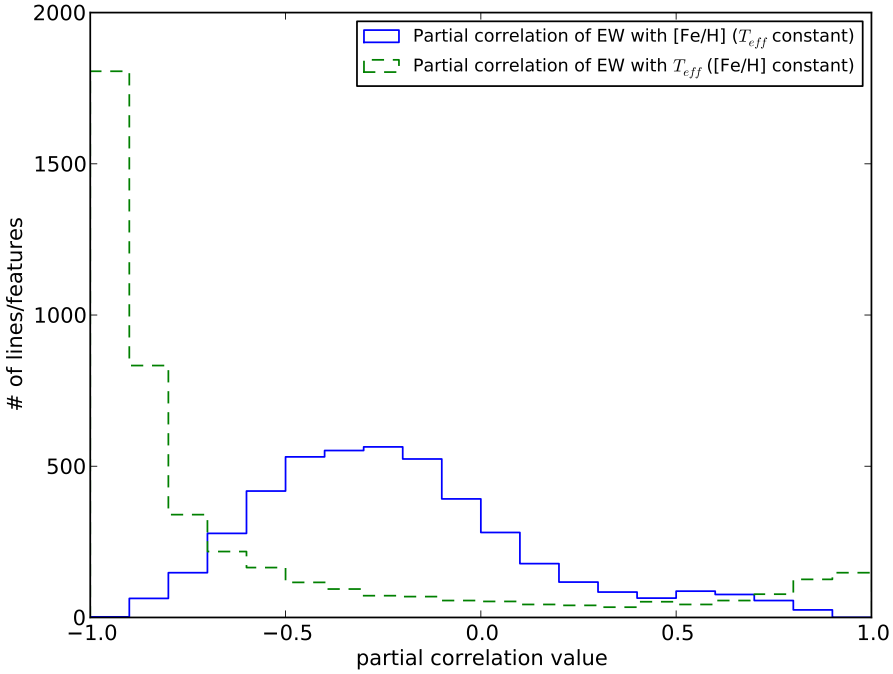

Figure 4.3: Histograms of the partial correlations of [Fe/H] (solid blue histogram) and T_{eff} (dashed green histogram).

where $W_{i,m}$ is a $i \times m$ matrix containing the EWs, and both $[Fe/H]_m$, and T_{effm} are $1 \times m$ vectors. The α and the β are the coefficients related to metallicity and effective temperature, respectively, while γ is an independent coefficient.

The error of each coefficient is calculated as

$$\varepsilon_i = \sqrt{RSS.J_{i,i}}, \tag{4.3}$$

where RSS is the residual sum of squares, expressed as

$$RSS = \frac{\sum (x_{i,model} - x_i)^2}{n_{obs} - n_{coef}}, \tag{4.4}$$

and $J_{i,i}$ is the diagonal of the estimate of the jacobian matrix around the solution. The $x_{i,model}$, x_i, n_{obs}, and n_{coef} from Eq. 4.3 are, respectively, the predicted value of the data, x_i, by the regression model, the data values, the number of data points, and the number of coefficients.

The total error of the coefficients can then be written as

$$\varepsilon = \sqrt{\varepsilon\alpha^2 + \varepsilon\beta^2 + \varepsilon\gamma^2}. \tag{4.5}$$

Here we assume that both [Fe/H] and temperature are independent and do not correlate with each other.

Our aim is to increase the metallicity precision using the photometric calibration as reference. In order to do this, we want to recover the values of the metallicity and temperature by doing a weighted least squares refit. To calculate the weights for the least squares refit we just invert the squared errors of the coefficients, and normalise the expression,

$$E_i = \frac{1/\varepsilon_i^2}{\sum 1/\varepsilon_i^2}. \tag{4.6}$$

To invert the fit of Eq. 4.2 we first take the calculated coefficients from the first fit and define the coefficient matrix as

$$C_{i,3} = \begin{bmatrix} \alpha_{1,1} & \beta_{1,2} & \gamma_{1,3} \\ \alpha_{2,1} & \beta_{2,2} & \gamma_{2,3} \\ \ldots & \ldots & \ldots \\ \alpha_{i,1} & \beta_{i,2} & \gamma_{i,3} \end{bmatrix}. \tag{4.7}$$

Then we invert Eq. 4.2. After some operations we have

$$[[Fe/H], T_{eff}, Ind]_{3,m} = (C_{3,i}^T C_{i,3})^{-1} C_{3,i}^T W_{i,m}, \tag{4.8}$$

where C^T is the transpose of C and Ind is the value of the independent parameter.

Finally, we use a *levenberg-marquardt* algorithm and apply the weights (Eq. 4.6) to Eq. 4.8, recovering one value of metallicity and effective temperature for each star.

We also tried other methods, such as choosing groups of lines with a high correlation or partial correlation coefficients and then applying the same method as described in this Section. However, the weighted least squares method using all 4441 lines performed best at minimising the uncertainties of both metallicity and effective temperature.

Using this method, we get a dispersion of metallicity and effective temperature of 0.08 dex and 80K respectively. Fig. 4.4 shows the comparison between the values obtained in this work and the reference calibrations for metallicity and effective temperature. We note that here we only get a measure of the precision. The accuracy of the calibration, as well as systematic errors, are tied to the original determinations of both [Fe/H] and temperature.

In order to test our calibration and obtain a measure of its accuracy, we compared the [Fe/H] and T_{eff} values obtained using our calibration with the values taken or calculated from other studies. Our determinations of [Fe/H] are shown in Table 2 of the paper, in Section 4.7. We compared them with the values obtained from the literature, taken from Önehag et al. (2012), Rojas-Ayala et al. (2012), and Mann et al. (2013) or calculated using the calibrations of Bonfils et al. (2005), Schlaufman & Laughlin (2010), and Johnson et al. (2012), detailed in Section 2.4.1. We restricted our analysis for stars with [Fe/H] between -0.7 and 0.30 dex, that correspond to the limits of our calibration. We compared our T_{eff} values with the determinations taken from Rojas-Ayala et al. (2012) or calculated with the K-band calibrations of Casagrande et al. (2008) and Boyajian et al. (2012). The sample was selected taking into account the validity regions of our calibration, between 2650 and 3750 K.

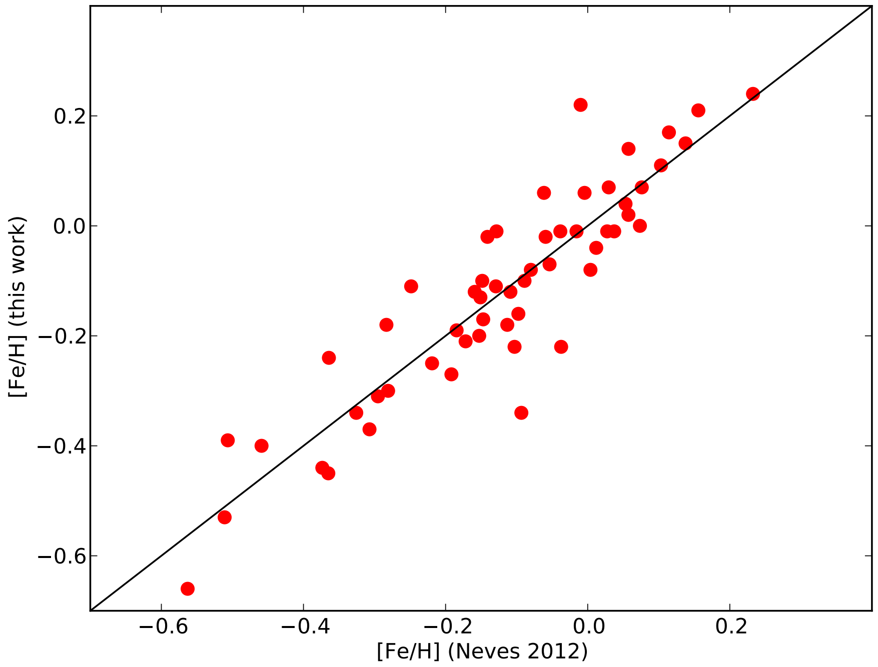

(a)

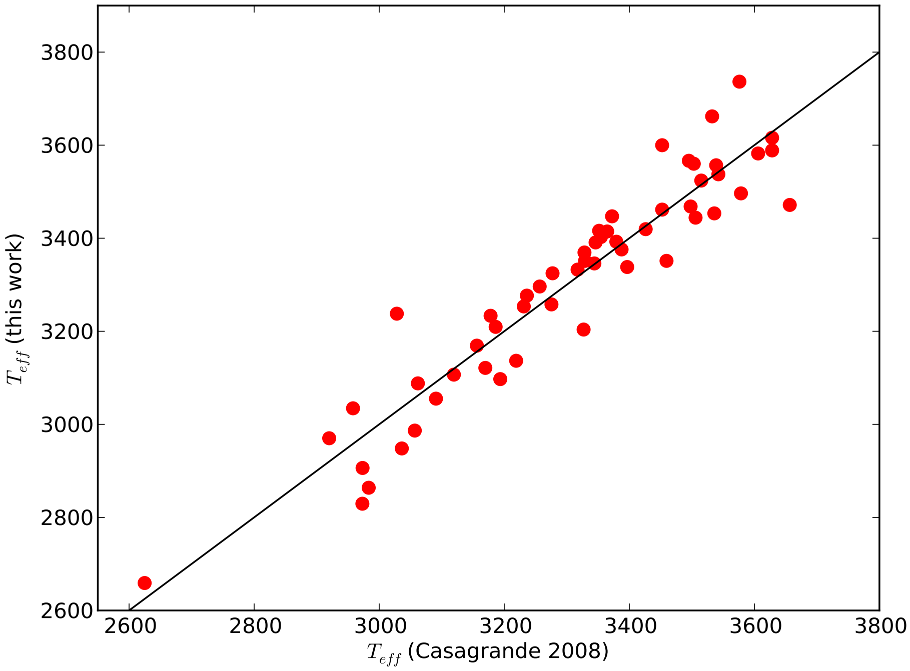

(b)

Figure 4.4: a) [Fe/H] comparison between this work and the photometric calibration of Neves et al. (2012); b) T_{eff} comparison between this work and the photometric calibration of Casagrande et al. (2008).

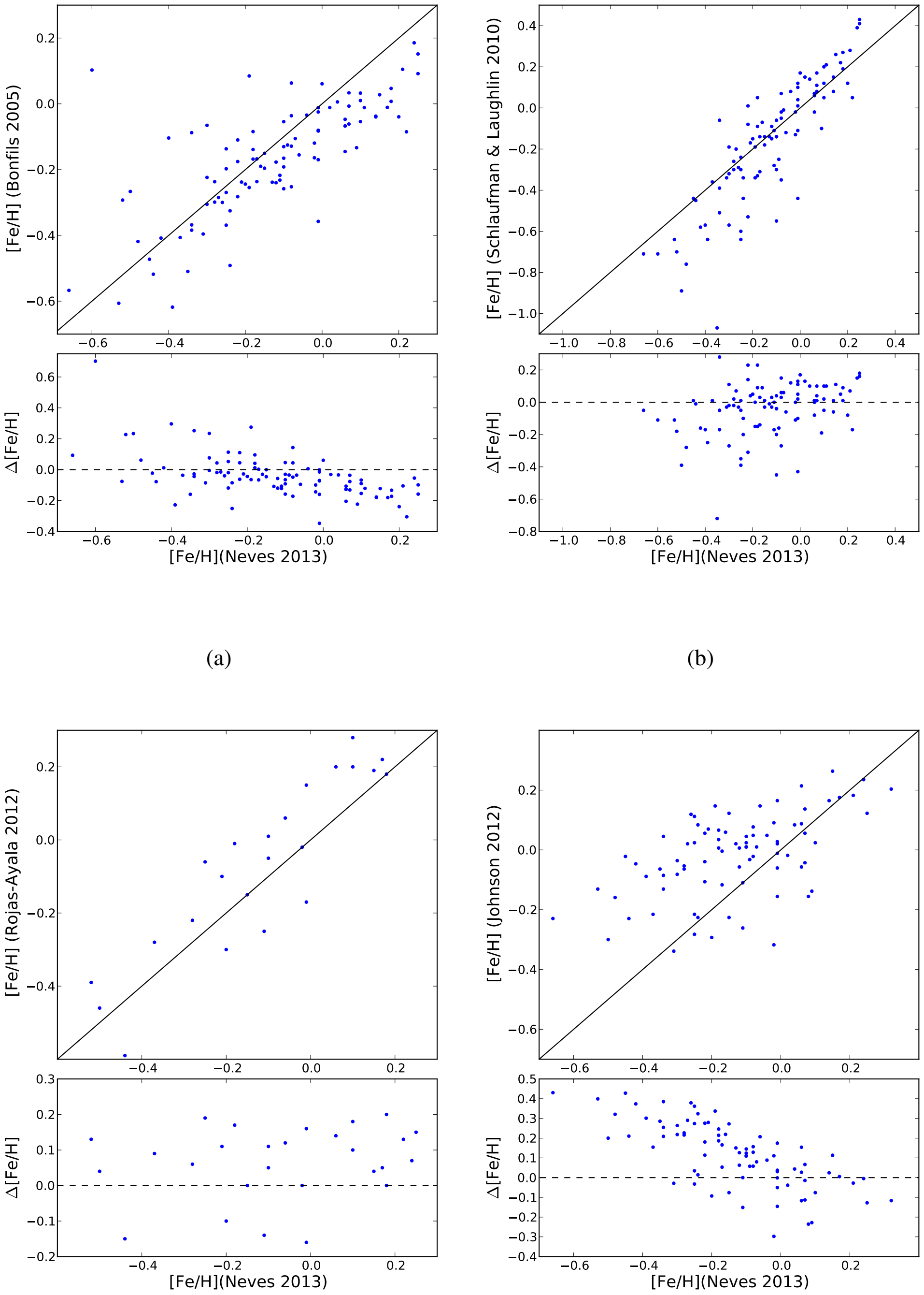

(a)

(b)

(c)

(d)

Figure 4.5: Upper panels: [Fe/H] of our calibration versus the [Fe/H] calculated with the calibration of Bonfils et al. (2005) (a), Schlaufman & Laughlin (2010) (b), Rojas-Ayala et al. (2012) (c), and Johnson et al. (2012) (d) ; Lower panels: Residuals of the difference between the values of the two calibrations.

Fig. 4.5 to Fig. 4.7 show the [Fe/H]-[Fe/H] and T_{eff}-T_{eff} plots of the mentioned calibrations, while Table 4.1 shows the dispersion of the difference between our [Fe/H] and T_{eff} calibrations and the values from the other calibrations and their respective offset.

We observe that, in general, the values of [Fe/H] between our scale and the test calibrations agree

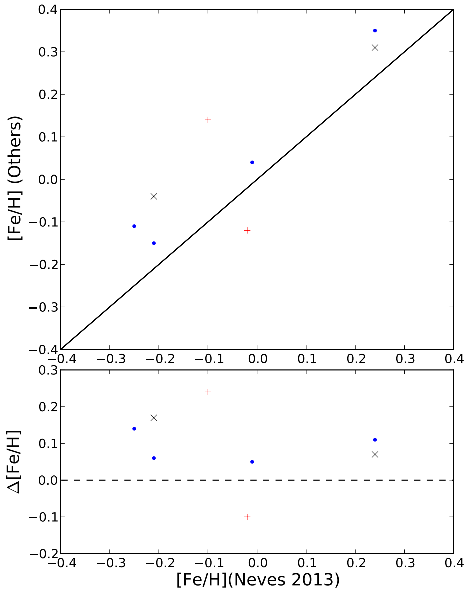

Figure 4.6: Upper panel: [Fe/H] of our calibration versus the [Fe/H] calculated with the values taken from Önehag et al. (2012) (blue circles), Terrien et al. (2012) (black crosses), and Mann et al. (2013) (red crosses); Lower panel: Residuals of the difference between the values of the different calibrations.

Table 4.1: Dispersion and mean offsets from the residuals of each test calibration agains our scale. The last column shows the number of stars in common.

Test calibration for [Fe/H]	*rms* [dex]	offset [dex]	N	Test calibration for T_{eff}	*rms* [K]	offset [K]	N
Bonfils et al. (2005)	0.15	-0.04	98	Casagrande et al. (2008)	181	-68	94
Schlaufman & Laughlin (2010)	0.17	-0.04	98	Boyajian et al. (2012)	271	161	94
Rojas-Ayala et al. (2012)	0.12	0.06	27	Rojas-Ayala et al. (2012)	279	104	22
Johnson et al. (2012)	0.20	0.12	82				

nicely, except for a few outliers and for the case of Johnson et al. (2012), where the dispersion and offset are the largest. The dispersion values of the comparison tests with the Bonfils et al. (2005) and Rojas-Ayala et al. (2012) calibrations are below their original calibration dispersion (see Section 2.4.1 for details). The offsets are also small, if we don't consider the Johnson et al. (2012) case. It is worth noting that we get a very good agreement with the spectroscopic calibration of Rojas-Ayala et al. (2012), in which we obtain the best value for precision, 0.12 dex, smaller than their original precision value of 0.17 dex. Moreover, the offset is also half of the value of the precision (0.06 dex), and below the value of our measured precision (0.08 dex). This attests the quality and accuracy of our calibration. Unfortunately, we could not test the latest [Fe/H] calibration from Mann et al. (2013), as we only have two stars with common, as shown in Fig. 4.6. This is also the case for the calibrations of Önehag et al. (2012), and Terrien et al. (2012). Nevertheless, all measurements agree well with our values. Finally, we also note a trend of unknown origin in the residuals of the difference between our calibration and the photometric scales of Bonfils et al. (2005) and Johnson et al. (2012).

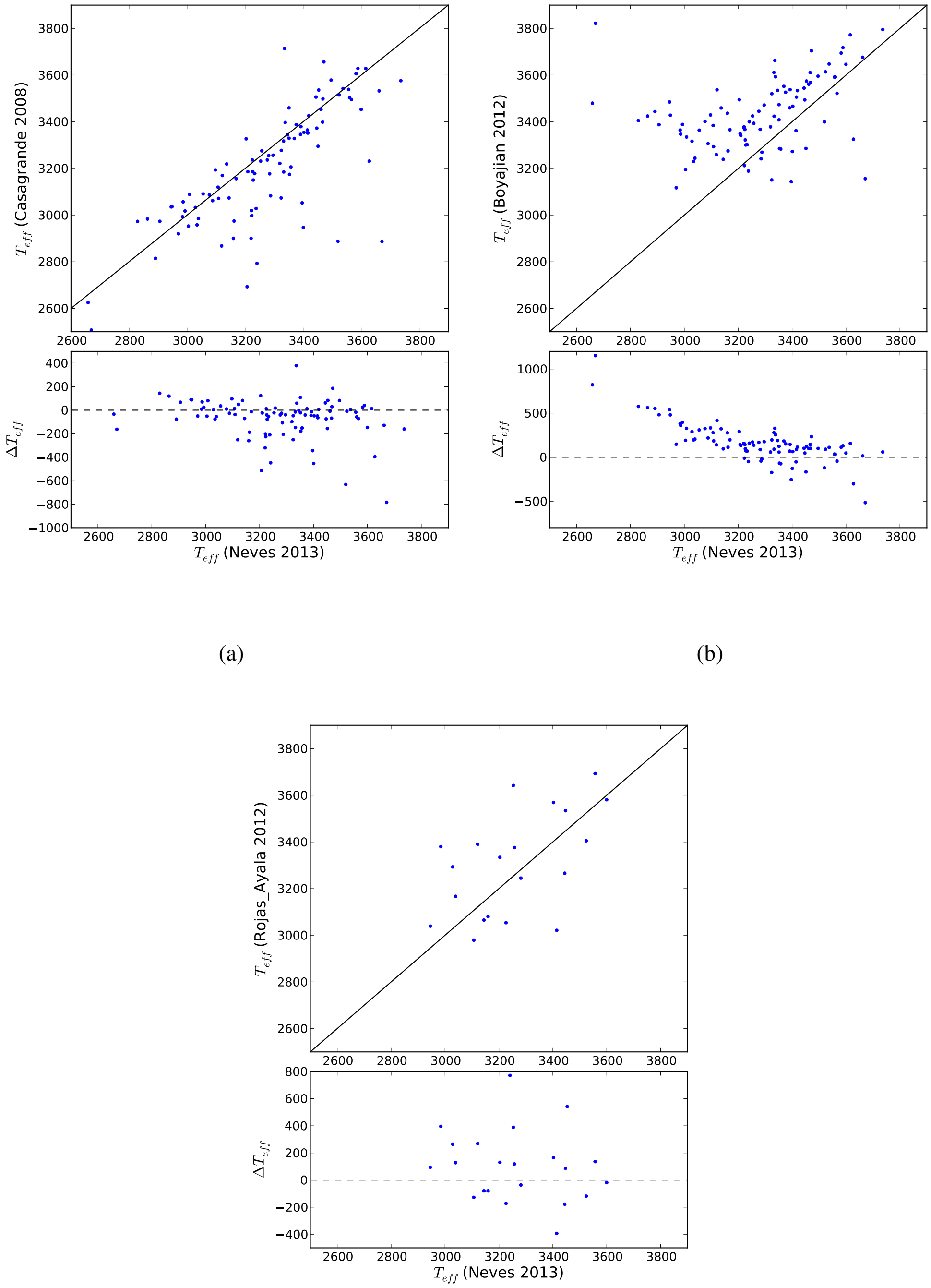

(a)

(b)

(c)

Figure 4.7: Upper panels: T_{eff} of our calibration versus the T_{eff} calculated with the calibration of Casagrande et al. (2008) (a), Boyajian et al. (2012) (b), and Rojas-Ayala et al. (2012) (c) ; Lower panels: Residuals of the difference between the values of the two calibrations.

Regarding temperature, we observe a modest agreement between our results and the test studies. As expected, our results agree best with the Casagrande et al. (2008) scale, as we used it as reference in our own calibration. However, there is a noticeable dispersion towards higher temperatures. The calibration of Boyajian et al. (2012) diverges below $T_{eff} < 3200$ K, but otherwise has a reasonable agreement. We also note the existence of a linear trend in the residuals of the difference between this calibration and ours. Regarding the comparison with the Rojas-Ayala et al. (2012) values, we notice a considerable scatter throughout the whole T_{eff} region. The results show that more work needs to be done to improve the accuracy of the effective temperature determinations.

4.3 The metallicity-planet correlation

Figure 4.8 shows the histogram of metallicity of our sample. The solid red histogram represent the stars without planets, while the filled dashed blue histogram the stars with Jovian planets, and the dotted black histogram the stars with Neptunians/smaller planets only. The vertical solid red, dashed blue, and dotted black lines above each histogram depict the value of the mean of the distribution. We note here that we assume that metallicity is not influenced by detection biases, due to the fact that we are using a volume-limited sample.

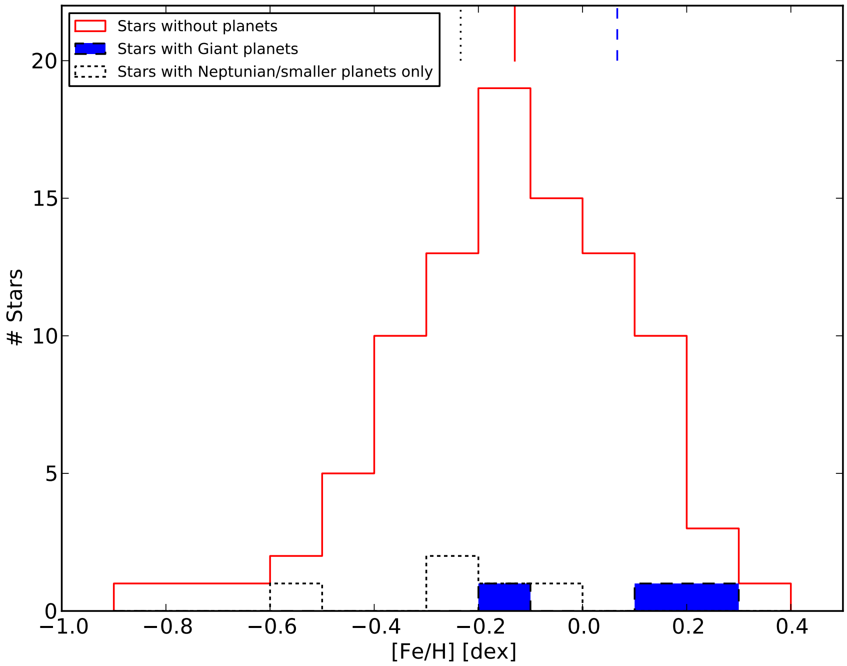

Figure 4.8: Histograms of stars without planets (solid red), with Jovian planets (filled dashed blue), and with Neptunians/smaller planets (dotted black) for metallicity. The vertical solid red, filled dashed blue, and dotted black lines above the histograms represent the mean of the [Fe/H] distribution.

We can observe in Table 4.2 that the difference of the averages (medians resp.) of the full sample between planet and non-planet host distributions is small (0.01 and -0.07 dex, respectively).

If we only take into account the three planet host stars with Jupiter-type planets, the difference of the averages and the medians of the [Fe/H] between stars with and without planets is higher (0.20 and 0.26 dex respectively). On the other hand, if we remove the 3 systems with Jovian hosts, we obtain a mean and median of -0.10 dex. The correlation we find between [Fe/H] and planet occurrence agrees with previous studies focused on giant planets around M dwarfs (e.g. Bonfils et al. 2007; Johnson &

Table 4.2: Difference of averages and medians of [Fe/H] between planet host and non-planet host distributions. N_h is the number of planet hosts.

[Fe/H]	Diff. of averages [dex]	Diff. of medians [dex]	KS test
Full sample (N_h=8)	0.01	-0.07	0.8151
Jovian hosts (N_h=3)	0.20	0.26	0.1949
Neptunian/smaller hosts (N_h=5)	-0.10	-0.10	0.3530

Apps 2009; Johnson et al. 2010a; Schlaufman & Laughlin 2010; Rojas-Ayala et al. 2010, 2012; Terrien et al. 2012). We confirm also, with better statistics, that such correlation is vanishing for Neptunian and smaller planet hosts (e.g. Rojas-Ayala et al. 2012; Terrien et al. 2012). In fact our result hints at an anti-correlation between [Fe/H] and planets though the difference (-0.10 dex) is at the limit of our measurement precision. Despite that, the results hint at a different type of planet formation mechanism for giant and Neptunian/Super Earth-type planets (e.g. Mordasini et al. 2012).

We performed a Kolmogorov-Smirnov (KS) test to check the probability of the sub-samples of stars with and without planets of belonging to the same parent distribution. All KS tests show that we cannot discard the possibility that the three sub-samples with planets belong to the same distribution of the stars without planets. We obtain a value of 0.195 for the Jovian hosts, but we do not have enough hosts (N=3) to calculate the KS test properly.

In order to explore the star-planet relation further, we divided the metallicity range in three bins and performed a frequency analysis for Jovian hosts and Neptunian/smaller planet hosts separately, as shown in Fig. 4.9. The upper panels of all figures are the same as in Fig. 4.8, but this time with only three bins.

The lower panels depict the relative frequency of the stars with planets. The solid red line corresponds to a direct least squares bin fitting, while the dashed black line is a Bayesian bin-independent parametric fitting, explained in Sect. 4.3.1. Both fits use the functional form $f = C10^{\alpha[Fe/H]}$, following previous works for FGK dwarfs (Valenti & Fischer 2005; Udry & Santos 2007; Sousa et al. 2011). The coefficients C and α of both methods and respective uncertainties are shown in Table 4.3. The errors in the frequency of each bin are calculated using the binomial distribution,

$$P(f_p, n, N) = \frac{N!}{n!(N-n)!} f_p^n (1-f_p)^{N-n}, \tag{4.9}$$

following the procedure outlined in, e.g., Burgasser et al. (2003); McCarthy & Zuckerman (2004); Endl et al. (2006), and Sozzetti et al. (2009). In short we calculate how many n detections we have in a bin of size N, as a function of the planet frequency f_p, of each bin. The upper errors, lower errors and upper limits of each bin are calculated by measuring the 68.2% of the integrated area around the peak of the binomial probability distribution function, that corresponds to the 1σ limit for a gaussian distribution. An example is shown in Fig. 4.10, depicting a normalised binomial probability distribution function with $n = 2$, $N = 20$, and $f_p = 0.1$.

From Fig. 4.9 it can be observed that there is a small statistical difference between the frequency

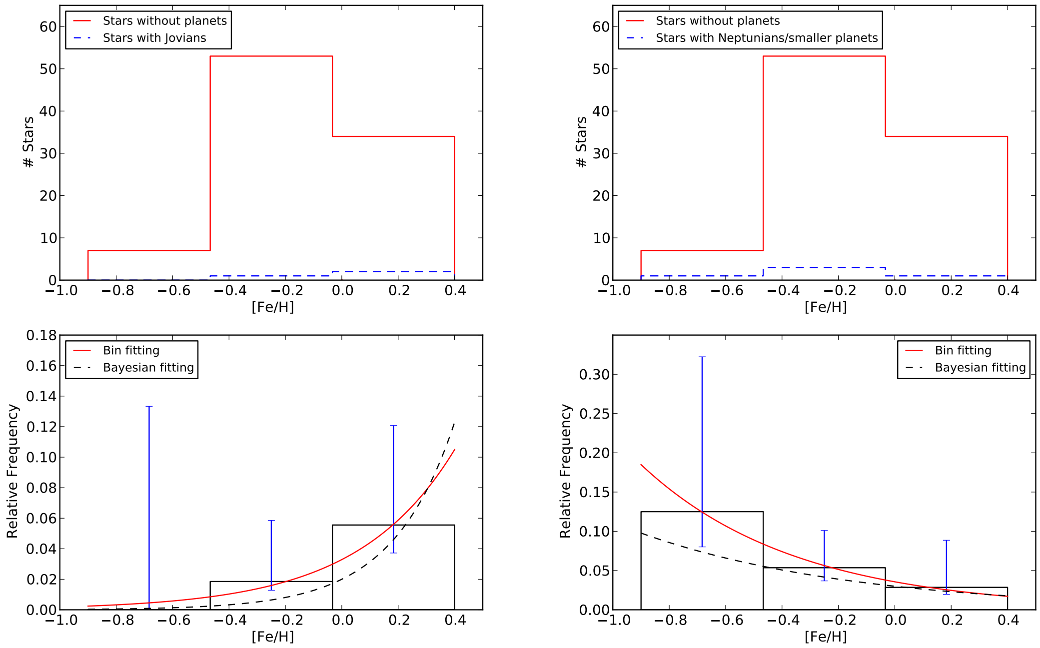

(a)

(b)

Figure 4.9: (a) Upper panel: Histogram of metallicity with 3 bins for stars without planets (solid red) and stars with Giant planets (dashed blue); Lower panel: Frequency of stars with Giant planets; (b) Upper panel: Histogram of metallicity with 3 bins for stars without planets (solid red) and stars with Neptunians and smaller planets only (dashed blue); Lower panel: Frequency of stars with Neptunians and smaller planets only.

bins for both Jovian-hosts and Neptunian and smaller planet hosts, as the uncertainties of each bin are high. The first bin of Fig. 4.9 (a) ([-0.9,0.47] dex) has an upper limit of 13.3%, with no planet detection, while the second and third bins ([-0.47,-0.03] and [-0.03,0.4] dex, resp.) have values of 1.9% and 5.6% respectively. Regarding Fig. 4.9 (b), we observe the frequencies of 12.5, 5.4, and 2.9% for the same bins.

We can observe a correlation with [Fe/H] for Jovian hosts and a hint of an anti-correlation for Neptunian and smaller planets only hosts. Interestingly, the later anti-correlation for smaller planet hosts is predicted by recent studies using core-accretion models (Mordasini et al. 2012), but we note that we only consider Neptunian hosts as stars with Neptunians and smaller planets only: if a multi-planet system has a Jovian and one or more smaller planets, for instance, we count the system as being a Jupiter host, not a Neptunian-host. Therefore, it is expected that the number of Neptunians and smaller planets will be higher at lower metallicities.

4.3.1 Bayesian approach

To test the metallicity results we performed a parametric and bin-independent fitting of the data based on Bayesian inference. We followed the Johnson et al. (2010a) approach, using two functional forms for the planet frequency, $f_{p1} = C$ and $f_{p2} = C10^{\alpha[Fe/H]}$, and choosing uniformly distributed priors for the parameters C and α. The choice of a power law for the functional form was based on previous works of

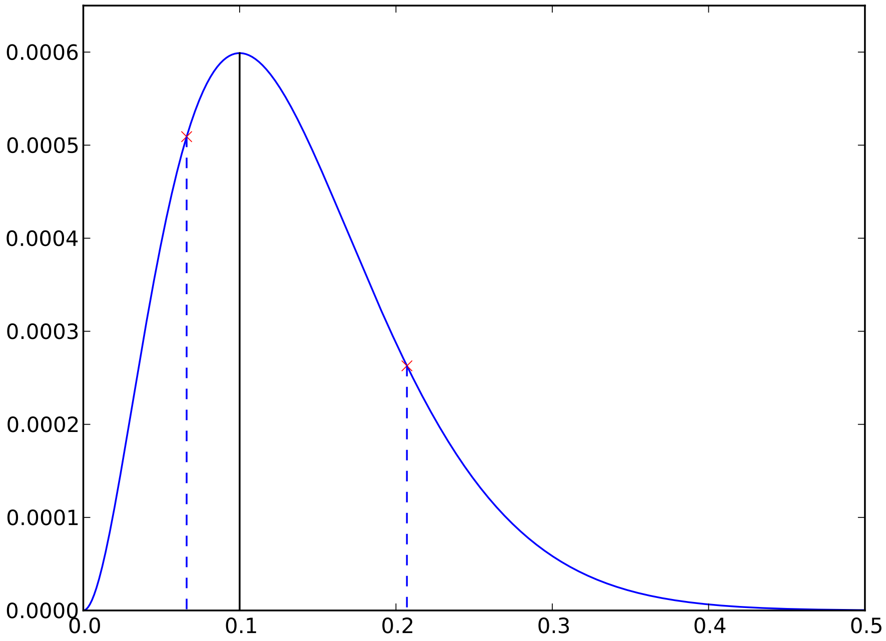

Figure 4.10: Normalised binomial probability distribution function for $n = 2$, $N = 20$, and $f_p = 0.1$.The solid vertical line depicts the observed frequency. The dashed lines show the 68.2% (1σ) limits around the maximum of the function.

[Fe/H] of FGK dwarfs (Valenti & Fischer 2005; Udry & Santos 2007; Sousa et al. 2011).

Table 4.3 summarises and compares the results of the Bayesian fitting to the ones obtained with the bin fitting. Column 1 shows the functional forms used and respective parameters, column 2 the uniform prior range, column 3 the most likely value for the fit parameters, along with the 1σ gaussian uncertainties and column 4 the fit parameters of the least squares bin fitting.

From Table 4.3 we can see that the Bayesian fit values are, in general, compatible with the bin fitting values. However, we observe that the α values obtained for the planet-host frequencies with the Bayesian method are higher than the same values using the bin fitting. This translates into a higher Giant-host frequency values with [Fe/H] and a lower Neptunian/smaller planet host frequencies as a function of metallicity. We also note that the α values calculated by the Bayesian method have large uncertainties in both scenarios. In the case of Neptunian-hosts, the α value can easily accommodate both positive or negative values.

4.3.2 Comparison with the California Planet Survey late-K and M-type dwarf sample

Our aim here is to compare our results to a similar sample regarding the difference between planet hosts and non-planet hosts only. The California Planet Survey (CPS) late-K and M-type dwarf sample (Rauscher & Marcy 2006; Johnson et al. 2010b) was chosen for this goal. It is a 152 star sample where 18 planets (7 Jovians and 11 Neptunian/smaller planets) are already detected around 11 hosts. Most of the jovian detections come from the CPS sample while almost all detections of Neptunians and smaller

Table 4.3: Parameters of the Bayesian and fit from binning models for the HARPS sample.

Parameters for Jovian hosts	Uniform Prior	most likely value	fit from binning
$f_{p1} = C$			
C	(0.01,0.30)	0.03 ± 0.02	0.02±0.02
$f_{p2} = C10^{\alpha[Fe/H]}$			
C	(0.01,0.30)	0.02 ± 0.02	0.03 ± 0.01
α	(-1.0,4.0)	1.97 ± 1.25	1.26 ± 0.30
Parameters for Neptunian hosts	**Uniform Prior**	**most likely value**	**fit from binning**
$f_{p1} = C$			
C	(0.01,0.30)	0.05 ± 0.02	0.07 ± 0.04
$f_{p2} = C10^{\alpha[Fe/H]}$			
C	(0.01,0.30)	0.03 ± 0.02	0.04 ± 0.01
α	(-4.0,1.0)	-0.57 ± 0.71	-0.79 ± 0.06

planets were made with HARPS. The metallicities and stellar masses were calculated using the Johnson & Apps (2009) and the Delfosse et al. (2000) calibration, respectively. We note that the Johnson & Apps (2009) [Fe/H] calibration has a dispersion around ~ 0.2 dex and a systematic offset towards higher [Fe/H], as shown in Neves et al. (2012). The offset amounts to 0.13 dex when we compare the [Fe/H] of the CPS sample computed from the Johnson & Apps (2009) calibration with the Neves et al. (2012) calibration.

We calculated the difference of averages and medians between planet hosts and non-planet hosts in the same way as we did for our sample, as shown in Table 4.2. Table 4.4 shows the results. For metallicity, we observe a much higher difference of averages and medians when compared to our sample, but as we noted before there is an offset when calculating the metallicity with different calibrations. The difference of averages and medians for Jupiter-type planets is higher than in our sample but is compatible with our results. For Neptunian-type hosts the difference of averages and medians are indistinguishable from the non-planet host sample.

We also performed a KS test for [Fe/H] between the three planet-host subsamples and the stars without planets, taking advantage of the higher number of stars with planets of the CPS sample, as shown in the forth column of Table 4.4. It can be seen that there is a very low probability (~0.2%) that the Jovian hosts and the stars without planets belong to the same distribution. For the case of Neptunian-hosts, however, the KS p-value is high (~98%). Again, this result is expected from previous works on FGK dwarfs (e.g. Sousa et al. 2011) and M dwarfs (e.g. Rojas-Ayala et al. 2012).

Regarding stellar mass, we do not see any trend. The difference of averages and medians between planet hosts and non-planet hosts is negligible. This result agrees with the findings of the HARPS sample as the trend we observe with stellar mass is biased.

Table 4.4: Difference of averages and medians between planet host and non-planet host distributions for the CPS late-K and M-type dwarf sample.

[Fe/H]	Diff. of averages [dex]	Diff. of medians [dex]	KS test
Full sample (N_h=11)	0.19	0.22	0.0272
Jovian hosts (N_h=6)	0.37	0.34	0.0015
Neptunian/smaller hosts (N_h=5)	-0.03	-0.05	0.9769
Stellar mass	Diff. of averages [$M_\odot$]	Diff. of medians [$M_\odot$]	
Full sample (N_h=11)	-0.04	-0.01	
Jovian hosts (N_h=6)	-0.03	-0.05	
Neptunian/smaller hosts (N_h=5)	-0.04	0.00	

4.4 Metallicity-planet relation from the HARPS+CPS joined sample

To improve our statistics and study the planet-metallicity correlation in more detail, we joined our HARPS sample with the CPS M dwarf sample. The [Fe/H] for the CPS sample was recalculated with the Neves et al. (2012) calibration, which has the same scale and accuracy of our new calibration, shown in Sect. 4.2. We kept the values of the [Fe/H] using our new spectroscopic calibration for the 49 stars in common. The joined sample has 205 stars, with 13 stars hosting 20 planets. Seven hosts have Jovian-type planets around them while six of them only have Neptunians and smaller planets.

Table 4.5 shows the results for the joined sample, and is similar to Table 4.4. We did not calculate the correlation between planet occurrence and stellar mass, because as discussed in Sect. 4.5 such relation is biased for the HARPS sample. The joined sample results are similar to both our sample and the CPS sample: the difference of averages and medians between Jovian hosts and non-planet hosts show a correlation with [Fe/H], while the same quantities for Neptunians and smaller hosts do not show this trend. The tentative hint of an anti-correlation with [Fe/H] for the Neptunians/smaller hosts of the HARPS sample, in Table 4.2 is observed but is smaller than the one observed for the HARPS sample. However, we must note that the CPS sample is not as sensitive as the HARPS sample in the detection of Neptunian and smaller planets. Therefore we consider that in this work the reference is the HARPS sample regarding the Neptunian-host metallicity relation.

Table 4.5: Difference of averages and medians between planet host and non-planet host distributions for the joined sample.

[Fe/H]	Diff. of averages [dex]	Diff. of medians [dex]	KS test
Full sample (N_h=13)	0.08	0.10	0.2985
Jovian hosts (N_h=7)	0.20	0.19	0.0159
Neptunian/smaller hosts (N_h=6)	-0.06	-0.08	0.6694

The KS test results are similar to the ones performed for the CPS sample, in Table 4.4. However we must note the higher value in the case of the Jovian hosts, just above the 1% p-value.

We now proceed to the frequency analysis of the stars with Jovian and Neptunians/smaller planets. Figures 4.11 (a) and 4.11 (b) show, in their upper panel, the histograms of stars with Jovian planets and stars with only Neptunians and smaller planets, respectively, depicted by a dashed blue line. The histogram of the non-host stars of the joined sample are depicted by a solid red line. The lower panels show the frequency of planets of each bin. The solid red and the dashed black lines represent the fit of the binned values and the fit given by a Bayesian model (see Sect. 4.3.1) respectively. The values of the coefficients for both fits are shown in Table 4.6 and will be discussed together in Sect. 4.4.1.

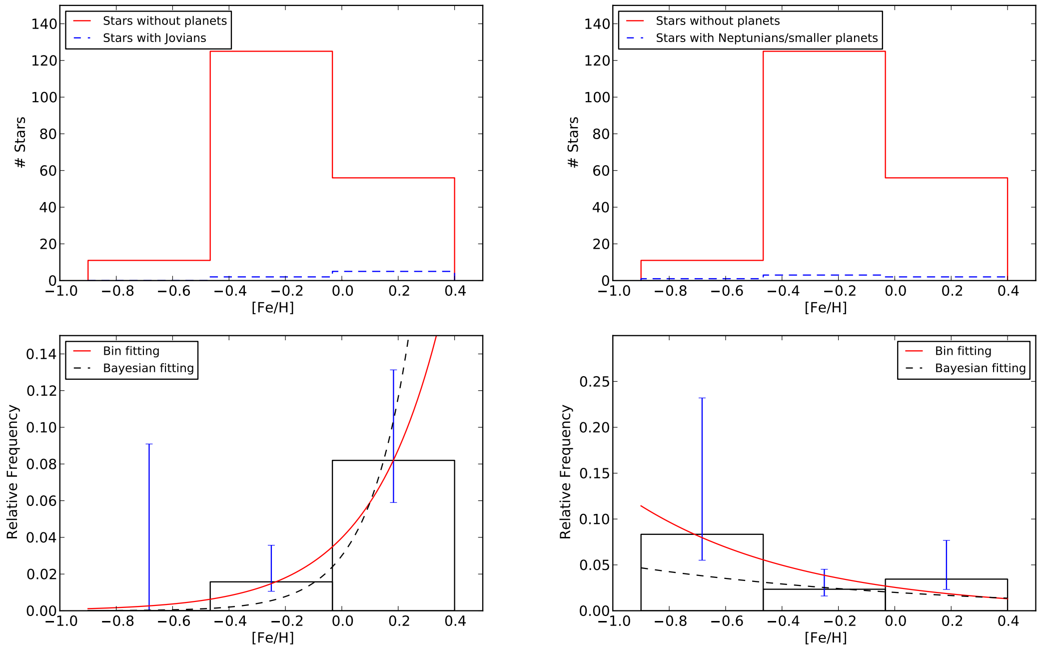

(a) (b)

Figure 4.11: (a) Upper panel: Histogram of metallicity of the joined sample with 3 bins for stars without planets (solid red) and stars with Giant planets (dashed blue); Lower panel: Frequency of stars with Giant planets; (b) Upper panel: Histogram of metallicity of the joined sample with 3 bins for stars without planets (solid red) and stars with Neptunians and smaller planets only (dashed blue); Lower panel: Frequency of stars with Neptunians and smaller planets only.

From Fig. 4.11 we can observe that the results are similar to the ones obtained with our sample (see Fig. 4.9, but with lower uncertainties. The correlation of Jovian-hosts and metallicity is now stronger, but the anti-correlation for Neptunians is weaker. The first bin of Fig. 4.11 (a), ranging from -0.9 to -0.47 dex has an upper limit of 9.1%, with no planet detection, while the second and third bins ([-0.47,-0.03] and [-0.03,0.4] dex, resp.) have values of 1.6% and 8.2% respectively. Regarding Fig. 4.11 (b), we observe the frequencies of 8.3, 2.3, and 3.4% for the same bins.

4.4.1 Bayesian approach for the joined sample

Here we perform the same Bayesian inference approach as done in Sect. 4.3.1 but this time for the joined sample. Table 4.6 summarises and compares the results of the Bayesian fitting to the ones obtained with the bin fitting. The columns are the same as in Table 4.3.

Table 4.6: Parameters of the two Bayesian and fit from binning models for the HARPS+CPS sample.

Parameters for Jovian hosts	Uniform Prior	most likely value	fit from binning
$f_{p1} = C$			
C	(0.01,0.30)	0.03 ± 0.01	0.03 ± 0.03
$f_{p2} = C10^{\alpha[Fe/H]}$			
C	(0.01,0.30)	0.03 ± 0.02	0.04 ± 0.01
α	(-1.0,4.0)	2.94 ± 1.03	1.72 ± 0.18
Parameters for Neptunian hosts	**Uniform Prior**	**most likely value**	**fit from binning**
$f_{p1} = C$			
C	(0.01,0.30)	0.03 ± 0.01	0.04 ± 0.03
$f_{p2} = C10^{\alpha[Fe/H]}$			
C	(0.01,0.30)	0.02 ± 0.02	0.03 ± 0.02
α	(-4.00,1.00)	-0.41 ± 0.77	-0.72 ± 0.46

From Table 4.6 we can see that both the direct bin fitting and the Bayesian fitting values are compatible with the ones obtained with the HARPS sample. As we have seen in Sect. 4.3.1, the α values are higher than the same values using the bin fitting, translating into a higher Giant-host frequency and a lower Neptunian/smaller planet host frequency. Again, the α values calculated by the Bayesian method have large uncertainties, and the α value, for the Neptunian and smaller planet hosts case, may easily have positive or negative values.

We can now compare the values for Giant planets obtained with both fitting methods to previous works. Valenti & Fischer (2005), Udry & Santos (2007), and Sousa et al. (2011) all use a similar power law to the one used in this work for the frequency of giants around FGK dwarfs and obtained α values of 2.0, 2.04, and 2.58 respectively through direct bin fitting. Our α results from the bin fitting (1.26 ± 0.30 from the HARPS sample and 1.72 ± 0.18 from the joined sample) are lower that those works, which might suggest a less efficient planet-formation process around M dwarfs. However, the α values obtained from the Bayesian fit for the HARPS sample are very similar to the ones obtained for FGK dwarfs: 1.97 ± 1.25, despite the high uncertainty. Regarding the combined sample we obtain a higher value of 2.94 ± 1.03 from the Bayesian fitting, suggesting a more efficient process of planet-formation around M dwarfs. Therefore, our quantification of the α parameter for Giant planets around M dwarfs, taking into account the large uncertainties involved, are compatible with the values found in FGK studies.

In order to check if the more complex power law functional form is preferred over the constant one, we used a method of Bayesian model comparison, following Kass & Raftery (1995). First, we calculate for both functional forms the total probability of the model conditioned on the data (the evidence) by integrating over the full parameter space. Computationally, in the case of uniformly distributed priors, we can calculate the evidence as

$$P(d|f) = \frac{\sum P(d|X)}{length(X)}, \tag{4.10}$$

where the $P(d|X)$ is the likelihood, or the probability of observing the data d given the parameters X, and $length(X)$ is the length of the full parameter space. Then, we calculate the Bayes factor that is just the ratio of the evidence of both functional forms,

$$B_f = \frac{P(d|f_{p2})}{P(d|f_{p1})}. \tag{4.11}$$

According to Kass & Raftery (1995) a B_f value over 20 gives a *strong* evidence that the model f_{p2} is better at fitting the data than the f_{p1} model.

For the Jovian hosts case, we obtained a Bayes factor of 2.07 and 66.04 for the HARPS and the joined sample respectively. This means that, in the case of the HARPS sample, the more complex model cannot explain much better the data than the constant model. On the other hand, the combined sample achieves a high Bayes factor, meaning that there is a strong evidence that the more complex model does a better fit than the constant model, supporting the planet-metallicity correlation for Giant planets.

Regarding the Neptunian hosts, we obtain values lower than the unity, which means that the constant model explain the data better than the more complex power model. Therefore, it is impossible at this moment to confirm the hypothetical anti-correlation observed for low [Fe/H] values. Despite this, we must note that our HARPS sample is much more sensitive in probing the Neptunian/Super-Earth mass regime than the CPS sample. Therefore the frequency parametrization of the HARPS sample for the Neptunian/Super-Earth mass range, and shown in detail in Sect. 4.3, is preferred over the joined one.

4.5 The stellar mass-planet correlation bias

From the mass-luminosity relation of Delfosse et al. (2000) in the K-band, we calculated the stellar mass for the M dwarfs of our sample. Fig. 4.12 shows the histogram of the stellar mass distribution of the whole sample. The solid blue and dashed vertical lines represent the mean and the median of the stellar mass of the sample respectively. The black vertical lines locate the systems with planet detections.

We can see that the planet detections are all on one side of the median of our sample distribution with stellar mass (all detected planets are around the more massive stars), as shown by Bonfils et al. (2013). This is also true for the V magnitude distribution (all detected planets are around the brighter stars). Therefore, any result regarding stellar mass will be checked, because its distribution may be subject to detection biases: on the one hand the reflex motion induced by a planetary companion is higher in lower mass stars, meaning a higher radial velocity (RV) signal, but on the other hand, the lower mass stars are on average fainter, thus having higher measurement uncertainties, which makes smaller planets harder to detect.

A lower star count in the [0.35-0.40] $M_\odot$ bin of Fig. 4.12 is observed. To check whether this feature is real or due to a small number statistical fluctuation we did a simple Monte-Carlo simulation by generating 100.000 virtual samples containing 102 stars in the [0.05-0.65] $M_\odot$ region, using a uniform distribution generator. Then, for each sample, we searched for a bin, in the [0.15-0.5] region, where the count difference with both adjacent bins was the same or higher than in the observed stellar mass distribution. To this end we chose a count difference of 6,7, and 8, obtaining a frequency of 10.6, 5.1, and 2.2% respectively. We thus attribute the low number of stars with a mass between 0.35 and 0.4 $M_\odot$

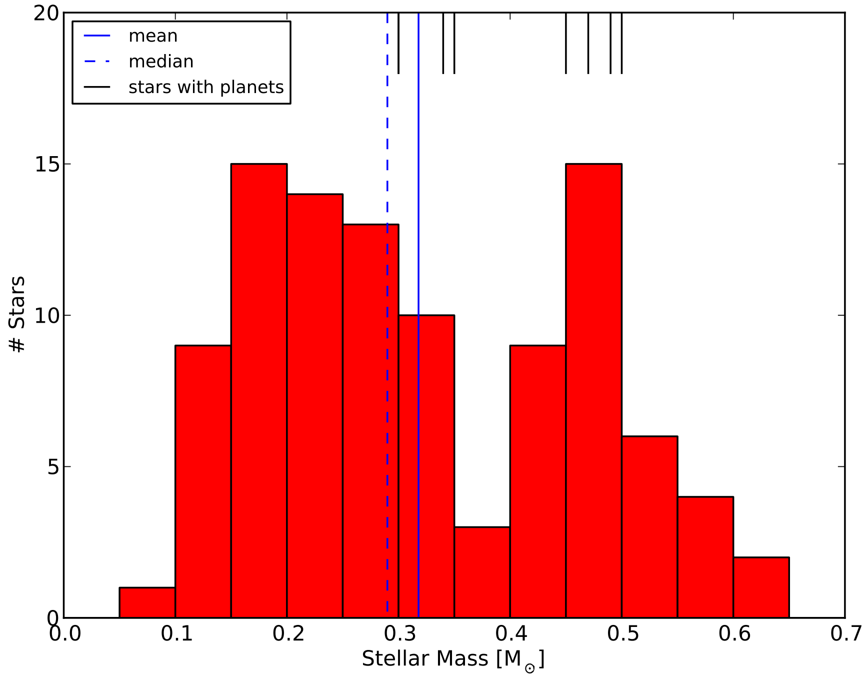

Figure 4.12: Stellar mass distribution of the sample. The blue solid and dashed vertical lines represent the mean and the median of the stellar mass of the sample respectively. The black vertical lines locate the systems with planet detections.

to a small number statistical fluctuation.

To check if there is any statistically significative bias due to the detection limits in the stellar mass distribution, we will first investigate the reason why all planet detections of our sample are located in the brightest and more massive halves of the two distributions, as it was seen in Fig. 4.12, for the stellar mass. We will then confirm or deny the existence of a stellar mass-planet correlation in our sample, as shown in Table 4.7, where we can observe a significative difference between the difference of averages and medians of Giant planet and non-planet hosts.

Table 4.7: Difference of averages and medians of stellar mass between planet host and non-planet host distributions. N_h is the number of planet hosts.

Stellar mass	Diff. of averages [M$_\odot$]	Diff. of medians [M$_\odot$]
Full sample (N_h=8)	0.08	0.13
Jovian hosts (N_h=3)	0.11	0.18
Neptunian/smaller hosts (N_h=5)	0.07	0.08

In order to do this, we divided the sample into two stellar mass ranges at the median value (0.29 M$_\odot$). Then, we calculated the frequency of stars with planets, using only the most massive planet in stars with multiple planets, and the frequency of planets. For both cases, we take into account the detection limits of our sample for different regions of the mass-period diagram following the procedure described in Sect. 7 of Bonfils et al. (2013).

In short, for each region, we calculate the frequency $f = N_d/N_{\star,eff}$, where N_d is the number of planet detections (or stars with planets), and $N_{\star,eff}$ is the number of stars whose detection limits exclude planets with similar mass and period at the 99% confidence level. The $N_{\star,eff}$ is evaluated with Monte-Carlo sampling as described in Bonfils et al. (2013): we draw random mass and period within each region of study, assuming a log-uniform probability for both quantities. Then, we evaluate if the draw falls above or below the detection limit of each star. If it sits above the detection limit we include the star in the $N_{\star,eff}$. The final value of $N_{\star,eff}$ will be the average of 10.000 trials. The confidence intervals are calculated using a poissonian distribution to calculate the 1σ gaussian-equivalent area of the probability distribution, as shown for the binomial distribution in Sect. 4.3.

The results for the two halves of the stellar mass distribution can be seen in Table 4.8 for the frequency of planet-hosts (N=8), and in Table 4.9 for the occurrence of planets (N=15). We observe that, in the planet-host case, all values between the upper limits for $M_\star \leq 0.29 M_\odot$ and the frequency values for $M_\star > 0.29 M_\odot$ are compatible with each other for all regions of planetary mass and period, except in the three regions with period between 10 and 10^4 days, and mass between 1 and 10 $M_\oplus$, where we cannot compare the values due to a low N_{eff} number. We observe the same regarding the results of the occurrence of planets.

Table 4.8: (a) Upper limits for the occurrence of planet-hosts for $M_\star \leq 0.29\ M_\odot$ ($N_\star$=52); (b) Frequencies and upper limits for the occurrence of planet-hosts for $M_\star > 0.29\ M_\odot$ ($N_\star$=49). Multi-planet hosts are characterised by their most massive planet.

(a)

$m\sin i$ [$M_\oplus$]	Period [day]			
	$1-10$	$10-10^2$	10^2-10^3	10^3-10^4
10^3-10^4	$N_d = 0$ $N_{eff} = 47.51$ $f < 0.02(1\sigma)$	$N_d = 0$ $N_{eff} = 46.85$ $f < 0.02(1\sigma)$	$N_d = 0$ $N_{eff} = 45.74$ $f < 0.02(1\sigma)$	$N_d = 0$ $N_{eff} = 42.67$ $f < 0.03(1\sigma)$
10^2-10^3	$N_d = 0$ $N_{eff} = 44.11$ $f < 0.03(1\sigma)$	$N_d = 0$ $N_{eff} = 41.19$ $f < 0.03(1\sigma)$	$N_d = 0$ $N_{eff} = 36.31$ $f < 0.03(1\sigma)$	$N_d = 0$ $N_{eff} = 24.39$ $f < 0.05(1\sigma)$
$10-10^2$	$N_d = 0$ $N_{eff} = 28.56$ $f < 0.04(1\sigma)$	$N_d = 0$ $N_{eff} = 18.86$ $f < 0.06(1\sigma)$	$N_d = 0$ $N_{eff} = 9.90$ $f < 0.12(1\sigma)$	$N_d = 0$ $N_{eff} = 3.43$ $f < 0.31(1\sigma)$
$1-10$	$N_d = 0$ $N_{eff} = 3.90$ $f < 0.28(1\sigma)$	$N_d = 0$ $N_{eff} = 1.45$ –	$N_d = 0$ $N_{eff} = 0.46$ –	$N_d = 0$ $N_{eff} = 0.01$ –

(b)

$m\sin i$ [$M_\oplus$]	Period [day]			
	$1-10$	$10-10^2$	10^2-10^3	10^3-10^4
10^3-10^4	$N_d = 0$ $N_{eff} = 48.93$ $f < 0.02(1\sigma)$	$N_d = 0$ $N_{eff} = 48.73$ $f < 0.02(1\sigma)$	$N_d = 0$ $N_{eff} = 48.34$ $f < 0.02(1\sigma)$	$N_d = 0$ $N_{eff} = 47.24$ $f < 0.02(1\sigma)$
10^2-10^3	$N_d = 0$ $N_{eff} = 47.79$ $f < 0.02(1\sigma)$	$N_d = 1$ $N_{eff} = 47.03$ $f = 0.02^{+0.05}_{-0.01}$	$N_d = 0$ $N_{eff} = 44.74$ $f < 0.03(1\sigma)$	$N_d = 2$ $N_{eff} = 34.66$ $f = 0.06^{+0.08}_{-0.02}$
$10-10^2$	$N_d = 2$ $N_{eff} = 40.26$ $f = 0.05^{+0.07}_{-0.02}$	$N_d = 0$ $N_{eff} = 31.78$ $f < 0.04(1\sigma)$	$N_d = 0$ $N_{eff} = 19.98$ $f < 0.06(1\sigma)$	$N_d = 0$ $N_{eff} = 7.18$ $f < 0.16(1\sigma)$
$1-10$	$N_d = 3$ $N_{eff} = 9.44$ $f = 0.32^{+0.31}_{-0.10}$	$N_d = 0$ $N_{eff} = 3.89$ $f < 0.28(1\sigma)$	$N_d = 0$ $N_{eff} = 0.98$ –	$N_d = 0$ $N_{eff} = 0.10$ –

Table 4.9: (a) Upper limits for the occurrence of planets for $M_\star \leq 0.29\ M_\odot$ ($N_\star$=52); (b) Frequencies and upper limits for the occurrence of planets for $M_\star > 0.29\ M_\odot$ ($N_\star$=49).

(a)

$m\sin i$ [$M_\oplus$]	Period [day]			
	$1-10$	$10-10^2$	10^2-10^3	10^3-10^4
10^3-10^4	$N_d = 0$ $N_{eff} = 47.51$ $f < 0.02(1\sigma)$	$N_d = 0$ $N_{eff} = 46.85$ $f < 0.02(1\sigma)$	$N_d = 0$ $N_{eff} = 45.74$ $f < 0.02(1\sigma)$	$N_d = 0$ $N_{eff} = 42.70$ $f < 0.03(1\sigma)$
10^2-10^3	$N_d = 0$ $N_{eff} = 44.13$ $f < 0.03(1\sigma)$	$N_d = 0$ $N_{eff} = 41.24$ $f < 0.03(1\sigma)$	$N_d = 0$ $N_{eff} = 36.45$ $f < 0.03(1\sigma)$	$N_d = 0$ $N_{eff} = 24.63$ $f < 0.05(1\sigma)$
$10-10^2$	$N_d = 0$ $N_{eff} = 28.51$ $f < 0.04(1\sigma)$	$N_d = 0$ $N_{eff} = 18.84$ $f < 0.06(1\sigma)$	$N_d = 0$ $N_{eff} = 9.89$ $f < 0.12(1\sigma)$	$N_d = 0$ $N_{eff} = 3.46$ $f < 0.31(1\sigma)$
$1-10$	$N_d = 0$ $N_{eff} = 3.92$ $f < 0.28(1\sigma)$	$N_d = 0$ $N_{eff} = 1.47$ –	$N_d = 0$ $N_{eff} = 0.47$ –	$N_d = 0$ $N_{eff} = 0.01$ –

(b)

$m\sin i$ [$M_\oplus$]	Period [day]			
	$1-10$	$10-10^2$	10^2-10^3	10^3-10^4
10^3-10^4	$N_d = 0$ $N_{eff} = 48.92$ $f < 0.02(1\sigma)$	$N_d = 0$ $N_{eff} = 48.71$ $f < 0.02(1\sigma)$	$N_d = 0$ $N_{eff} = 48.34$ $f < 0.02(1\sigma)$	$N_d = 0$ $N_{eff} = 47.21$ $f < 0.02(1\sigma)$
10^2-10^3	$N_d = 0$ $N_{eff} = 47.78$ $f < 0.02(1\sigma)$	$N_d = 2$ $N_{eff} = 47.02$ $f = 0.04^{+0.06}_{-0.01}$	$N_d = 0$ $N_{eff} = 44.65$ $f < 0.03(1\sigma)$	$N_d = 2$ $N_{eff} = 34.48$ $f = 0.06^{+0.08}_{-0.02}$
$10-10^2$	$N_d = 2$ $N_{eff} = 40.23$ $f = 0.05^{+0.07}_{-0.02}$	$N_d = 0$ $N_{eff} = 31.60$ $f < 0.04(1\sigma)$	$N_d = 1$ $N_{eff} = 19.85$ $f = 0.05^{+0.12}_{-0.01}$	$N_d = 0$ $N_{eff} = 7.23$ $f < 0.16(1\sigma)$
$1-10$	$N_d = 5$ $N_{eff} = 9.46$ $f = 0.53^{+0.36}_{-0.15}$	$N_d = 3$ $N_{eff} = 3.90$ $f = 0.77^{+0.75}_{-0.23}$	$N_d = 0$ $N_{eff} = 0.99$ –	$N_d = 0$ $N_{eff} = 0.10$ –

The fact that we do not observe a statistically significative ($> 2\sigma$) difference in any region of the mass-period diagram between the two stellar mass sub-samples indicate that the observed accumulation of planet hosts in the higher half of the stellar mass distribution is due to a stellar mass detection bias. Therefore, we will not study the stellar mass-planet relation any further for our HARPS sample.

We got similar results for the V magnitude distribution, as the brightness and stellar mass have similar effects regarding the precision of the RV measurements.

4.6 Discussion

In this work we investigate the metallicity and stellar mass correlations with planets. We use a new method, described in Sect. 4.2, to refine the precision of the metallicities of the HARPS GTO M dwarf sample calculated with the calibration of Neves et al. (2012). We use the established calibration of Delfosse et al. (2000) to calculate the stellar masses of our sample.

We confirm the trend of metallicity with the presence of Giant planets in our sample, as shown by previous studies on FGK dwarfs (e.g. Gonzalez 1997; Santos et al. 2004b; Sousa et al. 2011; Mayor et al. 2011) and M dwarfs (Bonfils et al. 2007; Johnson & Apps 2009; Schlaufman & Laughlin 2010; Rojas-Ayala et al. 2012; Terrien et al. 2012). For Neptunian and smaller planet hosts there is a hint that an anti-correlation may exist but our current statistic supports a flat relation, in concordance with previous results for FGK dwarfs (e.g. Sousa et al. 2008; Bouchy et al. 2009; Sousa et al. 2011) and M dwarfs (Rojas-Ayala et al. 2012). We calculate the difference of the averages and medians between planet and non-planet hosts, and most importantly the frequencies in three different bins, as well as a parametrization to both Jovian and Neptunian hosts.

We combined the HARPS sample with the California Planet Survey (CPS) late-K and M-type dwarf sample to improve our statistics, increasing the number of stars from 102 to 205 and the number of planet hosts from 8 to 13 (7 Jovian-hosts and 6 Neptunian/smaller planet hosts). The [Fe/H] of the CPS sample was calculated using the photometric calibration of Neves et al. (2012). The previous trend for Jovian-hosts is confirmed and reinforced, but the existence of an anti-correlation of Neptunian-hosts with [Fe/H] is inconclusive. The CPS sample is not as sensitive as the HARPS sample regarding the detection of Neptunian and smaller planets. Therefore the HARPS sample is the reference in this work regarding the Neptunian-host-metallicity relation.

Quantitatively, the difference of the averages and the medians between stars with and without planets for Jupiter-type hosts is 0.20 and 0.26 dex for the HARPS sample and 0.20 and 0.19 dex for the joined sample. Regarding the Neptunian and smaller planet hosts, the observed difference of the averages and the medians is -0.10 dex for the HARPS sample, respectively.

Regarding the frequency of Giant hosts, we have no detection in the [-0.9,-0.47] dex bin for both HARPS and the joined sample. For the [-0.47,-0.03] bin we obtained a frequency of 1.9% and 1.6%, and between -0.03 and 0.4 we have a frequency of 5.6% and 8.2% for the HARPS and the joined sample respectively. Regarding Neptunian hosts, we obtained, for the same samples and bins, the values of 12.5% and 8.3% for the first bin, 5.4% and 2.3% for the second bin, and 2.9% and 3.4% for the last [Fe/H] bin. As noted, the frequencies obtained using the joined sample for the Neptunian-hosts are not as precise as in the HARPS sample due to a lower sensitivity of the CPS sample to Neptunian and smaller planets.

The parametrization of the planet-metallicity relation was based on bin fit and Bayesian fit models, following a functional form of the type $f_p = C10^{\alpha[Fe/H]}$ used in previous works for FGK dwarfs (Valenti & Fischer 2005; Udry & Santos 2007; Sousa et al. 2011). The results for the parameters C and α using the functional forms calculated by direct bin fitting or by using the Bayesian fitting are compatible with each other. However, we note a high uncertainty on the determination of the α parameter using the Bayesian fitting. Therefore the results for this parameter for Giant planets vary a lot, between 1.26 ± 0.30 and 1.97 ± 1.25, using the bin fitting or the Bayesian fitting respectively, for the HARPS sample, and between 1.72 ± 0.18 to 2.94 ± 1.03 for the combined sample. At the actual statistical level, the α parameter we determine is compatible with the value found for FGK dwarfs in previous studies (Fischer & Valenti 2005; Udry & Santos 2007; Sousa et al. 2011). Regarding Neptunian-hosts, we obtain an α value, for the HARPS sample, between -0.79 ± 0.06 and -0.57 ± 0.71, using the bin fit or the Bayes fit model respectively. This result configures an anti-correlation for Neptunian hosts with [Fe/H], but with an insufficient statistical confidence level.

We therefore conclude that the power law functional form works best for Giant hosts, and that a constant functional form is preferred, for now, for Neptunian/smaller planet hosts. We also reject the possibility of a correlation for Neptunian-hosts of the same order of magnitude of that for Jupiter-hosts. In fact we suspect that an anti-correlation might exist but we lack the statistics to confirm it.

Regarding stellar mass, we detect a positive trend in planet detections towards higher masses. However, when we take the detection limits into account, we do not find any significant difference. Therefore, the trend of the frequency of planets with the stellar mass is due to a detection bias in our sample, stressing the importance of taking into account the planet detection biases in stellar mass studies.

4.7 Paper: Planet-metalllicity and planet-stellar mass correlations of the HARPS GTO M dwarf sample

Abstract.

Aims.The aim of this work is the study of the planet-metallicity and the planet-stellar mass correlations for M dwarfs from the HARPS GTO M dwarf subsample.

Methods. We use a new method that takes advantage of the HARPS high-resolution spectra to increase the precision of metallicity, using previous photometric calibrations of [Fe/H] and effective temperature as starting values.

Results. In this work we use our new calibration ($rms = 0.08$ dex) to study the planet-metallicity relation of our sample. The well-known correlation for Giant planet FGKM hosts with metallicity is present. Regarding Neptunians and smaller hosts no correlation is found but there is a hint that an anti-correlation with [Fe/H] may exist. We combined our sample with the California Planet Survey late-K and M-type dwarf sample to increase our statistics but found no new trends. We fitted a power law to the frequency histogram of the Jovian hosts for our sample and for the combined sample, $f_p = C10^{\alpha[Fe/H]}$, using two different approaches: a direct bin fitting and a Bayesian fitting procedure. We obtained a value for C between 0.02 and 0.04 and for α between 1.26 and 2.94. Regarding stellar mass, a hypothetical correlation with planets was discovered, but was found to be the result of a detection bias.

Contribution. This paper was completely written by me, and I did almost all the work. My co-authors contributed with observations, important ideas and suggestions and helped in the revision of the paper making relevant remarks and corrections.

A&A 551, A36 (2013)
DOI: 10.1051/0004-6361/201220574

Astronomy & Astrophysics

Metallicity of M dwarfs

III. Planet-metallicity and planet-stellar mass correlations of the HARPS GTO M dwarf sample[⋆],[⋆⋆]

V. Neves[1,2,3], X. Bonfils[2], N. C. Santos[1,3], X. Delfosse[2], T. Forveille[2], F. Allard[4], and S. Udry[5]

[1] Centro de Astrofísica, Universidade do Porto, Rua das Estrelas, 4150-762 Porto, Portugal
e-mail: `vasco.neves@astro.ua.pt`
[2] UJF-Grenoble 1/CNRS-INSU, Institut de Planétologie et d'Astrophysique de Grenoble (IPAG) UMR 5274, 38041 Grenoble, France
[3] Departamento de Física e Astronomia, Faculdade de Ciências, Universidade do Porto, Rua do Campo Alegre, 4169-007 Porto, Portugal
[4] Centre de Recherche Astrophysique de Lyon, UMR 5574: CNRS, Université de Lyon, École Normale Supérieure de Lyon, 46 allée d'Italie, 69364 Lyon Cedex 07, France
[5] Observatoire de Genève, Université de Genève, 51 chemin des Maillettes, 1290 Sauverny, Switzerland

Received 15 October 2012 / Accepted 13 December 2012

ABSTRACT

Aims. The aim of this work is the study of the planet-metallicity and the planet-stellar mass correlations for M dwarfs from the HARPS GTO M dwarf subsample.

Methods. We use a new method that takes advantage of the HARPS high-resolution spectra to increase the precision of metallicity, using previous photometric calibrations of [Fe/H] and effective temperature as starting values.

Results. In this work we use our new calibration (rms = 0.08 dex) to study the planet-metallicity relation of our sample. The well-known correlation for giant planet FGKM hosts with metallicity is present. Regarding Neptunians and smaller hosts no correlation is found but there is a hint that an anti-correlation with [Fe/H] may exist. We combined our sample with the California Planet Survey late-K and M-type dwarf sample to increase our statistics but found no new trends.

We fitted a power law to the frequency histogram of the Jovian hosts for our sample and for the combined sample, $f_p = C10^{\alpha[\mathrm{Fe/H}]}$, using two different approaches: a direct bin fitting and a Bayesian fitting procedure. We obtained a value for C between 0.02 and 0.04 and for α between 1.26 and 2.94.

Regarding stellar mass, an hypothetical correlation with planets was discovered, but was found to be the result of a detection bias.

Key words. stars: fundamental parameters – stars: late-type – stars: low-mass – stars: atmospheres – planetary systems

1. Introduction

Stellar mass and metallicity are two important observables directly connected to the formation and evolution of planetary systems. These quantities play an important role in core-accretion models of formation and evolution of planets, as shown by numerous works studying the relationship of both quantities with planet formation (e.g. Ida & Lin 2005; Kornet et al. 2006; Kennedy & Kenyon 2008; Thommes et al. 2008; Alibert et al. 2011; Mordasini et al. 2012).

The initial conditions of planet formation (e.g. disk mass, temperature and density profiles, gravity, gas-dissipation and migration timescales) all change with stellar mass (e.g. Ida & Lin 2005; Kornet et al. 2006; Kennedy & Kenyon 2008; Alibert et al. 2011). Metallicity also plays a major role in the efficiency of the formation of giant planets for FGK dwarfs, as shown by both models (e.g. Ida & Lin 2004; Mordasini et al. 2009, 2012) and observational data in the form of a planet-metallicity correlation (e.g. Gonzalez 1997; Santos et al. 2004; Fischer & Valenti 2005; Sousa et al. 2011; Mayor et al. 2011), that seems to partially vanish for Neptunian and smaller planet hosts (Sousa et al. 2008; Bouchy et al. 2009; Ghezzi et al. 2010; Sousa et al. 2011; Buchhave et al. 2012).

According to Thommes et al. (2008) and Mordasini et al. (2012), a lower metallicity can be compensated by a higher disk mass to allow giant planet formation (and vice-versa – the so called "compensation effect"). This result implies that M dwarfs, which are expected to have a lower disk mass (e.g. Vorobyov & Basu 2008; Alibert et al. 2011) can form giant planets, but only if they have high metallicities, thus suggesting an even stronger giant planet-metallicity correlation compared to FGK dwarfs.

Disk instability models (e.g. Boss 1997), on the other hand, do not predict, in general, the dependence of the planet formation on metallicity (Boss 2002) and they also don't seem to depend strongly on stellar mass, at least in the case of M dwarfs (Boss 2006). Contrary to the core-accretion paradigm (Pollack et al. 1996), the formation of planets does not originate from the collisional accretion of planetesimals, but from the collapse of an unstable part of the protoplanetary disk, forming in a timescale of thousands of years when compared to a timescale of Myrs for core-accretion models. Observational evidence, however, has shown that there is a dependence between planet occurrence and both stellar mass and metallicity over a wide range of dwarf types (AFGKM – e.g. Laws et al. 2003; Bonfils et al. 2007; Lovis & Mayor 2007; Johnson et al. 2007, 2010a), thus favoring

---

[⋆] Based on observations made with the HARPS instrument on the ESO 3.6-m telescope at La Silla Observatory under programme ID 072.C-0488.

[⋆⋆] Tables 2, 8, and Appendix A are available in electronic form at http://www.aanda.org the core-accretion scenario as the primary mechanism of planet formation, at least for closer-in planets.

In this context, the "pollution" scenario (e.g. Gonzalez 1997; Murray et al. 2002), defends that the observed enhanced metallicity is only at the surface of the photosphere, and that the formation of planets occurs at all metallicities, thus supporting disk instability models. Observationally, this would translate, for M dwarfs into a non-detection of the planet-metallicity correlation, as M dwarfs have very deep convective layers and are expected to be fully convective at masses below 0.4 $M_\odot$.

Recent observational works for M dwarfs are in line with a planet-metallicity correlation (e.g. Bonfils et al. 2007; Johnson & Apps 2009; Schlaufman & Laughlin 2010; Rojas-Ayala et al. 2012; Terrien et al. 2012). However, more detections of planets around M dwarfs and a more precise metallicity determination are needed to achieve higher confidence levels that remain low, below the $\sim3\sigma$ level (Bonfils et al. 2007; Schlaufman & Laughlin 2010). In this context it is important to use a volume-limited sample of stars, as several planet-hunting programs targeting FGK dwarfs have metallicity-biased samples (e.g. Baranne et al. 1996; Fischer et al. 2005; Melo et al. 2007).

In the course of this paper we implement a new method to derive the metallicities of a volume-limited sample of 102 M dwarfs from the HARPS GTO programme. This method uses the high-resolution spectra of HARPS to achieve a [Fe/H] precision of 0.08 dex and is described in the Appendix. Then, we search for correlations between the frequency of planets with stellar mass and metallicity. In Sect. 2, we describe our M dwarf sample and observations using the HARPS spectrograph. Then, in Sect. 3, we investigate the stellar mass/metallicity correlations with the frequency of planets. In Sect. 4 we explore the metallicity-planet relation from the joined HARPS+California planet search samples. Finally, we discuss our results in Sect. 5.

2. Sample and observations

Our sample of 102 M dwarfs is described in detail in Sect. 2 of Bonfils et al. (2013). It is a volume limited (11 pc) sample, containing stars with a declination $\delta < +20°$, with V magnitudes brighter than 14 mag, and including only stars with a projected rotational velocity $\upsilon \sin i \leq 6.5$ km s^{-1}. All known spectroscopic binaries and visual pairs with separation lower than 5 arcsec, as well as previously unknown fast rotators were removed a priori or a posteriori from the original sample.

The observations were gathered using the HARPS instrument (Mayor et al. 2003; Pepe et al. 2004), installed at the ESO 3.6-m telescope at the La Silla observatory in Chile. It is a high resolution ($R \sim 115\,000$) spectrograph in the visible, covering a region between 380 and 690 nm. During the time of the GTO program, from 11th February 2003 to the 1st of April 2009, a total of 1965 spectra were recorded. The aim of the HARPS M dwarf programme is to achieve a ∼1 m/s RV precision per exposure for the brightest targets. The chosen recording mode during this period was single fiber mode, that relies only on a single calibration but gives enough precision to reach the aim of the programme. Using single fiber mode has the advantage of obtaining non-contaminated spectra that can be used to perform studies other than measuring the star's RV, such as measuring activity diagnostics, using Ca II H and K lines, and calculating stellar parameters and abundances. A more detailed description of the observations is given in Sect. 3 of Bonfils et al. (2013).

From the 102 M dwarf stars, a total of 15 planets are currently detected, in 8 systems, from which 3 have more than one planet. Table 1 shows the planet hosts, planets, and planetary mass and period taken from Bonfils et al. (2013), except in the case of Gl 876e (Rivera et al. 2010). We refer to Table 1 of Bonfils et al. (2013) for the full planet parameters and respective references.

Table 1. Planet host stars in the sample, along with the planetary mass and period.

Star	Planet	$m \sin i^\dagger$		Period
		[$M_\oplus$]	[M_J]	[days]
Gl 176	b	8.4	0.026	8.78
Gl 433	b	6.4	0.0202	7.365
Gl 581	b	15.7	0.0492	5.3687
Gl 581	c	5.4	0.017	12.93
Gl 581	d	7.1	0.022	66.8
Gl 581	e	1.9	0.0060	3.15
Gl 667C	b	6.0	0.019	7.203
Gl 667C	c	3.9	0.012	28.15
Gl 674	b	11	0.034	4.69
Gl 832	b	200	0.64	3416
Gl 849	b	310	0.99	1852
Gl 876	b	839	2.64	61.07
Gl 876	c	264	0.83	30.26
Gl 876	d	6.3	0.020	1.93785
Gl 876^{1}	e	14.6	0.046	124.26

Notes. We refer to Bonfils et al. (2013) for the full references. $^{(\dagger)}$ The true mass (m_p) is reported for Gl876b,c (Correia et al. 2010). $^{(1)}$ Rivera et al. (2010).

The stellar masses were calculated using the empirical mass-luminosity relationship of Delfosse et al. (2000), using stellar parallaxes, taken mostly from the H catalogue (van Leeuwen 2007), but also from van Altena et al. (1995); Jahreiß & Wielen (1997); Hawley et al. (1997); Henry et al. (2006). The V band magnitudes were taken from the Sinbad database[1], and the infrared K_s magnitudes from 2MASS (Skrutskie et al. 2006). The stellar mass values range from 0.09 to 0.60 $M_\odot$, with a mean and median values of 0.32 and 0.29 $M_\odot$ respectively. We note that, Gl 803, a young (∼20 Myr) M dwarf star in our sample, with a circumstellar disk (Kalas et al. 2004), has a derived stellar mass value of 0.75, too high for a M dwarf. Therefore, the stellar mass calibration being used may not be adequate for the youngest M dwarfs.

The metallicities were first calculated with the photometric calibration provided by Neves et al. (2012), using stellar parallaxes, and V and K_s magnitudes. To improve on precedent photometric calibrations, we try to root the metallicity effect in the high-resolution HARPS spectra, using the measurements of the equivalent widths of the lines and features of the 26 red orders (533−690 nm region) of the HARPS spectra. The new calibration is detailed in the Appendix. We achieve a better precision with the new calibration reaching a [Fe/H] dispersion of the order of 0.08 dex. The metallicity values range from −0.88 to 0.32 dex, with a mean and median values of −0.13 and −0.11 dex respectively. We note that there is a slight offset towards lower metallicities when compared with the 582 FGK dwarfs from the HARPS-2 volume-limited sample (Sousa et al. 2011) with mean and median values of −0.10 and −0.08 dex respectively.

Table 2 depicts the sample used in this paper, where Cols. 2 and 3 list the right ascension and declination respectively, Col. 4 the parallaxes and their respective uncertainties, Col. 5 the source of the parallax, Col. 6 the spectral type of the M dwarf, and Cols. 7 and 8 the V- and K_s-band magnitudes respectively.

---

[1] `http://simbad.u-strasbg.fr/simbad/`

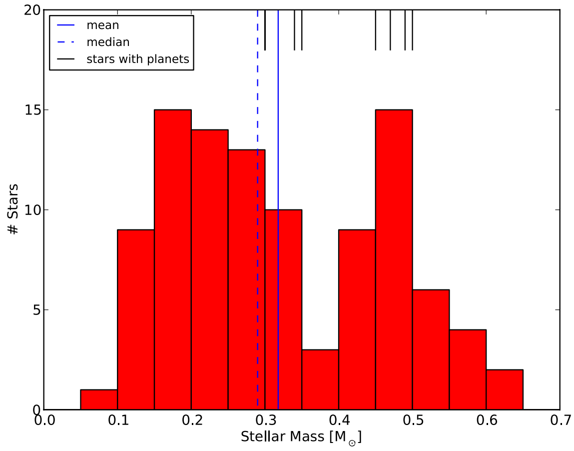

Fig. 1. Stellar mass distribution of the sample. The blue solid and dashed vertical lines represent the mean and the median of the stellar mass of the sample respectively. The black vertical lines locate the systems with planet detections.

Finally, Cols. 9 and 10 contain the calculated stellar mass and metallicity.

3. Stellar mass, metallicity, and planets from the HARPS study

In this section we use the new metallicity values (see the Appendix) as well as the stellar mass determinations from the HARPS M dwarf GTO sample to study the possible correlations of these quantities with the presence of planets. In this paper we consider Jovian hosts as stars having any planet with $M_p >$ 30 $M_\oplus$ and Neptunian/smaller planet hosts as stars having all planets with masses below 30 $M_\oplus$.

3.1. The stellar mass-planet correlation bias

Figure 1 shows the histogram of the stellar mass distribution of the whole sample. The solid blue and dashed vertical lines represent the mean and the median of the stellar mass of the sample respectively. The black vertical lines locate the systems with planet detections.

We can see that the planet detections are all on one side of the median of our sample distribution with stellar mass (all detected planets are around the more massive stars), as previously shown by Bonfils et al. (2013). This is also true for the V magnitude distribution (all detected planets are around the brighter stars). Therefore, any result regarding stellar mass will be checked, because its distribution may be subject to detection biases: on the one hand the reflex motion induced by a planetary companion is higher in lower mass stars, meaning a higher radial velocity (RV) signal, but on the other hand, the lower mass stars are on average fainter, thus having higher measurement uncertainties, which makes smaller planets harder to detect.

A lower star count in the [0.35−0.40] $M_\odot$ bin of Fig. 1 is observed. To check whether this feature is real or due to a small number statistical fluctuation we did a simple montecarlo simulation by generating 100.000 virtual samples containing 102 stars in the [0.05−0.65] $M_\odot$ region, using an uniform distribution generator. Then, for each sample, we searched for a bin, in the [0.15−0.5] region, where the count difference with both adjacent bins was the same or higher than in the observed stellar mass distribution. To this end we chose a count difference of 6, 7, and 8, obtaining a frequency of 10.6, 5.1, and 2.2% respectively. We thus attribute the low number of stars with a mass between 0.35 and 0.4 $M_\odot$ to a small number statistical fluctuation.

Table 3. Difference of averages and medians of stellar mass between planet host and non-planet host distributions.

Stellar mass	Diff. of averages [$M_\odot$]	Diff. of medians [$M_\odot$]
Full sample (N_h = 8)	0.08	0.13
Jovians hosts (N_h = 3)	0.11	0.18
Neptunian/smaller hosts (N_h = 5)	0.07	0.08

Notes. N_h is the number of planet hosts.

To check if there is any statistically significative bias due to the detection limits in the stellar mass distribution, we will first investigate the reason why all planet detections of our sample are located in the brightest and more massive halves of the two distributions, as it was seen in Fig. 1, for the stellar mass. We will then confirm or deny the existence of a stellar mass-planet correlation in our sample, as shown in Table 3, where we can observe a significative difference between the difference of averages and medians of giant planet and non-planet hosts.

In order to do this, we divided the sample into two stellar mass ranges at the median value (0.29 $M_\odot$). We note that we removed the star Gl803 from the sample, due to the fact that the mass for this star may have not been adequately calculated, as explained in Sect. 2. Then, we calculated the frequency of stars with planets, using only the most massive planet in stars with multiple planets, and the frequency of planets. For both cases, we take into account the detection limits of our sample for different regions of the mass-period diagram following the procedure described in Sect. 7 of Bonfils et al. (2013).

In short, for each region, we calculate the frequency $f = N_d/N_{\star,\mathrm{eff}}$, where N_d is the number of planet detections (or stars with planets), and $N_{\star,\mathrm{eff}}$ is the number of stars whose detection limits exclude planets with similar mass and period at the 99% confidence level. The $N_{\star,\mathrm{eff}}$ is evaluated with Monte-Carlo sampling as described in Bonfils et al. (2013): we draw random mass and period within each region of study, assuming a log-uniform probability for both quantities. Then, we evaluate if the draw falls above or below the detection limit of each star. If it sits above the detection limit we include the star in the $N_{\star,\mathrm{eff}}$. The final value of $N_{\star,\mathrm{eff}}$ will be the average of 10.000 trials. The confidence intervals are calculated using a Poissonian distribution to calculate the 1σ Gaussian-equivalent area of the probability distribution, as shown for the binomial distribution in Sect. 3.2.

The results for the two halves of the stellar mass distribution can be seen in Table 4 for the frequency of planet-hosts (N = 8), and in Table 5 for the occurrence of planets (N = 15). We observe that, in the planet-host case, all values between the upper limits for $M_\star \leq 0.29$ $M_\odot$ and the frequency values for $M_\star > 0.29$ $M_\odot$ are compatible with each other for all regions of planetary mass and period, except in the three regions with period between 10 and 10^4 days, and mass between 1 and 10 $M_\oplus$, where we cannot compare the values due to a low N_{eff} number. We observe the same regarding the results of the occurrence of planets.

The fact that we do not observe a statistically significative (>2σ) difference in any region of the mass-period diagram between the two stellar mass sub-samples indicate that the observed accumulation of planet hosts in the higher half of the

Table 4. a) Upper limits for the occurrence of planet-hosts for $M_\star \leq 0.29\ M_\odot$ ($N_\star = 52$); b) frequencies and upper limits for the occurrence of planet-hosts for $M_\star > 0.29\ M_\odot$ ($N_\star = 49$).

(a)

$m \sin i$ [$M_\oplus$]	Period [day] 1–10	10–10^2	10^2–10^3	10^3–10^4
10^3–10^4	$N_\mathrm{d} = 0$ $N_\mathrm{eff} = 47.51$ $f < 0.02(1\sigma)$	$N_\mathrm{d} = 0$ $N_\mathrm{eff} = 46.85$ $f < 0.02(1\sigma)$	$N_\mathrm{d} = 0$ $N_\mathrm{eff} = 45.74$ $f < 0.02(1\sigma)$	$N_\mathrm{d} = 0$ $N_\mathrm{eff} = 42.67$ $f < 0.03(1\sigma)$
10^2–10^3	$N_\mathrm{d} = 0$ $N_\mathrm{eff} = 44.11$ $f < 0.03(1\sigma)$	$N_\mathrm{d} = 0$ $N_\mathrm{eff} = 41.19$ $f < 0.03(1\sigma)$	$N_\mathrm{d} = 0$ $N_\mathrm{eff} = 36.31$ $f < 0.03(1\sigma)$	$N_\mathrm{d} = 0$ $N_\mathrm{eff} = 24.39$ $f < 0.05(1\sigma)$
10–10^2	$N_\mathrm{d} = 0$ $N_\mathrm{eff} = 28.56$ $f < 0.04(1\sigma)$	$N_\mathrm{d} = 0$ $N_\mathrm{eff} = 18.86$ $f < 0.06(1\sigma)$	$N_\mathrm{d} = 0$ $N_\mathrm{eff} = 9.90$ $f < 0.12(1\sigma)$	$N_\mathrm{d} = 0$ $N_\mathrm{eff} = 3.43$ $f < 0.31(1\sigma)$
1–10	$N_\mathrm{d} = 0$ $N_\mathrm{eff} = 3.90$ $f < 0.28(1\sigma)$	$N_\mathrm{d} = 0$ $N_\mathrm{eff} = 1.45$ –	$N_\mathrm{d} = 0$ $N_\mathrm{eff} = 0.46$ –	$N_\mathrm{d} = 0$ $N_\mathrm{eff} = 0.01$ –

(b)

$m \sin i$ [$M_\oplus$]	Period [day] 1–10	10–10^2	10^2–10^3	10^3–10^4
10^3–10^4	$N_\mathrm{d} = 0$ $N_\mathrm{eff} = 48.93$ $f < 0.02(1\sigma)$	$N_\mathrm{d} = 0$ $N_\mathrm{eff} = 48.73$ $f < 0.02(1\sigma)$	$N_\mathrm{d} = 0$ $N_\mathrm{eff} = 48.34$ $f < 0.02(1\sigma)$	$N_\mathrm{d} = 0$ $N_\mathrm{eff} = 47.24$ $f < 0.02(1\sigma)$
10^2–10^3	$N_\mathrm{d} = 0$ $N_\mathrm{eff} = 47.79$ $f < 0.02(1\sigma)$	$N_\mathrm{d} = 1$ $N_\mathrm{eff} = 47.03$ $f = 0.02^{+0.05}_{-0.01}$	$N_\mathrm{d} = 0$ $N_\mathrm{eff} = 44.74$ $f < 0.03(1\sigma)$	$N_\mathrm{d} = 2$ $N_\mathrm{eff} = 34.66$ $f = 0.06^{+0.08}_{-0.02}$
10–10^2	$N_\mathrm{d} = 2$ $N_\mathrm{eff} = 40.26$ $f = 0.05^{+0.07}_{-0.02}$	$N_\mathrm{d} = 0$ $N_\mathrm{eff} = 31.78$ $f < 0.04(1\sigma)$	$N_\mathrm{d} = 0$ $N_\mathrm{eff} = 19.98$ $f < 0.06(1\sigma)$	$N_\mathrm{d} = 0$ $N_\mathrm{eff} = 7.18$ $f < 0.16(1\sigma)$
1–10	$N_\mathrm{d} = 3$ $N_\mathrm{eff} = 9.44$ $f = 0.32^{+0.31}_{-0.10}$	$N_\mathrm{d} = 0$ $N_\mathrm{eff} = 3.89$ $f < 0.28(1\sigma)$	$N_\mathrm{d} = 0$ $N_\mathrm{eff} = 0.98$ –	$N_\mathrm{d} = 0$ $N_\mathrm{eff} = 0.10$ –

Notes. Multi-planet hosts are characterized by their most massive planet.

Table 5. a) Upper limits for the occurrence of planets for $M_\star \leq 0.29\ M_\odot$ ($N_\star$=52); b) frequencies and upper limits for the occurrence of planets for $M_\star > 0.29\ M_\odot$ ($N_\star = 49$).

(a)

$m \sin i$ [$M_\oplus$]	Period [day] 1–10	10–10^2	10^2–10^3	10^3–10^4
10^3–10^4	$N_\mathrm{d} = 0$ $N_\mathrm{eff} = 47.51$ $f < 0.02(1\sigma)$	$N_\mathrm{d} = 0$ $N_\mathrm{eff} = 46.85$ $f < 0.02(1\sigma)$	$N_\mathrm{d} = 0$ $N_\mathrm{eff} = 45.74$ $f < 0.02(1\sigma)$	$N_\mathrm{d} = 0$ $N_\mathrm{eff} = 42.70$ $f < 0.03(1\sigma)$
10^2–10^3	$N_\mathrm{d} = 0$ $N_\mathrm{eff} = 44.13$ $f < 0.03(1\sigma)$	$N_\mathrm{d} = 0$ $N_\mathrm{eff} = 41.24$ $f < 0.03(1\sigma)$	$N_\mathrm{d} = 0$ $N_\mathrm{eff} = 36.45$ $f < 0.03(1\sigma)$	$N_\mathrm{d} = 0$ $N_\mathrm{eff} = 24.63$ $f < 0.05(1\sigma)$
10–10^2	$N_\mathrm{d} = 0$ $N_\mathrm{eff} = 28.51$ $f < 0.04(1\sigma)$	$N_\mathrm{d} = 0$ $N_\mathrm{eff} = 18.84$ $f < 0.06(1\sigma)$	$N_\mathrm{d} = 0$ $N_\mathrm{eff} = 9.89$ $f < 0.12(1\sigma)$	$N_\mathrm{d} = 0$ $N_\mathrm{eff} = 3.46$ $f < 0.31(1\sigma)$
1–10	$N_\mathrm{d} = 0$ $N_\mathrm{eff} = 3.92$ $f < 0.28(1\sigma)$	$N_\mathrm{d} = 0$ $N_\mathrm{eff} = 1.47$ –	$N_\mathrm{d} = 0$ $N_\mathrm{eff} = 0.47$ –	$N_\mathrm{d} = 0$ $N_\mathrm{eff} = 0.01$ –

(b)

$m \sin i$ [$M_\oplus$]	Period [day] 1–10	10–10^2	10^2–10^3	10^3–10^4
10^3–10^4	$N_\mathrm{d} = 0$ $N_\mathrm{eff} = 48.92$ $f < 0.02(1\sigma)$	$N_\mathrm{d} = 0$ $N_\mathrm{eff} = 48.71$ $f < 0.02(1\sigma)$	$N_\mathrm{d} = 0$ $N_\mathrm{eff} = 48.34$ $f < 0.02(1\sigma)$	$N_\mathrm{d} = 0$ $N_\mathrm{eff} = 47.21$ $f < 0.02(1\sigma)$
10^2–10^3	$N_\mathrm{d} = 0$ $N_\mathrm{eff} = 47.78$ $f < 0.02(1\sigma)$	$N_\mathrm{d} = 2$ $N_\mathrm{eff} = 47.02$ $f = 0.04^{+0.06}_{-0.01}$	$N_\mathrm{d} = 0$ $N_\mathrm{eff} = 44.65$ $f < 0.03(1\sigma)$	$N_\mathrm{d} = 2$ $N_\mathrm{eff} = 34.48$ $f = 0.06^{+0.08}_{-0.02}$
10–10^2	$N_\mathrm{d} = 2$ $N_\mathrm{eff} = 40.23$ $f = 0.05^{+0.07}_{-0.02}$	$N_\mathrm{d} = 0$ $N_\mathrm{eff} = 31.60$ $f < 0.04(1\sigma)$	$N_\mathrm{d} = 1$ $N_\mathrm{eff} = 19.85$ $f = 0.05^{+0.12}_{-0.01}$	$N_\mathrm{d} = 0$ $N_\mathrm{eff} = 7.23$ $f < 0.16(1\sigma)$
1–10	$N_\mathrm{d} = 5$ $N_\mathrm{eff} = 9.46$ $f = 0.53^{+0.36}_{-0.15}$	$N_\mathrm{d} = 3$ $N_\mathrm{eff} = 3.90$ $f = 0.77^{+0.75}_{-0.23}$	$N_\mathrm{d} = 0$ $N_\mathrm{eff} = 0.99$ –	$N_\mathrm{d} = 0$ $N_\mathrm{eff} = 0.10$ –

stellar mass distribution is due to a stellar mass detection bias. Therefore, we will not study the stellar mass-planet relation any further for our HARPS sample.

We got similar results for the V magnitude distribution, as the brightness and stellar mass have similar effects regarding the precision of the RV measurements.

3.2. *The metallicity-planet correlation*

Figure 2 shows the histogram of metallicity of our sample. The solid red histogram represent the stars without planets, while the filled dashed blue histogram the stars with Jovians planets, and the dotted black histogram the stars with Neptunians/smaller planets only. The vertical solid red, dashed blue, and dotted black lines above each histogram depict the value of the mean of the distribution. We note here that we assume that metallicity is not influenced by detection biases, due to the fact that we are using a volume-limited sample.

We can observe in Table 6 that the difference of the averages (medians resp.) of the full sample between planet and non-planet host distributions is small (0.01 and −0.07 dex, respectively).

If we only take into account the three planet host stars with Jupiter-type planets, the difference of the averages and the medians of the [Fe/H] between stars with and without planets is higher (0.20 and 0.26 dex respectively). On the other hand, if we remove the 3 systems with Jupiters, we obtain a mean and median of −0.10 dex. The correlation we find between [Fe/H] and

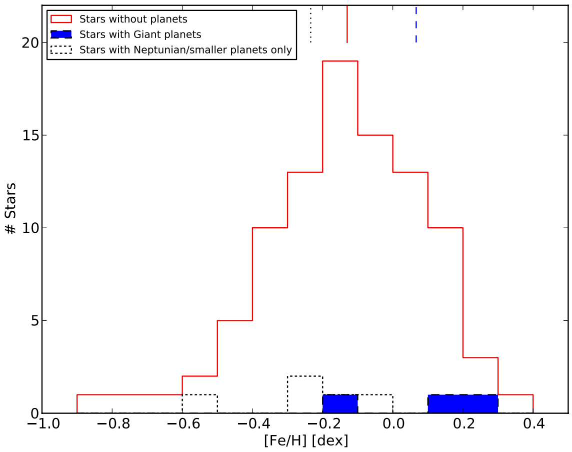

Fig. 2. Histograms of stars without planets (solid red), with Jovian planets (filled dashed blue), and with Neptunians/smaller planets (dotted black) for metallicity. The vertical solid red, filled dashed blue, and dotted black lines above the histograms represent the mean of the [Fe/H] distribution.

Table 6. Difference of averages and medians of [Fe/H] between planet host and non-planet host distributions.

[Fe/H]	Diff. of averages [dex]	Diff. of medians [dex]	KS test
Full sample ($N_h = 8$)	0.01	−0.07	0.8151
Jovians hosts ($N_h = 3$)	0.20	0.26	0.1949
Neptunian/smaller hosts ($N_h = 5$)	−0.10	−0.10	0.3530

Notes. N_h is the number of planet hosts.

planet ocurrence agrees with previous studies focused on giant planets around M dwarfs (e.g. Bonfils et al. 2007; Johnson & Apps 2009; Johnson et al. 2010a; Schlaufman & Laughlin 2010; Rojas-Ayala et al. 2010; Rojas-Ayala et al. 2012; Terrien et al. 2012). We confirm also, with better statistics, that such correlation is vanishing for Neptunian and smaller planet hosts (e.g. Rojas-Ayala et al. 2012; Terrien et al. 2012). In fact our result hints at a anti-correlation between [Fe/H] and planets though the difference (−0.10 dex) is at the limit of our measurement precision. Despite that, the results hint a different type of planet formation mechanism for giant and Neptunian/super Earth-type planets (e.g. Mordasini et al. 2012).

We performed a Kolmogorov-Smirnov (KS) test to check the probability of the sub-samples of stars with and without planets of belonging to the same parent distribution. All KS tests show that we cannot discard the possibility that the three sub-samples with planets belong to the same distribution of the stars without planets. We obtain a value of 0.195 for the Jovians hosts, but we do not have enough hosts ($N = 3$) to calculate the KS test properly.

In order to explore the star-planet relation further, we divided the metallicity range in three bins and performed a frequency analysis for Jovian hosts and Neptunian/smaller planet hosts separately, as shown in Figs. 3 and 4. The upper panels of all figures are the same as in Fig. 2, but this time with only three bins.

The lower panels depict the relative frequency of the stars with planets. The solid red line corresponds to a direct least squares bin fitting, while the dashed black line is a Bayesian bin-independent parametric fitting, explained in Sect. 3.3. Both fits use the functional form $f = C10^{\alpha[\mathrm{Fe/H}]}$, following previous works for FGK dwarfs (Valenti & Fischer 2005; Udry & Santos 2007; Sousa et al. 2011). The coefficients C and α of both methods and respective uncertainties are shown in Table 7. The errors in the frequency of each bin are calculated using the binomial distribution,

$$P(f_p, n, N) = \frac{N!}{n!(N-n)!} f_p^n (1-f_p)^{N-n}, \tag{1}$$

following the procedure outlined in, e.g., Burgasser et al. (2003); McCarthy & Zuckerman (2004); Endl et al. (2006), and Sozzetti et al. (2009). In short we calculate how many n detections we have in a bin of size N, as a function of the planet frequency f_p, of each bin. The upper errors, lower errors and upper limits of each bin are calculated by measuring the 68.2% of the integrated area around the peak of the binomial probability distribution function, that corresponds to the 1σ limit for a Gaussian distribution. An example is shown in Fig. 5, depicting a normalized binomial probability distribution function with $n = 2$, $N = 20$, and $f_p = 0.1$.

From Figs. 3 and 4 it can be observed that there is a small statistical difference between the frequency bins for both Jovian-hosts and Neptunian and smaller planet hosts, as the uncertainties of each bin are high. The first bin of Fig. 3 ([−0.9, 0.47] dex) has an upper limit of 13.3%, with no planet detection, while the second and third bins ([−0.47, −0.03] and [−0.03, 0.4] dex, resp.) have values of 1.9% and 5.6% respectively. Regarding Fig. 4, we observe the frequencies of 12.5, 5.4, and 2.9% for the same bins.

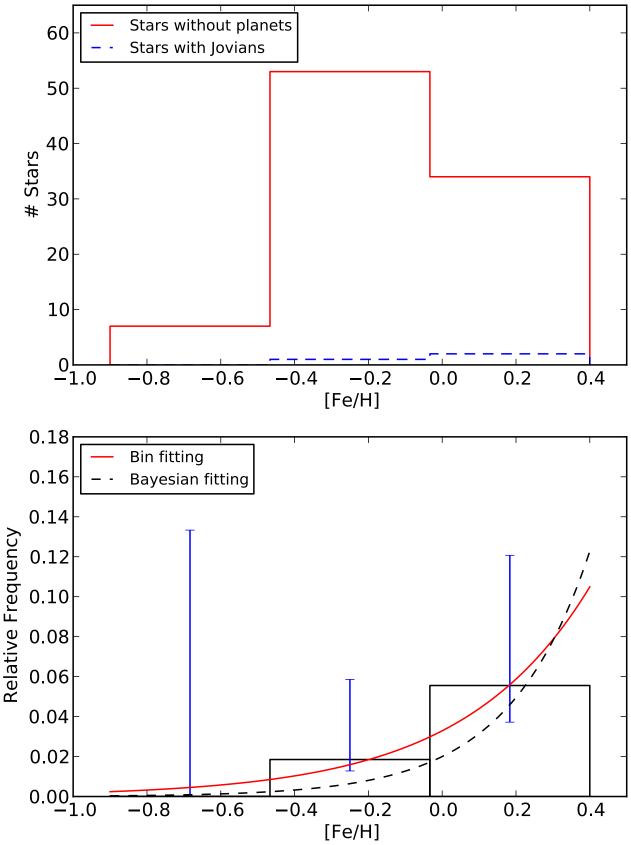

Fig. 3. *Upper panel*: histogram of metallicity with 3 bins for stars without planets (solid red) and stars with giant planets (dashed blue); *lower panel*: frequency of stars with giant planets.

We can observe a correlation with [Fe/H] for Jovian hosts and a hint of an anti-correlation for Neptunian and smaller planets only hosts. Interestingly, the later anti-correlation for smaller planet hosts is predicted by recent studies using core-accretion models (Mordasini et al. 2012), but we note that we only consider Neptunian hosts as stars with Neptunians and smaller planets only: if a multi-planet system has a Jovian and one or more smaller planets, for instance, we count the system as being a Jupiter host, not a Neptunian-host. Therefore, it is expected that the number of Neptunians and smaller planets will be higher at lower metallicities.

3.3. Bayesian approach

To test the metallicity results we performed a parametric and bin-independent fitting of the data based on Bayesian inference. We followed the Johnson et al. (2010a) approach, using two functional forms for the planet frequency, $f_{p1} = C$ and $f_{p2} = C10^{\alpha[\mathrm{Fe/H}]}$, and choosing uniformly distributed priors for the parameters C and α. The choice of a power law for the functional form was based on previous works of [Fe/H] of FGK dwarfs (Valenti & Fischer 2005; Udry & Santos 2007; Sousa et al. 2011).

Table 7 summarizes and compares the results of the Bayesian fitting to the ones obtained with the bin fitting. Column 1 shows

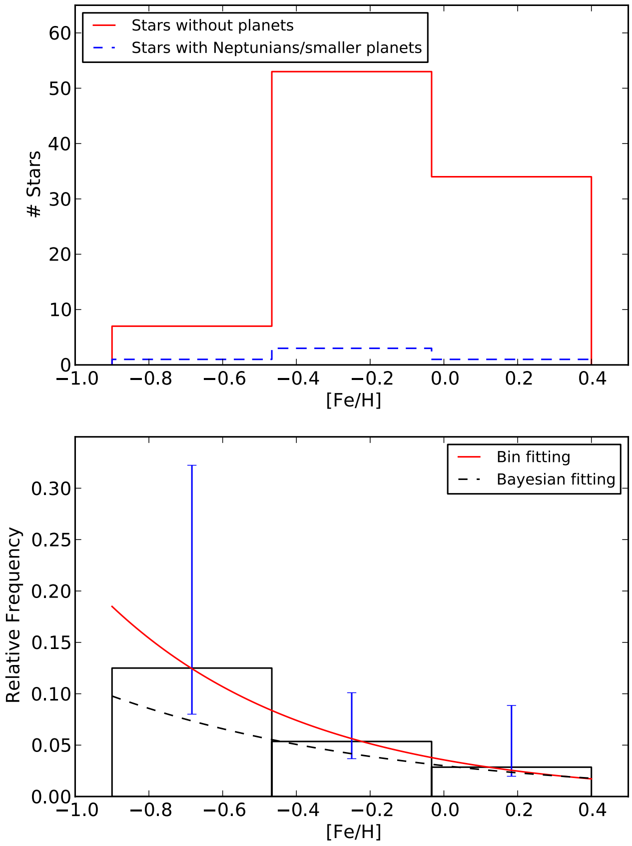

Fig. 4. *Upper panel*: histogram of metallicity with 3 bins for stars without planets (solid red) and stars with Neptunians and smaller planets only (dashed blue); *lower panel*: frequency of stars with Neptunians and smaller planets only.

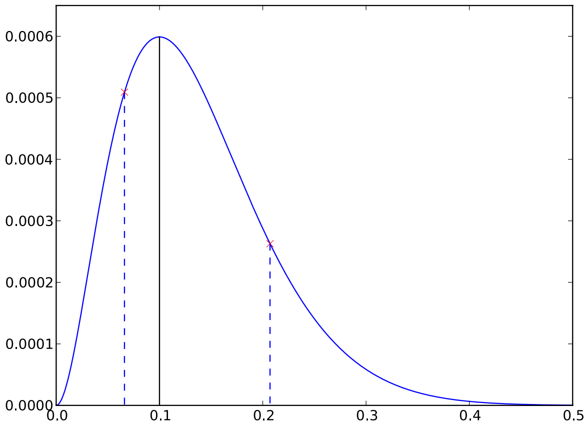

Fig. 5. Normalized binomial probability distribution function for $n = 2$, $N = 20$, and $f_{\rm p} = 0.1$.The solid vertical line depicts the observed frequency. The dashed lines show the 68.2% (1σ) limits around the maximum of the function.

the functional forms used and respective parameters, Col. 2 the uniform prior range, Col. 3 the most likely value for the fit parameters, along with the 1σ Gaussian uncertainties and Col. 4 the fit parameters of the least squares bin fitting.

From Table 7 we can see that the Bayesian fit values are, in general, compatible with the bin fitting values. However, we observe that the α values obtained for the planet-host frequencies with the Bayesian method are higher than the same values using the bin fitting. This translates into a higher giant-host frequency values with [Fe/H] and a lower Neptunian/smaller planet host frequencies as a function of metallicity. We also note that the α values calculated by the Bayesian method have large uncertainties in both scenarios. In the case of Neptunian-hosts, the α value can easily accommodate both positive or negative values.

Table 7. Parameters of the Bayesian and fit from binning models for the HARPS sample.

Parameters for Jovian hosts	Uniform prior	Most likely value	Fit from binning
$f_{\rm p1} = C$			
C	(0.01, 0.30)	0.03 ± 0.02	0.02±0.02
$f_{\rm p2} = C10^{\alpha[{\rm Fe/H}]}$			
C	(0.01, 0.30)	0.02 ± 0.02	0.03 ± 0.01
α	(−1.0, 4.0)	1.97 ± 1.25	1.26 ± 0.30
Parameters for Neptunian hosts	Uniform prior	Most likely value	Fit from binning
$f_{\rm p1} = C$			
C	(0.01, 0.30)	0.05 ± 0.02	0.07 ± 0.04
$f_{\rm p2} = C10^{\alpha[{\rm Fe/H}]}$			
C	(0.01, 0.30)	0.03 ± 0.02	0.04 ± 0.01
α	(−4.0, 1.0)	−0.57 ± 0.71	−0.79 ± 0.06

3.4. Comparison with the California Planet Survey late-K and M-type dwarf sample

Our aim here is to compare our results to a similar sample regarding the difference between planet hosts and non-planet hosts only. The California Planet Survey (CPS) late-K and M-type dwarf sample (Rauscher & Marcy 2006; Johnson et al. 2010b) was chosen for this goal. It is a 152 star sample where 18 planets (7 Jovians and 11 Neptunian/smaller planets) are already detected around 11 hosts. Most of the jovian detections come from the CPS sample while almost all detections of Neptunians and smaller planets were made with HARPS. The metallicities and stellar masses were calculated using the Johnson & Apps (2009) and the Delfosse et al. (2000) calibration, respectively. We note that the Johnson & Apps (2009) [Fe/H] calibration has a dispersion around ~0.2 dex and a systematic offset towards higher [Fe/H], as shown in Neves et al. (2012). The offset amounts to 0.13 dex when we compare the [Fe/H] of the CPS sample computed from the Johnson & Apps (2009) calibration with the Neves et al. (2012) calibration.

Table 8 depicts the CPS sample used in this paper, where Cols. 2 and 3 list the right ascension and declination respectively, Col. 4 the parallaxes and their respective uncertainties, Col. 5 the source of the parallax, Col. 6 the spectral type of the star, and Cols. 7 and 8 the V- and $K_{\rm s}$-band magnitudes respectively. Column 9 lists the stellar mass. Finally, Cols. 10 and 11 contain the calculated metallicity using the Johnson & Apps (2009) and the Neves et al. (2012) photometric calibrations respectively.

We calculated the difference of averages and medians between planet hosts and non-planet hosts in the same way as we did for our sample, as shown in Table 6. Table 9 shows the results. For metallicity, we observe a much higher difference of averages and medians when compared to our sample, but as we noted before there is an offset when calculating the metallicity with different calibrations. The difference of averages and medians for Jupiter-type planets is higher than in our sample but is compatible with our results. For Neptunian-type hosts the difference of averages and medians are indistinguishable from the non-planet host sample.

We also performed a KS test for [Fe/H] between the three planet-host subsamples and the stars without planets, taking

Table 9. Difference of averages and medians between planet host and non-planet host distributions for the CPS late-K and M-type dwarf sample.

[Fe/H]	Diff. of averages [dex]	Diff. of medians [dex]	KS test
Full sample (N_{h} = 11)	0.19	0.22	0.0272
Jovians hosts (N_{h} = 6)	0.37	0.34	0.0015
Neptunian/smaller hosts (N_{h} = 5)	–0.03	–0.05	0.9769
Stellar mass	Diff. of averages [$M_{\odot}$]	Diff. of medians [$M_{\odot}$]	
Full sample (N_{h} = 11)	–0.04	–0.01	
Jovians hosts (N_{h} = 6)	–0.03	–0.05	
Neptunian/smaller hosts (N_{h} = 5)	–0.04	0.00	

advantage of the higher number of stars with planets of the CPS sample, as shown in the forth column of Table 9. It can be seen that there is a very low probability (∼0.2%) that the Jovian hosts and the stars without planets belong to the same distribution. For the case of Neptunian-hosts, however, the KS *p*-value is high (∼98%). Again, this result is expected from previous works on FGK dwarfs (e.g. Sousa et al. 2011) and M dwarfs (e.g. Rojas-Ayala et al. 2012).

Regarding stellar mass, we do not see any trend. The difference of averages and medians between planet hosts and non-planet hosts is negligible. This result agrees with the findings of the HARPS sample as the trend we observe with stellar mass is biased.

4. Metallicity-planet relation from the HARPS+CPS joined sample

To improve our statistics and study the planet-metallicity correlation in more detail, we joined our HARPS sample with the CPS M dwarf sample. The [Fe/H] for the CPS sample was recalculated with the Neves et al. (2012) calibration, which has the same scale and accuracy of our new calibration, shown in the appendix. We kept the values of the [Fe/H] using our new spectroscopic calibration for the 49 stars in common. The joined sample has 205 stars, with 13 stars hosting 20 planets. Seven hosts have Jovian-type planets around them while six of them only have Neptunians and smaller planets.

Table 10 shows the results for the joined sample, and is similar to Table 9. We did not calculate the correlation between planet occurence and stellar mass, because as discussed in Sect. 3.1 such relation is biased. The joined sample results are similar to both our sample and the CPS sample: the difference of averages and medians between Jovian hosts and non-planet hosts show a correlation with [Fe/H], while the same quantities for Neptunians and smaller hosts do not show this trend. The tentative hint of an anti-correlation with [Fe/H] for the Neptunians/smaller hosts of the HARPS sample, in Table 6 is observed but is smaller than the one observed for the HARPS sample. However, we must note that the CPS sample is not as sensitive as the HARPS sample in the detection of Neptunian and smaller planets. Therefore we consider that in this paper the reference is the HARPS sample regarding the Neptunian-host metallicity relation.

The KS test results are similar to the ones performed for the CPS sample, in Table 9. However we must note the higher value in the case of the Jovian hosts, just above the 1% p-value.

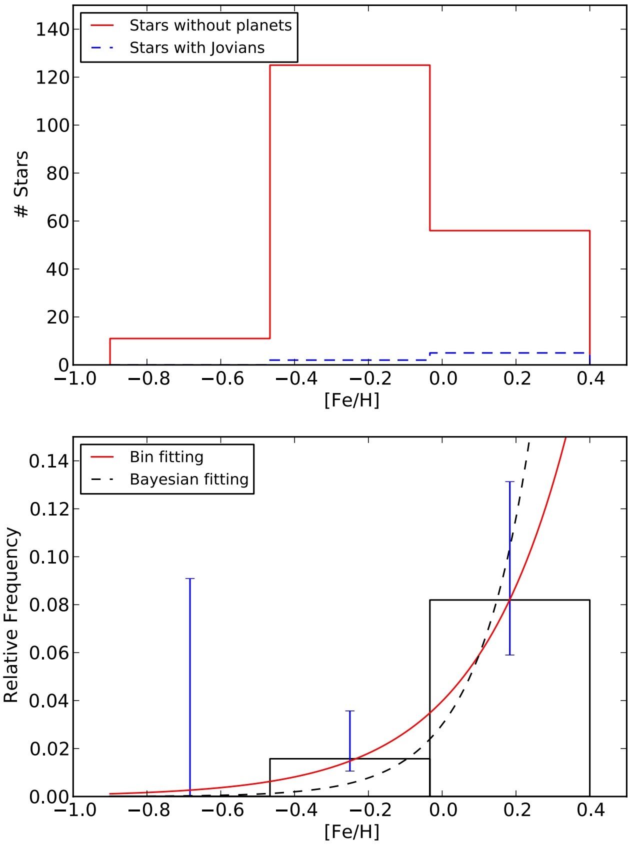

Fig. 6. *Upper panel*: histogram of metallicity of the joined sample with 3 bins for stars without planets (solid red) and stars with giant planets (dashed blue); *Lower panel*: frequency of stars with giant planets.

Table 10. Difference of averages and medians between planet host and non-planet host distributions for the joined sample.

[Fe/H]	Diff. of averages [dex]	Diff. of medians [dex]	KS test
Full sample (N_{h} = 13)	0.08	0.10	0.2985
Jovians hosts (N_{h} = 7)	0.20	0.19	0.0159
Neptunian/smaller hosts (N_{h} = 6)	–0.06	–0.08	0.6694

We now proceed to the frequency analysis of the stars with Jovians and Neptunians/smaller planets. Figures 6 and 7 show, in their upper panel, the histograms of stars with Jovian planets and stars with only Neptunians and smaller planets, respectively, depicted by a dashed blue line. The histogram of the non-host stars of the joined sample are depicted by a solid red line. The lower panels show the frequency of planets of each bin. The solid red and the dashed black lines represent the fit of the binned values and the fit given by a Bayesian model (see Sect. 3.3) respectively. The values of the coefficients for both fits are shown in Table 11 and will be discussed together in Sect. 4.1.

From both figures we can observe that the results are similar to the ones obtained with our sample (see Figs. 3 and 4), but with lower uncertainties. The correlation of Jovian-hosts and metallicity is now stronger, but the anti-correlation for Neptunians is weaker. The first bin of Fig. 6, ranging from −0.9 to −0.47 dex has an upper limit of 9.1%, with no planet detection, while the second and third bins ([−0.47, −0.03] and [−0.03, 0.4] dex, resp.) have values of 1.6% and 8.2% respectively. Regarding Fig. 7, we observe the frequencies of 8.3, 2.3, and 3.4% for the same bins.

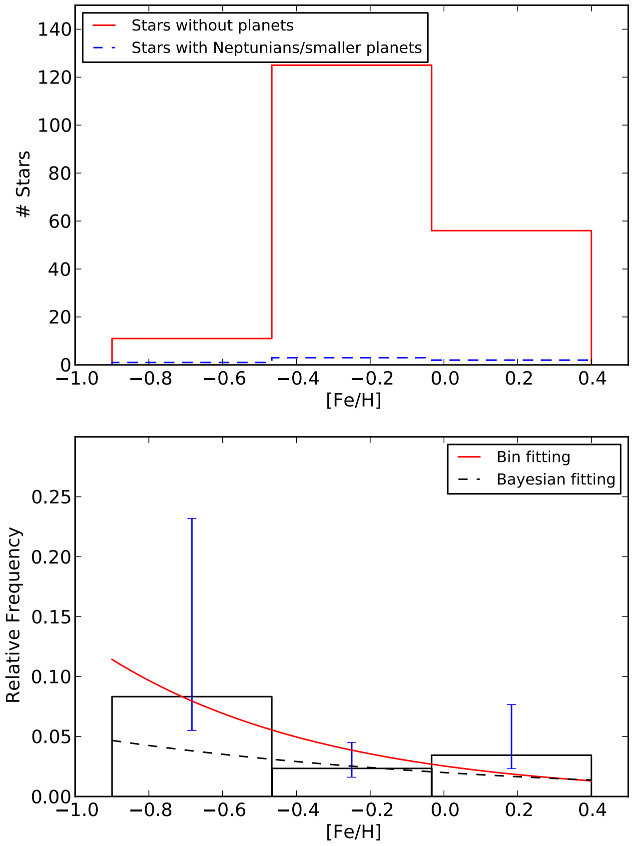

Fig. 7. *Upper panel*: histogram of metallicity of the joined sample with 3 bins for stars without planets (solid red) and stars with Neptunians and smaller planets only (dashed blue); *lower panel*: frequency of stars with Neptunians and smaller planets only.

Table 11. Parameters of the two Bayesian and fit from binning models for the HARPS+CPS sample.

Parameters for Jovian hosts	Uniform prior	Most likely value	Fit from binning
$f_{\rm p1} = C$			
C	(0.01, 0.30)	0.03 ± 0.01	0.03 ± 0.03
$f_{\rm p2} = C10^{\alpha[{\rm Fe/H}]}$			
C	(0.01, 0.30)	0.03 ± 0.02	0.04 ± 0.01
α	(−1.0, 4.0)	2.94 ± 1.03	1.72 ± 0.18
Parameters for Neptunian hosts	Uniform prior	Most likely value	Fit from binning
$f_{\rm p1} = C$			
C	(0.01, 0.30)	0.03 ± 0.01	0.04±0.03
$f_{\rm p2} = C10^{\alpha[{\rm Fe/H}]}$			
C	(0.01, 0.30)	0.02 ± 0.02	0.03 ± 0.02
α	(−4.00, 1.00)	−0.41 ± 0.77	−0.72 ± 0.46

4.1. Bayesian approach for the joined sample

Here we perform the same Bayesian inference approach as done in Sect. 3.3 but this time for the joined sample. Table 11 summarizes and compares the results of the Bayesian fitting to the ones obtained with the bin fitting. The columns are the same as in Table 7.

From Table 11 we can see that both the direct bin fitting and the Bayesian fitting values are compatible with the ones obtained with the HARPS sample. As we have seen in Sect. 3.3, the α values are higher than the same values using the bin fitting, translating into a higher giant-host frequency and a lower Neptunian/smaller planet host frequency. Again, the α values calculated by the Bayesian method have large uncertainties, and the α value, for the Neptunian and smaller planet hosts case, may easily have positive or negative values.

We can now compare the values for giant planets obtained with both fitting methods to previous works. Valenti & Fischer (2005), Udry & Santos (2007), and Sousa et al. (2011) all use a similar power law to the one used in this work for the frequency of giants around FGK dwarfs and obtained α values of 2.0, 2.04, and 2.58 respectively through direct bin fitting. Our α results from the bin fitting (1.26 ± 0.30 from the HARPS sample and 1.72 ± 0.18 from the joined sample) are lower than those works, which might suggest a less efficient planet-formation process around M dwarfs. However, the α values obtained from the Bayesian fit for the HARPS sample are very similar to the ones obtained for FGK dwarfs: 1.97 ± 1.25, despite the high uncertainty. Regarding the combined sample we obtain a higher value of 2.94 ± 1.03 from the Bayesian fitting, suggesting a more efficient process of planet-formation around M dwarfs. Therefore, our quantification of the α parameter for giant planets around M dwarfs, taking into account the large uncertainties involved, are compatible with the values found in FGK studies.

In order to check if the more complex power law functional form is preferred over the constant one, we used a method of Bayesian model comparison, following Kass & Raftery (1995). First, we calculate for both functional forms the total probability of the model conditioned on the data (the evidence) by integrating over the full parameter space. Computationally, in the case of uniformly distributed priors, we can calculate the evidence as

$$P(d|f) = \frac{\sum P(d|X)}{length(X)}, \tag{2}$$

where the $P(d|X)$ is the likelihood, or the probability of observing the data d given the parameters X, and $length(X)$ is the length of the full parameter space. Then, we calculate the Bayes factor that is just the ratio of the evidence of both functional forms,

$$B_f = \frac{P(d|f_{\rm p2})}{P(d|f_{\rm p1})}. \tag{3}$$

According to Kass & Raftery (1995) a B_f value over 20 gives a *strong* evidence that the model $f_{\rm p2}$ is better at fitting the data than the $f_{\rm p1}$ model.

For the Jovian hosts case, we obtained a Bayes factor of 2.07 and 66.04 for the HARPS and the joined sample respectively. This means that, in the case of the HARPS sample, the more complex model cannot explain much better the data than the constant model. On the other hand, the combined sample achieves a high Bayes factor, meaning that there is a strong evidence that the more complex model does a better fit than the constant model, supporting the planet-metallicity correlation for giant planets.

Regarding the Neptunian hosts, we obtain values lower than the unity, which means that the constant model explain the data better than the more complex power model. Therefore, it is impossible at this moment to confirm the hypothetical anti-correlation observed for low [Fe/H] values. Despite this, we must note that our HARPS sample is much more sensitive in probing the Neptunian/super-Earth mass regime than the CPS sample. Therefore the frequency parametrization of the HARPS sample for the Neptunian/super-Earth mass range, and shown in detail in Sect. 3.2, is preferred over the joined one.

5. Discussion

In this paper we investigate the metallicity and stellar mass correlations with planets. We use a new method, described in the Appendix, to refine the precision of the metallicities of the HARPS GTO M dwarf sample calculated with the calibration of Neves et al. (2012). We use the established calibration of Delfosse et al. (2000) to calculate the stellar masses of our sample.

We confirm the trend of metallicity with the presence of giant planets in our sample, as shown by previous studies on FGK dwarfs (e.g. Gonzalez 1997; Santos et al. 2004; Sousa et al. 2011; Mayor et al. 2011) and M dwarfs (Bonfils et al. 2007; Johnson & Apps 2009; Schlaufman & Laughlin 2010; Rojas-Ayala et al. 2012; Terrien et al. 2012). For Neptunian and smaller planet hosts there is a hint that an anti-correlation may exist but our current statistic supports a flat relation, in concordance with previous results for FGK dwarfs (e.g. Sousa et al. 2008; Bouchy et al. 2009; Sousa et al. 2011) and M dwarfs (Rojas-Ayala et al. 2012). We calculate the difference of the averages and medians between planet and non-planet hosts, and most importantly the frequencies in three different bins, as well as a parametrization to both Jovian and Neptunian hosts.

We combined the HARPS sample with the California Planet Survey (CPS) late-K and M-type dwarf sample to improve our statistics, increasing the number of stars from 102 to 205 and the number of planet hosts from 8 to 13 (7 Jovian-hosts and 6 Neptunian/smaller planet hosts). The [Fe/H] of the CPS sample was calculated using the photometric calibration of Neves et al. (2012). The previous trend for Jovian-hosts is confirmed and reinforced, but the existence of an anti-correlation of Neptunian-hosts with [Fe/H] is inconclusive. The CPS sample is not as sensitive as the HARPS sample regarding the detection of Neptunian and smaller planets. Therefore the HARPS sample is the reference in this work regarding the Neptunian-host-metallicity relation.

Quantitatively, the difference of the averages and the medians between stars with and without planets for Jupiter-type hosts is 0.20 and 0.26 dex for the HARPS sample and 0.20 and 0.19 dex for the joined sample. Regarding the Neptunian and smaller planet hosts, the observed difference of the averages and the medians is −0.10 dex for the HARPS sample.

Regarding the frequency of giant hosts, we have no detection in the [−0.9, −0.47] dex bin for both HARPS and the joined sample. For the [−0.47, −0.03] bin we obtained a frequency of 1.9% and 1.6%, and between −0.03 and 0.4 we have a frequency of 5.6% and 8.2% for the HARPS and the joined sample respectively. Regarding Neptunian hosts, we obtained, for the same samples and bins, the values of 12.5%, and 8.3% for the first bin, 5.4% and 2.3% for the second bin and 2.9% and 3.4% for the last [Fe/H] bin. As noted, the frequencies obtained using the joined sample for the Neptunian-hosts are not as precise as in the HARPS sample due to a lower sensitivity of the CPS sample to Neptunian and smaller planets.

The parametrization of the planet-metallicity relation was based on bin fit and Bayesian fit models, following a functional form of the type $f_\mathrm{p} = C10^{\alpha[\mathrm{Fe/H}]}$ used in previous works for FGK dwarfs (Valenti & Fischer 2005; Udry & Santos 2007; Sousa et al. 2011). The results for the parameters C and α using the functional forms calculated by direct bin fitting or by using the Bayesian fitting are compatible with each other. However, we note a high uncertainty on the determination of the α parameter using the Bayesian fitting. Therefore the results for this parameter for giant planets vary a lot, between 1.26 ± 0.30 and 1.97 ± 1.25, using the bin fitting or the Bayesian fitting respectively, for the HARPS sample, and between 1.72 ± 0.18 to 2.94 ± 1.03 for the combined sample. At the actual statistical level, the α parameter we determine is compatible with the value found for FGK dwarfs in previous studies (Fischer & Valenti 2005; Udry & Santos 2007; Sousa et al. 2011). Regarding Neptunian-hosts, we obtain an α value, for the HARPS sample, between −0.79 ± 0.06 and −0.57 ± 0.71, using the bin fit or the bayes fit model respectively. This result configures an anti-correlation for Neptunian hosts with [Fe/H], but with an insufficient statistical confidence level.

We therefore conclude that the power law functional form works best for giant hosts, and that a constant functional form is preferred, for now, for Neptunian/smaller planet hosts. We also reject the possibility of a correlation for Neptunian-hosts of the same order of magnitude of that for Jupiter-hosts. In fact we suspect that an anti-correlation might exist but we lack the statistics to confirm it.

Regarding stellar mass, we detect a positive trend in planet detections towards higher masses. However, when we take the detection limits into account, we do not find any significant difference. Therefore, the trend of the frequency of planets with the stellar mass is due to a detection bias in our sample, stressing the importance of taking into account the planet detection biases in stellar mass studies.

Acknowledgements. We would like to thank Annelies Mortier for useful discussions. We would also like to thank John Asher Johnson and Kevin Apps for kindly providing the CPS M dwarf sample. We acknowledge the support by the European Research Council/European Community under the FP7 through Starting Grant agreement number 239953. The financial support from the "Programme National de Planétologie" (PNP) of CNRS/INSU, France, is gratefully acknowledged. N.C.S. and V.N. also acknowledges the support from Fundação para a Ciência e a Tecnologia (FCT) through program Ciência 2007 funded by FCT/MCTES (Portugal) and POPH/FSE (EC), and in the form of grant reference PTDC/CTE-AST/098528/2008. V.N. would also like to acknowledge the support from the FCT in the form of the fellowship SFRH/BD/60688/2009. This research has made use of the SIMBAD database, operated at CDS, Strasbourg, France, and of the Extrasolar Planet Encyclopaedia at `exoplanet.eu`. This publication makes use of data products from the Two Micron All Sky Survey, which is a joint project of the University of Massachusetts and the Infrared Processing and Analysis Center/California Institute of Technology, funded by the National Aeronautics and Space Administration and the National Science Foundation.

References

Alibert, Y., Mordasini, C., & Benz, W. 2011, A&A, 526, A63
Anglada-Escudé, G., Boss, A. P., Weinberger, A. J., et al. 2012, ApJ, 746, 37
Baranne, A., Queloz, D., Mayor, M., et al. 1996, A&AS, 119, 373
Benedict, G. F., McArthur, B., Chappell, D. W., et al. 1999, AJ, 118, 1086
Benedict, G. F., McArthur, B. E., Forveille, T., et al. 2002, ApJ, 581, L115
Bonfils, X., Mayor, M., Delfosse, X., et al. 2007, A&A, 474, 293
Bonfils, X., Delfosse, X., Udry, S., et al. 2013, A&A, 549, A109
Boss, A. P. 1997, Science, 276, 1836
Boss, A. P. 2002, ApJ, 567, L149
Boss, A. P. 2006, ApJ, 643, 501
Bouchy, F., Mayor, M., Lovis, C., et al. 2009, A&A, 496, 527
Buchhave, L. A., Latham, D. W., Johansen, A., et al. 2012, Nature, 486, 375
Burgasser, A. J., Kirkpatrick, J. D., Reid, I. N., et al. 2003, ApJ, 586, 512
Casagrande, L., Flynn, C., & Bessell, M. 2008, MNRAS, 389, 585
Correia, A. C. M., Couetdic, J., Laskar, J., et al. 2010, A&A, 511, A21
Delfosse, X., Forveille, T., Ségransan, D., et al. 2000, A&A, 364, 217
Endl, M., Cochran, W. D., Kürster, M., et al. 2006, ApJ, 649, 436
Fabricius, C., & Makarov, V. V. 2000, AAPS, 144, 45
Fischer, D. A., & Valenti, J. 2005, ApJ, 622, 1102
Fischer, D. A., Laughlin, G., Butler, P., et al. 2005, ApJ, 620, 481
Gatewood, G. 2008, AJ, 136, 452
Gatewood, G., Kiewiet de Jonge, J., & Persinger, T. 1998, AJ, 116, 1501
Ghezzi, L., Cunha, K., Smith, V. V., et al. 2010, ApJ, 720, 1290
Gonzalez, G. 1997, MNRAS, 285, 403

Hawley, S. L., Gizis, J. E., & Reid, N. I. 1997, AJ, 113, 1458
Henry, T. J., Jao, W.-C., Subasavage, J. P., et al. 2006, AJ, 132, 2360
Ida, S., & Lin, D. N. C. 2004, ApJ, 616, 567
Ida, S., & Lin, D. N. C. 2005, ApJ, 626, 1045
Jahreiß, H., & Wielen, R. 1997, in H – Venice ’97, eds. R. M. Bonnet, E. Høg, P. L. Bernacca, et al., ESA SP, 402, 675
Jao, W.-C., Henry, T. J., Subasavage, J. P., et al. 2005, AJ, 129, 1954
Johnson, J. A., & Apps, K. 2009, ApJ, 699, 933
Johnson, J. A., Butler, R. P., Marcy, G. W., et al. 2007, ApJ, 670, 833
Johnson, J. A., Aller, K. M., Howard, A. W., & Crepp, J. R. 2010a, PASP, 122, 905
Johnson, J. A., Howard, A. W., Marcy, G. W., et al. 2010b, PASP, 122, 149
Kalas, P., Liu, M. C., & Matthews, B. C. 2004, Science, 303, 1990
Kass, R. E., & Raftery, A. E. 1995, J. Am. Statist. Association, 90, 773
Kennedy, G. M., & Kenyon, S. J. 2008, ApJ, 673, 502
Kornet, K., Wolf, S., & Różyczka, M. 2006, A&A, 458, 661
Laws, C., Gonzalez, G., Walker, K. M., et al. 2003, AJ, 125, 2664
Lovis, C., & Mayor, M. 2007, A&A, 472, 657
Mayor, M., Pepe, F., Queloz, D., et al. 2003, The Messenger, 114, 20
Mayor, M., Marmier, M., Lovis, C., et al. 2011, A&A, submitted [arXiv:1109.2497]
McCarthy, C., & Zuckerman, B. 2004, AJ, 127, 2871
Melo, C., Santos, N. C., Gieren, W., et al. 2007, A&A, 467, 721
Mordasini, C., Alibert, Y., & Benz, W. 2009, A&A, 501, 1139
Mordasini, C., Alibert, Y., Benz, W., Klahr, H., & Henning, T. 2012, A&A, 541, A97
Murray, N., Paskowitz, M., & Holman, M. 2002, ApJ, 565, 608
Neves, V., Bonfils, X., Santos, N. C., et al. 2012, A&A, 538, A25
Pepe, F., Mayor, M., Queloz, D., et al. 2004, A&A, 423, 385
Pollack, J., Hubickyj, O., Bodenheimer, P., et al. 1996, Icarus, 124, 62
Rauscher, E., & Marcy, G. W. 2006, PASP, 118, 617
Reid, I. N., Hawley, S. L., & Gizis, J. E. 1995, AJ, 110, 1838
Rivera, E. J., Laughlin, G., Butler, R. P., et al. 2010, ApJ, 719, 890
Rojas-Ayala, B., Covey, K. R., Muirhead, P. S., & Lloyd, J. P. 2010, ApJ, 720, L113
Rojas-Ayala, B., Covey, K. R., Muirhead, P. S., & Lloyd, J. P. 2012, ApJ, 748, 93
Santos, N. C., Israelian, G., & Mayor, M. 2004, A&A, 415, 1153
Schlaufman, K. C., & Laughlin, G. 2010, A&A, 519, A105
Skrutskie, M. F., Cutri, R. M., Stiening, R., et al. 2006, AJ, 131, 1163
Söderhjelm, S. 1999, A&A, 341, 121
Sousa, S. G., Santos, N. C., Mayor, M., et al. 2008, A&A, 487, 373
Sousa, S. G., Santos, N. C., Israelian, G., Mayor, M., & Udry, S. 2011, A&A, 533, A141
Sozzetti, A., Torres, G., Latham, D. W., et al. 2009, ApJ, 697, 544
Terrien, R. C., Mahadevan, S., Bender, C. F., et al. 2012, ApJ, 747, L38
Thommes, E. W., Matsumura, S., & Rasio, F. A. 2008, Science, 321, 814
Udry, S., & Santos, N. 2007, ARA&A, 45, 397
Valenti, J. A., & Fischer, D. A. 2005, ApJS, 159, 141
van Altena, W. F., Lee, J. T., & Hoffleit, E. D. 1995, The general catalogue of trigonometric [stellar] parallaxes, eds. W. F. van Altena, J. T. Lee, & E. D. Hoffleit
van Leeuwen, F. 2007, A&A, 474, 653
Vorobyov, E. I., & Basu, S. 2008, ApJ, 676, L139

Pages 11 to 17 are available in the electronic edition of the journal at http://www.aanda.org

Table 2. HARPS M dwarf sample, sorted by right ascension.

Star	α (2000)	δ (2000)	π [mas]	π src	Stype	V [mag]	K_S [mag]	$M_\star$ [$M_\odot$]	[Fe/H] [dex]
Gl1	00:05:25	–37:21:23	230.4 ± 0.9	H	M3V	8.6	4.501 ± 0.030	0.39 ± 0.03	–0.45
GJ1002	00:06:44	–07:32:23	213.0 ± 3.6	H	M5.5V	13.8	7.439 ± 0.021	0.11 ± 0.01	–0.19
Gl12	00:15:49	+13:33:17	88.8 ± 3.5	H	M3	12.6	7.807 ± 0.020	0.22 ± 0.02	–0.34
LHS1134	00:43:26	–41:17:36	101.0 ± 16.0	R	M3	13.1	7.710 ± 0.016	0.20 ± 0.01	–0.10
Gl54.1	01:12:31	–17:00:00	271.0 ± 8.4	H	M4.5V	12.0	6.420 ± 0.017	0.13 ± 0.01	–0.40
L707-74	01:23:18	–12:56:23	97.8 ± 13.5	Y	M	13.0	8.350 ± 0.021	0.15 ± 0.02	–0.35
Gl87	02:12:21	+03:34:30	96.0 ± 1.7	H	M1.5	10.1	6.077 ± 0.020	0.45 ± 0.03	-0.31
Gl105B	02:36:16	+06:52:12	139.3 ± 0.5	H	M3.5V	11.7	6.574 ± 0.020	0.25 ± 0.02	–0.02
CD-44-836A	02:45:11	–43:44:30	113.9 ± 38.7	C	M4	12.3	7.270 ± 0.024	0.22 ± 0.02	–0.08
LHS1481	02:58:10	–12:53:06	95.5 ± 10.9	H	M2.5	12.7	8.199 ± 0.026	0.17 ± 0.02	–0.72
LP771-95A	03:01:51	–16:35:36	146.4 ± 2.9	H06	M3	11.5	6.285 ± 0.020	0.24 ± 0.02	–0.34
LHS1513	03:11:36	–38:47:17	130.0 ± 20.0	R	M3.5	11.5	9.016 ± 0.022	0.09 ± 0.02	–0.11
GJ1057	03:13:23	+04:46:30	117.1 ± 3.5	H	M5	13.9	7.833 ± 0.024	0.16 ± 0.01	0.10
Gl145	03:32:56	–44:42:06	93.1 ± 1.9	H	M2.5	11.5	6.907 ± 0.016	0.32 ± 0.02	–0.28
GJ1061	03:36:00	–44:30:48	271.9 ± 1.3	H	M5.5V	13.1	6.610 ± 0.021	0.12 ± 0.01	–0.08
GJ1065	03:50:44	–06:05:42	105.4 ± 3.2	H	M4V	12.8	7.751 ± 0.020	0.19 ± 0.02	–0.22
GJ1068	04:10:28	–53:36:06	143.4 ± 1.9	H	M4.5	13.6	7.900 ± 0.021	0.13 ± 0.01	–0.30
Gl166C	04:15:22	–07:39:23	200.6 ± 0.2	H	M4.5V	11.2	5.962 ± 0.026	0.23 ± 0.02	0.08
Gl176	04:42:56	+18:57:29	106.2 ± 2.5	H	M2.5	10.0	4.310 ± 0.034	0.50 ± 0.03	–0.01
LHS1723	05:01:57	–06:56:47	187.9 ± 1.3	H	M3.5V	12.2	6.736 ± 0.024	0.17 ± 0.01	–0.25
LHS1731	05:03:20	–17:22:23	108.6 ± 2.7	H	M3.0V	11.7	6.936 ± 0.021	0.27 ± 0.02	–0.26
Gl191	05:11:40	–45:01:06	255.3 ± 0.9	H	M1 pV	8.8	5.049 ± 0.021	0.27 ± 0.03	–0.88
Gl203	05:28:00	+09:38:36	113.5 ± 5.0	H	M3.5V	12.4	7.542 ± 0.017	0.19 ± 0.02	–0.25
Gl205	05:31:27	–03:40:42	176.8 ± 1.2	H	M1.5V	8.0	4.039 ± 0.260	0.60 ± 0.07	0.22
Gl213	05:42:09	+12:29:23	171.6 ± 4.0	H	M4V	11.5	6.389 ± 0.016	0.22 ± 0.02	–0.11
Gl229	06:10:34	–21:51:53	173.8 ± 1.0	H	M1V	8.2	4.166 ± 0.232	0.58 ± 0.06	–0.01
HIP31293	06:33:43	–75:37:47	110.9 ± 2.2	H	M3V	10.5	5.862 ± 0.024	0.43 ± 0.03	–0.04
HIP31292	06:33:47	–75:37:30	114.5 ± 3.2	H	M3/4V	11.4	6.558 ± 0.021	0.31 ± 0.02	–0.10
G108-21	06:42:11	+03:34:53	103.1 ± 8.5	H	M3.5	12.1	7.334 ± 0.031	0.23 ± 0.02	–0.01
Gl250B	06:52:18	–05:11:24	114.8 ± 0.4	H	M2.5V	10.1	5.723 ± 0.036	0.45 ± 0.03	–0.10
Gl273	07:27:24	+05:13:30	263.0 ± 1.4	H	M3.5V	9.8	4.857 ± 0.023	0.29 ± 0.02	–0.01
LHS1935	07:38:41	–21:13:30	94.3 ± 3.3	H	M3	11.7	7.063 ± 0.023	0.29 ± 0.02	–0.24
Gl285	07:44:40	+03:33:06	167.9 ± 2.3	H	M4V	11.2	5.698 ± 0.017	0.31 ± 0.02	0.18
Gl299	08:11:57	+08:46:23	146.3 ± 3.1	H	M4V	12.8	7.660 ± 0.026	0.14 ± 0.01	–0.50
Gl300	08:12:41	–21:33:12	125.8 ± 1.0	H	M3.5V	12.1	6.705 ± 0.027	0.26 ± 0.02	0.14
GJ2066	08:16:08	+01:18:11	109.6 ± 1.5	H	M2	10.1	5.766 ± 0.024	0.46 ± 0.03	–0.18
GJ1123	09:17:05	–77:49:17	110.9 ± 2.0	H	M4.5V	13.1	7.448 ± 0.021	0.21 ± 0.01	0.20
Gl341	09:21:38	–60:16:53	95.6 ± 0.9	H	M0V	9.5	5.587 ± 0.021	0.55 ± 0.03	–0.13
GJ1125	09:30:44	+00:19:18	103.5 ± 3.9	H	M3.0V	11.7	6.871 ± 0.024	0.29 ± 0.02	–0.30
Gl357	09:36:02	–21:39:42	110.8 ± 1.9	H	M3V	10.9	6.475 ± 0.017	0.33 ± 0.03	–0.34
Gl358	09:39:47	–41:04:00	105.6 ± 1.6	H	M3.0V	10.8	6.056 ± 0.023	0.42 ± 0.03	–0.01
Gl367	09:44:30	–45:46:36	101.3 ± 3.2	H	M1	10.1	5.780 ± 0.020	0.49 ± 0.03	–0.07
GJ1129	09:44:48	–18:12:48	90.9 ± 3.8	H	M3.5V	12.5	7.257 ± 0.020	0.28 ± 0.02	0.07
Gl382	10:12:17	–03:44:47	127.1 ± 1.9	H	M2V	9.3	5.015 ± 0.020	0.54 ± 0.03	0.04
Gl388	10:19:36	+19:52:12	204.6 ± 2.8	H	M4.5	9.4	4.593 ± 0.017	0.42 ± 0.03	0.07
Gl393	10:28:55	+00:50:23	141.5 ± 2.2	H	M2V	9.7	5.311 ± 0.023	0.44 ± 0.03	–0.22
LHS288	10:44:32	–61:11:35	209.7 ± 2.7	H	M5.5	13.9	7.728 ± 0.027	0.10 ± 0.01	–0.60
Gl402	10:50:52	+06:48:30	147.9 ± 3.5	H	M4V	11.7	6.371 ± 0.016	0.26 ± 0.02	0.06
Gl406	10:56:29	+07:00:54	419.1 ± 2.1	H	M6V	13.4	6.084 ± 0.017	0.10 ± 0.00	0.18
Gl413.1	11:09:31	–24:36:00	93.0 ± 1.7	H	M2	10.4	6.097 ± 0.023	0.46 ± 0.03	–0.12
Gl433	11:35:27	–32:32:23	112.6 ± 1.4	H	M2.0V	9.8	5.623 ± 0.021	0.47 ± 0.03	–0.17
Gl438	11:43:20	–51:50:23	119.0 ± 10.2	R	M0	10.4	6.320 ± 0.021	0.33 ± 0.03	–0.39
Gl447	11:47:44	+00:48:16	299.6 ± 2.2	H	M4	11.1	5.654 ± 0.024	0.17 ± 0.01	–0.18
Gl465	12:24:53	–18:14:30	113.0 ± 2.5	H	M3V	11.3	6.950 ± 0.021	0.26 ± 0.02	–0.66
Gl479	12:37:53	–52:00:06	103.2 ± 2.3	H	M3V	10.7	6.020 ± 0.021	0.43 ± 0.03	0.02
LHS337	12:38:50	–38:22:53	156.8 ± 2.0	H	M4.5V	12.7	7.386 ± 0.021	0.15 ± 0.01	–0.25
Gl480.1	12:40:46	–43:34:00	128.5 ± 3.9	H	M3.0V	12.2	7.413 ± 0.021	0.18 ± 0.02	–0.48
Gl486	12:47:57	+09:45:12	119.5 ± 2.7	H	M3.5	11.4	6.362 ± 0.018	0.32 ± 0.02	0.06
Gl514	13:30:00	+10:22:36	130.6 ± 1.1	H	M1V	9.1	5.036 ± 0.027	0.53 ± 0.03	–0.16
Gl526	13:45:44	+14:53:30	185.5 ± 1.1	H	M1.5V	8.5	4.415 ± 0.017	0.50 ± 0.03	–0.20
Gl536	14:01:03	–02:39:18	98.3 ± 1.6	H	M1	9.7	5.683 ± 0.020	0.52 ± 0.03	–0.12

Notes. π src: (H) revised H catalog (van Leeuwen 2007); (R95) (Reid et al. 1995); (Y) (van Altena et al. 1995); (H06) (Henry et al. 2006); (C) CNS4 catalog (Jahreiss, priv. comm.) (†) Gl803 is a young (~20 Myr) M dwarf with a circumstellar disk (Kalas et al. 2004). The equation to determine its mass may not be adequate for this age.

Table 2. continued.

Star	α (2000)	δ (2000)	π [mas]	π src	Stype	V [mag]	K_S [mag]	$M_\star$ [$M_\odot$]	[Fe/H] [dex]
Gl551	14:29:43	–62:40:47	771.6 ± 2.6	H	M5.5	11.1	4.310 ± 0.030	0.12 ± 0.01	–0.00
Gl555	14:34:17	–12:31:06	165.0 ± 3.3	H	M3.5V	11.3	5.939 ± 0.034	0.28 ± 0.02	0.17
Gl569A	14:54:29	+16:06:04	101.9 ± 1.7	H	M2.5	10.2	5.770 ± 0.018	0.49 ± 0.03	–0.08
Gl581	15:19:26	–07:43:17	160.9 ± 2.6	H	M2.5V	10.6	5.837 ± 0.023	0.30 ± 0.02	–0.21
Gl588	15:32:13	–41:16:36	168.7 ± 1.3	H	M2.5V	9.3	4.759 ± 0.024	0.47 ± 0.03	0.07
Gl618A	16:20:04	–37:31:41	119.8 ± 2.5	H	M3V	10.6	5.950 ± 0.021	0.39 ± 0.03	–0.08
Gl628	16:30:18	–12:39:47	233.0 ± 1.6	H	M3V	10.1	5.075 ± 0.024	0.30 ± 0.02	–0.02
Gl643	16:55:25	–08:19:23	148.9 ± 4.0	H	M3.5V	11.8	6.724 ± 0.017	0.21 ± 0.02	–0.28
Gl667C	17:18:58	–34:59:42	146.3 ± 9.0	H	M2V	10.2	6.036 ± 0.020	0.30 ± 0.03	–0.53
Gl674	17:28:40	–46:53:42	220.2 ± 1.4	H	M3V	9.4	4.855 ± 0.018	0.35 ± 0.03	–0.25
Gl678.1A	17:30:22	+05:32:53	100.2 ± 1.1	H	M1V	9.3	5.422 ± 0.029	0.57 ± 0.03	–0.11
Gl680	17:35:13	–48:40:53	102.8 ± 2.8	H	M1.5	10.2	5.829 ± 0.021	0.47 ± 0.03	–0.22
Gl682	17:37:03	–44:19:11	196.9 ± 2.1	H	M4.5V	11.0	5.606 ± 0.020	0.27 ± 0.02	0.11
Gl686	17:37:53	+18:35:30	123.0 ± 1.6	H	M1	9.6	5.572 ± 0.020	0.45 ± 0.03	–0.37
Gl693	17:46:35	–57:19:11	171.5 ± 2.3	H	M3.5V	10.8	6.016 ± 0.017	0.26 ± 0.02	–0.30
Gl699	17:57:49	+04:41:36	549.0 ± 1.6	H	M4V	9.6	4.524 ± 0.020	0.16 ± 0.01	–0.52
Gl701	18:05:07	–03:01:53	128.9 ± 1.4	H	M0V	9.4	5.306 ± 0.021	0.48 ± 0.03	–0.27
GJ1224	18:07:33	–15:57:47	132.6 ± 3.7	H	M4.5V	13.6	7.827 ± 0.027	0.14 ± 0.01	–0.10
G141-29	18:42:44	+13:54:17	93.3 ± 11.5	H	M4	12.8	7.551 ± 0.021	0.23 ± 0.02	0.09
Gl729	18:49:49	–23:50:12	336.7 ± 2.0	H	M3.5V	10.5	5.370 ± 0.016	0.17 ± 0.01	–0.10
GJ1232	19:09:51	+17:40:07	93.6 ± 2.8	H	M4.5	13.6	7.902 ± 0.020	0.20 ± 0.01	0.14
Gl752A	19:16:55	+05:10:05	170.4 ± 1.0	H	M3V	9.1	4.673 ± 0.020	0.48 ± 0.03	0.06
Gl754	19:20:48	–45:33:30	169.2 ± 1.6	H	M4.5	12.2	6.845 ± 0.026	0.18 ± 0.01	–0.17
GJ1236	19:22:03	+07:02:36	92.9 ± 2.5	H	M3	12.4	7.688 ± 0.020	0.22 ± 0.02	–0.42
GJ1256	20:40:34	+15:29:57	102.0 ± 2.2	H	M4.5	13.4	7.749 ± 0.031	0.19 ± 0.01	0.10
Gl803[†]	20:45:10	–31:20:30	100.9 ± 1.1	H	M0V e	8.8	4.529 ± 0.020	0.75 ± 0.03	0.32
LHS3583	20:46:37	–81:43:12	77.1 ± 21.2	C	M2.5	11.5	6.826 ± 0.034	0.40 ± 0.03	–0.18
LP816-60	20:52:33	–16:58:30	175.0 ± 3.4	H	M	11.4	6.199 ± 0.021	0.23 ± 0.02	–0.06
Gl832	21:33:34	–49:00:36	201.9 ± 1.0	H	M1V	8.7	4.473 ± 0.050	0.45 ± 0.03	–0.19
Gl846	22:02:10	+01:24:00	97.6 ± 1.5	H	M0.5V	9.2	5.322 ± 0.023	0.60 ± 0.03	0.06
LHS3746	22:02:29	–37:04:54	134.3 ± 1.3	H	M3.5	11.8	6.718 ± 0.020	0.24 ± 0.02	–0.15
Gl849	22:09:40	–04:38:30	109.9 ± 2.1	H	M3V	10.4	5.594 ± 0.017	0.49 ± 0.03	0.24
GJ1265	22:13:42	–17:41:12	96.0 ± 3.9	H	M4.5	13.6	8.115 ± 0.018	0.17 ± 0.01	–0.09
LHS3799	22:23:07	–17:36:23	134.4 ± 4.9	H	M4.5V	13.3	7.319 ± 0.018	0.18 ± 0.01	0.18
Gl876	22:53:17	–14:15:48	213.3 ± 2.1	H	M3.5V	10.2	5.010 ± 0.021	0.34 ± 0.02	0.15
Gl877	22:55:46	–75:27:36	116.1 ± 1.2	H	M2.5	10.4	5.811 ± 0.021	0.43 ± 0.03	–0.01
Gl880	22:56:35	+16:33:12	146.1 ± 1.0	H	M1.5V	8.7	4.523 ± 0.016	0.58 ± 0.03	0.07
Gl887	23:05:52	–35:51:12	303.9 ± 0.9	H	M2V	7.3	3.465 ± 0.200	0.47 ± 0.05	–0.24
LHS543	23:21:37	+17:17:25	91.0 ± 2.9	H	M4	11.7	6.507 ± 0.016	0.40 ± 0.02	0.25
Gl908	23:49:13	+02:24:06	167.3 ± 1.2	H	M1V	9.0	5.043 ± 0.020	0.42 ± 0.03	–0.44
LTT9759	23:53:50	–75:37:53	100.1 ± 1.1	H	M	10.0	5.549 ± 0.027	0.54 ± 0.03	0.21

Table 8. California Planet Survey (CPS) sample, sorted by right ascension.

Star	α (2000)	δ (2000)	π [mas]	$\pi_{\rm src}$	Stype	V [mag]	$K_{\rm S}$ [mag]	$M_\star$ [$M_\odot$]	[Fe/H]$_{JA09}$ [dex]	[Fe/H]$_{N12}$ [dex]
GJ2	00:05:10	45:47:11	88.9 ± 1.4	H	M1	9.9	5.853 ± 0.018	0.53 ± 0.03	0.06	–0.09
GJ1	00:05:24	–37:21:26	230.4 ± 0.9	H	M1.5	8.6	4.523 ± 0.017	0.39 ± 0.03	–0.39	–0.40
GJ4 A	00:05:41	45:48:43	88.4 ± 1.6	H	K6	9.0	5.262 ± 0.016	0.66 ± 0.03	0.10	–0.05
GJ4 B	00:05:41	45:48:43	88.4 ± 1.6	H	K7	9.0	5.284 ± 0.023	0.65 ± 0.04	0.11	–0.04
GJ14	00:17:06	40:56:53	66.7 ± 0.9	H	M0.5	9.0	5.577 ± 0.024	0.72 ± 0.03	0.08	–0.10
GJ15 A	00:18:22	44:01:22	278.8 ± 0.8	H	M1	8.1	4.018 ± 0.020	0.41 ± 0.03	–0.32	–0.36
GJ15 B	00:18:25	44:01:38	278.8 ± 0.8	H	M3.5	11.1	5.948 ± 0.024	0.16 ± 0.01	–0.50	–0.52
GJ1009	00:21:56	–31:24:21	55.6 ± 2.3	H	M1.5	11.2	6.785 ± 0.017	0.55 ± 0.03	0.35	0.11
GJ26	00:38:59	30:36:58	80.1 ± 3.9	Y	M2.5	11.1	6.606 ± 0.029	0.43 ± 0.03	0.09	–0.08
GJ27.1	00:39:58	–44:15:11	41.7 ± 2.8	H	M0.5	11.4	7.394 ± 0.029	0.55 ± 0.03	0.06	–0.09
GJ34 B	00:49:06	57:48:54	134.1 ± 0.5	H	M0	7.5	3.881 ± 0.490	0.76 ± 0.11	0.32	0.09
GJ48	01:02:32	71:40:47	121.4 ± 1.2	H	M3	10.0	5.449 ± 0.017	0.48 ± 0.03	0.28	0.05
GJ49	01:02:38	62:20:42	100.4 ± 1.5	H	M1.5	9.6	5.371 ± 0.020	0.58 ± 0.03	0.26	0.06
GJ54.1	01:12:30	–16:59:56	268.8 ± 3.2	Y	M4.5	12.1	6.420 ± 0.017	0.13 ± 0.01	–0.33	–0.43
GJ70	01:43:20	04:19:18	87.6 ± 2.0	H	M2	10.9	6.516 ± 0.023	0.41 ± 0.03	–0.02	–0.15
GJ83.1	02:00:12	13:03:11	224.8 ± 2.9	Y	M4.5	12.3	6.648 ± 0.017	0.14 ± 0.01	–0.25	–0.35
GJ3126	02:01:35	63:46:12	78.4 ± 10.6	Y	M3	11.0	6.389 ± 0.018	0.48 ± 0.03	0.39	0.12
GJ87	02:12:20	03:34:32	96.0 ± 1.7	H	M1.5	10.0	6.077 ± 0.020	0.45 ± 0.03	–0.26	–0.32
GJ96	02:22:14	47:52:48	83.8 ± 1.1	H	M0.5	9.4	5.554 ± 0.026	0.62 ± 0.03	0.11	–0.05
GJ105 B	02:36:15	06:52:18	139.3 ± 0.5	H	M3.5	11.7	6.574 ± 0.020	0.25 ± 0.02	0.00	–0.13
GJ109	02:44:15	25:31:24	133.2 ± 2.3	H	M3	10.6	5.961 ± 0.021	0.35 ± 0.03	–0.06	–0.18
GJ156	03:54:35	–06:49:33	64.2 ± 1.1	H	M0	9.0	5.629 ± 0.024	0.73 ± 0.03	0.08	–0.10
GJ169	04:29:00	21:55:21	87.8 ± 1.0	H	K7	8.3	4.875 ± 0.016	0.74 ± 0.03	0.14	–0.05
GJ172	04:37:40	52:53:37	98.9 ± 1.0	H	K8	8.6	5.047 ± 0.018	0.65 ± 0.04	–0.00	–0.14
GJ173	04:37:41	–11:02:19	90.1 ± 1.7	H	M1.5	10.3	6.091 ± 0.021	0.48 ± 0.03	0.04	–0.11
GJ176	04:42:55	18:57:29	107.8 ± 2.9	H	M2	9.9	5.607 ± 0.034	0.50 ± 0.03	0.17	–0.02
GJ179	04:52:05	06:28:35	81.4 ± 4.0	H	M3.5	11.9	6.942 ± 0.018	0.36 ± 0.02	0.34	0.08
GJ180	04:53:49	–17:46:24	82.5 ± 2.4	H	M2	10.9	6.598 ± 0.021	0.42 ± 0.03	–0.09	–0.20
GJ3325	05:03:20	–17:22:24	108.6 ± 2.7	H	M3	11.7	6.936 ± 0.021	0.27 ± 0.02	–0.22	–0.28
GJ191	05:11:40	–45:01:06	255.7 ± 0.9	H	M1.0	8.8	5.049 ± 0.021	0.27 ± 0.03	–1.01	–0.82
GJ192	05:12:42	19:39:56	81.3 ± 4.1	H	M2	10.8	6.470 ± 0.024	0.45 ± 0.03	0.04	–0.11
GJ205	05:31:27	–03:40:38	176.8 ± 1.2	H	M1.5	8.0	3.870 ± 0.030	0.63 ± 0.03	0.32	0.11
GJ3356	05:34:52	13:52:46	80.6 ± 9.8	Y	M3.5	11.8	6.936 ± 0.016	0.37 ± 0.02	0.25	0.02
GJ208	05:36:30	11:19:40	89.0 ± 1.0	H	M0	8.8	5.269 ± 0.023	0.65 ± 0.04	–0.04	–0.17
GJ212	05:41:30	53:29:23	80.4 ± 1.7	H	M0.5	9.8	5.759 ± 0.016	0.60 ± 0.03	0.18	0.00
GJ213	05:42:09	12:29:21	171.7 ± 1.1	G08	M4	11.6	6.389 ± 0.016	0.22 ± 0.02	–0.11	–0.21
GJ3378	06:01:11	59:35:49	132.1 ± 4.9	Y	M3.5	11.7	6.639 ± 0.018	0.25 ± 0.02	–0.02	–0.14
GJ	06:07:43	–25:44:41	88.1 ± 2.5	H	n/a	11.9	7.169 ± 0.023	0.30 ± 0.02	–0.14	–0.23
GJ226	06:10:19	82:06:24	106.7 ± 1.3	H	M2	10.5	6.061 ± 0.018	0.41 ± 0.03	–0.00	–0.14
GJ229	06:10:34	–21:51:52	173.8 ± 1.0	H	M0.5	8.1	4.150 ± 0.030	0.58 ± 0.03	0.11	–0.05
GJ239	06:37:10	17:33:53	102.6 ± 1.6	H	M0	9.6	5.862 ± 0.024	0.47 ± 0.03	–0.40	–0.43
GJ250 B	06:52:18	–05:11:25	114.8 ± 0.4	H	M2	10.1	5.723 ± 0.036	0.45 ± 0.03	0.05	–0.10
GJ251	06:54:48	33:16:05	179.0 ± 1.6	H	M3	9.9	5.275 ± 0.023	0.35 ± 0.03	–0.02	–0.15
GJ273	07:27:24	05:13:32	267.4 ± 0.8	G08	M3.5	9.9	4.857 ± 0.023	0.29 ± 0.02	0.08	–0.09
GJ1097	07:28:45	–03:17:53	81.4 ± 2.5	H	M3	11.5	6.704 ± 0.027	0.40 ± 0.03	0.27	0.04
GJ277.1	07:34:27	62:56:29	87.2 ± 2.3	H	M0.5	10.4	6.556 ± 0.018	0.40 ± 0.03	–0.50	–0.49
GJ3459	07:38:40	–21:13:28	94.3 ± 3.3	H	M3	11.7	7.063 ± 0.023	0.29 ± 0.02	–0.24	–0.29
GJ285	07:44:40	03:33:08	167.9 ± 2.3	H	M4.5	11.2	5.698 ± 0.017	0.31 ± 0.02	0.58	0.27
GJ2066	08:16:07	01:18:09	109.6 ± 1.5	H	M2	10.1	5.766 ± 0.024	0.46 ± 0.03	0.05	–0.11
GJ308.1	08:29:56	61:43:32	50.7 ± 1.8	H	M0	10.3	6.781 ± 0.017	0.59 ± 0.03	–0.20	–0.30
GJ310	08:36:25	67:17:42	72.6 ± 1.3	H	M1	9.3	5.580 ± 0.015	0.68 ± 0.03	0.16	–0.01
GJ317	08:40:59	–23:27:22	65.3 ± 0.4	AE12	M3.5	12.0	7.028 ± 0.020	0.43 ± 0.03	0.50	0.19
GJ324 B	08:52:40	28:18:59	81.0 ± 0.8	H	M4	13.2	7.666 ± 0.023	0.26 ± 0.02	0.34	0.11
GJ338 A	09:14:22	52:41:11	162.8 ± 2.9	Y	M0	7.6	3.988 ± 0.036	0.65 ± 0.04	0.04	–0.10
GJ338 B	09:14:24	52:41:11	162.8 ± 2.9	Y	M0	7.7	4.136 ± 0.020	0.62 ± 0.04	–0.11	–0.22
GJ1125	09:30:44	+00:19:21	103.5 ± 3.9	H	M3.5	11.7	6.871 ± 0.024	0.29 ± 0.02	–0.07	–0.18
GJ353	09:31:56	36:19:12	71.9 ± 1.8	H	M0	10.2	6.302 ± 0.020	0.53 ± 0.03	–0.10	–0.20
GJ357	09:36:01	–21:39:38	110.8 ± 1.9	H	M2.5	10.9	6.475 ± 0.017	0.33 ± 0.03	–0.26	–0.31
GJ361	09:41:10	13:12:34	88.8 ± 1.7	H	M1.5	10.4	6.128 ± 0.020	0.48 ± 0.03	0.04	–0.11
GJ362	09:42:51	70:02:21	88.1 ± 2.4	H	M3	11.2	6.469 ± 0.016	0.42 ± 0.03	0.27	0.03
GJ373	09:56:08	62:47:18	94.7 ± 1.3	H	M0	9.0	5.200 ± 0.024	0.64 ± 0.04	0.11	–0.04

Notes. $\pi_{\rm src}$: (H) revised H catalog (van Leeuwen 2007); (Y) (van Altena et al. 1995); (G08) (Gatewood 2008); (AE12) (Anglada-Escudé et al. 2012); (J05) (Jao et al. 2005); (S99) (Söderhjelm 1999); (F00) (Fabricius & Makarov 2000); (H06) (Henry et al. 2006); (B99) (Benedict et al. 1999); (G98) (Gatewood et al. 1998); (B02) (Benedict et al. 2002).

Table 8. continued.

Star	α (2000)	δ (2000)	π [mas]	$\pi_{\rm src}$	Stype	V [mag]	$K_{\rm S}$ [mag]	$M_\star$ [$M_\odot$]	[Fe/H]$_{JA09}$ [dex]	[Fe/H]$_{N12}$ [dex]
GJ380	10:11:22	49:27:15	205.2 ± 0.5	H	K7	6.6	3.210 ± 0.030	0.71 ± 0.03	0.02	–0.14
GJ382	10:12:17	–03:44:44	127.1 ± 1.9	H	M1.5	9.3	5.015 ± 0.020	0.54 ± 0.03	0.22	0.02
GJ388	10:19:36	19:52:12	204.6 ± 2.8	Y	M3	9.4	4.593 ± 0.017	0.42 ± 0.03	0.37	0.10
GJ390	10:25:10	–10:13:43	81.0 ± 1.9	H	M1	10.2	6.032 ± 0.017	0.54 ± 0.03	0.09	–0.06
GJ393	10:28:55	+00:50:27	141.5 ± 2.2	H	M2	9.7	5.311 ± 0.023	0.44 ± 0.03	0.01	–0.14
GJ394	10:30:25	55:59:56	74.9 ± 5.6	Y	K7	8.7	5.361 ± 0.016	0.71 ± 0.03	0.01	–0.16
GJ397	10:31:24	45:31:33	63.5 ± 1.1	H	K7	8.8	5.564 ± 0.024	0.75 ± 0.03	0.07	–0.13
GJ402	10:50:52	06:48:29	147.9 ± 3.5	H	M4	11.6	6.371 ± 0.016	0.26 ± 0.02	0.16	–0.02
GJ406	10:56:28	07:00:53	419.1 ± 2.1	Y	M5.5	13.5	6.084 ± 0.017	0.10 ± 0.00	0.43	0.19
GJ408	11:00:04	22:49:58	150.1 ± 1.7	H	M2.5	10.0	5.540 ± 0.030	0.37 ± 0.03	–0.07	–0.19
GJ410	11:02:38	21:58:01	85.0 ± 1.1	H	M0	9.6	5.688 ± 0.021	0.59 ± 0.03	0.04	–0.10
GJ411	11:03:20	35:58:11	392.6 ± 0.7	H	M2	7.5	3.360 ± 0.030	0.39 ± 0.03	–0.32	–0.35
GJ412 A	11:05:28	43:31:36	206.3 ± 1.0	H	M0.5	8.8	4.769 ± 0.020	0.39 ± 0.03	–0.39	–0.40
GJ413.1	11:09:31	–24:35:55	93.0 ± 1.7	H	M2	10.4	6.097 ± 0.023	0.46 ± 0.03	0.08	–0.08
GJ414 A	11:11:05	30:26:45	84.2 ± 0.9	H	K9	8.3	4.979 ± 0.018	0.74 ± 0.03	0.08	–0.11
GJ414 B	11:11:02	30:26:41	84.2 ± 0.9	H	M1.5	10.0	5.734 ± 0.020	0.58 ± 0.03	0.32	0.10
GJ424	11:20:04	65:50:47	112.1 ± 1.0	H	M0	9.3	5.534 ± 0.017	0.49 ± 0.03	–0.29	–0.35
GJ433	11:35:26	–32:32:23	112.6 ± 1.4	H	M1.5	9.8	5.623 ± 0.021	0.47 ± 0.03	–0.02	–0.15
GJ1148	11:41:44	42:45:07	90.1 ± 2.8	H	M4	11.9	6.822 ± 0.016	0.35 ± 0.02	0.32	0.07
GJ436	11:42:11	26:42:23	98.6 ± 2.3	H	M2.5	10.7	6.073 ± 0.016	0.44 ± 0.03	0.24	0.02
GJ445	11:47:41	78:41:28	186.9 ± 1.7	H	M3.5	10.8	5.954 ± 0.027	0.25 ± 0.02	–0.25	–0.30
GJ447	11:47:44	+00:48:16	298.2 ± 1.7	Y	M4	11.1	5.654 ± 0.024	0.17 ± 0.01	–0.14	–0.24
GJ450	11:51:07	35:16:19	116.5 ± 1.2	H	M1	9.8	5.606 ± 0.017	0.46 ± 0.03	–0.08	–0.19
GJ3708	12:11:11	–19:57:38	79.4 ± 2.4	H	M3	11.7	7.044 ± 0.016	0.35 ± 0.03	–0.01	–0.15
GJ3709	12:11:16	–19:58:21	79.4 ± 2.4	H	M3.5	12.6	7.777 ± 0.000	0.25 ± 0.02	–0.23	–0.29
GJ465	12:24:52	–18:14:32	113.0 ± 2.5	H	M2	11.3	6.950 ± 0.021	0.26 ± 0.02	–0.65	–0.56
GJ486	12:47:56	09:45:05	119.5 ± 2.7	H	M3.5	11.4	6.362 ± 0.018	0.32 ± 0.02	0.23	0.01
GJ488	12:50:43	–00:46:05	94.6 ± 0.8	H	M0.5	8.5	4.882 ± 0.020	0.71 ± 0.03	0.17	–0.01
GJ494	13:00:46	12:22:32	85.5 ± 1.5	H	M0.5	9.8	5.578 ± 0.016	0.61 ± 0.03	0.34	0.12
GJ514	13:29:59	10:22:37	130.6 ± 1.1	H	M0.5	9.0	5.036 ± 0.027	0.53 ± 0.03	–0.03	–0.15
GJ519	13:37:28	35:43:03	91.4 ± 1.2	H	M0	9.1	5.486 ± 0.021	0.60 ± 0.03	–0.15	–0.25
GJ526	13:45:43	14:53:29	185.5 ± 1.1	H	M1.5	8.5	4.415 ± 0.017	0.50 ± 0.03	–0.07	–0.18
GJ3804	13:45:50	–17:58:05	97.6 ± 5.0	H	M3.5	11.9	6.902 ± 0.044	0.31 ± 0.02	0.12	–0.06
GJ536	14:01:03	–02:39:17	99.7 ± 1.6	H	M1	9.7	5.683 ± 0.020	0.52 ± 0.03	–0.04	–0.16
GJ552	14:29:29	15:31:57	71.4 ± 2.1	H	M2	10.7	6.393 ± 0.018	0.52 ± 0.03	0.18	–0.01
GJ553.1	14:31:01	–12:17:45	92.4 ± 3.9	H	M3.5	11.9	6.961 ± 0.021	0.32 ± 0.02	0.14	–0.05
GJ555	14:34:16	–12:31:10	158.5 ± 2.6	J05	M3.5	11.3	5.939 ± 0.034	0.29 ± 0.02	0.40	0.14
GJ9492	14:42:21	66:03:20	93.2 ± 1.3	H	M1.5	10.9	6.491 ± 0.024	0.39 ± 0.03	–0.10	–0.21
GJ569 A	14:54:29	16:06:03	103.6 ± 1.7	H	M2.5	10.2	5.770 ± 0.018	0.48 ± 0.03	0.16	–0.03
GJ570 B	14:57:26	–21:24:41	169.7 ± 1.0	S99	M1	8.0	4.246 ± 0.033	0.57 ± 0.03	–0.08	–0.19
GJ581	15:19:26	–07:43:20	160.9 ± 2.6	H	M3	10.6	5.837 ± 0.023	0.30 ± 0.02	–0.10	–0.20
GJ617 A	16:16:42	67:14:19	93.6 ± 0.9	H	M1	8.6	4.953 ± 0.018	0.70 ± 0.03	0.17	–0.00
GJ617 B	16:16:45	67:15:22	93.1 ± 1.5	H	M3	10.7	6.066 ± 0.020	0.47 ± 0.03	0.34	0.09
GJ623 A	16:24:09	48:21:10	124.1 ± 1.2	H	M2.5	10.3	5.915 ± 0.023	0.38 ± 0.03	–0.15	–0.24
GJ625	16:25:24	54:18:14	153.5 ± 1.0	H	M1.5	10.1	5.833 ± 0.024	0.32 ± 0.03	–0.42	–0.41
GJ628	16:30:18	–12:39:45	233.0 ± 1.6	H	M3.5	10.1	5.075 ± 0.024	0.30 ± 0.02	0.11	–0.06
GJ638	16:45:06	33:30:33	102.0 ± 0.7	H	K7	8.1	4.712 ± 0.021	0.71 ± 0.03	0.03	–0.13
GJ649	16:58:08	25:44:39	96.7 ± 1.4	H	M1	9.7	5.624 ± 0.016	0.54 ± 0.03	0.07	–0.08
GJ655	17:07:07	21:33:14	74.8 ± 3.1	H	M3	11.6	7.042 ± 0.016	0.38 ± 0.03	0.01	–0.13
GJ3992	17:11:34	38:26:33	83.3 ± 2.0	H	M3.5	11.5	6.801 ± 0.021	0.38 ± 0.03	0.17	–0.03
GJ667 C	17:18:58	–34:59:48	138.0 ± 0.6	F00	M1.5	10.2	6.036 ± 0.020	0.32 ± 0.03	–0.50	–0.47
GJ671	17:19:52	41:42:49	80.8 ± 1.7	H	M2.5	11.4	6.915 ± 0.018	0.37 ± 0.03	–0.11	–0.21
GJ673	17:25:45	02:06:41	129.9 ± 0.7	H	K7	7.5	4.170 ± 0.030	0.71 ± 0.03	0.03	–0.14
GJ678.1	17:30:22	05:32:54	100.2 ± 1.1	H	M0	9.3	5.422 ± 0.029	0.57 ± 0.03	0.01	–0.12
GJ687	17:36:25	68:20:20	220.8 ± 0.9	H	M3	9.2	4.548 ± 0.021	0.40 ± 0.03	0.12	–0.06
GJ686	17:37:53	18:35:30	123.7 ± 1.6	H	M1	9.6	5.572 ± 0.020	0.44 ± 0.03	–0.25	–0.31
GJ694	17:43:55	43:22:43	105.5 ± 1.2	H	M2.5	10.5	5.964 ± 0.020	0.44 ± 0.03	0.16	–0.03
GJ2130	17:46:12	–32:06:12	71.5 ± 2.6	H06	M1.5	10.5	6.251 ± 0.026	0.55 ± 0.03	0.23	0.03
GJ699	17:57:48	04:41:36	545.4 ± 0.3	B99	M4	9.6	4.524 ± 0.020	0.16 ± 0.01	–0.59	–0.58
GJ701	18:05:07	–03:01:52	128.9 ± 1.4	H	M1	9.4	5.306 ± 0.021	0.48 ± 0.03	–0.12	–0.22
GJ4048	18:18:04	38:46:34	88.4 ± 3.6	Y	M3	11.9	7.222 ± 0.020	0.29 ± 0.02	–0.23	–0.29
GJ4070	18:41:59	31:49:49	87.4 ± 2.7	H	M3	11.3	6.722 ± 0.020	0.37 ± 0.03	–0.01	–0.15
GJ725 A	18:42:46	59:37:49	280.2 ± 2.2	H	M3	8.9	4.432 ± 0.020	0.33 ± 0.03	–0.22	–0.28
GJ725 B	18:42:46	59:37:36	289.5 ± 3.2	H	M3.5	9.7	5.000 ± 0.023	0.25 ± 0.02	–0.38	–0.39

Table 8. continued.

Star	α (2000)	δ (2000)	π [mas]	π_{src}	Stype	V [mag]	K_{S} [mag]	$M_\star$ [$M_\odot$]	[Fe/H]$_{JA09}$ [dex]	[Fe/H]$_{N12}$ [dex]
GJ729	18:49:49	–23:50:10	336.7 ± 2.0	H	M3.5	10.5	5.370 ± 0.016	0.17 ± 0.01	–0.41	–0.44
GJ745 A	19:07:05	20:53:17	117.5 ± 2.3	H	M1.5	10.8	6.521 ± 0.021	0.30 ± 0.03	–0.52	–0.48
GJ745 B	19:07:13	20:52:37	114.2 ± 2.3	H	M2	10.8	6.517 ± 0.023	0.31 ± 0.03	–0.49	–0.46
GJ752 A	19:16:55	05:10:08	170.4 ± 1.0	H	M2.5	9.1	4.673 ± 0.020	0.48 ± 0.03	0.23	0.02
GJ1245	19:53:54	44:24:54	220.2 ± 1.0	Y	M5.5	14.0	7.387 ± 0.018	0.11 ± 0.00	–0.07	–0.18
GJ786	20:10:52	77:14:20	59.1 ± 0.7	H	K7	8.9	5.667 ± 0.016	0.76 ± 0.03	0.06	–0.15
GJ793	20:30:32	65:26:58	125.1 ± 1.1	H	M2.5	10.6	5.933 ± 0.023	0.38 ± 0.03	0.06	–0.10
GJ806	20:45:04	44:29:56	81.2 ± 1.7	H	M1.5	10.8	6.533 ± 0.016	0.44 ± 0.03	–0.07	–0.19
GJ	20:52:33	–16:58:29	175.0 ± 3.4	H	M4	11.5	6.199 ± 0.021	0.23 ± 0.02	0.04	–0.10
GJ809	20:53:19	62:09:15	141.9 ± 0.6	H	M0.5	8.6	4.618 ± 0.024	0.58 ± 0.03	0.06	–0.09
GJ820 B	21:06:55	38:44:31	285.9 ± 0.5	H	K7	6.0	2.700 ± 0.030	0.66 ± 0.04	–0.12	–0.25
GJ821	21:09:17	–13:18:09	82.2 ± 2.2	H	M1	10.9	6.909 ± 0.029	0.36 ± 0.03	–0.54	–0.51
GJ846	22:02:10	01:24:00	97.6 ± 1.5	H	M0	9.2	5.322 ± 0.023	0.60 ± 0.03	0.05	–0.09
GJ849	22:09:40	–04:38:26	109.9 ± 2.1	H	M3.5	10.4	5.594 ± 0.017	0.49 ± 0.03	0.54	0.22
GJ851	22:11:30	18:25:34	86.1 ± 1.4	H	M2	10.2	5.823 ± 0.016	0.55 ± 0.03	0.40	0.14
GJ860 A	22:27:59	57:41:45	249.9 ± 1.9	H	M3	9.8	4.777 ± 0.029	0.32 ± 0.02	0.25	0.03
GJ873	22:46:49	44:20:02	199.0 ± 0.9	G98	M3.5	10.2	5.299 ± 0.024	0.32 ± 0.02	0.11	–0.07
GJ876	22:53:16	–14:15:49	214.6 ± 0.2	B02	M4	10.2	5.010 ± 0.021	0.33 ± 0.02	0.40	0.12
GJ880	22:56:34	16:33:12	146.1 ± 1.0	H	M1.5	8.7	4.523 ± 0.016	0.58 ± 0.03	0.25	0.05
GJ884	23:00:16	–22:31:27	121.7 ± 0.7	H	K7	7.9	4.478 ± 0.016	0.68 ± 0.03	–0.05	–0.19
GJ887	23:05:52	–35:51:11	305.3 ± 0.7	H	M0.5	7.3	3.380 ± 0.030	0.49 ± 0.03	–0.15	–0.24
GJ891	23:10:15	–25:55:52	62.2 ± 3.3	H	M2	11.3	6.995 ± 0.021	0.46 ± 0.03	0.01	–0.13
GJ4333	23:21:37	17:17:25	91.0 ± 2.9	H	M4	11.7	6.507 ± 0.016	0.40 ± 0.02	0.61	0.26
GJ895	23:24:30	57:51:15	77.2 ± 1.3	H	M1	10.0	5.871 ± 0.021	0.59 ± 0.03	0.28	0.07
GJ905	23:41:54	44:10:40	316.0 ± 1.1	Y	M5	12.3	5.929 ± 0.020	0.14 ± 0.01	0.17	0.05
GJ908	23:49:12	02:24:04	167.3 ± 1.2	H	M1	9.0	5.043 ± 0.020	0.42 ± 0.03	–0.39	–0.41
GJ911	23:54:46	–21:46:28	41.2 ± 2.6	H	M0.5	10.8	7.117 ± 0.034	0.62 ± 0.04	–0.03	–0.15

Appendix A: A new M dwarf metallicity and effective temperature calibration based on line and feature measurements of HARPS M dwarf spectra

Here we briefly explain the method that we developed to estimate the metallicity and effective temperature of M dwarfs. A paper regarding the full details of this calibration is in preparation (Neves et al., in prep.).

The method is based on the measurement of "peak-to-peak" equivalent widths (EW) of lines and features from the spectra of our volume-limited M dwarf HARPS sample and uses existing photometric calibrations for metallicity (Neves et al. 2012) and effective temperature (Casagrande et al. 2008), as starting values. Our method achieves an increase in precision of the metallicity and effective temperature but the accuracy of the new scale is tied to the accuracy of the photometric calibrations.

A.1. Calibration sample

From the initial 102 M dwarf star spectra of the Bonfils et al. (2013) sample we initially chose 62 stars with S/N greater than 100. Seven stars (Gl191, Gl285, Gl388, Gl699, Gl729, Gl803, GJ1125) were then discarded a posteriori, due to a bad correlation of the line measurements with either the reference metallicity or temperature scales, that can be attributed to high activity/rotation (Gl191, Gl285, Gl388, Gl729, Gl803) or to a bad value of the radial velocity (GJ1125). We ended up with a sample of 55 stars, shown in Table A.1 in which we based our calibration. Column 1 shows the star designation, Col. 2 the initial photometric [Fe/H] from Neves et al. (2012), Col. 3 the calibrated [Fe/H] value, Col. 4 the initial photometric effective temperature, and Col. 5 the calibrated $T_{\rm eff}$ value.

A.2. Method

From our calibration sample we first measured "peak-to-peak" equivalent widths (EWs) of lines and features using the 26 redder orders of median normalized HARPS spectra, in the region between 530 to 690 nm. Here we consider features as blended lines. We define the "peak-to-peak" equivalent widths as

$$W = \sum \frac{F_{\rm pp} - F_{\lambda}}{F_{\rm pp}} \Delta\lambda, \tag{A.1}$$

where $F_{\rm pp}$ is the value of the flux between the peaks of the line/feature at each integration step and F_{λ} the flux of the line/feature. The measurement of the EWs is illustrated in Fig. A.1, where the "peak-to-peak" flux corresponds to the red dotted lines, and the black line is the flux of the reference spectra. The EW is thus measured between the red dotted line and the solid black line. We used the very high S/N (~1430 @ 550 nm) spectral orders of the star Gl 205 as a reference from where the line/feature regions are going to be measured for all other stars. We rejected lines/features with $EW < 8$ mÅ and very steep lines/features.

We investigated the correlations and partial correlations of [Fe/H] and $T_{\rm eff}$ with the line/feature EWs. Figure A.2 shows the histograms of the partial correlation values of [Fe/H] with $T_{\rm eff}$ kept constant (solid blue histogram) and the partial correlation values of $T_{\rm eff}$ with [Fe/H] kept constant (dashed green histogram). We observe that a significant number of lines have a good correlation with the parameters.

Table A.1. Calibration sample.

Star	$[\rm Fe/H]_{\it N12}$	$[\rm Fe/H]_{\rm NEW}$	$T_{\rm eff\ \it C08}$	$T_{\rm eff\ NEW}$
Gl465	–0.56	–0.66	3365	3415
Gl438	–0.51	–0.39	3506	3444
Gl667C	–0.51	–0.53	3460	3351
Gl54.1	–0.46	–0.40	2920	2970
Gl887	–0.36	–0.24	3657	3472
Gl1	–0.37	–0.45	3495	3566
Gl908	–0.37	–0.44	3579	3496
Gl357	–0.33	–0.34	3329	3351
Gl686	–0.31	–0.37	3536	3453
Gl87	–0.30	–0.31	3539	3557
Gl447	–0.28	–0.18	2958	3034
Gl693	–0.28	–0.30	3178	3233
Gl213	–0.25	–0.11	3062	3088
Gl674	–0.22	–0.25	3276	3258
LP771-95A	–0.09	–0.34	3028	3238
Gl832	–0.18	–0.19	3426	3419
Gl701	–0.19	–0.27	3498	3468
Gl536	–0.16	–0.12	3542	3537
HIP31292	–0.15	–0.10	3156	3169
Gl105B	–0.14	–0.02	3057	2987
Gl341	–0.15	–0.13	3606	3582
Gl273	–0.13	–0.01	3119	3107
Gl581	–0.17	–0.21	3186	3209
Gl526	–0.15	–0.20	3503	3560
Gl433	–0.15	–0.17	3453	3461
GJ2066	–0.11	–0.18	3372	3447
Gl678.1A	–0.13	–0.11	3628	3589
Gl413.1	–0.11	–0.12	3388	3376
Gl618A	–0.08	–0.08	3231	3253
Gl393	–0.10	–0.22	3346	3391
Gl514	–0.10	–0.16	3515	3524
Gl250B	–0.09	–0.10	3352	3416
Gl628	–0.06	–0.02	3091	3055
Gl367	–0.05	–0.07	3379	3392
Gl229	–0.04	–0.01	3532	3662
Gl846	–0.06	0.06	3628	3616
Gl680	–0.04	–0.22	3355	3403
Gl752A	–0.00	0.06	3328	3369
Gl877	–0.02	–0.01	3257	3296
HIP31293	0.01	–0.04	3236	3277
Gl569A	0.00	–0.08	3327	3204
Gl588	0.03	0.07	3277	3325
Gl205	–0.01	0.22	3576	3736
Gl358	0.04	–0.01	3194	3097
Gl551	0.07	–0.00	2625	2659
Gl176	0.03	–0.01	3344	3346
Gl382	0.05	0.04	3397	3338
Gl300	0.06	0.14	2973	2829
Gl479	0.06	0.02	3219	3137
Gl880	0.08	0.07	3453	3600
Gl682	0.10	0.11	2973	2906
Gl555	0.11	0.17	2983	2864
Gl876	0.14	0.15	3036	2948
LTT9759	0.16	0.21	3317	3333
Gl849	0.23	0.24	3170	3121

Then we calculated a linear fit of the EWs with the metallicity (taken from Neves et al. 2012) and effective temperature (taken from Casagrande et al. 2008), using a least squares approach. For each EW i and for each star m we have,

$$W_{i,m} = \alpha_i [{\rm Fe/H}]^{\rm T}_m + \beta_i T^{\rm T}_{{\rm eff}m} + \gamma_i, \tag{A.2}$$

where $W_{i,m}$ is a $i \times m$ matrix containing the EWs, and both $[{\rm Fe/H}]_m$, and $T_{{\rm eff}m}$ are $1 \times m$ vectors. The α and the β are the coefficients related to metallicity and effective temperature, respectively, while γ is an independent coefficient.

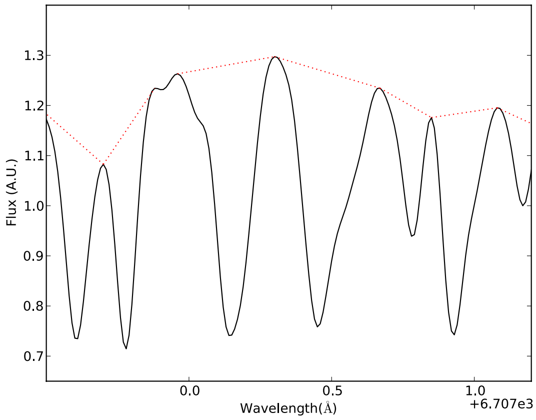

Fig. A.1. Small region of the Gl 205 spectra illustrating the "peak to peak" equivalent width line measurement. The red dotted line represents the "peak-to-peak" flux.

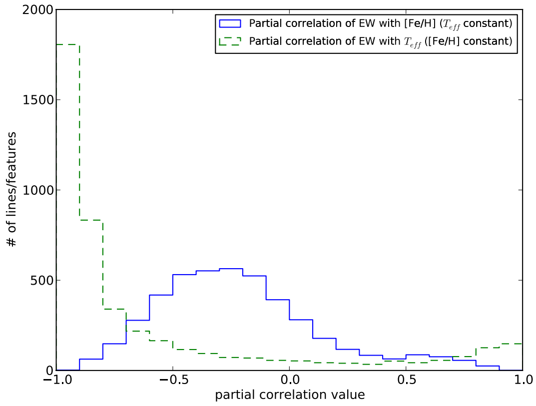

Fig. A.2. Histograms of the partial correlations of [Fe/H] (solid blue histogram) and T_{eff} (dashed green histogram).

The error of each coefficient is calculated as

$$\epsilon_i = \sqrt{RSS.J_{i,i}}, \tag{A.3}$$

where RSS is the residual sum of squares, expressed as

$$RSS = \frac{\sum (x_{i,\mathrm{model}} - x_i)^2}{n_{\mathrm{obs}} - n_{\mathrm{coef}}}, \tag{A.4}$$

and $J_{i,i}$ is the diagonal of the estimate of the jacobian matrix around the solution. The $x_{i,\mathrm{model}}$, x_i, n_{obs}, and n_{coef} from Eq. (A.3) are, respectively, the predicted value of the data, x_i, by the regression model, the data values, the number of data points, and the number of coefficients.

The total error of the coefficients can then be written as

$$\epsilon = \sqrt{\epsilon\alpha^2 + \epsilon\beta^2 + \epsilon\gamma^2}. \tag{A.5}$$

Here we assume that both [Fe/H] and temperature are independent and do not correlate with each other.

Our aim is to increase the metallicity precision using the photometric calibration as reference. In order to do this, we want to recover the values of the metallicity and temperature by doing a weighted least squares refit. To calculate the weights for the least squares refit we just invert the squared errors of the coefficients, and normalize the expression,

$$E_i = \frac{1/\epsilon_i^2}{\sum 1/\epsilon_i^2}. \tag{A.6}$$

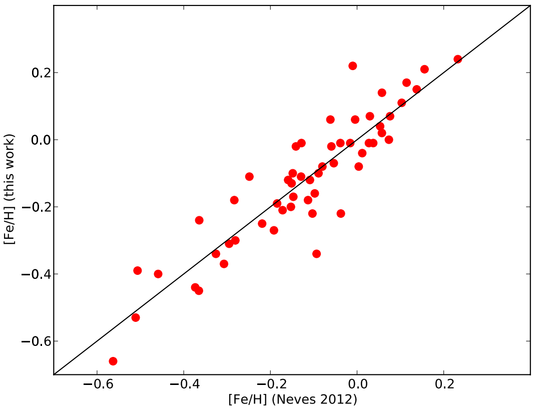

Fig. A.3. [Fe/H] comparison between this work and the photometric calibration of Neves et al. (2012).

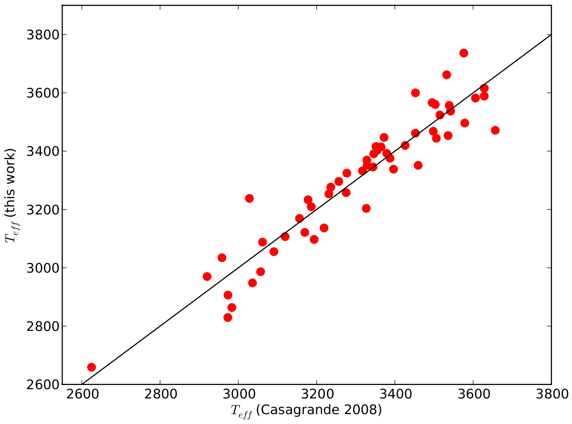

Fig. A.4. T_{eff} comparison between this work and the photometric calibration of Casagrande et al. (2008).

To invert the fit of Eq. (A.2) we first take the calculated coefficients from the first fit and define the coefficient matrix as

$$C_{i,3} = \begin{bmatrix} \alpha_{1,1} & \beta_{1,2} & \gamma_{1,3} \\ \alpha_{2,1} & \beta_{2,2} & \gamma_{2,3} \\ \dots & \dots & \dots \\ \alpha_{i,1} & \beta_{i,2} & \gamma_{i,3} \end{bmatrix}. \tag{A.7}$$

Then we invert Eq. (A.2). After some operations we have

$$[[\mathrm{Fe/H}], T_{\mathrm{eff}}, Ind]_{3,m} = (C^{\mathrm{T}}_{3,i}C_{i,3})^{-1}C^{\mathrm{T}}_{3,i}W_{i,m}, \tag{A.8}$$

where C^{T} is the transpose of C and Ind is the value of the independent parameter.

Finally, we use a *levenberg-marquardt* algorithm and apply the weights (Eq. (A.6) to Eq. (A.8)), recovering one value of metallicity and effective temperature for each star.

We also tried other methods, such as choosing groups of lines with a high correlation or partial correlation coefficients and then applying the same method as described in this Appendix. However, the weighted least squares method using all 4441 lines performed best at minimizing the uncertainties of both metallicity and effective temperature.

Using this method, we get a dispersion of metallicity and effective temperature of 0.08 dex and 80 K respectively. Figures A.3 and A.4 show the comparison between the values obtained in this work and the reference calibrations for metallicity and effective temperature, respectively. We emphasize that we only get an improvement of the precision. The accuracy of the calibration, as well as systematic errors, are tied to the original determinations of both [Fe/H] and temperature.

Chapter 5

SPITZER observations of GJ 3470b: a very low-density Neptune-size planet orbiting a metal-rich M dwarf

5.1 Introduction

Concurrently to my work on M dwarf parameters, me and my collaborators were involved in the observation of the M dwarf GJ3470 , that culminated in the detection of the 'Hot Uranus' GJ3470 b (Bonfils et al. 2012) using both the radial velocity technique, with the HARPS spectrograph, and photometry, with the TRAPPIST telescope (Jehin et al. 2011). The transit was later observed with the SPITZER telescope (Demory et al. 2012), with the aim of refining the stellar and planetary parameters of the system.

GJ3470 b is one of the few confirmed lower-mass planets that transit its star. Its host star is bright (M1.5 dwarf with K_S = 7.99 mag) and has a radius small enough to allow detailed follow-up studies. GJ3470 b has a published mass of 14.0 ± 1.7 Earth masses and a radius of 4.2 ± 0.6 Earth radii (Bonfils et al. 2012). Along with GJ436 b (Butler et al. 2004; Gillon et al. 2007) and GJ1214 b (Charbonneau et al. 2009), it is part of the smallest planets orbiting M dwarfs with a K magnitude brighter than nine. GJ 3470 b has a mean density $\rho = 1.07 \pm 0.43$ gcm^{-3} that is significantly smaller than that of GJ 436 b. The Kepler mission confirmed several of these so-called "low-density Neptunes", Kepler-11 d, e (Lissauer et al. 2011) and Kepler-18 c (Cochran et al. 2011). These objects represent the tip of the iceberg, as several hundred Neptune-size planet candidates have already been detected by Kepler and await confirmation. Unfortunately, most of these Kepler planets orbit faint stars and exhibit shallow transit depths that render follow-up studies very challenging, if not impractical altogether.

Before this work all transit photometry available for GJ 3470 was from the ground. Unfortunately, it is not possible to precisely constrain the transit parameters with that data, resulting in poorly determined planetary properties. Using our Spitzer observations we were able to significantly refine the system parameters, as shown in the following sections and in our published paper (Demory et al. 2013), in Sect. 5.6.

5.2 Data analysis

5.2.1 Spitzer photometry

The first step in the analysis concerned the determination of the stellar density from the light curve, following Seager & Mallén-Ornelas (2003). It was derived using a combined MCMC fit with both our data from the Spitzer transits and the 61 HARPS radial velocities (RVs) from the discovery paper (Bonfils et al. 2012). We use a quadratic law for the limb-darkening. We draw the theoretical values and corresponding uncertainties of the coefficients u_1 and u_2 from the tables of Claret & Bloemen (2011) for the T_{eff},$\log g$, and [Fe/H] determinations reported in Sect. 5.3. The resulting distributions of u_1 and u_2 are then used as normal priors in the fit. The first run yields an eccentricity signal compatible with a circular orbit ($\sqrt{e}\cos\omega = -0.09 \pm 0.14$ and $\sqrt{e}\sin\omega = 0.00 \pm 0.22$). Our analysis assuming a circular orbit yields a stellar density $\rho = 2.91^{+0.37}_{-0.33}\rho_\odot$ that we use as a constraint for the derivation of the stellar parameters in Sect. 5.3. The phase-folded Spitzer light curve is shown in Fig. 5.1.

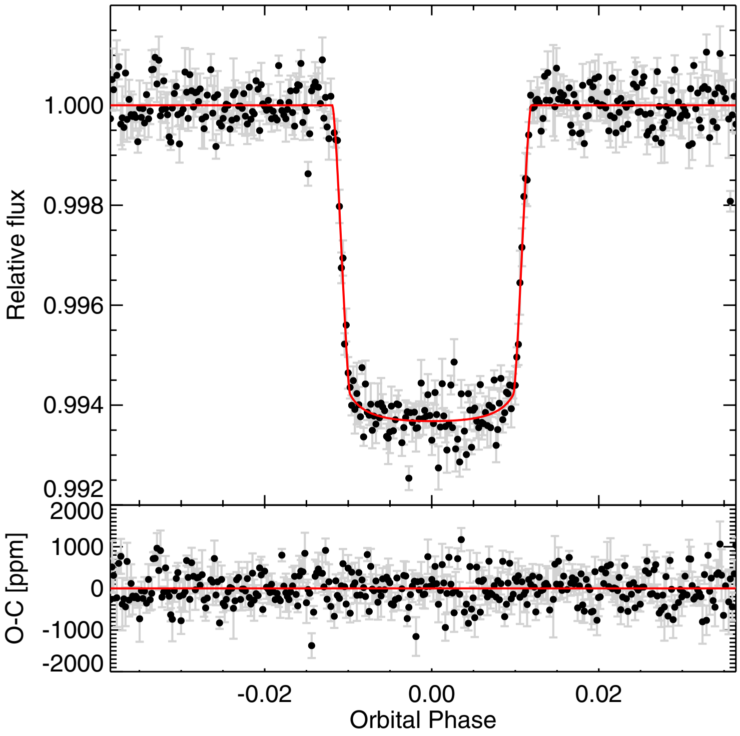

Figure 5.1: GJ 3470 b detrended and phase-folded transit light curve combining our two 4.5 μm Spitzer/IRAC visits, with the best-fit transit model superimposed (see Section 5.4). Data points are binned in 2 minute intervals, and residuals are shown in the bottom panel.

5.2.2 Spectroscopic measurements

In order to obtain the metallicity and effective temperature of GJ3470 we analysed the spectra from two different spectrographs, FIRE (Simcoe et al. 2008), in the infrared and HARPS (Mayor et al. 2003; Pepe et al. 2004) in the visible. From the FIRE spectrum we measured a number of spectral features for the purpose of deriving its spectroscopic properties, particularly [Fe/H] and T_{eff} , using recent calibrations presented for M dwarfs. We follow closely the prescriptions of Rojas-Ayala et al. (2012), Terrien et al. (2012), and Mann et al. (2013) to measure equivalent widths (EWs) as well as water indices, and to estimate the pseudo-continuum needed for the above metallicity calibrations. The EWs and spectral indices computed from our FIRE spectrum yield the metallicities for GJ 3470 shown in the first four lines of Table 2 of the paper that resulted from this work (see Sect. 5.6). A spectroscopic estimate of the effective temperature of GJ 3470 was obtained using the temperature-sensitive H_2O-K2 index in the K band as defined by Rojas-Ayala et al. (2012), resulting in an effective temperature of 3750 ± 300 K.

An additional spectroscopic estimate of the metallicity of GJ 3470 was obtained from our calibration described in Sect. 4.2. This calibration achieves an improved precision of ~ 0.10 dex. The result of this measurement for GJ 3470 is $+0.08 \pm 0.10$, and is also collected in Table 2. The five estimates of [Fe/H] from the FIRE and HARPS spectra are consistent with each other, and we therefore adopt the weighted average, [Fe/H] = $+0.20 \pm 0.10$, in which the uncertainty is a more conservative estimate than the formal error of the mean.

5.3 Stellar characterisation

Mass ($M_\star$) and radius ($R_\star$) estimates for exoplanet hosts are typically obtained via stellar evolutionary models (e.g. Baraffe et al. 1998; Dotter et al. 2008). However, there are significant disagreements between predictions from models and very precise measurements of low mass stars in double lined eclipsing binaries (e.g. Torres 2013). Therefore, we will only use empirical relations for the stellar parameters, as well as the stellar density calculated from the Spitzer light curve in Sect. 5.2.1. There is no measurement for the parallax. As a consequence, we used the infrared mass-luminosity relations of Delfosse et al. (2000) and the surface-brightness relations of Kervella et al. (2004) simultaneously to obtain an estimate of the stellar mass and radius consistent with the measured mean density.

The next step followed a Monte-Carlo approach by calculating for 10^5 times the values of $M_\star$, $R_\star$, and parallax using the above relations, and drawing the photometry and stellar density from appropriate gaussian distributions. Then, we took the mode of the distributions assigning 1σ uncertainties given by the 15.85 and 84.13 percentiles of these distributions. At the end of each draw, we calculate the mass as the average of the J-, H-, and K-band relations of Delfosse et al. (2000), each considered to have a conservative uncertainty of 10%. The radius is the average of the two relations of Kervella et al. (2004) that yield the smallest scatter in the angular diameter ($\sim$ 1% for the V-H and V-K relations). The uncertainties include all the photometric errors, the error on $\rho_\star$, as well as the scatter in the empirical relations.

We obtained $M_\star = 0.539^{+0.047}_{-0.043}$, $R_\star = 0.568^{+0.037}_{-0.031}$, and $\pi = 32.4^{+2.1}_{-1.9}$. Fig. 5.2 shows the location of GJ3470 in the mass-radius diagram for low-mass stars, along with all the measurements for all similar objects with a $M_\star$ and $R_\star$ with a precision better than 5%, taken from Torres (2013). The constraint regarding the stellar density is also indicated. Our mass is very close to the one obtained in the discovery paper ($M_\star = 0.54 \pm 0.07 M_\odot$) but our radius is 13% larger (the Bonfils et al. (2012) radius is $0.50 \pm 0.06 R_\odot$.

For consistency reasons we decided to obtain radius values from the calibrations recently proposed

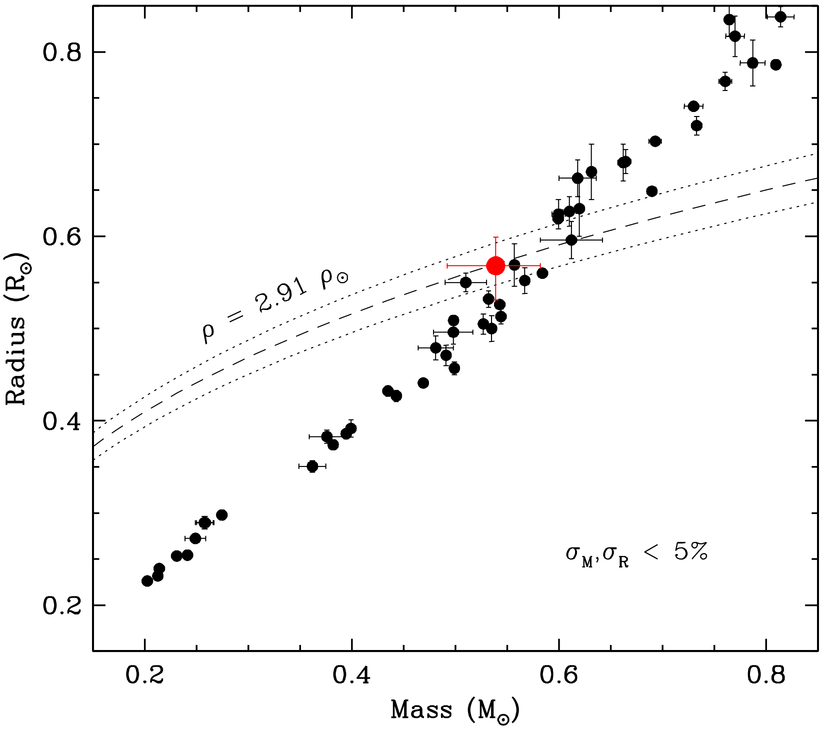

Figure 5.2: Mass and radius estimates for GJ 3470 (large red dot) compared with measurements for other low-mass stars in double-lined eclipsing binaries with relative errors in $M_\star$ and $R_\star$ less than 5% (see Torres 2013). The constraint on the mean stellar density derived from our Spitzer observations is indicated with the dashed line (dotted lines representing the 1σ uncertainties).

by Boyajian et al. (2012), based on angular diameter measurements from interferometry and HIPPARCOS parallaxes (van Leeuwen 2007), and include a dependence on metallicity. We obtained a value of $0.513 \pm 0.043 R_\odot$, within 1σ of our value, by averaging the $V-H$, $V-J$, and $V-K_s$ calibrations. We also used the same colour indexes, along with the adopted value of [Fe/H] to make another estimate of the T_{eff}, using the calibrations presented in the same paper. This exercise yielded an average value for temperature of 3630 ± 100K. A final T_{eff} estimate is inferred from the colour-temperature calibrations of Casagrande et al. (2008) using the same indices, but adjusted for the metallicity using evolutionary models of Dotter et al. (2008), in a differential sense, first reading off from a [Fe/H] = +0.20 dex isochrone the stellar mass that yields the same colour indices as we measure, and then comparing the corresponding temperature with that for a star of the same mass on a solar-metallicity isochrone. This exercise is insensitive to the age adopted for the isochrone. This exercise yields a correction of +140K, giving a temperature of 3500 ± 100 K. Finally, by using the three determinations, we end up with a weighted average of $T_{eff} = 3600 \pm 100 K$.

5.4 Planetary and orbital parameters

The final planetary and orbital parameters were calculated using the stellar parameters calculated in Sects. 5.2.2 and 5.3, within a MCMC framework, similar to the one used in Sect. 5.2.1, with the addition of a stellar mass prior, using the distribution derived in the previous section, and drawing from it a random value at each step of the MCMC procedure. The light curves from Spitzer and the 61 RVs from HARPS were also included. The results are included in Table 2 of the paper that resulted from this work (see Sect. 5.6), where the adopted value for each parameter is the marginalised posterior distribution from the MCMC fit. The uncertainties correspond to the 68.3% region around the mean of the same distributions. The final model and phase-folded Spitzer light curve is displayed in Fig. 5.1.

The planetary radius is estimated to be $R_p = 4.83^{+0.22}_{-0.21} R_\oplus$, which is 13% larger than reported by Bonfils et al. (2012). The increase is mainly due to the larger stellar radius derived in Sect. 5.3. We obtain a value of $13.9^{+1.5}_{-1.4} M_\oplus$ for the planetary mass. Combining planetary mass and radius, we reach to a very low value for the density of GJ3470 b, $\rho_p = 0.72^{0.13}_{-0.12} gcm^{-3}$, which is 33% smaller than the estimate from the discovery paper.

5.5 Exploring the interior composition of GJ3470 b

GJ3470 b is a vey interesting planet in the context of planet formation in evolution due to its low density. Its radius is $20\% \pm 6\%$ larger than Uranus ($R_{♅} = 4.01 R_\oplus$), despite having a similar mass ($M_{♅} = 14.5 M_\oplus$). Among the low mass transiting planets ($M_p < 30 M_\oplus$), only Kepler-11, Kepler-18, Kepler-30, and HAT-P-26 have planets with lower densities, as shown in Fig. 5.3.

The most probable source of the H/He gas of GJ3470 b is the protoplanetary nebula. Alternative sources such as sublimated ices and outgassing may be important for less massive and denser planets (e.g. GJ1214 b, Rogers & Seager 2010), but they cannot be dominant in our case, because its bulk density is too low for the ices (e.g., H_2O, CO2) to dominate the gas layer of the planet. Moreover, the gas layer of GJ3470 b is too big, as the planet radius exceed the upper limits for outgassed planets during formation (Rogers et al. 2011). Quantitatively, the nebular H/He may contribute between 5% to 24% to GJ3470 mass, according to our models.

Following Rogers & Seager (2010), we apply a fully differentiated model for the planet's interior structure consisting of (from the centre of the planet outward) an iron core, silicate layer, ice layer, and H/He gas envelope to explore which bulk compositions are consistent with the measured mass and radius of GJ 3470 b. Both the planet's bond albedo A (that scales with the planet's temperature $T_{eq} = (1-A)^{1/4}(683 \pm 27)$K, and the planet's intrinsic luminosity L_p (used as proxy for the planet's age) are unknown. We therefore adopt fiducial values of $A = 0.3$ and $L_p/M_p = 10^{-10} Wkg^{-1}$. Varying the planet mass and radius within their 1σ bounds, and considering a range of plausible planet energy budgets affects the H/He mass fractions by up to ± 0.05. For a rocky Earth-like heavy element interior composition (32% Fe, 68% silicate, 0% H_2O), GJ 3470 b's H/He envelope mass is constrained to $M_{XY}/M_p = 0.16 \pm 0.05$, while for a denser iron-enhanced Mercury-like rocky interior (70% Fe, 30% silicate, 0% H_2O), $M_{XY}/M_p = 0.17 \pm 0.05$. Less H/He is needed if GJ 3470 b has an ice-rich interior composition; for instance, for a heavy element interior with 16% Fe, 34% silicate, 50% H_2O, $M_{XY}/M_p = 0.12 \pm^{0.05}_{0.04}$.

It is not possible to constraint the interior composition of GJ3470 b by its mass and radius alone. Planet formation and evolution theories can give us some insights. If GJ3470 b was formed outside the snow line and then migrated inward, its interior would be ice-rich. However, if it was formed *in situ*, its interior would be rock dominated. Despite that , the planetesimals beyond the ice line could also provide

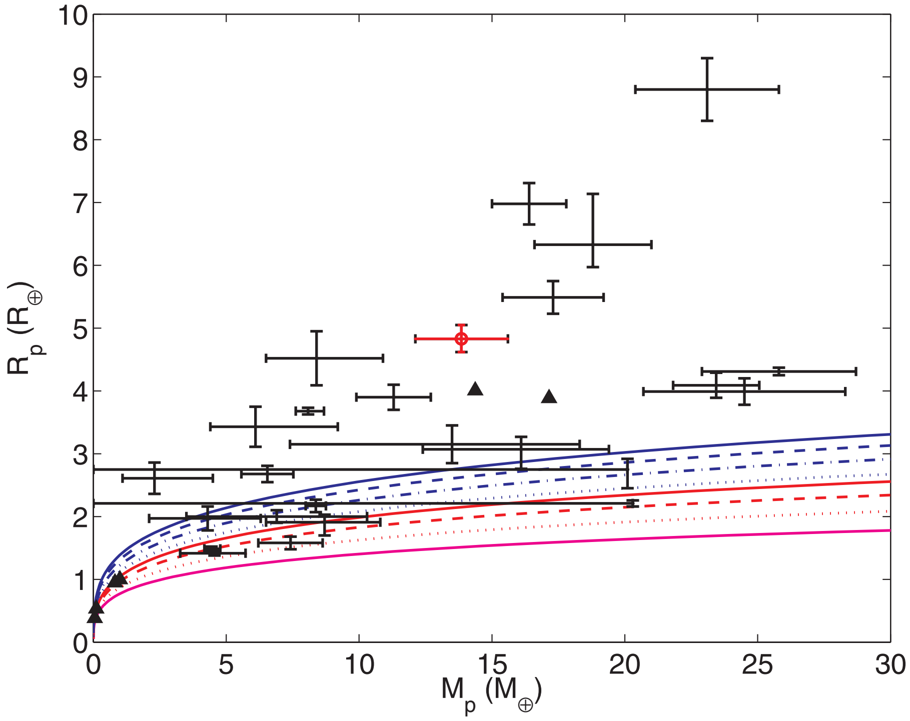

Figure 5.3: Mass-radius relationships of small transiting planets. GJ 3470 b is highlighted in red. Other small transiting exoplanets with dynamical mass constraints (CoRoT-7 b, Kepler-4 b, Kepler-10 b, Kepler-11 b, c, d, e, f, Kepler- 18 b, c, d, Kepler-19 b, Kepler-20 b, c, d, Kepler-30 b, d, Kepler-36 b, c, 55 Cnc e, GJ 1214 b, GJ 436 b, HAT-P-11 b, and HAT-P-26 b) are plotted in black. The solar system planets are indicated with solid triangles. The curves are illustrative constant-temperature mass-radius relations from Seager et al. (2007). The solid lines are homogeneous-composition planets: water ice (blue solid), MgSiO3 perovskite (red solid), and iron (magenta solid). The non-solid lines are mass-radius relations for differentiated planets: 75% water ice, 22% silicate shell, and 3% iron core (blue dashed); Ganymede-like with 45% water ice, 48.5% silicate shell, and 6.5% iron core (blue dot-dashed); 25% water ice, 52.5% silicate shell, and 22.5% iron core (blue dotted); Earth-like with 67.5% silicate mantle and 32.5% iron core (red dashed); and Mercury-like with 30% silicate mantle and 70% iron core.

icy materials to closer-in planets (Ogihara & Ida 2008). On the other hand, Lissauer (2007) and Kennedy et al. (2007) predict that planets and planetesimals formed within 1 AU of M dwarfs are unlikely to have large quantities of ices when the effect of the M dwarf pre-main sequence evolution is taken into account.

5.5.1 Summary

Our 4.5 μm Spitzer observations have enabled us to refine the planetary and system parameters of the Neptune-size planet GJ 3470 b, improving its radius to $R_p = 4.8 \pm 0.2 R_\oplus$, which is 13% larger than previously reported in the literature. As a result, the revised planetary density, $\rho_p = 0.72 \pm 0.13 gcm^{-3}$, is 33% smaller than before. These changes come mostly from revisions of the stellar parameters (particularly $R_\star$), which have been frustratingly difficult to determine accurately in the past due to known discrepancies between observations and standard stellar evolution models for lower main-sequence stars. In this work we have relied for this only on empirical mass-luminosity and surface-brightness relations that have been widely employed in other contexts, and on the strong constraint on the mean stellar density provided by our Spitzer observations. In the process we have inferred an accurate distance for the star.

GJ 3470 b provides a valuable example of an extremely low-density planet, representative of a significant portion of the exoplanet candidates found by the Kepler mission to date. The brightness of the host star ($K_s = 7.99$ mag) combined with its large planet-to-star radius ratio renders GJ 3470 b a promising candidate for future atmospheric characterisation, which could provide clues on its formation pathway. Indeed, GJ 3470 b's low surface gravity translates to a large atmospheric scale height for a given atmospheric composition, favouring follow-up studies applying transmission spectroscopy. GJ 3470 b, GJ 436 b, and GJ 1214 b are a remarkable sample of volatile-rich planets orbiting bright nearby stars, pushing the field of comparative exoplanetology further toward low-mass planets.

5.6 Paper: *SPITZER* observations of Gj 3470b: a very low-density Neptune-size planet orbiting a metal-rich M dwarf

Abstract.

We present Spitzer/IRAC 4.5μm transit photometry of GJ 3470 b, a Neptune-size planet orbiting an M1.5 dwarf star with a 3.3 day period recently discovered in the course of the HARPS M-dwarf survey. We refine the stellar parameters by employing purely empirical mass-luminosity and surface brightness relations constrained by our updated value for the mean stellar density, and additional information from new near-infrared spectroscopic observations. We derive a stellar mass of $M_\star = 0.539^{+0.047}_{-0.03} M_\odot$ and a radius of $R_\star = 0.568^{+0.037}_{-0.031} R_\odot$. We determine the host star of GJ 3470 b to be metal-rich, with a metallicity of [Fe/H] = $+0.20 \pm 0.10$ and an effective temperature of T_{eff} = 3600 ± 100 K. The revised stellar parameters yield a planetary radius $R_p = 4.83^{+0.22}_{-0.21} R_\oplus$ that is 13% larger than the value previously reported in the literature. We find a planetary mass $M_p = 13.9^{+1.5}_{-1.4} M_\oplus$ that translates to a very low planetary density, $\rho_p = 0.72^{+0.13}_{-0.12} gcm^{-3}$, which is 33% smaller than the original value. With a mean density half of that of GJ 436 b, GJ 3470 b is an example of a very low-density low-mass planet, similar to Kepler-11 d, Kepler-11 e, and Kepler-18 c, but orbiting a much brighter nearby star that is more conducive to follow-up studies.

Contribution. In this paper I contributed to the observations of GJ3470 using the HARPS spectrograph. I also did the data analysis of the HARPS and FIRE spectra using different methods to obtain the metallicity and effective temperature for this star.

The Astrophysical Journal, 768:154 (9pp), 2013 May 10 doi:10.1088/0004-637X/768/2/154

SPITZER OBSERVATIONS OF GJ 3470 b: A VERY LOW-DENSITY NEPTUNE-SIZE PLANET ORBITING A METAL-RICH M DWARF*

Brice-Olivier Demory[1], Guillermo Torres[2], Vasco Neves[3,4,5], Leslie Rogers[6], Michaël Gillon[7], Elliott Horch [8,12], Peter Sullivan[9], Xavier Bonfils[5], Xavier Delfosse[5], Thierry Forveille[5], Christophe Lovis[10], Michel Mayor[10], Nuno Santos[3,4], Sara Seager[1,9], Barry Smalley[11], and Stephane Udry[10]
[1] Department of Earth, Atmospheric and Planetary Sciences, Massachusetts Institute of Technology,
77 Massachusetts Ave., Cambridge, MA 02139, USA; demory@mit.edu
[2] Harvard-Smithsonian Center for Astrophysics, 60 Garden St., Cambridge, MA 02138, USA
[3] Centro de Astrofísica, Universidade do Porto, Rua das Estrelas, 4150-762 Porto, Portugal
[4] Departamento de Física e Astronomia, Faculdade de Ciências, Universidade do Porto, Rua do Campo Alegre, 4169-007 Porto, Portugal
[5] UJF-Grenoble 1/CNRS-INSU, Institut de Planétologie et d'Astrophysique de Grenoble (IPAG) UMR 5274, Grenoble, F-38041, France
[6] Department of Astrophysics, California Institute of Technology, MC 249-17, Pasadena, CA 91125, USA
[7] Institut d'Astrophysique et de Géophysique, Université de Liège, Allée du 6 Août, 17, Bat. B5C, Liège 1, Belgium
[8] Department of Physics, 501 Crescent Street, Southern Connecticut State University, New Haven, CT 06515, USA
[9] Department of Physics and Kavli Institute for Astrophysics and Space Research, MIT, 77 Massachusetts Avenue, Cambridge, MA 02138, USA
[10] Observatoire de Genève, Université de Genève, 51 ch. des Maillettes, CH-1290 Versoix, Switzerland
[11] Astrophysics Group, Keele University, Staffordshire, ST55BG, UK

Received 2013 January 28; accepted 2013 March 4; published 2013 April 25

ABSTRACT

We present *Spitzer*/IRAC 4.5 μm transit photometry of GJ 3470 b, a Neptune-size planet orbiting an M1.5 dwarf star with a 3.3 day period recently discovered in the course of the HARPS M-dwarf survey. We refine the stellar parameters by employing purely empirical mass–luminosity and surface brightness relations constrained by our updated value for the mean stellar density, and additional information from new near-infrared spectroscopic observations. We derive a stellar mass of $M_\star = 0.539^{+0.047}_{-0.043}\,M_\odot$ and a radius of $R_\star = 0.568^{+0.037}_{-0.031}\,R_\odot$. We determine the host star of GJ 3470 b to be metal-rich, with a metallicity of $[\mathrm{Fe/H}] = +0.20 \pm 0.10$ and an effective temperature of $T_{\rm eff} = 3600 \pm 100$ K. The revised stellar parameters yield a planetary radius $R_p = 4.83^{+0.22}_{-0.21}\,R_\oplus$ that is 13% larger than the value previously reported in the literature. We find a planetary mass $M_p = 13.9^{+1.5}_{-1.4}\,M_\oplus$ that translates to a very low planetary density, $\rho_p = 0.72^{+0.13}_{-0.12}$ g cm^{-3}, which is 33% smaller than the original value. With a mean density half of that of GJ 436 b, GJ 3470 b is an example of a very low-density low-mass planet, similar to Kepler-11 d, Kepler-11 e, and Kepler-18 c, but orbiting a much brighter nearby star that is more conducive to follow-up studies.

Key words: planetary systems – stars: individual (GJ 3470) – techniques: photometric – techniques: spectroscopic

Online-only material: color figures

1. INTRODUCTION

In the regime of low mass exoplanets only a handful of those known to periodically pass in front of their host stars have transits that are deep enough and orbit parent stars that are bright enough to make them amenable to extensive follow-up observations. The *Kepler* mission has recently announced a harvest of more than 2700 planetary candidates identified since the launch of the spacecraft in 2009 (Batalha et al. 2013). About 10% are Jupiter-size planets with radii between 0.7 and 2.0 Jupiter radii, while more than 55% are Neptune-size planets with radii between 2 and 6 Earth radii. On the other hand, among the 241 confirmed transiting exoplanets (coming mainly from ground-based surveys), 62% are Jupiter-size planets with radii between 0.7 and 2.0 Jupiter radii.[13] It is now clear from *Kepler* and other studies that short-period Jupiter-size objects make up a relatively small fraction of the exoplanet population (e.g., Howard et al. 2010, 2012; Wittenmyer et al. 2011). This stark contrast between confirmed exoplanets and the large underlying population glimpsed by *Kepler* has motivated intense efforts toward the characterization of smaller planets, in order to reach a comparable state of knowledge to what has been learned about the hot-Jupiter population. These efforts already began several years ago with the launch of a number of ground-based projects dedicated to M-dwarf monitoring using both spectroscopy (e.g., the HARPS program; Bonfils et al. 2013) and photometry (e.g., MEarth; Nutzman & Charbonneau 2008). Planets orbiting M-dwarf stars offer the possibility to probe smaller planets for a given transit depth, because of the favorable star-to-planet radius ratio. GJ 436 b (Butler et al. 2004; Gillon et al. 2007) and GJ 1214 b (Charbonneau et al. 2009) are the smallest planets orbiting M stars with *K* magnitude brighter than nine, enabling detailed follow-up studies both from the ground and from space (e.g., Stevenson et al. 2010; Bean et al. 2010).

In the Neptune-mass range, thanks to its relatively large transit depth and host star brightness, GJ 436 b remains a "Rosetta stone" for our understanding of a whole class of exoplanets, shown to be ubiquitous in our Galaxy. With a mass 22 times that of Earth and a radius 4 times larger than our home planet, GJ 436 b has a relatively high density ($\rho_p = 1.69^{+0.14}_{-0.12}$ g cm^{-3}; Torres et al. 2008), suggesting the presence of a massive core made of

---

* This paper includes data gathered with the 6.5 m Magellan Telescopes located at Las Campanas Observatory, Chile.

[12] Visiting Astronomer, Kitt Peak National Observatory, National Optical Astronomy Observatories, which is operated by the Association of Universities for Research in Astronomy (AURA), Inc., under cooperative agreement with the National Science Foundation.

[13] Source: http://www.exoplanets.org

silicates and/or ices. However, a H/He envelope is needed to reproduce its observed radius (e.g., Figueira et al. 2009; Rogers & Seager 2010a). The improvement in the planetary radius of this object brought about by *Spitzer* observations placed significant constraints on the range of possible compositions of GJ 436 b's interior. A key question that still needs to be addressed, however, is the extent to which GJ 436 b is representative of the entire exo-Neptune population.

GJ 3470 b is a new transiting Neptune-size planet discovered in the past year (Bonfils et al. 2012). It orbits a $K_s = 7.99$ mag, M1.5 dwarf with a period of 3.337 days. With a published mass of 14.0 ± 1.7 Earth masses and a radius of 4.2 ± 0.6 Earth radii (Bonfils et al. 2012), GJ 3470 b has a mean density $\rho_p = 1.07 \pm 0.43$ g cm^{-3} that is significantly smaller than that of GJ 436 b. The *Kepler* mission confirmed several of these so-called "low-density Neptunes." The first two were Kepler-11 d and e (Lissauer et al. 2011), both belonging to the most populated transiting planet system known to date, and the third was Kepler-18 c (Cochran et al. 2011), also a member of a multi-planet system. These objects represent the tip of the iceberg, as several hundred Neptune-size planet candidates have already been detected by *Kepler* and await confirmation. Unfortunately, most of these *Kepler* planets orbit faint stars and exhibit shallow transit depths that render follow-up studies very challenging, if not impractical altogether. Aside from *Kepler*, the ground-based survey HAT discovered the low-density Neptune HAT-P-26 b (Hartman et al. 2011) which, until the discovery of GJ 3470 b, represented the most promising target for follow-up studies. However, as compared to GJ 3470 b, the smaller planet-to-star area ratio coupled with the lower brightness of its larger K1 host star ($K = 9.6$) makes HAT-P-26 b a less favorable target for follow-up studies. GJ 3470 b therefore presents an ideal opportunity to investigate the internal structure, atmospheric composition, and possible formation pathways of low-density Neptune-size planets (e.g., Rogers et al. 2011).

All transit photometry available so far for GJ 3470 has been collected from the ground. While these time series confirm the transiting nature of GJ 3470 b, they do not precisely constrain the transit parameters, resulting in poorly determined planetary properties. We present in this paper the analysis of two transits of GJ 3470 b obtained with the *Spitzer Space Telescope* at 4.5 μm in the frame of our DDT program (Demory et al. 2012a), submitted shortly after GJ 3470 b's discovery. These data yield a significant refinement of the system parameters. The paper is organized as follows. Section 2 describes the observations and data reduction, while Section 3 presents the photometric and spectroscopic data analyses. Section 4 is dedicated to the stellar characterization, and the resulting planetary parameters are reported in Section 5. We discuss GJ 3470 b's internal structure and composition in Section 6.

2. OBSERVATIONS AND DATA REDUCTION

2.1. *Spitzer IRAC 4.5 μm Photometry*

We observed two consecutive transits of GJ 3470 b at 4.5 μm using *Spitzer*'s InfraRed Array Camera (IRAC; Fazio et al. 2004). Observations took place on 2012 June 11 and 15 UTC as part of our DDT program PID 80261. For each transit we obtained 780 sets of 64 subarray frames each, with an exposure time of 0.40 s per frame. Each Astronomical Observation Request (AOR) lasted 6.5 hr, including 30 minutes overhead for the Pointing Calibration and Reference Sensor peak-up sequence. This step allowed GJ 3470 to be precisely slewed on the position of maximum sensitivity on the 4.5 μm channel subarray field-of-view (Ingalls et al. 2012; Demory et al. 2012b). All data were processed by the *Spitzer* pipeline version S19.1.0, which produced the basic calibrated data necessary for our reductions. We first convert fluxes from the *Spitzer* units of specific intensity (MJy/sr) to photon counts, and transform the data timestamps from $\mathrm{BJD_{UTC}}$ to $\mathrm{BJD_{TDB}}$ following Eastman et al. (2010). We then perform aperture photometry on each subarray image using the APER routine from the IDL Astronomy User's Library.[14] We compute the stellar fluxes in aperture radii ranging between 1.8 and 4.0 pixels, the best results being obtained with an aperture radius of 3 pixels. We use background annuli extending from 11 to 15.5 pixels from the Point Response Function center. For each block of 64 subarray images, we discard the discrepant values for the measurements of flux, background, and x–y centroid positions using a 10σ median clipping for the four parameters. We then average the resulting values, the photometric errors being taken as the uncertainties on the average flux measurements. At this stage, a 50σ clipping moving average is used on the resulting light curve to discard obviously discrepant subarray-averaged fluxes. Close examination of the resulting time-series reveals a sharp increase of the background and stellar fluxes, corresponding to the well-known "ramp" effect seen in other warm *Spitzer* observations (see, e.g., Knutson et al. 2012). The raw photometry for both AORs is shown in Figure 1.

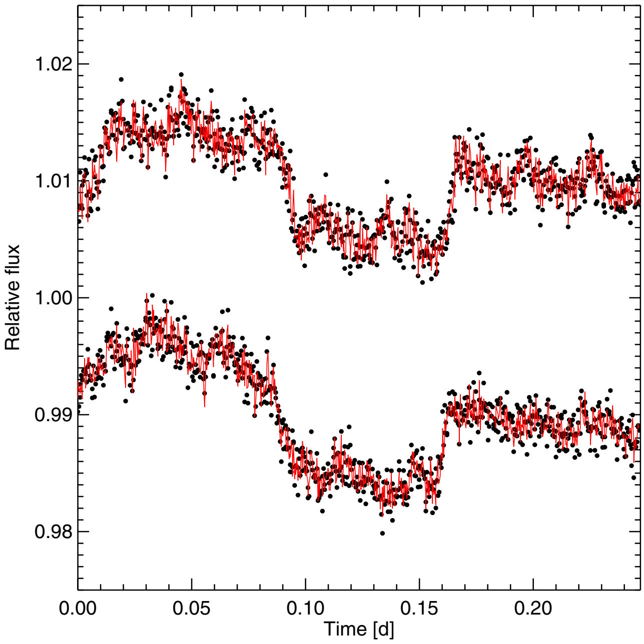

Figure 1. *Spitzer*/IRAC 4.5 μm photometry. Raw photometry from the two AORs is displayed after normalization. The optimal baseline model (logarithmic ramp model added to a second-order polynomial fit for the centroid position and a time-dependent trend (see Section 3) is superimposed for each AOR in red.

(A color version of this figure is available in the online journal.)

2.2. *WIYN Speckle Observations*

We supplemented our GJ 3470 b *Spitzer* photometry with speckle observations to explore the possibility of blended companions at close angular separations from GJ 3470. Speckle observations of GJ 3470 were obtained at the WIYN 3.5 m

---

[14] http://idlastro.gsfc.nasa.gov/contents.html

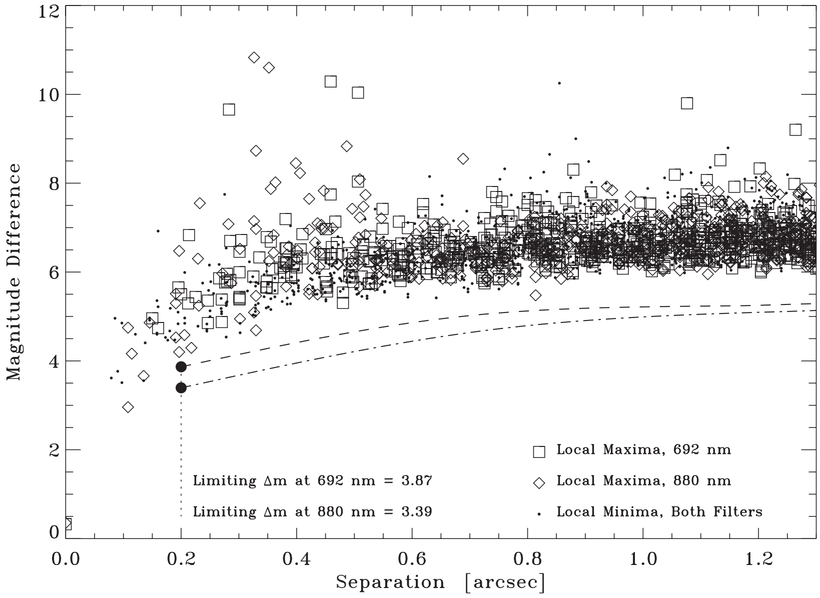

Figure 2. Detection limit analysis of GJ 3470 based on speckle data. The squares and diamonds indicate the magnitude differences of local maxima in each reconstructed image as a function of separation from the central star, and points are local minima. The curves indicate the 5σ detection limit based on the statistics of the these maxima and minima. The dashed curve is the result for the 692 nm reconstructed image, and the dot-dashed curve is the result for the 880 nm image. These curves indicate a greater than 4 mag sensitivity in the limiting Δm at most separations.

telescope on 2012 December 2. The camera used was the Differential Speckle Survey Instrument, which is described by Horch et al. (2009). It is a dual-channel instrument that records images in two colors simultaneously. In the case of this observation, the filters used had center wavelengths of 692 nm and 880 nm, with filter widths of 40 and 50 nm, respectively. A speckle sequence of 3000 50 ms frames was taken on the target, followed by 1000 frames taken on a bright point source (HR 3163) located near in the sky to GJ 3470. These latter data are used as an estimate of the speckle transfer function for deconvolution in the reduction process. Reconstructed images are formed from the speckle data using the technique of bispectral analysis, which is described, e.g., by Horch et al. (2012). We then analyze the final images to determine the detection limits of faint companions near GJ 3470 using the technique described in the same paper.

Figure 2 shows these detection limits based on the final diffraction-limited images in each filter. It is clear that there is no companion to the limit of our detection capabilities at a separation greater than 0.″2. At 0.″2 the limiting Δm for the 692 nm image is 3.87 mag, and for the 880 nm image it is 3.39 mag. Inside of this limit, as one approaches the central star, the limiting Δm becomes smaller as the peaks and valleys of the reconstructed image get larger. In studying the two images, we find that none of the peaks near the central star are in the same position in both images, which is a good indication that they are probably not real stars but noise peaks. One of the advantages of the two independent channels in the instrument is to see if the positions of faint peaks match. We conclude that, to the limit of our detection at WIYN, there is no resolvable companion.

2.3. *Magellan/FIRE Near-infrared Spectroscopy*

Spectroscopic properties such as the effective temperature, T_{eff}, and metallicity, [Fe/H], needed to establish the physical parameters of the parent stars of transiting planets have usually been difficult to determine for M dwarfs. Several studies in the past year have presented calibrations of [Fe/H] or T_{eff} in terms of easily measurable spectroscopic indices in the *H*-band and *K*-band regions that represent a significant advancement in the field. Toward this goal, we obtained a near-infrared spectrum of GJ 3470 on 2012 November 12 with the Folded-port Infrared Echellette (FIRE) spectrograph at the 6.5 m Magellan Baade telescope. FIRE delivers $R = 6000$ spectra from 0.83 to 2.5 μm in a single-object, cross-dispersed setup (Simcoe et al. 2008). We used an exposure time of 8.5 minutes on GJ 3470 and 105 s on the A0V telluric standard HD 58296. We reduce the data using FIRE's pipeline FIREHOSE, which employs the methods of Vacca et al. (2003) for telluric correction. An internal ThAr lamp provides wavelength calibration of both the GJ 3470 and HD 58296 spectra. The signal-to-noise ratio in the reduced spectrum is $>$200 in the *K* band, where H_2O features near 2.21 and 2.26 μm fall on order 20 of FIRE's 21 cross-dispersed grating orders. Strong OH emission lines from the sky (which can introduce shot noise and residuals from sky subtraction) do not fall directly on these features. The measurement of various spectroscopic indices from this FIRE observation is described in Section 3.2.1.

3. DATA ANALYSIS

3.1. *Spitzer Photometry*

3.1.1. *Baseline Model Selection*

We first perform an individual analysis of each *Spitzer* AOR to determine the optimal baseline model, which accounts for time- and position-dependent systematic effects relevant to our IRAC 4.5 μm observations. We employ for this purpose our adaptive Markov Chain Monte Carlo (MCMC) implementation described by Gillon et al. (2010). We test six baseline models of increasing complexity, and compare their Bayesian information criteria (BIC; see, e.g., Gelman et al. 2003) to choose the baseline model that yields the highest marginal likelihood. We correct for the well-known "pixel-phase" effect using a second- to fourth-order *x*–*y* position-dependent polynomial, while the "ramp" is corrected using a second-order logarithmic model. We also check for time-dependent trends of instrumental and/or stellar origin by adding linear or quadratic functions of time to our baseline models. We additionally explore the correlation of the stellar flux and background time series with the full width at half-maximum of the point response function (Demory et al. 2012b). We find for both AORs the lowest BIC to correspond to a model including a second-order position-dependent polynomial, a second-order logarithmic ramp, and a time-dependent linear trend. Our analysis yields an rms of 362 ppm and 369 ppm per 5 minute interval in the first and second AORs, respectively, with negligible contribution from correlated noise.

3.1.2. Determination of the Stellar Density

We perform a combined MCMC fit including our two *Spitzer* transits and the 61 HARPS radial velocities (RVs) published in the discovery paper (Bonfils et al. 2012). The main goal of this step is to derive the stellar density from the *Spitzer* photometry (Seager & Mallén-Ornelas 2003), to enable the derivation of the stellar and planetary physical parameters. The following system parameters ("jump parameters") are left free in the MCMC fit, using uniform priors: the orbital period P, transit depth dF (planet-to-star area ratio, $(R_p/R_\star)^2$), transit duration W, time of minimum light T_0, impact parameter $b = a\cos i/R_\star$, the parameter $K' = K\sqrt{1-e^2}P^{1/3}$, where K is the RV semi-amplitude, $\sqrt{e}\cos\omega$ and $\sqrt{e}\sin\omega$. We use a quadratic law for the limb-darkening. We draw the theoretical values and corresponding uncertainties of the coefficients u_1 and u_2 from the tables of Claret & Bloemen (2011) for the $T_{\rm eff}$, $\log g$, and [Fe/H] determinations reported in Section 4. We use the resulting distributions for u_1 and u_2 as normal priors in our MCMC fit. We use the linear combinations $c_1 = 2u_1 + u_2$ and $c_2 = u_1 - 2u_2$ as jump parameters, rather than u_1 and u_2, to minimize the correlations of the resulting uncertainties (Holman et al. 2006). At each step of the MCMC fit, the stellar density is derived from this set of parameters and Kepler's third law. We run two chains of 10^5 steps each, where the first 20% are discarded. We assess the good convergence and mixing of the chains employing the Gelman–Rubin statistic (Gelman & Rubin 1992). We add a 2.0 m s^{-1} jitter contribution in quadrature to the RV error bars to match the rms of the residuals. This first combined run yields an eccentricity signal compatible with a circular orbit ($\sqrt{e}\cos\omega = -0.09 \pm 0.14$ and $\sqrt{e}\sin\omega = 0.00 \pm 0.22$). We therefore repeat the fit setting $\sqrt{e}\cos\omega$ and $\sqrt{e}\sin\omega$ to zero. The difference in BIC between an eccentric and a circular orbit is ΔBIC = 15, translating to an odds ratio of ~1800, hence favoring the circular model we adopt in the following. Our analysis assuming a circular orbit yields a stellar density $\rho_\star = 2.91^{+0.37}_{-0.33}\,\rho_\odot$ that we use as a constraint for the derivation of the stellar parameters in Section 4. The phase-folded *Spitzer* light curve is shown in Figure 3.

3.2. Spectroscopic Measurements

3.2.1. FIRE Spectral Analysis

We measure a number of spectral features in our FIRE spectrum of GJ 3470 for the purpose of deriving its spectroscopic properties, particularly [Fe/H] and $T_{\rm eff}$, using recent calibrations presented for M dwarfs. We follow closely the prescriptions of Rojas-Ayala et al. (2012), Terrien et al. (2012), and Mann et al. (2013) for measuring equivalent widths (EWs) as well as water indices, and to estimate the pseudo-continuum needed for the above metallicity calibrations.

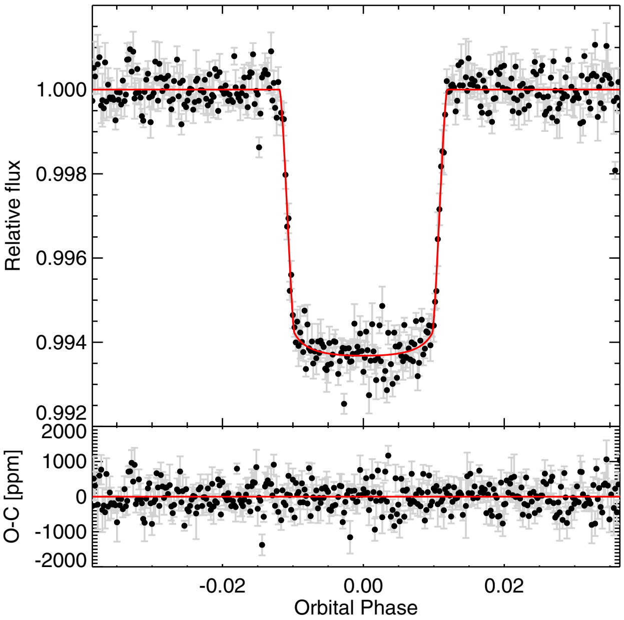

Figure 3. GJ 3470 b detrended and phase-folded transit light curve combining our two 4.5 μm *Spitzer*/IRAC visits, with the best-fit transit model superimposed (see Section 5). Data points are binned in 2 minute intervals, and residuals are shown in the bottom panel.

(A color version of this figure is available in the online journal.)

For the Rojas-Ayala et al. (2012) calibration, we measure the Na doublet (2.206 and 2.209 μm) and the Ca triplet (2.261, 2.263, and 2.265 μm) following the integration limits and continuum points of their Table 2. The pseudo-continuum flux of each feature is taken from a linear fit to the median flux within a 3 nm region around each continuum point. The water index, H_2O-K2, is measured following Equation (5) of Rojas-Ayala et al. (2012). For the application of the *H*-band and *K*-band metallicity calibrations of Terrien et al. (2012), we measure the EW of the Na (2.2074 μm), Ca (1.6159, 1.6203, 2.2638 μm), and K (1.5171 μm) features following the prescription detailed in Section 3.1 of their study. The pseudo-continuum is estimated by fitting a fourth-order Legendre polynomial to the regions shown in their Figure 1(A) for the *H* band, and in their Figure 1(B) for the *K* band. The water indices, H_2O-H and H_2O-K, are also measured following the definitions in their paper. For the Mann et al. (2013) calibration, the EW of the metal-sensitive features F19 (2.2079 μm), F20 (2.3242 μm), and F22 (2.3844 μm) in the *K* band are measured using the parameters listed in their Table 5. The pseudo-continuum is measured by a linear fit in the spectral regions specified in their Table 4, immediately redward and blueward of each feature. The water index used for this *K*-band calibration is the same as the one described by Rojas-Ayala et al. (2012).

The EWs and spectral indices computed from our FIRE spectrum as described above yield the metallicities for GJ 3470 shown in the first four lines of Table 1. A spectroscopic estimate of the effective temperature of GJ 3470 is obtained using the temperature-sensitive H_2O-K2 index in the *K* band as defined by Rojas-Ayala et al. (2012). The result is 3750 ± 300 K.

3.2.2. HARPS Spectral Analysis

An additional spectroscopic estimate of the metallicity of GJ 3470 is obtained from a recent calibration (V. Neves et al., in

Table 1
Metallicity Estimates (dex) for GJ 3470 from Near-infrared and Visible Spectroscopy

Calibration Reference	Bandpass	Value
Rojas-Ayala et al. (2012)	K	$+0.15 \pm 0.17$
Terrien et al. (2012)	H	$+0.25 \pm 0.12$
Terrien et al. (2012)	K	$+0.19 \pm 0.12$
Mann et al. (2013)	K	$+0.32 \pm 0.11$
Neves et al. (2013)	Visible	$+0.08 \pm 0.10$
Adopted	...	$+0.20 \pm 0.10$

preparation) based on the visible-light HARPS spectra of Bonfils et al. (2012). This calibration was established on the basis of EWs measured for a total of 4441 lines in the spectra of 55 stars from the HARPS volume-limited M-dwarf sample (Bonfils et al. 2013), and is anchored on existing photometric calibrations for metallicity (Neves et al. 2012) and effective temperature (Casagrande et al. 2008). The procedure, described briefly in the appendix of the study by Neves et al. (2013), achieves an improved precision over previous methods of 0.10 dex. The result of this measurement for GJ 3470 is $+0.08 \pm 0.10$, and is also collected in Table 1.

The five estimates of [Fe/H] from the FIRE and HARPS spectra are consistent with each other, and we therefore adopt for the remainder of the paper the weighted average, $[\mathrm{Fe/H}] = +0.20 \pm 0.10$, in which the uncertainty is a more conservative estimate than the formal error of the mean.

4. STELLAR CHARACTERIZATION

Mass ($M_\star$) and radius ($R_\star$) estimates for exoplanet host stars are typically obtained by appealing to stellar evolution models. For M dwarfs this, too, has been problematic (beyond the challenges for determining T_{eff} and [Fe/H] alluded to earlier in Section 2.3) because of known disagreements between predictions from theory and accurate measurements of $M_\star$ and $R_\star$ for low-mass stars in double-lined eclipsing binaries (see, e.g., Torres 2013 and references therein). We therefore rely here exclusively on empirical relations, on the mean stellar density inferred from our *Spitzer* light curve in Section 3.1.2 ($\rho_\star = 2.91^{+0.37}_{-0.33}\,\rho_\odot$), and on brightness measurements for GJ 3470 from Two Micron All Sky Survey (2MASS) and in the optical ($V = 12.33 \pm 0.01$; Weis 1986; Evans et al. 2002; Zacharias et al. 2013). For a given parallax and ignoring extinction, the near-infrared mass–luminosity (M–L) relations of Delfosse et al. (2000) provide estimates of the absolute mass, and are insensitive to metallicity. On the other hand, the surface-brightness (SB) relations by Kervella et al. (2004) allow one to estimate the angular diameter, which may be converted to a linear radius with knowledge of the parallax. The latter relations are valid for [Fe/H] between -0.5 and $+0.5$, and are thus applicable to GJ 3470, with its metallicity of $[\mathrm{Fe/H}] = +0.20 \pm 0.10$. While a trigonometric parallax has not been measured for this star, we may use the above relations simultaneously to solve for the distance that yields values of $M_\star$ and $R_\star$ consistent with the measured mean density.

We proceeded in a Monte Carlo fashion, drawing all measured quantities ($VJHK_s$ photometry and *Spitzer* mean density) from appropriate Gaussian distributions. For each set of draws we solve for the value of the parallax that gives a mass and radius through the M–L and SB relations resulting in a mean density equal to the randomly drawn value of $\rho_\star$ for the set. We repeat the process 10^5 times, and adopt as final values the mode of the corresponding posterior probability distributions, assigning 1σ uncertainties given by the 15.85 and 84.13 percentiles of those distributions. We obtain $M_\star = 0.539^{+0.047}_{-0.043}\,M_\odot$ and $R_\star = 0.568^{+0.037}_{-0.031}\,R_\odot$, and a parallax of $\pi = 32.4^{+2.1}_{-1.9}$ mas, corresponding to a distance of $30.7^{+2.1}_{-1.7}$ pc. The mass is an average of the J-, H-, and K-band relations by Delfosse et al. (2000), each of which is assumed conservatively to carry an uncertainty of 10%. The radius is an average of the two SB relations of Kervella et al. (2004) that yield the smallest scatter in the angular diameters (about 1% for the relations that depend on V–H and V–K). Prior to using them, the 2MASS magnitudes are converted to the native photometric system of the M–L and SB relations (CIT and Johnson, respectively) using the transformations of Carpenter (2001). The uncertainties listed above include all photometric errors, the error in $\rho_\star$, as well as the scatter of the empirical relations. We note that our stellar mass is very close to that reported by Bonfils et al. (2012), but our radius is 13% larger.

Table 2
Adopted System Parameters for GJ 3470 from our MCMC Fit of Section 5

Parameter	Value
Jump parameters	
Planet/star area ratio R_p/R_s	$0.07798^{+0.00046}_{-0.00045}$
$b = a\cos i/R_\star$ ($R_\star$)	$0.40^{+0.06}_{-0.08}$
Transit width W (d)	0.0791 ± 0.0005
$T_0 - 2{,}450{,}000$ ($\mathrm{BJD_{TDB}}$)	6090.47701 ± 0.00010
Orbital period P (d)[a]	3.33665 ± 0.00005
RV K' ($\mathrm{m\,s^{-1}\,d^{1/3}}$)	13.4 ± 1.2
$\sqrt{e}\cos\omega$	0.0 (fixed)
$\sqrt{e}\sin\omega$	0.0 (fixed)
$c_1 = 2u_1 + u_2$	0.246 ± 0.027
$c_2 = u_1 - 2u_2$	-0.329 ± 0.020
Stellar parameters	
u_1	0.033 ± 0.015
u_2	0.181 ± 0.010
Mean density $\rho_\star$ ($\rho_\odot$)	$2.91^{+0.37}_{-0.33}$
Surface gravity $\log g_\star$ (cgs)	4.658 ± 0.035
Mass $M_\star$ ($M_\odot$)[b]	$0.539^{+0.047}_{-0.043}$
Radius $R_\star$ ($R_\odot$)[b]	$0.568^{+0.037}_{-0.031}$
Parallax π (mas)[b]	$32.4^{+2.1}_{-1.9}$
Distance (pc)[b]	$30.7^{+2.1}_{-1.7}$
Effective temperature T_{eff} (K)[b]	3600 ± 100
Metallicity [Fe/H] (dex)[b]	$+0.20 \pm 0.10$
Planetary parameters	
RV semi-amplitude K ($\mathrm{m\,s^{-1}}$)	8.9 ± 1.1
Orbital semi-major axis a (AU)	$0.03557^{+0.00096}_{-0.00100}$
Orbital inclination i (deg)	$88.3^{+0.5}_{-0.4}$
Mean density ρ_p ($\mathrm{g\,cm^{-3}}$)	$0.72^{+0.13}_{-0.12}$
Surface gravity $\log g_p$ (cgs)	$2.76^{+0.06}_{-0.07}$
Mass M_p ($M_\oplus$)	$13.9^{+1.5}_{-1.4}$
Radius R_p ($R_\oplus$)	$4.83^{+0.22}_{-0.21}$
Individual transit timings	
$T_{0,1} - 2{,}450{,}000$ ($\mathrm{BJD_{TDB}}$)	6090.47705 ± 0.00014
$T_{0,2} - 2{,}450{,}000$ ($\mathrm{BJD_{TDB}}$)	6093.81372 ± 0.00015

Notes

[a] Derived using our two *Spitzer* light curves along with published ground based photometry and RVs (see Section 5).

[b] Parameters derived either in Section 3 or in Section 4, and repeated here for convenience.

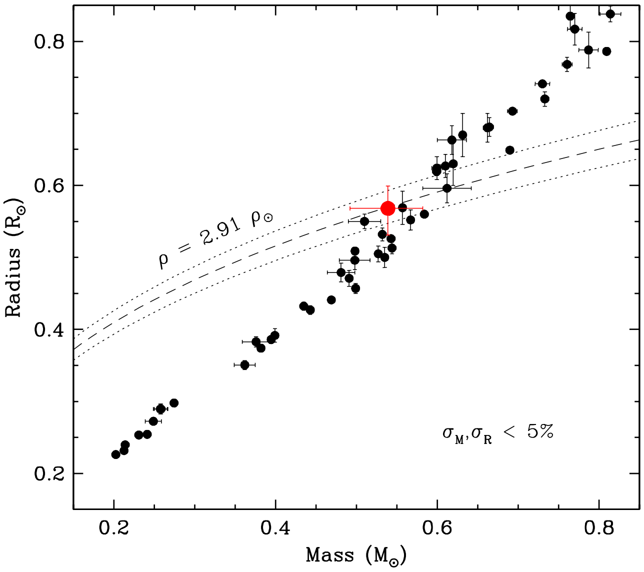

Figure 4. Mass and radius estimates for GJ 3470 (large red dot) compared with measurements for other low-mass stars in double-lined eclipsing binaries with relative errors in $M_\star$ and $R_\star$ less than 5% (see Torres 2013). The constraint on the mean stellar density derived from our *Spitzer* observations is indicated with the dashed line (dotted lines representing the 1σ uncertainties).

(A color version of this figure is available in the online journal.)

As a check on the above absolute radius determination, we obtain additional estimates of $R_\star$ from color indices and the calibrations recently published by Boyajian et al. (2012), which are based on angular diameter measurements from the CHARA interferometer and HIPPARCOS parallaxes, and have a dependence on metallicity. Results using $V-J$, $V-H$, and $V-K_s$ for the measured metallicity of GJ 3470 give very consistent values for $R_\star$ averaging $0.513 \pm 0.043\ R_\odot$, in agreement with our *Spitzer*-based determination within about 1σ. Figure 4 displays the location of GJ 3470 in the mass–radius diagram for low-mass stars, along with the measurements for all other such objects in double-lined eclipsing binaries that have relative measurement precisions under 5% for $M_\star$ and $R_\star$. The constraint afforded by the mean stellar density is also indicated.

While an estimate of the effective temperature of the star was obtained earlier using our FIRE spectrum, the precision is relatively low. We obtain a further estimate using the color/temperature calibrations of Boyajian et al. (2012), which are based on bolometric fluxes and angular diameter measurements, and include metallicity terms. The $V-J$, $V-H$, and $V-K_s$ indices along with our adopted value of [Fe/H] lead to a weighted average temperature of 3630 ± 100 K. A final $T_{\rm eff}$ estimate is inferred from the same three indices and the color/temperature calibrations of Casagrande et al. (2008), which rely on the Infrared Flux Method. However, these relations do not take into account the metallicity, and implicitly assume a composition near solar whereas GJ 3470 is metal-rich. Therefore, the resulting estimate (3360 ± 100 K) requires an adjustment for metallicity. We determine this by using the stellar evolution models of Dotter et al. (2008) in a differential sense, first reading off from a $[\mathrm{Fe/H}] = +0.20$ isochrone the stellar mass that yields the same color indices as we measure, and then comparing the corresponding temperature with that for a star of the same mass on a solar-metallicity isochrone. This exercise is insensitive to the age adopted for the isochrone. Consistent results using the three color indices separately give an average correction of +140 K, which results in a final temperature of 3500 ± 150 K. As the two photometric determinations above are consistent with each other and with the spectroscopic determination in Section 3.2.1, we adopt the weighted average of the three values, $T_{\rm eff} = 3600 \pm 100$ K.

While this paper was under review, we learned that Pineda et al. (2013) performed an independent characterization of GJ 3470's stellar properties. We refer the reader to that study for a description of their analysis and results.

5. PLANETARY AND ORBITAL PARAMETERS

Our final parameters for GJ 3470 b were derived using the stellar properties from the preceding section, and an MCMC fit analogous to that described in Section 3 with the addition of a prior on the stellar mass. For this prior we used the posterior probability distribution derived in Section 4, drawing from it a random value of the mass at each step of the MCMC fit. As before, we included the light curves from both *Spitzer* visits, along with the 61 HARPS RVs reported by Bonfils et al. (2012). The results are presented in Table 2, where the value adopted for each parameter is the median of the corresponding marginalized posterior distribution from the MCMC fit. Error bars are the corresponding 68.3% probability intervals from the same distributions. The final model and phase-folded *Spitzer* light curves are displayed in Figure 3.

We find for GJ 3470 b a radius of $R_p = 4.83^{+0.22}_{-0.21}\ R_\oplus$, which is 13% larger than previously reported in the literature. This increase is driven mainly by the larger stellar radius from Section 4. Combining the planetary radius with the mass $M_p = 13.9^{+1.5}_{-1.4}\ M_\oplus$ that relies on the RV data set yields a very low planetary density of $\rho_p = 0.72^{+0.13}_{-0.12}$ g cm^{-3}, which is 33% smaller than the estimate in the discovery paper. These planetary parameters are also listed in Table 2.

Finally, we performed a new fit for the purpose of assessing the robustness of the orbital period determination for GJ 3470 b, which in our solution is constrained both by the two *Spitzer* transits and the RVs. However, the two *Spitzer* visits are consecutive (2012 June 11 and 15), so the lever arm for the orbital period determination is very short. We therefore incorporated the two `TRAPPIST` transit light curves from Bonfils et al. (2012), as well as the ones from *EulerCam* and the `NITES` telescope. The light curves from the first two sources show only the ingress portion of the transit, but may still be combined with our two full *Spitzer* light curves that constrain the transit shape, if we assume the latter does not change across wavelengths. The `NITES` light curve has a higher level of correlated noise, but does cover the transit completely. These ground-based light curves were obtained between 2012 February and April, and therefore contribute to build up a much longer baseline.

As expected, most of the system parameters in this new fit are tightly constrained by the *Spitzer* photometry alone, but the period is considerably improved. The new value is included in Table 2, and is only 19 ± 11 s shorter than the one that relies on the two *Spitzer* transits alone.

6. INTERIOR COMPOSITION OF A LOW-DENSITY EXO-NEPTUNE

GJ 3470 b presents a valuable test case for planet formation and evolution theories. It stands out from the crowd of accumulating transiting exo-Neptunes due to its low mean density and bright M dwarf host star. GJ 3470 b's measured radius is $20\% \pm 6\%$ larger than Uranus ($R_{♅} = 4.01\ R_\oplus$) despite having a

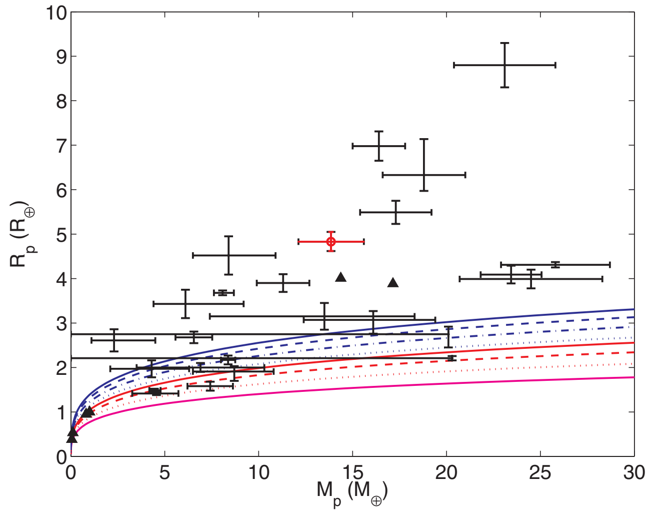

Figure 5. Mass–radius relationships of small transiting planets. GJ 3470 b is highlighted in red. Other small transiting exoplanets with dynamical mass constraints (CoRoT-7 b, Kepler-4 b, Kepler-10 b, Kepler-11 b, c, d, e, f, Kepler-18 b, c, d, Kepler-19 b, Kepler-20 b, c, d, Kepler-30 b, d, Kepler-36 b, c, 55 Cnc e, GJ 1214 b, GJ 436 b, HAT-P-11 b, and HAT-P-26 b) are plotted in black. The solar system planets are indicated with solid triangles. The curves are illustrative constant-temperature mass–radius relations from Seager et al. (2007). The solid lines are homogeneous-composition planets: water ice (blue solid), $MgSiO_3$ perovskite (red solid), and iron (magenta solid). The non-solid lines are mass–radius relations for differentiated planets: 75% water ice, 22% silicate shell, and 3% iron core (blue dashed); Ganymede-like with 45% water ice, 48.5% silicate shell, and 6.5% iron core (blue dot-dashed); 25% water ice, 52.5% silicate shell, and 22.5% iron core (blue dotted); Earth-like with 67.5% silicate mantle and 32.5% iron core (red dashed); and Mercury-like with 30% silicate mantle and 70% iron core.

(A color version of this figure is available in the online journal.)

similar mass ($M_{♆} = 14.5\,M_\oplus$). The planet radius corresponds to roughly 20% of its Roche lobe radius. Among currently known low-mass ($M_p < 30\,M_\oplus$) transiting planets, only the Kepler-11, Kepler-18, Kepler-30, and HAT-P-26 systems have planets with lower densities (see Figure 5).

GJ 3470 b must have acquired H/He gas from the protoplanetary nebula. Alternative gas layer sources such as sublimated ices and outgassing from a rocky interior may be important for less massive, more dense planets (such as GJ 1214b; Rogers & Seager 2010b), but cannot be the dominant gas layer source for GJ 3470 b. Its bulk density is too low for astrophysical ices (H_2O, CO_2, etc.) alone to comprise the planet volatiles; significant quantities of light gases (hydrogen and helium) must be present. Further, GJ 3470 b's gas layer is too voluminous to have been formed by outgassing of light gases during formation; the planet radius exceeds the upper limit for outgassed planets from Rogers et al. (2011).

Nebular H/He contributes between 5% and 24% to GJ 3470 b's mass, according to our interior structure models. Following Rogers & Seager (2010b), we apply a fully differentiated model for the planet's interior structure consisting of (from the center of the planet outward) an iron core, silicate layer, ice layer, and H/He gas envelope to explore which bulk compositions are consistent with the measured mass and radius of GJ 3470 b. Both the planet's bond albedo A (which scales the equilibrium temperature $T_{\rm eq} = (1 - A)^{1/4}\,(683 \pm 27)$ K), and the planet's intrinsic luminosity L_p (a proxy for the poorly constrained age of the planet) are unknown. We adopt fiducial values of $A = 0.3$ and $L_p/M_p = 10^{-10}$ W kg^{-1}, while also exploring the ranges of $A = 0$–0.5 and $L_p/M_p = 10^{-10.5}$ W kg^{-1} to $10^{-9.5}$ W kg^{-1}. Figure 6 presents the H/He gas mass fraction ($M_{\rm XY}/M_p$) in our models as a function of the Fe-silicate-H_2O abundances of the heavy element interior (assuming the median values of the planet mass and radius, and our nominal planet energy budget parameters). Varying the planet mass and radius within their 1σ bounds, and considering a range of plausible planet energy budgets affects the H/He mass fractions by up to ±0.05. For a rocky Earth-like heavy element interior composition (32% Fe, 68% silicate, 0% H_2O), GJ 3470 b's H/He envelope mass is constrained to $M_{\rm XY}/M_p = 0.16 \pm 0.05$, while for a denser iron-enhanced Mercury-like rocky interior (70% Fe, 30% silicate, 0% H_2O), $M_{\rm XY}/M_p = 0.17 \pm 0.05$. Less H/He is needed if GJ 3470 b has an ice-rich interior composition; for instance, for a heavy element interior with 16% Fe, 34% silicate, 50% H_2O, $M_{\rm XY}/M_p = 0.12^{+0.05}_{-0.04}$.

Which heavy element interior compositions are plausible for GJ 3470 b? The planet interior ice-to-rock ratio is not constrained by measurements of the planets mass and radius alone, so we look to planet formation theory for insights. If GJ 3470 b formed beyond the snow line and migrated inward to its current orbit, its heavy element interior would be ice-rich. If instead GJ 3470 b formed in situ (inside the snow line) its heavy element interior would be rock dominated with a lower proportion of ices. Theoretical predictions for how much ice is likely included in planets formed inside the snow line of M dwarfs are a topic of ongoing debate. Ogihara & Ida (2008) proposed that migration of planetesimals from beyond the snow line could supply icy material to the inner regions of the protoplanetary disk. On the other hand, Lissauer (2007) and Kennedy et al. (2007) predict that planets and planetesimals formed within 1 AU of M dwarfs are unlikely to have large volatile inventories when the effect of the M dwarfs' pre-main sequence luminosity evolution is taken into account. In Figure 6 we present interior bulk compositions for the full range of ice-to-rock ratios.

7. SUMMARY

Our 4.5 μm *Spitzer* observations have enabled us to refine the planetary and system parameters of the Neptune-size planet GJ 3470 b, improving its radius to $R_p = 4.8 \pm 0.2\,R_\oplus$, which is 13% larger than previously reported in the literature. As a result, the revised planetary density, $\rho_p = 0.72 \pm 0.13$ g cm^{-3}, is 33% smaller than before. These changes come mostly from revisions of the stellar parameters (particularly $R_\star$), which have been frustratingly difficult to determine accurately in the past due to known discrepancies between observations and standard stellar evolution models for lower main-sequence stars. In this paper we have relied for this only on empirical M–L and SB relations that have been widely employed in other contexts, and on the strong constraint on the mean stellar density provided by our *Spitzer* observations. In the process we have inferred an accurate distance for the star.

GJ 3470 b provides a valuable example of an extremely low-density planet, representative of a significant portion of the exoplanet candidates found by the *Kepler* mission to date. The brightness of the host star ($K_s = 7.99$) combined with its large planet-to-star radius ratio renders GJ 3470 b a promising candidate for future atmospheric characterization, which could provide clues on its formation pathway. Indeed, GJ 3470 b's low surface gravity translates to a large atmospheric scale height for a given atmospheric composition, favoring follow-up studies applying transmission spectroscopy. GJ 3470 b, GJ 436 b, and

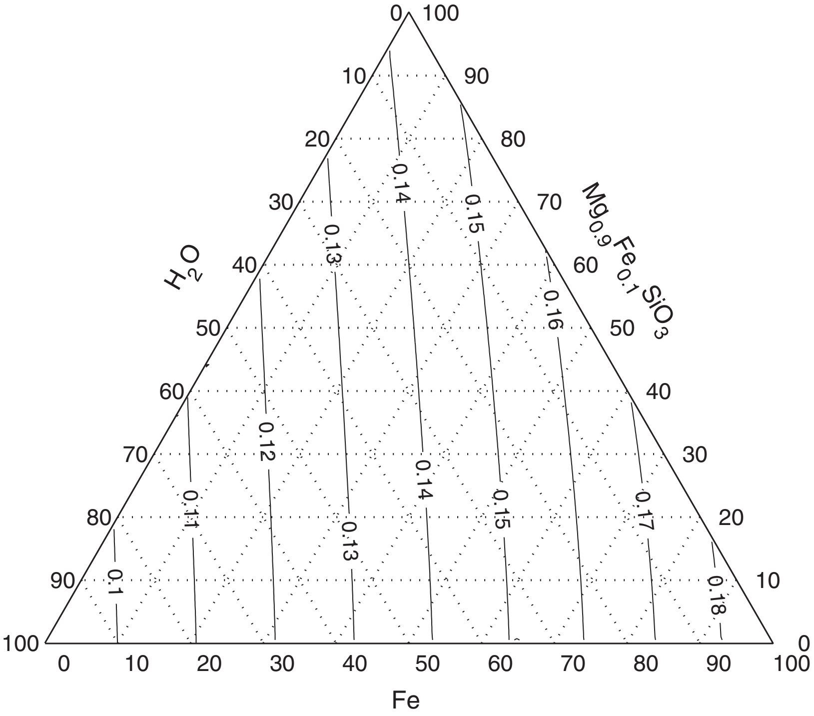

Figure 6. Fraction of GJ 3470 b's mass contributed by H/He, as a function of the planet's heavy-element interior composition. Each point within the diagram corresponds to a specific combination of Fe, $Mg_{0.9}Fe_{0.1}SiO_3$, and H_2O (by mass) in the heavy element interior of GJ 3470 b. For instructions on how to read ternary diagrams, see, e.g., Valencia et al. (2007) and Zeng & Seager (2008). Each contour is labeled with M_{XY}/M_p for our fiducial model parameters (median M_p, median R_p, $A = 0.3$, and $L_p/Mp = 10^{-10}$ W kg^{-1}). Uncertainties in the planet mass, radius, and energy budget can affect M_{XY}/M_p by ±0.03–0.05.

GJ 1214 b are a remarkable sample of volatile-rich planets orbiting bright nearby stars, pushing the field of comparative exoplanetology further toward low-mass planets.

We thank Zach Berta and Elisabeth Newton for helpful discussions regarding near-IR M-dwarf spectral characterization. We are grateful to Rob Simcoe, Paul Schechter, Elisabeth Adams, and David Ciardi for their help in obtaining the ground-based observations presented in this paper. We thank the anonymous referee for a report that improved the paper. We thank the *Spitzer* Science Center staff, and especially Nancy Silbermann, for the efficient scheduling of our observations. We also wish to thank the staff of the Magellan Telescopes and Las Campanas Observatory for their assistance in obtaining the FIRE observations. This work is based on observations made with the *Spitzer Space Telescope*, which is operated by the Jet Propulsion Laboratory, California Institute of Technology, under a contract with NASA. Support for this work was provided by NASA through an award issued by JPL/Caltech. The WIYN Observatory is a joint facility of the University of Wisconsin-Madison, Indiana University, Yale University, and the National Optical Astronomy Observatory. Support for LAR was provided by NASA through Hubble Fellowship grant HF-51313.01-A awarded by the Space Telescope Science Institute, which is operated by the Association of Universities for Research in Astronomy, Inc., for NASA, under contract NAS 5-26555. This work was supported by the European Research Council/European Community under the FP7 through Starting Grant agreement number 239953 and by Fundação para a Ciência e a Tecnologia (FCT) in the form of grants PTDC/CTE-AST/098528/2008 and PTDC/CTE-AST/120251/2010. The financial support from the "Programme National de Planétologie" (PNP) of CNRS/INSU, France, is gratefully acknowledged. G.T. acknowledges partial support for this work through NSF grant AST-1007992. V.N. also acknowledges the support from the FCT in the form of the fellowship SFRH/BD/60688/2009. M.G. is Research Associate at the Belgian Fonds National de la Recherche Scientifique (FNRS).

Facilities: Spitzer, Magellan:Baade, WIYN

REFERENCES

Batalha, N. M., Rowe, J. F., Bryson, S. T., et al. 2013, ApJS, 204, 24
Bean, J. L., Kempton, E. M.-R., & Homeier, D. 2010, Natur, 468, 669
Bonfils, X., Delfosse, X., Udry, S., et al. 2013, A&A, 549, A109
Bonfils, X., Gillon, M., Udry, S., et al. 2012, A&A, 546, A27
Boyajian, T. S., von Braun, K., van Belle, G., et al. 2012, ApJ, 757, 112
Butler, R. P., Vogt, S. S., Marcy, G. W., et al. 2004, ApJ, 617, 580
Carpenter, J. M. 2001, AJ, 121, 2851
Casagrande, L., Flynn, C., & Bessell, M. 2008, MNRAS, 389, 585
Charbonneau, D., Berta, Z. K., Irwin, J., et al. 2009, Natur, 462, 891
Claret, A., & Bloemen, S. 2011, A&A, 529, 75
Cochran, W. D., Fabrycky, D. C., Torres, G., et al. 2011, ApJS, 197, 7
Delfosse, X., Forveille, T., Ségransan, D., et al. 2000, A&A, 364, 217
Demory, B.-O., Gillon, M., Bonfils, X., et al. 2012a, Spitzer Proposal, 80261
Demory, B.-O., Gillon, M., Seager, S., et al. 2012b, ApJL, 751, L28
Dotter, A., Chaboyer, B., Jevremović, D., et al. 2008, ApJS, 178, 89
Eastman, J., Siverd, R., & Gaudi, B. S. 2010, PASP, 122, 935
Evans, D. W., Irwin, M. J., & Helmer, L. 2002, A&A, 395, 347
Fazio, G. G., Hora, J. L., Allen, L. E., et al. 2004, ApJS, 154, 10
Figueira, P., Pont, F., Mordasini, C., et al. 2009, A&A, 493, 671
Gelman, A., Carlin, J. B., Stern, H. S., & Rubin, D. B. 2003, Bayesian Data Analysis (Chapman & Hall/CRC Texts in Statistical Science, 2nd ed.; London: Chapman and Hall)
Gelman, A., & Rubin, D. B. 1992, StaSc, 7, 457
Gillon, M., Lanotte, A. A., Barman, T., et al. 2010, A&A, 511, 3
Gillon, M., Pont, F., Demory, B.-O., et al. 2007, A&A, 472, L13
Hartman, J. D., Bakos, G. Á., Kipping, D. M., et al. 2011, ApJ, 728, 138
Holman, M. J., Winn, J. N., Latham, D. W., et al. 2006, ApJ, 652, 1715
Horch, E. P., Howell, S. B., Everett, M. E., & Ciardi, D. R. 2012, AJ, 144, 165
Horch, E. P., Veillette, D. R., Baena Gallé, R., et al. 2009, AJ, 137, 5057

Howard, A. W., Marcy, G. W., Bryson, S. T., et al. 2012, ApJS, 201, 15

Howard, A. W., Marcy, G. W., Johnson, J. A., et al. 2010, Sci, 330, 653

Ingalls, J. G., Krick, J. E., Carey, S. J., et al. 2012, Proc. SPIE, 8442, 1

Kennedy, G. M., Kenyon, S. J., & Bromley, B. C. 2007, Ap&SS, 311, 9

Kervella, P., Thévenin, F., Di Folco, E., & Ségransan, D. 2004, A&A, 426, 297

Knutson, H. A., Lewis, N., Fortney, J. J., et al. 2012, ApJ, 754, 22

Lissauer, J. J. 2007, ApJL, 660, L149

Lissauer, J. J., Fabrycky, D. C., Ford, E. B., et al. 2011, Natur, 470, 53

Mann, A. W., Brewer, J. M., Gaidos, E., Lepine, S., & Hilton, E. J. 2013, AJ, 145, 52

Neves, V., Bonfils, X., Santos, N. C., et al. 2012, A&A, 538, A25

Neves, V., Bonfils, X., Santos, N. C., et al. 2013, A&A, 551, A36

Nutzman, P., & Charbonneau, D. 2008, PASP, 120, 317

Ogihara, M., & Ida, S. 2008, in IAU Symp. 249, Exoplanets: Detection, Formation and Dynamics, ed. Y.-S. Sun, S. Ferraz-Mello, & J.-L. Zhou (Cambridge: Cambridge Univ. Press), 305

Pineda, J. S., Bottom, M., & Johnson, J. A. 2013, arXiv:1302.6231

Rogers, L. A., Bodenheimer, P., Lissauer, J. J., & Seager, S. 2011, ApJ, 738, 59

Rogers, L. A., & Seager, S. 2010a, ApJ, 712, 974

Rogers, L. A., & Seager, S. 2010b, ApJ, 716, 1208

Rojas-Ayala, B., Covey, K. R., Muirhead, P. S., & Lloyd, J. P. 2012, ApJ, 748, 93

Seager, S., Kuchner, M., Hier-Majumder, C. A., & Militzer, B. 2007, ApJ, 669, 1279

Seager, S., & Mallén-Ornelas, G. 2003, ApJ, 585, 1038

Simcoe, R. A., Burgasser, A. J., Bernstein, R. A., et al. 2008, Proc. SPIE, 7014, 70140U

Stevenson, K. B., Harrington, J., Nymeyer, S., et al. 2010, Natur, 464, 1161

Terrien, R. C., Mahadevan, S., Bender, C. F., et al. 2012, ApJL, 747, L38

Torres, G. 2013, AN, 334, 4

Torres, G., Winn, J. N., & Holman, M. J. 2008, ApJ, 677, 1324

Vacca, W. D., Cushing, M. C., & Rayner, J. T. 2003, PASP, 115, 389

Valencia, D., Sasselov, D. D., & O'Connell, R. J. 2007, ApJ, 665, 1413

Weis, E. W. 1986, AJ, 91, 626

Wittenmyer, R. A., Tinney, C. G., Butler, R. P., et al. 2011, ApJ, 738, 81

Zacharias, N., Finch, C. T., Girard, T. M., et al. 2013, AJ, 145, 44

Zeng, L., & Seager, S. 2008, PASP, 120, 983

Chapter 6

Conclusions and future prospects

During my thesis I searched for ways to improve the stellar parameters of M dwarfs, especially metallicity and effective temperature. I started by investigating photometric methods of improving existing [Fe/H] calibrations, with the aid precise V and infrared photometry from various sources, and with the parallaxes from van Leeuwen (2007). Afterwards, I continued our investigation by moving to medium and high-resolution spectroscopy, as well as using data from transits.

In the first part of our work, described in Chapter 3, I tested three photometric metallicity calibrations and marginally refined the one I found best, from Schlaufman & Laughlin (2010). Although I used a strict selection of V photometry and [Fe/H], the observed dispersion around the calibration is well in excess of the [Fe/H] and photometric uncertainties, suggesting that the origin of the remaining dispersion is astrophysical rather than observational. The possible causes could be related to nonlinearities in the metallicity dependence of the $V-K$ colour, or to rotation and magnetic activity. Stellar evolution has been discarded as a main contributor, since early M dwarfs evolve rapidly in the main sequence and remain there for much longer than a Hubble time. I conclude then, that unless a quantitative understanding of this astrophysical dispersion emerges, the photometric methods have reached their limit (i.e. ~ 0.20 dex).

Following my first work, I investigated the correlations of stellar mass and metallicity with the presence of planets, as shown in Chapter 4. I calculated the metallicity and effective temperature of the M dwarfs with a new spectroscopic method, based on high-resolution HARPS M dwarf spectra. This technique uses the values from the [Fe/H] calibration of Neves et al. (2012) and the T_{eff} calibration of Casagrande et al. (2008) as initial values, and has uncertainties around 0.08 dex for [Fe/H] and 100 K for T_{eff}. The stellar mass was calculated with the K-band relation of the established calibration of Delfosse et al. (2000).

The first result from this work is the confirmation of the correlation of [Fe/H] with the presence of giant planets, as shown by previous studies on FGK dwarfs (e.g. Gonzalez 1997; Santos et al. 2004b; Sousa et al. 2011; Mayor et al. 2011) and M dwarfs (Bonfils et al. 2007; Johnson & Apps 2009; Schlaufman & Laughlin 2010; Rojas-Ayala et al. 2012; Terrien et al. 2012). This relation is quantified by a power law, $f_p = C10^{\alpha[Fe/H]}$, using two different approaches: a direct bin fitting and a Bayesian fitting procedure. We obtained a value for C between 0.02 and 0.04 and for α between 1.26 and 2.94.

Secondly, we detected a hint of an anti-correlation of the metallicity with the presence of Neptunian and smaller planets. This result is predicted by studies using core-accretion models (Mordasini et al. 2012). However, our current statistic supports a flat relation, in agreement with previous results for FGK dwarfs (e.g. Sousa et al. 2008; Bouchy et al. 2009; Sousa et al. 2011) and M dwarfs (Rojas-Ayala et al. 2012). Regarding stellar mass, I confirmed that our sample was biased, so I could not analyze the stellar mass-planet relation.

Finally, me and my collaborators conducted a research on the refinement of the planetary mass and radius of the exoplanet GJ3470 b. The planetary parameters depend directly on the stellar parameters. It is therefore critical to obtain very precise values from the star. Using the value of the stellar density from the Spitzer light curve, we derive a stellar mass of $M_{\star} = 0.539^{+0.047}_{-0.03} M_{\odot}$ and a radius of $R_{\star} = 0.568^{+0.037}_{-0.031} R_{\odot}$, as well as a metallicity of [Fe/H] = $+0.20 \pm 0.10$ and an effective temperature of T_{eff} = 3600 ± 100 K. Using the obtained stellar parameters and the information from the light curve and the RVs as priors in a MCMC approach, we obtain a planetary radius $R_p = 4.83^{+0.22}_{-0.21} R_{\oplus}$ that is 13% larger than the value previously reported in the literature, and a planetary mass $M_p = 13.9^{+1.5}_{-1.4} M_{\oplus}$ that translates to a very low planetary density, $\rho_p = 0.72^{+0.13}_{-0.12} gcm^{-3}$, which is 33% smaller than the original value. The brightness of the host star ($K_s = 7.99$ mag) combined with its large planet-to-star radius ratio makes GJ 3470 b a promising candidate for future atmospheric characterisation, which may provide clues on its formation and evolution.

The work towards the better understanding of M dwarfs and its relation to planets is still in its infancy. Several methods and calibrations exist, but the systematics between them are still too large. Regarding metallicity, for instance, the photometric methods seem to have hit a limit of around 0.20 dex, but the spectroscopic methods still hold some promise, and may reach the same level of precision as obtained in FGK dwarfs soon, either with spectral synthesis or calibrations. For effective temperature, the scenario seems more complicated, as systematics between the calibrations are very high, of the order of 300 K and theoreticians warn that, for now, the accuracy obtained by synthetic spectra methods cannot be better than 200-300 K, at least in the visible. In the case of the mass-radius relationship, the models are able to qualitatively predict the known variations when very high precision data is used (lower than 2% for either stellar mass and radius). However, a quantitative understanding of the variation of the radii, especially for the case of the well known ‘bloated’ M dwarfs, was not achieved yet. In this scenario, the disentanglement of the age, metallicity, and activity contributions is important. In fact, the calculation of precise stellar mass and radius is critical to the determination of the planetary parameters.

Taking this context into account, the next steps regarding the better understanding of M dwarf and improvement of its parameters are as follows:

- Work on already obtained X-SHOOTER data, in order to obtain a precise [Fe/H] calibration in the visible and infrared.
- Use techniques comparing synthetic spectra, using the most recent photospheric models of M dwarfs, with high-resolution spectra, in the infrared, to obtain precise values of metallicity, effective temperature, microturbulence, and surface gravity, as well as elemental abundances.
- Investigate methods to improve stellar mass and radius determinations, and use them, along with data from transits and RV, to refine the precision of planetary masses, radii, and density.

References

Adams, F. C., Cai, M. J., & Lizano, S. 2009, ApJL, 702, L182

Adibekyan, V. Z., Santos, N. C., Sousa, S. G., et al. 2012a, A&A, 543, A89

Adibekyan, V. Z., Sousa, S. G., Santos, N. C., et al. 2012b, A&A, 545, A32

Alibert, Y., Mordasini, C., & Benz, W. 2011, A&A, 526, A63

Alibert, Y., Mordasini, C., Benz, W., & Winisdoerffer, C. 2005, A&A, 434, 343

Allard, F. 1990, PhD thesis, Centre de Recherche Astrophysique de Lyon ¡EMAIL¿fallard@ens-lyon.fr¡/EMAIL¿

Allard, F. & Hauschildt, P. H. 1995, ApJ, 445, 433

Allard, F., Homeier, D., & Freytag, B. 2010, ArXiv e-prints. ID: 1011.5405. To appear in the proceedings of Cool Stars 16

Allard, F., Homeier, D., & Freytag, B. 2012, Royal Society of London Philosophical Transactions Series A, 370, 2765

Armitage, P. J. 2010, Astrophysics of Planet Formation

Arthur, W. & Morphy, F. 2005, Macquarie atlas of indigenous Australia: culture and society through space and time (Macquarie)

Asplund, M., Grevesse, N., Sauval, A. J., & Scott, P. 2009, ARAA, 47, 481

Auman, Jr., J. R. 1969, ApJ, 157, 799

Bailes, M., Lyne, A. G., & Shemar, S. L. 1991, Nature, 352, 311

Baraffe, I., Chabrier, G., Allard, F., & Hauschildt, P. H. 1998, A&A, 337, 403

Baranne, A., Queloz, D., Mayor, M., et al. 1996, A&AS, 119, 373

Barclay, T., Rowe, J. F., Lissauer, J. J., et al. 2013, Nature, 494, 452

Batalha, N. M., Rowe, J. F., Bryson, S. T., et al. 2013, ApJs, 204, 24

Bean, J. L., Benedict, G. F., & Endl, M. 2006a, ApJ, 653, L65

Bean, J. L., Sneden, C., Hauschildt, P. H., Johns-Krull, C. M., & Benedict, G. F. 2006b, ApJ, 652, 1604

Beaulieu, J.-P., Bennett, D. P., Fouqué, P., et al. 2006, Nature, 439, 437

Beirão, P., Santos, N. C., Israelian, G., & Mayor, M. 2005, ArXiv Astrophysics e-prints

Benedict, G. F., McArthur, B. E., Forveille, T., et al. 2002, ApJ, 581, L115

Benz, W., Mordasini, C., Alibert, Y., & Naef, D. 2006, in Tenth Anniversary of 51 Peg-b: Status of and prospects for hot Jupiter studies, ed. L. Arnold, F. Bouchy, & C. Moutou, 24–34

Berger, D. H., Gies, D. R., McAlister, H. A., et al. 2006, ApJ, 644, 475

Beuzit, J.-L., Feldt, M., Dohlen, K., et al. 2008, in Society of Photo-Optical Instrumentation Engineers (SPIE) Conference Series, Vol. 7014, Society of Photo-Optical Instrumentation Engineers (SPIE) Conference Series

Blackwell, D. E. & Shallis, M. J. 1977, MNRAS, 180, 177

Bochanski, J. J., Hawley, S. L., Covey, K. R., et al. 2010, AJ, 139, 2679

Bodaghee, A., Santos, N. C., Israelian, G., & Mayor, M. 2003, A&A, 404, 715

Bond, I. A., Udalski, A., Jaroszyński, M., et al. 2004, ApJ, 606, L155

Bond, J. C., Lauretta, D. S., Tinney, C. G., et al. 2008, ApJ, 682, 1234

Bond, J. C., Tinney, C. G., Butler, R. P., et al. 2006, MNRAS, 370, 163

Bonfils, X. 2012, in EAS Publications Series, Vol. 57, EAS Publications Series, ed. C. Reylé, C. Charbonnel, & M. Schultheis, 193–207

Bonfils, X., Delfosse, X., Udry, S., et al. 2011, ArXiv e-prints

Bonfils, X., Delfosse, X., Udry, S., et al. 2013, A&A, 549, A109

Bonfils, X., Delfosse, X., Udry, S., et al. 2005, A&A, 442, 635

Bonfils, X., Gillon, M., Udry, S., et al. 2012, A&A, 546, A27

Bonfils, X., Mayor, M., Delfosse, X., et al. 2007, A&A, 474, 293

Borucki, W. J., Koch, D., Basri, G., et al. 2010, Science, 327, 977

Borucki, W. J. & Summers, A. L. 1984, ICARUS, 58, 121

Boss, A. P. 1997, Science, 276, 1836

Boss, A. P. 2006a, ApJ, 643, 501

Boss, A. P. 2006b, ApJ, 644, L79

Bouchy, F., Mayor, M., Lovis, C., et al. 2009, A&A, 496, 527

Bouchy, F. & The Sophie Team. 2006, in Tenth Anniversary of 51 Peg-b: Status of and prospects for hot Jupiter studies, ed. L. Arnold, F. Bouchy, & C. Moutou, 319–325

Boyajian, T. S., von Braun, K., van Belle, G., et al. 2012, ApJ, 757, 112

Brett, J. M. 1995a, A&A, 295, 736

Brett, J. M. 1995b, A&AS, 109, 263

Brott, I. & Hauschildt, P. H. 2005, in ESA Special Publication, Vol. 576, The Three-Dimensional Universe with Gaia, ed. C. Turon, K. S. O'Flaherty, & M. A. C. Perryman, 565

Brugamyer, E., Dodson-Robinson, S. E., Cochran, W. D., & Sneden, C. 2011, ApJ, 738, 97

Bruno, G. 1584

Buchhave, L. A., Latham, D. W., Johansen, A., et al. 2012, Nature, 486, 375

Burgasser, A. J., Kirkpatrick, J. D., Reid, I. N., et al. 2003, ApJ, 586, 512

Butler, R. P., Johnson, J. A., Marcy, G. W., et al. 2006, PASP, 118, 1685

Butler, R. P., Vogt, S. S., Marcy, G. W., et al. 2004, ApJ, 617, 580

Caffau, E., Ludwig, H.-G., Steffen, M., Freytag, B., & Bonifacio, P. 2011, SOLPHYS, 268, 255

Campbell, B. & Walker, G. A. H. 1979, PASP, 91, 540

Campbell, B., Walker, G. A. H., & Yang, S. 1988, ApJ, 331, 902

Casagrande, L., Flynn, C., & Bessell, M. 2008, MNRAS, 389, 585

Casagrande, L., Portinari, L., & Flynn, C. 2006, MNRAS, 373, 13

Chabrier, G. 2003, PASP, 115, 763

Chabrier, G. & Baraffe, I. 2000, ARAA, 38, 337

Chanamé, J. & Gould, A. 2004, ApJ, 601, 289

Charbonneau, D., Berta, Z. K., Irwin, J., et al. 2009, Nature, 462, 891

Charbonneau, D., Brown, T., Latham, D., & Mayor, M. 2000, ApJ, 529, L45

Chen, Y. Q. & Zhao, G. 2006, AJ, 131, 1816

Churchill, C. 2010, Interstellar Medium lecture notes - Spring 2010

Claret, A. & Bloemen, S. 2011, A&A, 529, A75

Cochran, W. D., Fabrycky, D. C., Torres, G., et al. 2011, ApJS, 197, 7

Cochran, W. D., Hatzes, A. P., & Hancock, T. J. 1991, ApJL, 380, L35

Copernicus, N. 1543, On the revolution of heavenly spheres

Cosentino, R., Lovis, C., Pepe, F., et al. 2012, in Society of Photo-Optical Instrumentation Engineers (SPIE) Conference Series, Vol. 8446, Society of Photo-Optical Instrumentation Engineers (SPIE) Conference Series

Covey, K. R., Hawley, S. L., Bochanski, J. J., et al. 2008, AJ, 136, 1778

Cumming, A., Marcy, G. W., & Butler, R. P. 1999, ApJ, 526, 890

Cusa, N. 1440, De docta ignorantia

Delfosse, X., Forveille, T., Beuzit, J.-L., et al. 1999, A&A, 344, 897

Delfosse, X., Forveille, T., Ségransan, D., et al. 2000, A&A, 364, 217

Delgado Mena, E., Israelian, G., González Hernández, J. I., et al. 2010, ApJ, 725, 2349

Delgado Mena, E., Israelian, G., González Hernández, J. I., Santos, N. C., & Rebolo, R. 2011, ApJ, 728, 148

Delgado Mena, E., Israelian, G., González Hernández, J. I., Santos, N. C., & Rebolo, R. 2012, ApJ, 746, 47

Demarque, P., Woo, J.-H., Kim, Y.-C., & Yi, S. K. 2004, ApJS, 155, 667

Demory, B., Ségransan, D., Forveille, T., et al. 2009, A&A, 505, 205

Demory, B.-O., Gillon, M., Bonfils, X., et al. 2012, Spitzer Proposal, 80261

Demory, B.-O., Torres, G., Neves, V., et al. 2013, ApJ, 768, 154

Dodson-Robinson, S. E., Veras, D., Ford, E. B., & Beichman, C. A. 2009, ApJ, 707, 79

Dotter, A., Chaboyer, B., Jevremović, D., et al. 2008, ApJS, 178, 89

Doyle, L. R., Carter, J. A., Fabrycky, D. C., et al. 2011, Science, 333, 1602

Dumusque, X., Pepe, F., Lovis, C., et al. 2012, Nature, 491, 207

Dumusque, X., Santos, N. C., Udry, S., Lovis, C., & Bonfils, X. 2011a, A&A, 527, A82

Dumusque, X., Udry, S., Lovis, C., Santos, N. C., & Monteiro, M. J. P. F. G. 2011b, A&A, 525, A140

Ecuvillon, A., Israelian, G., Santos, N. C., Mayor, M., & Gilli, G. 2006, A&A, 449, 809

Eggenberger, A. & Udry, S. 2010, EAS Publications Series, 41, 27

Endl, M., Cochran, W. D., Kürster, M., et al. 2006, ApJ, 649, 436

Fischer, D. A. & Valenti, J. 2005, ApJ, 622, 1102

Ford, E. B. & Rasio, F. A. 2006, ApJL, 638, L45

Forestini, M. 1994, A&A, 285, 473

Galilei, G. 1610, Sidereus nuncius

Gálvez-Ortiz, M. C., Delgado-Mena, E., González Hernández, J. I., et al. 2011, A&A, 530, A66

Gardner, J. P., Mather, J. C., Clampin, M., et al. 2006, SSR, 123, 485

Ghezzi, L., Cunha, K., Smith, V. V., et al. 2010, ApJ, 720, 1290

Ghezzi, L., Cunha, K., Smith, V. V., et al. 2009, ApJ, 698, 451

Gilli, G., Israelian, G., Ecuvillon, A., Santos, N. C., & Mayor, M. 2006, A&A, 449, 723

Gillon, M., Pont, F., Demory, B. ., et al. 2007, ArXiv e-prints, 705

Gizis, J. E. 1997, AJ, 113, 806

Gliese, W. & Jahreiß, H. 1991, Preliminary Version of the Third Catalogue of Nearby Stars, Tech. rep.

Goldreich, P. & Sari, R. 2003, ApJ, 585, 1024

Gonzalez, G. 1997, MNRAS, 285, 403

Gonzalez, G. 1998, A&A, 334, 221

Gonzalez, G. 2008, MNRAS, 386, 928

Gonzalez, G., Carlson, M. K., & Tobin, R. W. 2010, MNRAS, 407, 314

González Hernández, J. I., Israelian, G., Santos, N. C., et al. 2010, ApJ, 720, 1592

González Hernández, J. I., Israelian, G., Santos, N. C., et al. 2011, in IAU Symposium, Vol. 276, IAU Symposium, ed. A. Sozzetti, M. G. Lattanzi, & A. P. Boss, 422–423

Gould, A. & Chanamé, J. 2004, ApJS, 150, 455

Gray, D. F. 2005, The Observation and Analysis of Stellar Photospheres (The Observation and Analysis of Stellar Photospheres, 3rd Edition, by D.F. Gray. ISBN 0521851866.Cambridge, UK: Cambridge University Press, 2005.)

Griffin, R. & Griffin, R. 1973, MNRAS, 162, 255

Gustafsson, B. 1989, ARAA, 27, 701

Gustafsson, B., Edvardsson, B., Eriksson, K., et al. 2008, A&A, 486, 951

Haisch, K. E., Lada, E. A., & Lada, C. J. 2001, ApJ, 553, L153

Hale, A. 1995, PASP, 107, 22

Han, I., Black, D. C., & Gatewood, G. 2001, ApJL, 548, L57

Hansen, B. M. S. & Barman, T. 2007, ApJ, 671, 861

Hauschildt, P. H., Allard, F., & Baron, E. 1999, ApJ, 512, 377

Hekker, S. & Meléndez, J. 2007, A&A, 475, 1003

Henry, G. W., Marcy, G. W., Butler, R. P., & Vogt, S. S. 2000, ApJ, 529, L41

Henry, T. J. & McCarthy, Jr., D. W. 1993, AJ, 106, 773

Hills, J. G. 1970, Nature, 226, 730

Hocking, R. R. 1976, Biometrics, 32, 1

Howard, A. W., Marcy, G. W., Johnson, J. A., et al. 2010, Science, 330, 653

Hubble, E. P. 1929, ApJ, 69, 103

Huygens, C. 1698, [Kosmotheoros]; sive, de terris coelestibus earumque ornatu conjecturae.

Ida, S. & Lin, D. N. C. 2004a, ApJ, 604, 388

Ida, S. & Lin, D. N. C. 2004b, ApJ, 616, 567

Ida, S. & Lin, D. N. C. 2005, ApJ, 626, 1045

Irwin, J., Charbonneau, D., Nutzman, P., & Falco, E. 2009, in IAU Symposium, Vol. 253, IAU Symposium, ed. F. Pont, D. Sasselov, & M. J. Holman, 37–43

Irwin, J. M., Quinn, S. N., Berta, Z. K., et al. 2011, ApJ, 742, 123

Israelian, G., Delgado Mena, E., Santos, N. C., et al. 2009, Nature, 462, 189

Israelian, G., Santos, N. C., Mayor, M., & Rebolo, R. 2001, Nature, 411, 163

Israelian, G., Santos, N. C., Mayor, M., & Rebolo, R. 2003, A&A, 405, 753

Israelian, G., Santos, N. C., Mayor, M., & Rebolo, R. 2004, A&A, 414, 601

Jackson, B., Barnes, R., & Greenberg, R. 2009, ApJ, 698, 1357

Jacob, W. S. 1855, MNRAS, 15, 228

Jehin, E., Gillon, M., Queloz, D., et al. 2011, The Messenger, 145, 2

Johnson, J. A., Aller, K. M., Howard, A. W., & Crepp, J. R. 2010a, PASP, 122, 905

Johnson, J. A. & Apps, K. 2009, ApJ, 699, 933

Johnson, J. A., Butler, R. P., Marcy, G. W., et al. 2007, ApJ, 670, 833

Johnson, J. A., Gazak, J. Z., Apps, K., et al. 2012, AJ, 143, 111

Johnson, J. A., Howard, A. W., Marcy, G. W., et al. 2010b, PASP, 122, 149

Jorissen, A., Mayor, M., & Udry, S. 2001, A&A, 379, 992

Kaeufl, H.-U., Ballester, P., Biereichel, P., et al. 2004, in Society of Photo-Optical Instrumentation Engineers (SPIE) Conference Series, Vol. 5492, Society of Photo-Optical Instrumentation Engineers (SPIE) Conference Series, ed. A. F. M. Moorwood & M. Iye, 1218–1227

Kalas, P., Graham, J. R., Chiang, E., et al. 2008, Science, 322, 1345

Kass, R. E. & Raftery, A. E. 1995, Journal of the American Statistical Association, 90, 773

Kennedy, G. M. & Kenyon, S. J. 2008, ApJ, 673, 502

Kennedy, G. M., Kenyon, S. J., & Bromley, B. C. 2007, APSS, 311, 9

Kepler, J., Ptolemaeus, C., & Fludd, R. 1619, Harmonices mvndi libri v. qvorvm primus geometricvs, de figurarum regularium, quae proportiones harmonicas constituunt, ortu architectonicvs, SEU EX geometria figvrata, de figurarum regularium congruentia in plano vel solido: tertius proprie harmonicvs, de proportionum harmonicarum ortu EX figuris

Kervella, P., Thévenin, F., Di Folco, E., & Ségransan, D. 2004, A&A, 426, 297

Koch, D. G., Borucki, W. J., Basri, G., et al. 2010, ApJL, 713, L79

Konacki, M. & Wolszczan, A. 2003, ApJL, 591, L147

Kornet, K., Wolf, S., & Różyczka, M. 2006, A&A, 458, 661

Kui, R. 1991, PhD thesis, PhD. thesis. Natl. Univ. Aust. , (1991)

Kurucz, R. 1993, ATLAS9 Stellar Atmosphere Programs and 2 km/s grid. Kurucz CD-ROM No. 13. Cambridge, Mass.: Smithsonian Astrophysical Observatory, 1993., 13

Kurucz, R. L. 1970, SAO Special Report, 309

Laertius, D. & Yonge, C. 1853, The Lives and Opinions of Eminent Philosophers, Bohn's classical library, v. 43 (H. G. Bohn)

Latham, D., Stefanik, R., Mazeh, T., Mayor, M., & Burki, G. 1989, Nature, 339, 38

Laughlin, G., Bodenheimer, P., & Adams, F. C. 2004, ApJ, 612, L73

Launhardt, R., Queloz, D., Henning, T., et al. 2008, in Society of Photo-Optical Instrumentation Engineers (SPIE) Conference Series, Vol. 7013, Society of Photo-Optical Instrumentation Engineers (SPIE) Conference Series

Laws, C., Gonzalez, G., Walker, K. M., et al. 2003, AJ, 125, 2664

Lee, J. W., Kim, S.-L., Kim, C.-H., et al. 2009, AJ, 137, 3181

Lenzen, R., Hartung, M., Brandner, W., et al. 2003, in Society of Photo-Optical Instrumentation Engineers (SPIE) Conference Series, Vol. 4841, Society of Photo-Optical Instrumentation Engineers (SPIE) Conference Series, ed. M. Iye & A. F. M. Moorwood, 944–952

Lépine, S., Hilton, E. J., Mann, A. W., et al. 2013, AJ, 145, 102

Lépine, S., Rich, R. M., & Shara, M. M. 2007, ApJ, 669, 1235

Levison, H. F. & Agnor, C. 2003, AJ, 125, 2692

Levison, H. F., Lissauer, J. J., & Duncan, M. J. 1998, AJ, 116, 1998

Lin, D. N. C., Bodenheimer, P., & Richardson, D. C. 1996, Nature, 380, 606

Lin, D. N. C. & Papaloizou, J. 1986, ApJ, 309, 846

Lindegren, L. 2009, in IAU Symposium #261, American Astronomical Society, Vol. 261, 1601

Lissauer, J. J. 2007, ApJL, 660, L149

Lissauer, J. J., Fabrycky, D. C., Ford, E. B., et al. 2011, Nature, 470, 53

Livio, M. & Pringle, J. E. 2003, MNRAS, 346, L42

López-Morales, M. 2007, ApJ, 660, 732

Lovelace, R. V. E., Romanova, M. M., & Barnard, A. W. 2008, MNRAS, 389, 1233

Lovis, C. & Mayor, M. 2007, A&A, 472, 657

Luck, R. E. & Heiter, U. 2006, AJ, 131, 3069

Macintosh, B. A., Graham, J. R., Palmer, D. W., et al. 2008, in Society of Photo-Optical Instrumentation Engineers (SPIE) Conference Series, Vol. 7015, Society of Photo-Optical Instrumentation Engineers (SPIE) Conference Series

Mann, A. W., Brewer, J. M., Gaidos, E., Lépine, S., & Hilton, E. J. 2013, AJ, 145, 52

Marcy, G., Butler, R. P., Fischer, D., et al. 2005, Progress of Theoretical Physics Supplement, 158, 24

Marois, C., Zuckerman, B., Konopacky, Q. M., Macintosh, B., & Barman, T. 2010, Nature, 468, 1080

Marzari, F., Baruteau, C., & Scholl, H. 2010, A&A, 514, L4

Marzari, F. & Weidenschilling, S. J. 2002, Icarus, 156, 570

Masset, F. & Snellgrove, M. 2001, MNRAS, 320, L55

Matsuyama, I., Johnstone, D., & Murray, N. 2003, ApJL, 585, L143

Matzner, C. D. & Levin, Y. 2005, ApJ, 628, 817

Mayor, M., Marmier, M., Lovis, C., et al. 2011, ArXiv e-prints

Mayor, M., Pepe, F., Queloz, D., et al. 2003, The Messenger, 114, 20

Mayor, M. & Queloz, D. 1995, Nature, 378, 355

McArthur, B. E., Benedict, G. F., Barnes, R., et al. 2010, ApJ, 715, 1203

McCarthy, C. & Zuckerman, B. 2004, AJ, 127, 2871

McCarthy, Jr., D. W., Probst, R. G., & Low, F. J. 1985, ApJL, 290, L9

McKee, C. F. & Ostriker, E. C. 2007, ARAA, 45, 565

Meléndez, J., Asplund, M., Gustafsson, B., & Yong, D. 2009, ApJL, 704, L66

Mermilliod, J., Mermilliod, M., & Hauck, B. 1997, A&AS, 124, 349

Montalbán, J. & Rebolo, R. 2002, A&A, 386, 1039

Morales, J. C., Gallardo, J., Ribas, I., et al. 2010, ApJ, 718, 502

Mordasini, C., Alibert, Y., & Benz, W. 2009a, A&A, 501, 1139

Mordasini, C., Alibert, Y., Benz, W., Klahr, H., & Henning, T. 2012, ArXiv e-prints

Mordasini, C., Alibert, Y., Benz, W., & Naef, D. 2008, in Astronomical Society of the Pacific Conference Series, Vol. 398, Extreme Solar Systems, ed. D. Fischer, F. A. Rasio, S. E. Thorsett, & A. Wolszczan, 235

Mordasini, C., Alibert, Y., Benz, W., & Naef, D. 2009b, A&A, 501, 1161

Mortier, A., Santos, N. C., Sousa, S., et al. 2013, A&A, 551, A112

Mould, J. R. 1976, A&A, 48, 443

Mould, J. R. & Hyland, A. R. 1976, ApJ, 208, 399

Mould, J. R. & Wyckoff, S. 1978, MNRAS, 182, 63

Moulton, F. R. 1899, AJ, 20, 33

Moutou, C., Hébrard, G., Bouchy, F., et al. 2009, A&A, 498, L5

Murray, N., Hansen, B., Holman, M., & Tremaine, S. 1998, Science, 279, 69

Nelan, E. P., Lupie, O. L., McArthur, B., et al. 1998, in Society of Photo-Optical Instrumentation Engineers (SPIE) Conference Series, Vol. 3350, Society of Photo-Optical Instrumentation Engineers (SPIE) Conference Series, ed. R. D. Reasenberg, 237–247

Neves, V., Bonfils, X., Santos, N. C., et al. 2012, a&a, 538, A25

Neves, V., Bonfils, X., Santos, N. C., et al. 2013, A&A, 551, A36

Neves, V., Santos, N. C., Sousa, S. G., Correia, A. C. M., & Israelian, G. 2009, A&A, 497, 563

Newton, I. 1760, Philosophiae naturalis principia mathematica, vol. 1 - 4

Nordström, B., Mayor, M., Andersen, J., et al. 2004, A&A, 418, 989

Nutzman, P. & Charbonneau, D. 2008, PASP, 120, 317

Ogihara, M. & Ida, S. 2008, in IAU Symposium, Vol. 249, IAU Symposium, ed. Y.-S. Sun, S. Ferraz-Mello, & J.-L. Zhou, 305–308

Önehag, A., Heiter, U., Gustafsson, B., et al. 2012, A&A, 542, A33

Papaloizou, J. & Lin, D. N. C. 1984, ApJ, 285, 818

Papaloizou, J. C. B. & Terquem, C. 2006, Reports of Progress in Physics, 69, 119

Pasquini, L., Avila, G., Dekker, H., et al. 2008, in Society of Photo-Optical Instrumentation Engineers (SPIE) Conference Series, Vol. 7014, Society of Photo-Optical Instrumentation Engineers (SPIE) Conference Series

Pasquini, L., Döllinger, M. P., Weiss, A., et al. 2007, A&A, 473, 979

Pepe, F., Mayor, M., Queloz, D., et al. 2004, A&A, 423, 385

Pepe, F. A., Cristiani, S., Rebolo Lopez, R., et al. 2010, in Society of Photo-Optical Instrumentation Engineers (SPIE) Conference Series, Vol. 7735, Society of Photo-Optical Instrumentation Engineers (SPIE) Conference Series

Perryman, M. 2011, The Exoplanet Handbook

Perryman, M. A. C., de Boer, K. S., Gilmore, G., et al. 2001, A&A, 369, 339

Pickles, A. J. 1998, PASP, 110, 863

Pinsonneault, M. H., DePoy, D. L., & Coffee, M. 2001, ApJ, 556, L59

Piskunov, N. E. 1992, in Stellar Magnetism, ed. Y. V. Glagolevskij & I. I. Romanyuk, 92–+

Piskunov, N. E., Kupka, F., Ryabchikova, T. A., Weiss, W. W., & Jeffery, C. S. 1995, A&AS, 112, 525

Pollack, J., Hubickyj, O., Bodenheimer, P., et al. 1996, Icarus, 124, 62

Pont, F. 2009, MNRAS, 396, 1789

Poveda, A., Herrera, M. A., Allen, C., Cordero, G., & Lavalley, C. 1994, RMxAA, 28, 43

Press, W. H., Teukolsky, S. A., Vetterling, W. T., & Flannery, B. P. 1992, Numerical recipes in FORTRAN. The art of scientific computing

Queloz, D., Mayor, M., Naef, D., et al. 2000a, in From Extrasolar Planets to Cosmology: The VLT Opening Symposium, ed. J. Bergeron & A. Renzini, 548–+

Queloz, D., Mayor, M., Weber, L., et al. 2000b, A&A, 354, 99

Quirrenbach, A., Coudé du Foresto, V., Daigne, G., et al. 1998, in Society of Photo-Optical Instrumentation Engineers (SPIE) Conference Series, Vol. 3350, Society of Photo-Optical Instrumentation Engineers (SPIE) Conference Series, ed. R. D. Reasenberg, 807–817

Ramírez, I., Asplund, M., Baumann, P., Meléndez, J., & Bensby, T. 2010, A&A, 521, A33

Rauscher, E. & Marcy, G. W. 2006, PASP, 118, 617

Raymond, S. N., Barnes, R., & Mandell, A. M. 2008, MNRAS, 384, 663

Reddy, B. E., Lambert, D. L., Laws, C., Gonzalez, G., & Covey, K. 2002, MNRAS, 335, 1005

Reid, I. N. & Hawley, S. L. 2005, New light on dark stars : red dwarfs, low-mass stars, brown dwarfs

Reuyl, D. & Holmberg, E. 1943, ApJ, 97, 41

Ribas, I. 2006, APSS, 304, 89

Robinson, S. E., Laughlin, G., Bodenheimer, P., & Fischer, D. 2006, ApJ, 643, 484

Rogers, L. A., Bodenheimer, P., Lissauer, J. J., & Seager, S. 2011, ApJ, 738, 59

Rogers, L. A. & Seager, S. 2010, ApJ, 716, 1208

Rojas-Ayala, B., Covey, K. R., Muirhead, P. S., & Lloyd, J. P. 2010, ApJ, 720, L113

Rojas-Ayala, B., Covey, K. R., Muirhead, P. S., & Lloyd, J. P. 2012, ApJ, 748, 93

Rousset, G., Lacombe, F., Puget, P., et al. 2003, in Society of Photo-Optical Instrumentation Engineers (SPIE) Conference Series, Vol. 4839, Society of Photo-Optical Instrumentation Engineers (SPIE) Conference Series, ed. P. L. Wizinowich & D. Bonaccini, 140–149

Ruiz, M. T. & Anguita, C. 1993, AJ, 105, 614

Safronov, V. S. 1972, Evolution of the protoplanetary cloud and formation of the earth and planets.

Sahlmann, J., Ségransan, D., Mérand, A., et al. 2012, in Society of Photo-Optical Instrumentation Engineers (SPIE) Conference Series, Vol. 8445, Society of Photo-Optical Instrumentation Engineers (SPIE) Conference Series

Sahlmann, J., Ségransan, D., Queloz, D., & Udry, S. 2011, in IAU Symposium, Vol. 276, IAU Symposium, ed. A. Sozzetti, M. G. Lattanzi, & A. P. Boss, 117–120

Sandars, N. 1960, The Epic of Gilgamesh: An English Version with an Introduction, Penguin classics (Penguin Group US)

Santerne, A., Díaz, R. F., Moutou, C., et al. 2012, A&A, 545, A76

Santerne, A., Fressin, F., Díaz, R. F., et al. 2013, ArXiv e-prints

Santos, N. C. 2008, New Astronomy Reviews, 52, 154

Santos, N. C., García López, R. J., Israelian, G., et al. 2002, A&A, 386, 1028

Santos, N. C., Israelian, G., García López, R. J., et al. 2004a, A&A, 427, 1085

Santos, N. C., Israelian, G., & Mayor, M. 2001, A&A, 373, 1019

Santos, N. C., Israelian, G., & Mayor, M. 2004b, A&A, 415, 1153

Santos, N. C., Israelian, G., Mayor, M., Rebolo, R., & Udry, S. 2003, A&A, 398, 363

Santos, N. C., Israelian, G., Randich, S., García López, R. J., & Rebolo, R. 2004c, A&A, 425, 1013

Schlaufman, K. C. & Laughlin, G. 2010, A&A, 519, A105+

Schneider, J., Dedieu, C., Le Sidaner, P., Savalle, R., & Zolotukhin, I. 2011, A&A, 532, A79

Seager, S. 2011, Exoplanets

Seager, S., Kuchner, M., Hier-Majumder, C. A., & Militzer, B. 2007, ApJ, 669, 1279

Seager, S. & Mallén-Ornelas, G. 2003, ApJ, 585, 1038

See, T. J. J. 1896, AJ, 16, 17

Ségransan, D., Delfosse, X., Forveille, T., et al. 2003a, in IAU Symposium, Vol. 211, Brown Dwarfs, ed. E. Martín, 413

Ségransan, D., Kervella, P., Forveille, T., & Queloz, D. 2003b, A&A, 397, L5

Silvotti, R., Schuh, S., Janulis, R., et al. 2007, Nature, 449, 189

Simcoe, R. A., Burgasser, A. J., Bernstein, R. A., et al. 2008, in Society of Photo-Optical Instrumentation Engineers (SPIE) Conference Series, Vol. 7014, Society of Photo-Optical Instrumentation Engineers (SPIE) Conference Series

Skrutskie, M. F., Cutri, R. M., Stiening, R., et al. 2006, AJ, 131, 1163

Smith, V. V., Cunha, K., & Lazzaro, D. 2001, AJ, 121, 3207

Sneden, C. 1973, Ph.D. Thesis, Univ. of Texas,

Sousa, S. G., Santos, N. C., Israelian, G., Mayor, M., & Udry, S. 2011, A&A, 533, A141

Sousa, S. G., Santos, N. C., Mayor, M., et al. 2008, A&A, 487, 373

Sozzetti, A. 2004, MNRAS, 354, 1194

Sozzetti, A., Torres, G., Latham, D. W., et al. 2009, ApJ, 697, 544

Stauffer, J. R. & Hartmann, L. W. 1986, ApJS, 61, 531

Strand, K. A. 1943, PASP, 55, 29

Struve, O. 1952, The Observatory, 72, 199

Takeda, G. & Rasio, F. A. 2005, ArXiv Astrophysics e-prints

Takeda, Y. 2007, PASJ, 59, 335

Takeda, Y., Kawanomoto, S., Honda, S., Ando, H., & Sakurai, T. 2007, A&A, 468, 663

Takeda, Y., Sato, B., & Murata, D. 2008, PASJ, 60, 781

Takeda, Y., Tajitsu, A., Honda, S., et al. 2011, PASJ, 63, 697

Terrien, R. C., Mahadevan, S., Bender, C. F., et al. 2012, ApJL, 747, L38

Thommes, E. W., Matsumura, S., & Rasio, F. A. 2008, Science, 321, 814

Tirard, H. & Naville, E. 2004, The Book of the Dead 1910 (Kessinger Publishing)

Torres, G. 2013, Astronomische Nachrichten, 334, 4

Torres, G., Andersen, J., & Giménez, A. 2010, A&AR, 18, 67

Trilling, D., Benz, W., Guillot, T., et al. 1998, ApJ, 500, 428

Trilling, D., Lunine, J., & Benz, W. 2002, A&A, 394, 241

Tsuji, T. 1966, PASJ, 18, 127

Udry, S., Mayor, M., Benz, W., et al. 2006, A&A, 447, 361

Udry, S., Mayor, M., Naef, D., et al. 2002, A&A, 390, 267

Udry, S., Mayor, M., Naef, D., et al. 2000, A&A, 356, 590

Udry, S. & Santos, N. 2007, ARAA, 45, 397

Valenti, J. A. & Fischer, D. A. 2005, VizieR Online Data Catalog, 215, 90141

Valenti, J. A. & Piskunov, N. 1996, A&AS, 118, 595

Valenti, J. A., Piskunov, N., & Johns-Krull, C. M. 1998, ApJ, 498, 851

van Belle, G. T., van Belle, G., Creech-Eakman, M. J., et al. 2008, ApJS, 176, 276

van de Kamp, P. 1963, AJ, 68, 515

van Leeuwen, F. 2007, A&A, 474, 653

Vogt, S. S., Allen, S. L., Bigelow, B. C., et al. 1994, in Society of Photo-Optical Instrumentation Engineers (SPIE) Conference Series, Vol. 2198, Society of Photo-Optical Instrumentation Engineers (SPIE) Conference Series, ed. D. L. Crawford & E. R. Craine, 362

Winn, J. N., Albrecht, S., Johnson, J. A., et al. 2011, ApJL, 741, L1

Wolszczan, A. 1994, Science, 264, 538

Wolszczan, A. 1997, Celestial Mechanics and Dynamical Astronomy, 68, 13

Wolszczan, A. & Frail, D. A. 1992, Nature, 355, 145

Woolf, V. M., Lépine, S., & Wallerstein, G. 2009, PASP, 121, 117

Woolf, V. M. & Wallerstein, G. 2004, MNRAS, 350, 575

Woolf, V. M. & Wallerstein, G. 2005, MNRAS, 356, 963

Woolf, V. M. & Wallerstein, G. 2006, PASP, 118, 218

Wright, J. T., Fakhouri, O., Marcy, G. W., et al. 2011, PASP, 123, 412

Wright, J. T., Marcy, G. W., Howard, A. W., et al. 2012, ArXiv e-prints

Wu, Y. & Murray, N. 2003, ApJ, 589, 605

Youdin, A. N. 2010, in EAS Publications Series, Vol. 41, EAS Publications Series, ed. T. Montmerle, D. Ehrenreich, & A.-M. Lagrange, 187–207

Zakamska, N. L. & Tremaine, S. 2004, AJ, 128, 869

Appendix **A**

Planet detection techniques

In the current year of 2013 the most important techniques of exoplanet detection are the radial velocity (RV) and the photometric transits, accounting for 58 and 35% of the detections respectively, according to the extrasolar planet encyclopaedia at 10/07/2013.

Other techniques, such as direct imaging, microlensing, and pulsar timing will also be mentioned but with fewer details. Fig A.1 shows, at November 2010, the existing and projected planet detection methods, along with their current and potential detection limits, as well as the number of planets discovered using each method.

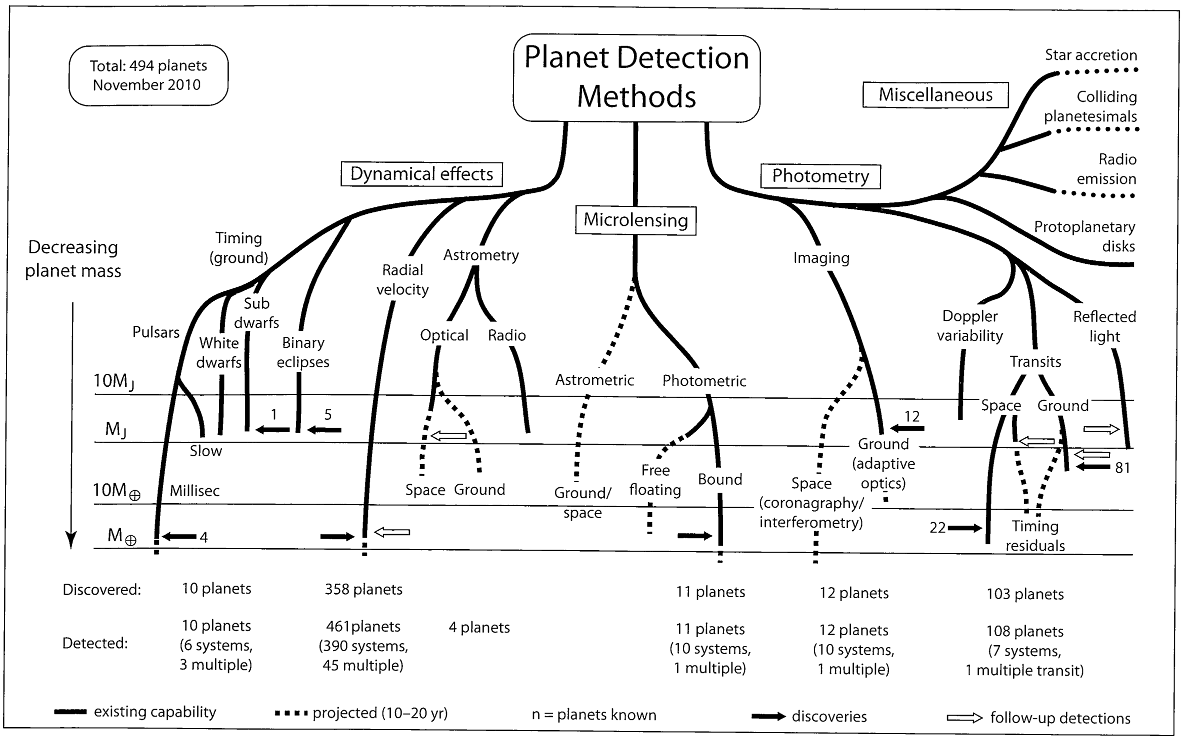

Figure A.1: Detection methods for exoplanets. The lower limits of the lines show the detectable masses that are within reach today (solid lines) and in the next 10 to 20 years (dashed lines). A mass scale is shown on the left hand side of the plot. Solid lines indicate measurements and the white arrows indicate confirmation detections of exoplanets previously discovered using other technique. From Perryman (2011).

A.1 The radial velocity technique

The RV technique, first proposed by Struve (1952), consists in the detection of the radial component of the Doppler shift of the star about the centre of mass of the star+planet system, induced by the unseen planetary companion. The Doppler effect is illustrated in Fig. A.2 a) and Fig. A.2 b) shows the RV curve of the first planet discovery around a solar-type star (Mayor & Queloz 1995).

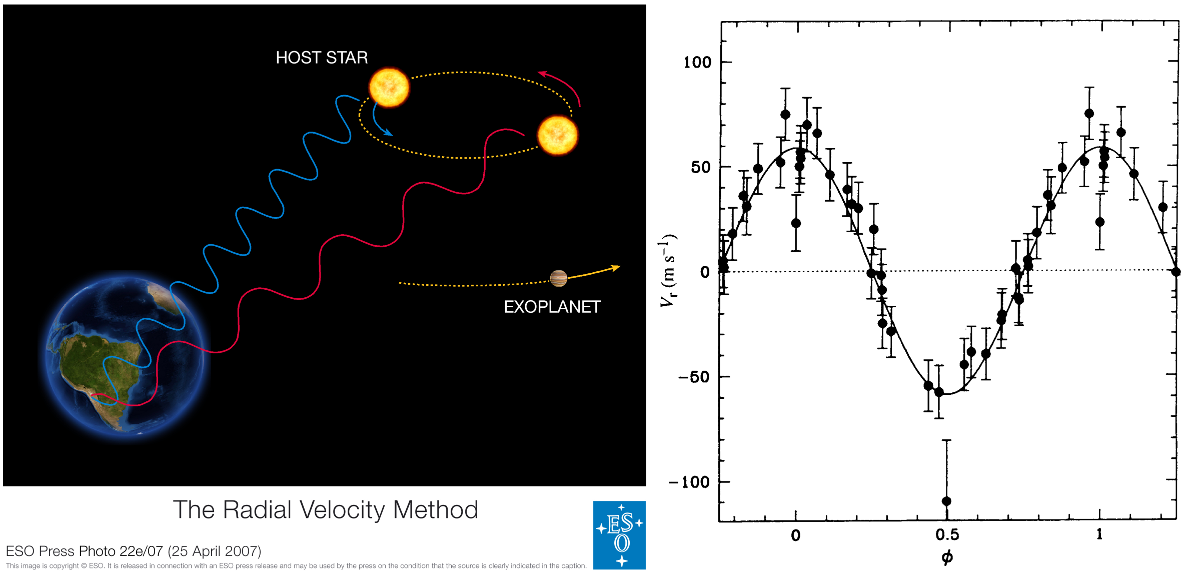

(a) (b)

Figure A.2: a) Illustration showing how the RV technique works; b) Radial velocity curve of the detection of the first extrasolar planet around the star 51 Peg. Taken from Mayor & Queloz (1995).

The measured RV signal is expressed in terms of a velocity semi-amplitude (e.g. Cumming et al. 1999),

$$K = \left(\frac{2\pi G}{P}\right)^{1/3} \frac{M_P \sin i}{(M_P + M_*)^{2/3}} \frac{1}{\sqrt{1-e^2}}, \tag{A.1}$$

where G is the gravitational constant, P the period, M_P the planetary mass, M_* the stellar mass, i the inclination, and e the eccentricity. The values of P, e and K, as well as the semi-major axis of the ellipse, can be calculated directly from the RV curve. From here we can calculate the mass function,

$$f(m) = \frac{(M_p \sin i)^3}{(M_P + M_*)^2} = 1.036 \times 10^{-7} K^2 (1-e)^{3/2} P, [M_\odot], \tag{A.2}$$

and obtain the value of the minimum mass, $M_P \sin i$. For a detailed analysis refer to Santos (2008). Unfortunately the RV technique is not as suited to measure planets around massive stars, and is very sensitive to stellar activity and rotation. Therefore, the RV technique is most effective with 'quiet' FGKM dwarfs. Moreover, we do not obtain the radius with RV nor the inclination of the orbit. In order to lift the $m \sin i$ degeneracy and acquire the radius to measure the mean density of a planet one needs to combine the RV method with other techniques, such as photometric transits or astrometry (see Sect. A.2 and A.3).

We can easily observe, from Eq. A.1, that the detection of more massive and/or closer planets is easier, as the measured signal is greater for theses cases. Moreover, the RV semi-amplitude also increases with decreasing stellar mass, M_*. It is then easier to detect closer-in, more massive planets around less massive stars with RV.

Present instruments include the highly successful HARPS spectrograph (Mayor et al. 2003; Pepe et al. 2004) (see Appendix C.3 for more details) with more than 130 planets discovered so far. Similar spectrographs include the CORALIE (Queloz et al. 2000b) and SOPHIE (Bouchy & The Sophie Team 2006) spectrographs, as well as the HIRES (Vogt et al. 1994) and HARPS-N (Cosentino et al. 2012). The latter is the HARPS twin of the northern hemisphere, installed on the TNG telescope at La Palma.

The future will bring novel instruments, such as the ESPRESSO spectrograph (Pepe et al. 2010), to be commissioned in 2014 on the VLT. The aim of ESPRESSO is to reach an RV accuracy of 10 cms^{-1} that will enable the detection of Earth-type planets in the habitable zone of solar-type stars. Further into the future the CODEX spectrograph (Pasquini et al. 2008) is predicted to be installed at the European Extremely Large Telescope (E-ELT) around 2018. This new instrument will bring the unprecedented precision of 1 cms^{-1} enabling the detection of most planets around the Solar Neighbourhood brighter stars.

A.2 Transits

A transit is detected when a tiny attenuation of the light flux coming from a star is observed, while a planet crosses its disk. If the crossing happens in front of the disk, the event is called a transit. Otherwise, if the planet goes behind the star, we loose the light reflected in the planet's surface, and the event is called an occultation. In this case, the observed attenuation of the light flux is even smaller than during the transit, and is very hard to observe from the ground. Fig. A.3 shows an illustration of a transit and an occultation.

The first transit was observed by Henry et al. (2000); Charbonneau et al. (2000) around the star HD 209458. Since then, more than 300 planets were found. From the Kepler mission (Borucki et al. 2010; Koch et al. 2010) alone there are 2740 planet candidates, as of 7 January 2013 (Batalha et al. 2013). The smallest transiting planet discovered so far is Kepler-37b, with a radius only slightly larger than the Moon (Barclay et al. 2013).

Measuring a transiting exoplanet is of particular importance as it gives its radii, along with the distance and the period of the orbit. An example of an observed transit curve is shown in Fig A.4.

Following Seager & Mallén-Ornelas (2003), the light flux variation, for circular orbits ($e = 0$), during the transit can be roughly approximated as

$$\frac{\Delta F}{F} \simeq \left(\frac{R_P}{R_*}\right)^2 . \tag{A.3}$$

This variation is proportional to the square of the ratio of the planetary radius, R_P, with the stellar radius R_*. For a Jupiter type planet orbiting a solar-type star, for instance, the ΔF will be approximately 1%. If

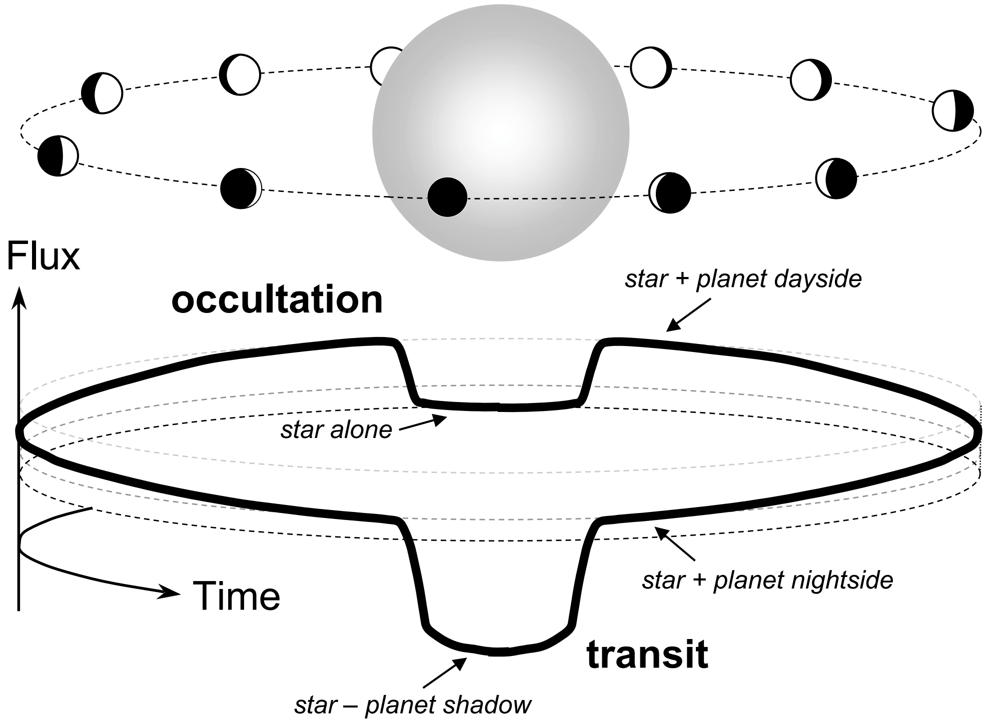

Figure A.3: Illustration of a transit and occultation. During a transit a fraction of the star light is blocked by the disc of the planet. The flux then rises as the reflected light from the planet's dayside comes into view. The flux drops again, but much lower, when the reflected light from the planet disappears. From Seager (2011).

we consider a smaller star, for example, a typical M dwarf with a radius of 0.30 $M_\odot$, the dip in the flux will jump to $\sim 11\%$. Therefore, if we have the measurement of the stellar radius and the light curve we can calculate the planetary radius.

From the duration of the transit we can calculate the period of the planet. Considering the approximation to an equatorial transit in a circular orbit ($e = 0$), the transit duration can be computed from

$$t_T \simeq 13 \left(\frac{M_*}{M_\odot}\right)^{-\frac{1}{2}} \left(\frac{a}{AU}\right)^{\frac{1}{2}} \left(\frac{R_*}{R_\odot}\right) [hours], \tag{A.4}$$

where M_* is the stellar mass, a is the semi-major axis of the orbit, and R_* is the stellar radius.

Having the measurement of the stellar mass and radius, it is straightforward to calculate the semi-major axis of the orbit a, and one can then calculate the period P using $Kepler's$ third law (Kepler et al. 1619).

It is only possible to observe a transit within an angular range very close to an edge-on configuration. In fact, the minimum inclination where a transit can occur can be estimated using $\cos i = R_*/a$. Also, and according to Borucki & Summers (1984), the probability for a transit to occur in a randomly-oriented planet on a circular orbit and assuming the $R_P << R_*$ approximation is

$$p = \frac{R_*}{a} \simeq 0.005 \left(\frac{R_*}{R_\odot}\right) \left(\frac{a}{AU}\right)^{-1} \tag{A.5}$$

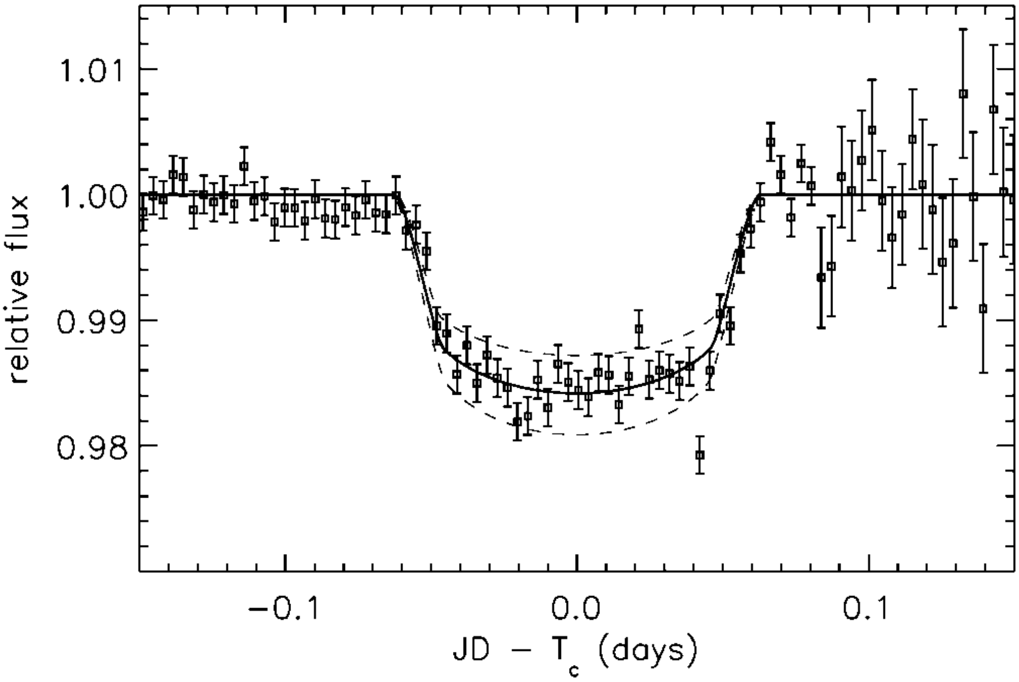

Figure A.4: Observed photometric curve of a transit, binned into 5 minute averages. The solid line represents the best fit for data. The dashed lines represent transit curves if the transit planet had a radius ±10% bigger. Taken from Charbonneau et al. (2000).

From this equation we can see that the probability is independent of the radius of the planet. For example, the probability that a planet situated at 0.1 *AU* from a solar-type star transits is 5%. In a typical M-dwarf, with $R_* = 0.3R_\odot$, this probability decreases to 1.5%. From a realistic evaluation of the value of i and p we can conclude that transits only occur for $i \simeq 90^\circ$, and p is always very small.

One of the biggest disadvantages of this method is its high rates of false positives, as shown in Santerne et al. (2012), that may go as high as 35% for the bigger Kepler field planet candidates while the average global false-positive rate of the Kepler mission is estimated to be around $11.3 \pm 1.1\%$ (Santerne et al. 2013). The ‘intruders’ disguised as planets might be eclipsing binaries, grazing stellar eclipses, brown dwarfs or simply activity-induced chromospheric variations. Therefore, it is very important that transit-search programs have a follow-up program using RVs to confirm the planets and fully characterise the systems.

Using both RV and transit measurements we can also lift the minimum mass degeneracy and obtain the true mass of the planet, as well as calculate its mean density.

A.3 Other methods

In this subsection we will only give a very brief overview about other exoplanet detection techniques, such as pulsar timing, direct imaging, microlensing, and astrometry.

Timing

This planet detection method consists in the precise measurement of the perturbation of the periodic time signatures that the star may have. There are three kinds of stars that offer this possibility, namely, radio pulsars (e.g. Wolszczan 1997), pulsating stars (mainly post-main sequence stars, and specifically, pulsating white dwarfs) (e.g. Silvotti et al. 2007), and eclipsing binaries (e.g. Lee et al. 2009). The timing technique is, thus, very interesting to probe into the late-part evolutionary sequence of stars and their planetary companions and, in this context, is complementary to RV and photometry.

The first planet around a stellar body, a 6.2 millisecond pulsar, was discovered using the timing technique, in 1992 (Wolszczan & Frail 1992). Among the few candidates around pulsars, pulsating stars and eclipsing binaries, 15 planets are confirmed in 12 planetary systems in 10/07/2013.

Interestingly, the smallest extrasolar planet to date was found around a millisecond pulsar, with a tiny mass of 0.02 $M_{\oplus}$, roughly the size of our Moon (Wolszczan 1994). Fig A.5 shows the time-of arrival residuals of the pulsar PSR B1257+12, with three planets. Three timing models, shown as a solid line, are fit to the observations where a) represents the fit for the model with two planets, b) shows the fit of the third planet, after removing two planets, and c) the residuals after removing all three planets. The keplerian orbits of planets A and B, with masses of $4.3 \pm 0.2 M_{\oplus}$ and $3.9 \pm 0.2 M_{\oplus}$, are shown in a), and the third keplerian orbit of planet C, with a tiny mass of $0.02 \pm 0.002 M_{\oplus}$ is shown in b).

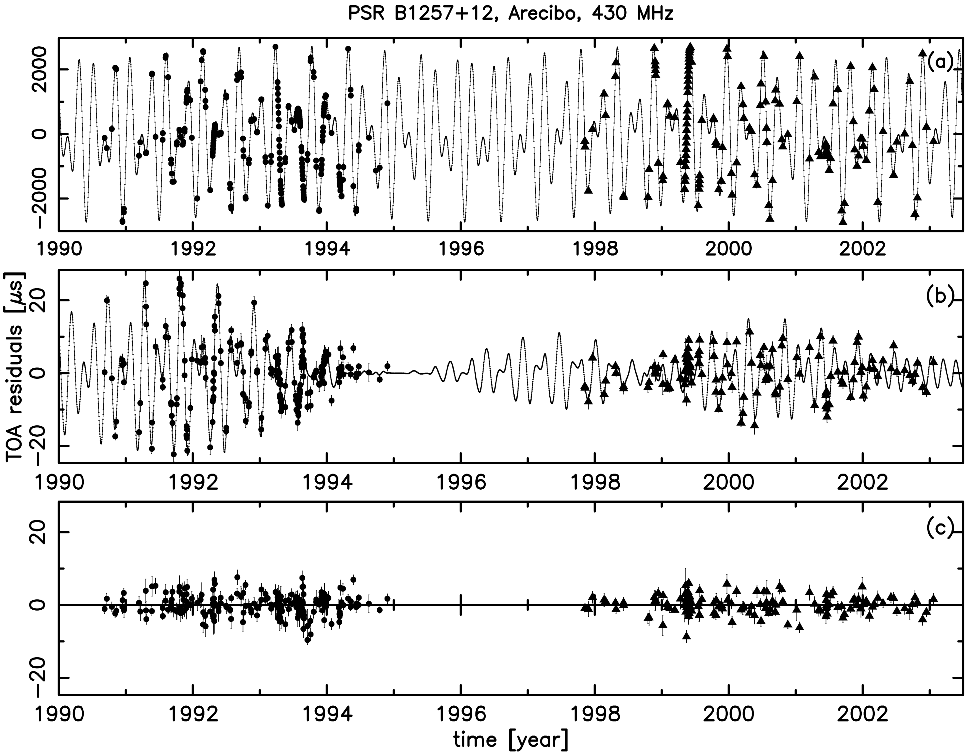

Figure A.5: Time-of-arrival residuals from the pulsar PSR B1257+12. The fits using three different models are depicted as a solid line. From Konacki & Wolszczan (2003).

Microlensing

As of 10/07/2013, microlensing accounted for 21 planets around 19 hosts. The first planet using this technique was found by Bond et al. (2004), a $2.6^{+0.8}_{-0.6} M_J$ planet, with a semi-major axis of about 4.3 AU, orbiting a K dwarf star. The technique consists in the detection of a microlensing event, that results from the magnification of the light from a distant star caused by the gravitational field of a nearer, but still distant star (from $\sim$ 700 to $\sim$ 7100 pc), that act as a gravitational lens. The star of the lens causes the primary effect, but the field of the planetary bodies around it may also make a detectable contribution. The microlensing effect can be observed in the light curve of OGLE-2005-BLG-390 (Fig. A.6), taken from Beaulieu et al. (2006).

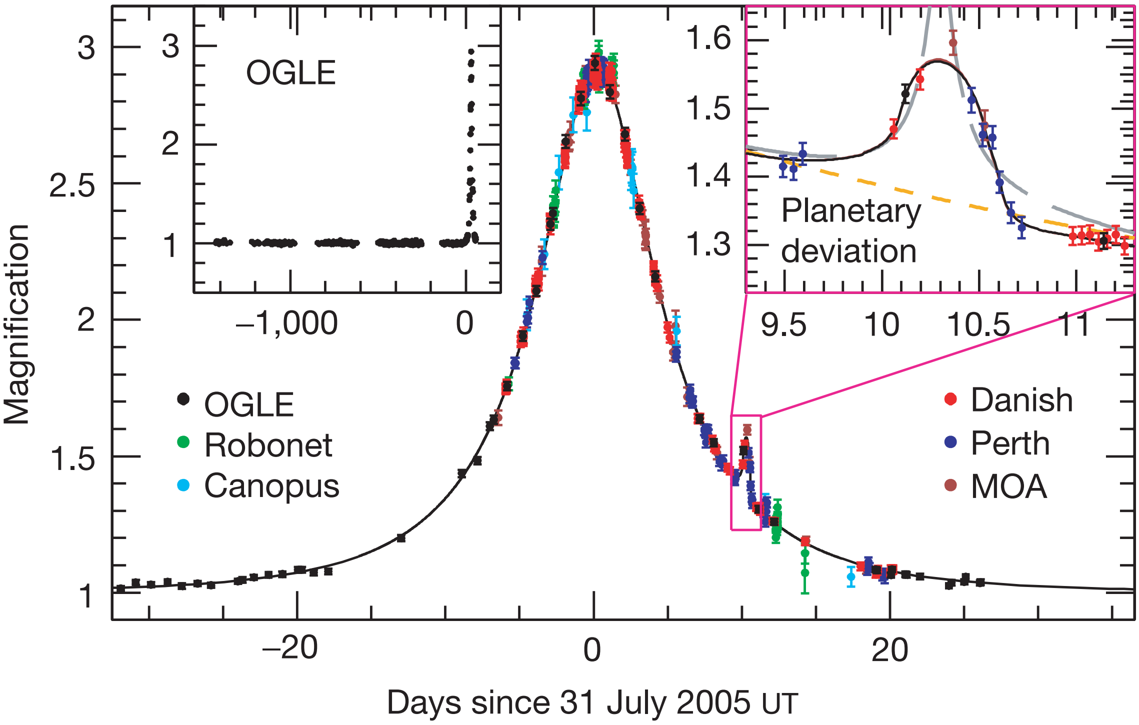

Figure A.6: Observed light curve of the OGLE-2005-BLG-390 microlensing event and best-fit model plotted as a function of time. The planetary deviation from the brightness amplification of the stellar lens is shown in the subset. The planetary mass is estimated to be $5.5^{+5.5}_{-2.7}$. From Beaulieu et al. (2006).

From the light curve of the microlensing effect we can calculate the mass, period and semi-major axis of the planet. The great advantage of this technique is the possibility of exploring planetary systems that are in distant regions of our Galaxy. Also, the technique is complementary to RVs and transits in the sense that it has a higher sensitivity of detection in the outer regions of planetary systems.

However, the probability that the same alignment is produced again is very close to zero, meaning that each single event is not reproducible. Moreover, it is impossible today to do a follow-up of these systems with current technologies, like RV and transits.

Direct imaging

As the name states, direct imaging aims to gather an image of the exoplanet light separated from the light of its host star. The greatest challenge posed to obtain a point source image of an exoplanet is the tiny ratio of the planet to stellar flux. This ratio depends on the stellar type and luminosity class, on the distance of the planet to the star, on the planet's mass, composition radius and age, on the composition and height of the atmosphere, and on the wavelength region of observation. If we take the example of Jupiter, and consider visible wavelength with a Jupiter-Sun separation of 0.5 arcsec at a distance of 10 pc, this ratio is around 10^{-9}, while for the Earth it increases to 10^{-10}. In the infrared, however, the flux ratio values increase several orders of magnitude, with a typical 10^{-5} value.

To date, it was only possible to obtain direct images of massive exoplanets (2 to 30 M_J) with wide orbits (few to hundreds of AU) using instruments such as NACO (Lenzen et al. 2003; Rousset et al. 2003) at the VLT and GPI (Gemini Planet Imager Macintosh et al. 2008) at the Gemini south telescopes. A photograph of HR8799 showing 4 planets captured by imaging can be seen in Fig. A.7 (Marois et al. 2010). It is the biggest planetary system found so far with this technique. Their mass estimation and distances range from 5 to 10 M_J and 10 to 65 AU, respectively.

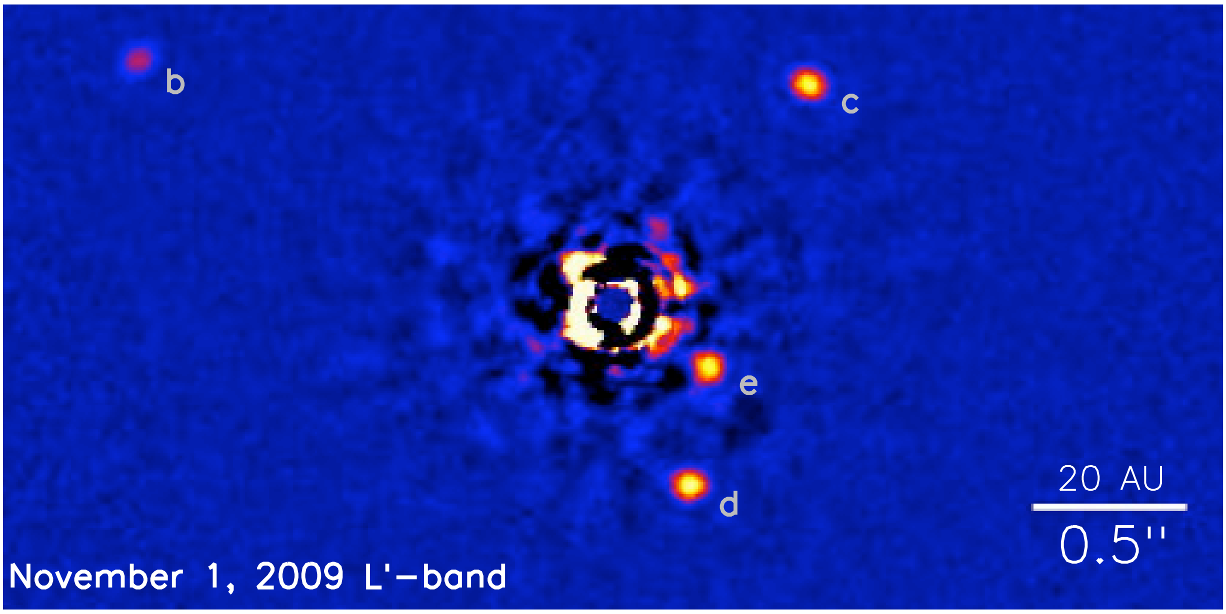

Figure A.7: Image in the L-band of the planetary system around HR8799. From Marois et al. (2010).

Up to now (10/07/2013) 34 planets in 30 planetary systems have been discovered using this technique. Direct imaging is complementary to RV and photometry, as it detects very long period planets.

In the early future instruments like SPHERE (Beuzit et al. 2008, Spectro-Polarimetric High-contrast Exoplanet Research) on the ground and JWST (Gardner et al. 2006, James Webb Space Telescope) in space will be able to detect and characterise smaller and closer exoplanets.

Astrometry

Astrometry, in the exoplanetary context, consists in the high-precision determination of the transverse component of the tiny displacements of a star around its centre of mass, due to the presence of an unseen planetary companion.

Interestingly, the first attempts to discover the first exoplanet were made using this technique (e.g. Jacob 1855, see Sect. 1.2). Until now, all attempts to independently discover a planet with astrometry have failed, and it was only in 2002 (Benedict et al. 2002), that the first confirmation of a RV planet detection was achieved, using the Fine Guiding Sensor (Nelan et al. 1998) of the Hubble Space Telescope (HST). Indeed, a precision of the order of 10 micro-arcsecond will be needed to independently and reliably detect a planetary body using this method. Fig. A.8 shows one of such efforts (McArthur et al. 2010).

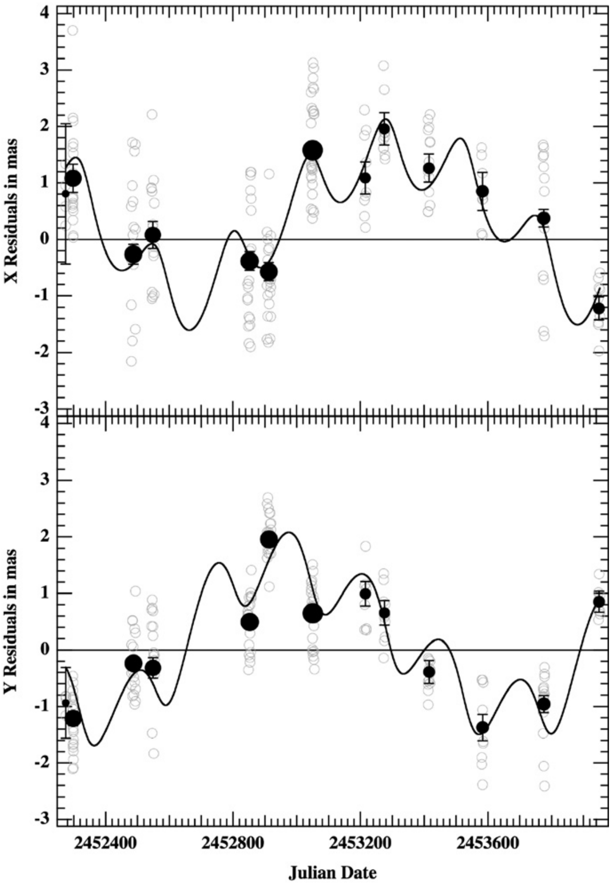

Figure A.8: Astrometric motion from μ *And* due to planets b and c. The astrometric orbit is shown by the solid line. The open circles are the individual astrometric measurements, and the solid circles are the normal points made from an astrometric fits to the individual measurements. Its size is proportional to the individual measurements. From McArthur et al. (2010).

However, the future of astrometry looks bright. At the end of 2013, the European Space Agency GAIA mission (Perryman et al. 2001; Lindegren 2009) will be launched to space and will measure the proper motions and parallaxes of approximately $\sim 1\%$ of all stars in the Galaxy, or 1 billion stars, at typical accuracies of 20-25 μas. This unprecedented precision will allow the detection of thousands of new planets and astrometry will become, quite ironically, the prime discoverer of extrasolar planets. Along with GAIA, the ground-based program ESPRI (Exoplanet Search with PRIMA, Launhardt et al. 2008; Sahlmann et al. 2012) using the PRIMA (Phase-Referenced Imaging and Microarcsecond Astrometry, Quirrenbach et al. 1998) facility at the VLTI has started its first-light test at the end of 2012, and achieved a precision of 30 $\mu arcsec$. With astrometry one can directly obtain the true planetary masses, as well as the semi-major axis, inclination, and distance.

Astrometry is complementary of RV and transit searches, in the sense that it is more sensitive to longer period planets ($P > 1$ year), as the astrometric signature is directly proportional to the semi-major axis of the orbit of the planet. Moreover, it enables the detection of stellar companions where the RV technique is more complicated, such as in BA stars, and young stars.

Appendix B

Exoplanet properties

Fig. B.1 shows a plot of the mass of discovered exoplanets with time, for the RV (blue circles) and transit (open red circles) detection. The exoplanet mass value is equal to the minimum mass when the inclination *i* is not known, as it is the case in most of the RV detections, according to `exoplanet.org`(Wright et al. 2011). We can observe the spectacular progress that the exoplanet field has made in less than 25 years. During this time we were able to detect and characterise planetary systems from the Jupiter type regime down to one earth mass planets and lower (e.g. Wolszczan 1994; Dumusque et al. 2012; Barclay et al. 2013). From Fig. B.1 we can also observe that transit detections have an increasing weight, where the contribution of the Kepler mission (Borucki et al. 2010; Koch et al. 2010), with 134 confirmed planets so far (on 10/07/2013), is of paramount importance.

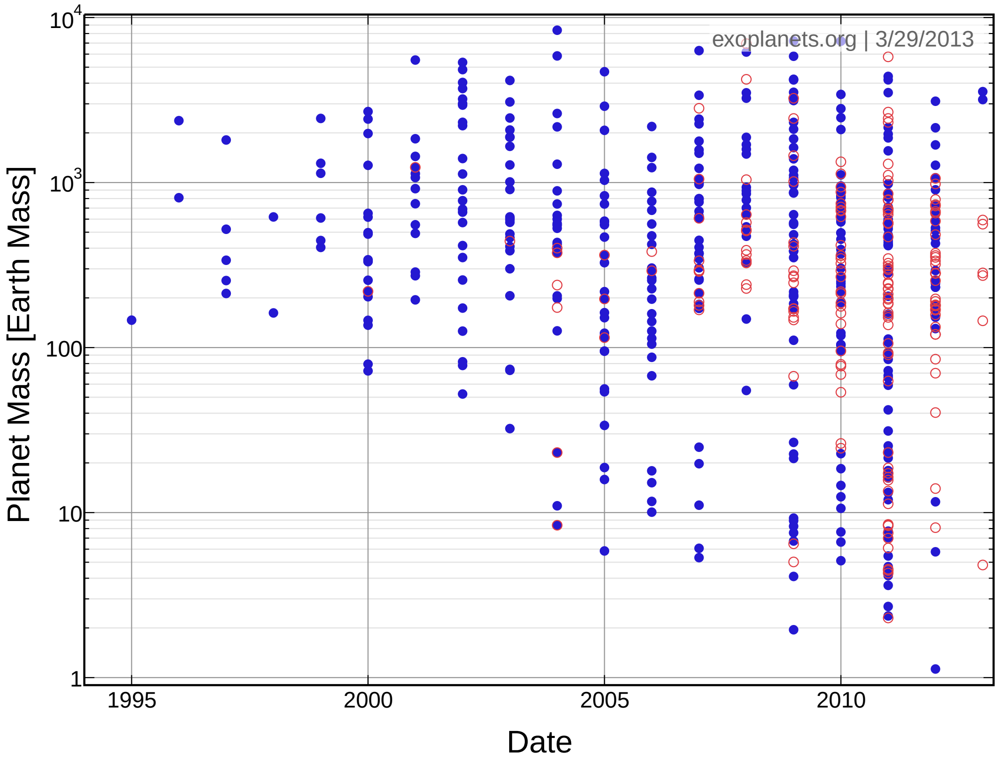

Figure B.1: Exoplanet mass as a function of discovery date. The RV detections are depicted with solid circles, while the transit ones are represented by open circles. Plot made using `exoplanets.org` (Wright et al. 2012).

B.1 Mass distribution

Fig B.2 shows the distribution of mass of the transiting and RV planets, in Jupiter mass. This value is equal to the minimum mass when the inclination i is not known, as it is the case in most of the RV detections, according to `exoplanet.org`.(Wright et al. 2011).

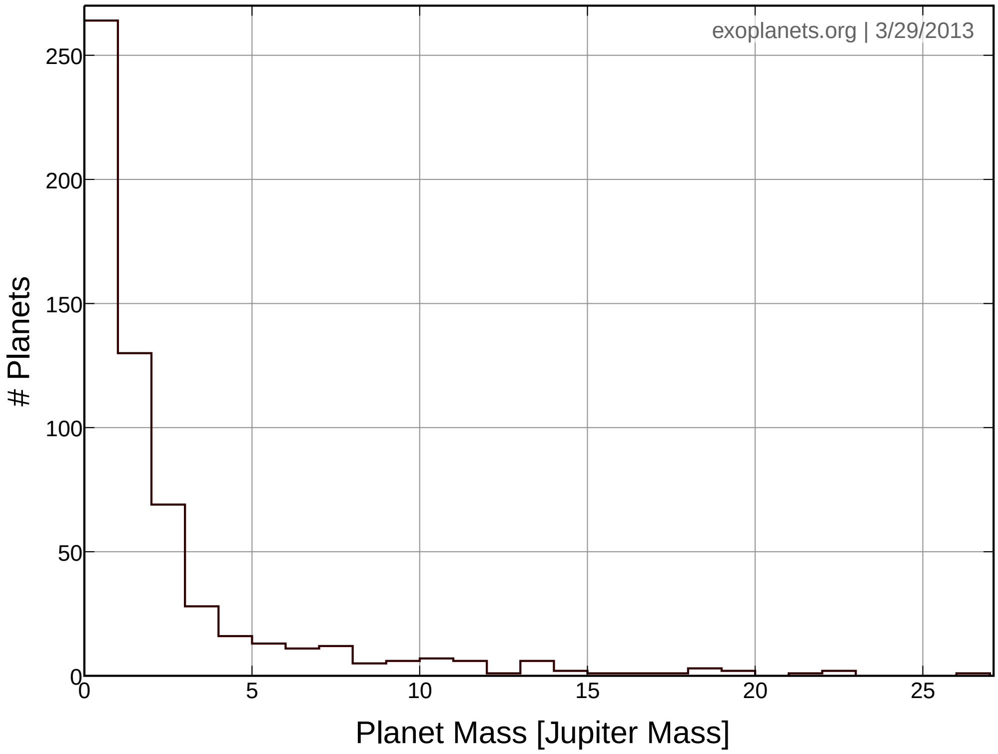

Figure B.2: Mass distribution of exoplanets detected by transit and RV surveys. Plot made using `exoplanets.org` (Wright et al. 2012).

We can observe that most planets accumulate below 5 M_J. For higher masses there is a paucity of substellar companions commonly known as the Brown Dwarf desert. The mass distribution increases again towards higher masses, when it reaches the lower-mass M dwarfs (e.g. Sahlmann et al. 2011). This separation between exoplanets and stars strongly suggests that there is a different process of planet formation, but a scenario where most Brown Dwarfs may migrate inwards and merge with a primary star in an evolving protoplanetary disk is not excluded (e.g Matzner & Levin 2005). At present we do not have yet a clear picture of the upper limit of exoplanet mass or if the transition between exoplanets and brown dwarfs is continuous or discrete, as we only have true masses for a few planets from RVs and transit surveys alike.

Fig. B.3 shows the minimum mass distributions from one of the largest RV programs, the combined HARPS + CORALIE surveys (Mayor et al. 2011). We show this study here because the HARPS spectrograph is the only instrument that has enough precision to adequately study the Super-Earth mass regime. We consider that the minimum mass distribution is a good proxy for the distribution of real mass, as shown by Jorissen et al. (2001, (see this better)).

In Fig. B.3 a) we can observe a binomial distribution, with peaks around ~ 10 and ~ 500 $M_\oplus$, separating a population of Super-Earths and Neptunes, and Jovian-Type planets. We can also see a steep decline in the number of planets from 15 to 30 $M_\oplus$. The observed minimum, around $\sim$ 50 $M_\oplus$ is predicted from planet synthesis theoretical models (e.g. Mordasini et al. 2009b).

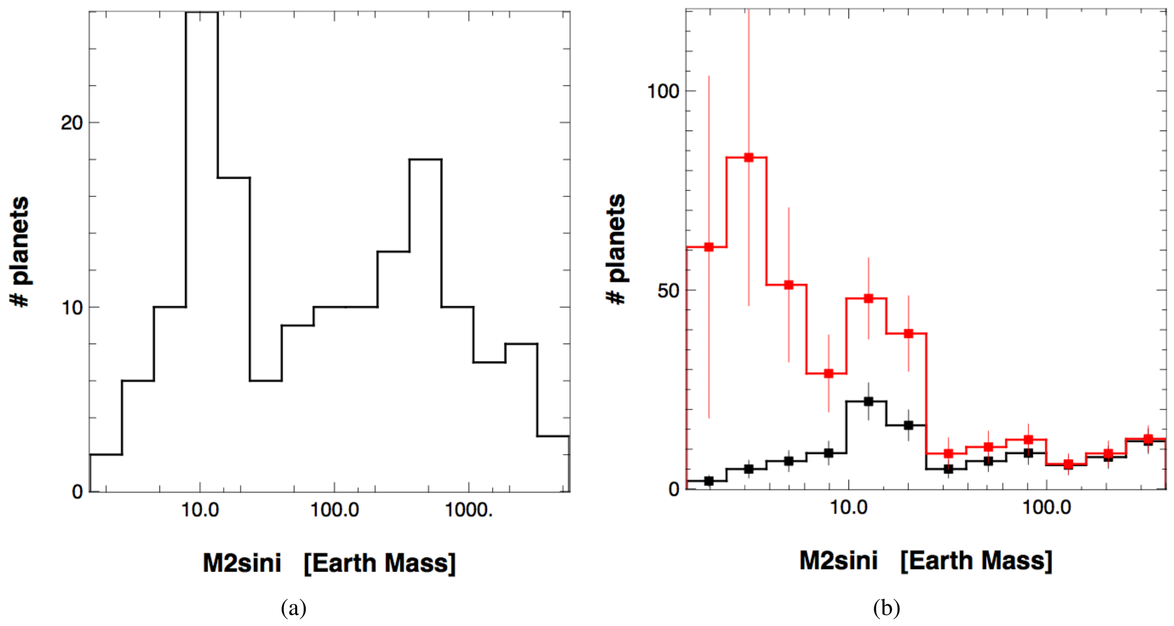

Figure B.3: (a) Planetary minimum mass histogram for the HARPS+CORALIE volume-limited sample; (b) Same histogram as in a) (black line) and detection bias corrected histogram (red line). From Mayor et al. (2011).

The separation region between Super-Earth/Neptune-type planets and Jovian-type planets can be interpreted, in the light of the core-accretion paradigm, as the region where the runaway gas accretion phase takes place (see Sect. 1.5). This implies that most protoplanets that reach this mass range will undergo a fast increase of their mass, ending up with Jovian-type masses.

The distribution depicted in Fig B.3 b) is the same as in Fig. B.3 a), depicted in black, but with the bias corrected distribution shown in red. This correction is computed as in Howard et al. (2010). In the bias corrected distribution we can observe that the sharp decrease after the Super-Earth/Neptune-type region is even steeper, and a new and even more numerous population of Earth-type planets should also be present and waiting to be discovered with higher precision instruments.

It is also worth noting that, for periods below 100 days, there is an even greater accumulation of low mass planets around the10 $M_\oplus$ peak. Indeed, the first kind of detected planets were massive and very close to their hosts (the so-called Hot Jupiters). However we can now observe that their contribution to the total number of planets is very small, accounting for less than 1% of planets detected in RV surveys (Mayor et al. 2011) and in transit observations (e.g. Kepler - Batalha et al. 2013). Regarding M dwarfs, we can observe, in Fig. B.4 that, in general, the planet mass distribution follows a similar trend as in the FGK hosts. The relative importance of the two peaks of the binomial distribution is uncertain as the number of M dwarfs with planets is still low. However, it is now clear that the paucity of hot Jupiters around M dwarfs (only one found so far - Johnson et al. 2010a) does not seem to translate into a lack of higher mass planets around M dwarfs (e.g. Bonfils et al. 2013). This result suggests that the stellar mass may have an important role in the formation of Jovian planets, and that a compensation effect between mass and metallicity may be important for the formation of these bodies (e.g. Thommes et al. 2008; Mordasini et al. 2012), and that this effect may be detected indirectly because it implies a stronger planet-metallicity relation that in the case of the FGK dwarfs.

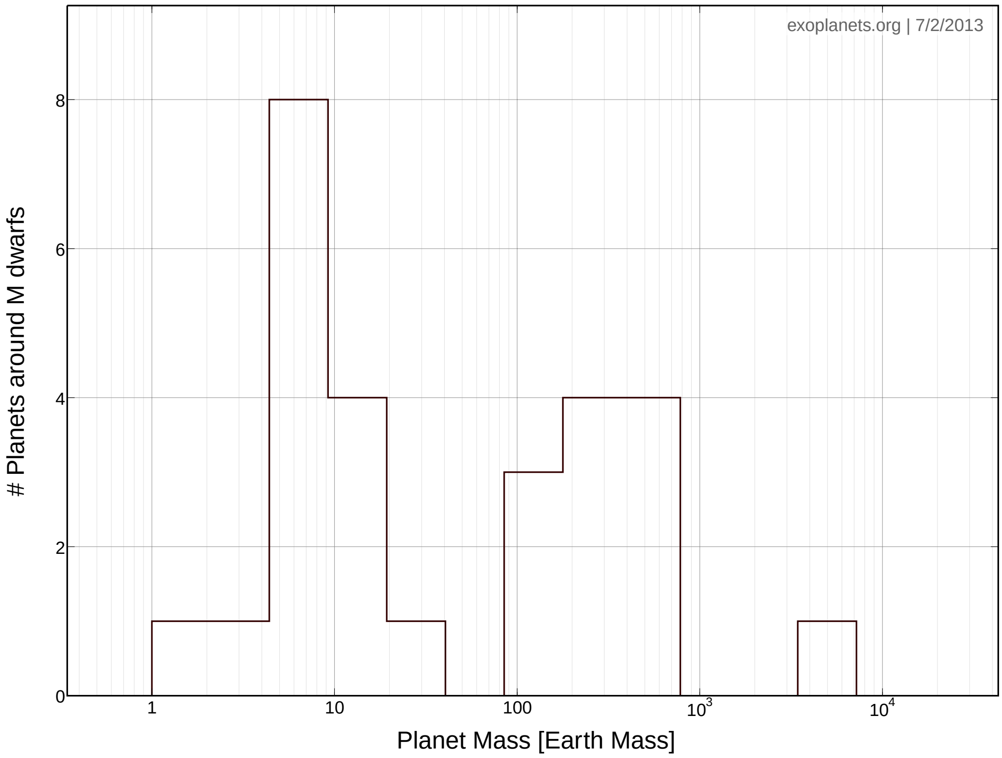

Figure B.4: Mass distribution of exoplanets detected by transit and RV surveys around M dwarfs. Plot made using `exoplanets.org` (Wright et al. 2012).

B.2 Period distribution

Regarding the exoplanet period distribution we can observe in Fig. B.5 a) that there is a bimodal distribution peaking around ~ 4 and ~ 400 days. From Fig. B.5 b) we can discern the different period distributions according to the exoplanet's mass. The black histogram corresponds to masses greater than 2 M_J, the red to masses between 0.5 and 2 M_J, the green to masses lower than 0.5 M_J, and the blue to masses lower than 0.158 M_J, that corresponds to M$\sim$ 50 $M_\oplus$. We observe that planets with $M_P < 0.5\ M_J$ are the most important contributors to the first peak of the distribution, whereas the second peak is mostly populated by planets with mass greater than 2 M_J. As the mass increases, the relative population between the two peaks changes, increasing in the second peak, and decreasing in the first. Regarding the period distribution of the lowest planet mass ($M_P < 50\ M_\oplus$) we observe a big cut-off after the 100-150 day bin, but it is difficult to know yet if this trend is real or just the effect of a detection bias (e.g. Mayor et al. 2011).

The accumulation of higher mass planets around the first peak can be explained by migration (e.g. Papaloizou & Lin 1984; Trilling et al. 1998; Papaloizou & Terquem 2006), where giant planets could efficiently migrate from their birth place, beyond the ice line, to an orbit very close to the star by changing angular momentum with the gas or/and with planetesimals until the disk has dissipated (e.g. Trilling et al. 1998; Ida & Lin 2004a; Alibert et al. 2005; Mordasini et al. 2008) or that some mechanism has stopped the migration, such as the existence of a central cavity in the disk due to the stellar magnetosphere (e.g. Lin et al. 1996; Adams et al. 2009), stellar winds (Lovelace et al. 2008) or photoevaporation (Matsuyama

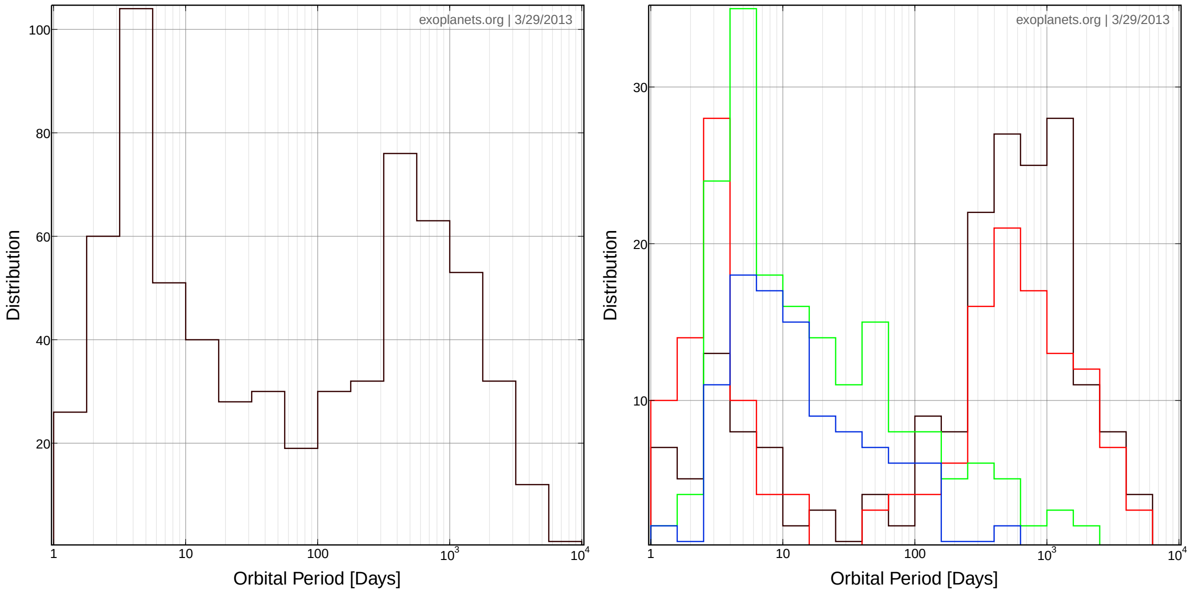

(a) (b)

Figure B.5: (a) Period distribution of exoplanets detected with RV and photometry; (b) Period distributions of exoplanets according to planetary mass. The black histogram corresponds to masses greater than 2 M_J, the red to masses between 0.5 and 2 M_J, the green to masses lower than 0.5 M_J, and the blue to masses lower than 0.158 M_J, or 50 $M_\oplus$. Histograms made using `exoplanets.org` (Wright et al. 2012).

et al. 2003), tidal friction (e.g. Lin & Papaloizou 1986; Trilling et al. 1998), Roche Lobe overflow (e.g. Trilling et al. 1998; Hansen & Barman 2007) and resonant trapping, leading to an outward migration (e.g. Masset & Snellgrove 2001), among many others. Alternatively the migration could also be originated by planet-planet scattering and halted by tidal circularization (e.g. Marzari & Weidenschilling 2002; Ford & Rasio 2006). For a review regarding migration see Armitage (2010) and Perryman (2011).

The smaller planets in very short orbits may have different origins: they could have simply formed *in situ*, accreting material from their surroundings; formed at larger distances and then migrated near the host star; formed from material being gravitationally trapped in a resonant orbit with a migrating giant planet; from mass loss of a giant or icy planet that migrated into a close orbit (see Raymond et al. 2008).

Regarding the second peak of the period distribution, is it populated mostly by Gas giants with masses greater than 0.5 M_J. This feature is easier to explain, as, according to core-accretion theory, giant planets are formed at these distances, beyond the ice line of their host stars, and migration at these longer distances may be less efficient due to the fact that a larger portion of the disk has to be disturbed to initiate the migration process. Alternatively, planet-planet scattering could also be important, as results for certain models show that there is easier to migrate low-mass planets than provoke a significant migration on higher mass ones (e.g. Marzari & Weidenschilling 2002; Levison & Agnor 2003).

For M dwarfs there exists a peak around $\sim$ 6 days, and a long tail towards longer periods. However, the number of planets found around M dwarfs is still small, and the majority of planets have masses below 30 $M_\oplus$, which they are also more difficult to detect and therefore the distribution is more affected with detection biases.

B.3 Mass-period relation

The plot of the mass versus the logarithm of the period is shown in Fig. B.6. The black open circles depict the RV detected planets, while the red open squares the planets found by transits. The black crosses identify planets around a star in a multiple system. We observe that, in the region above 5 M_J and $P < 40$ day, there are much fewer planets than for larger periods. If we discard binary systems and account only for RV detections we observe only one planet in the region with $M > 2M_J$ and $P < 20$ day. Even this lone planet (HD162020) might be a brown dwarf (Udry et al. 2002). This feature is similar as in previous studies (e.g. Udry & Santos 2007; Eggenberger & Udry 2010) but less significant, due to the transit detections.

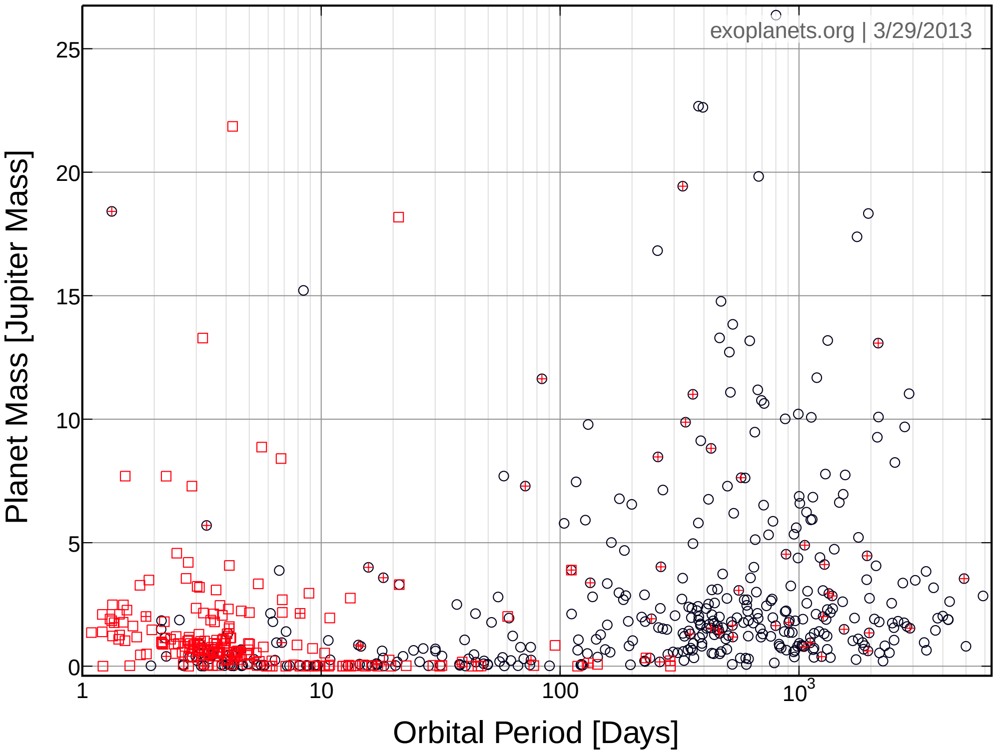

Figure B.6: Mass-Period plot of exoplanets detected by transits (red open squares) and RV (black open circles). The black cross identify planets around a star in a multiple system. Plot made using `exoplanets.org` (Wright et al. 2012).

The different migration theories attempt to explain this paucity of massive planets in shorter periods. For instance, type II migration (i.e. happens when a planet has enough mass, above 0.5 to 1 M$_J$, to open a gap in the disk) seems to be less effective for massive planets (e.g. Trilling et al. 1998, 2002), effectively stranding them at longer periods or near their birth place, at a few AU. On the other hand, a fast migration followed by engulfment could also explain this feature, where planets that ventured too far suffer tidal decay and slowly spiral down into the star (e.g. Trilling et al. 1998; Jackson et al. 2009). The massive transiting planets with masses higher than 5 M$_J$ that can be observed in Fig. B.6 might be part of this ‘condemned’ population, or just a transition population soon-to-be circularised or synchronised by tidal effects (Pont 2009).

B.4 Eccentricity-period relation

Fig. B.7 shows the eccentricity versus period. We can observe that, on average, there is an increase of the eccentricity with the log of the period. This picture clearly show the contrast and variety of the different planetary systems, when compared with our own Solar System, where the eccentricity is near zero. If we take into account the effect of the mass, we observe that, on average, the higher mass planets have a higher eccentricity (Marcy et al. 2005), but there is no clear reason for this, as it is easier to change significantly the orbits of smaller planets than the massive ones. Moreover, Udry & Santos (2007) noted that the distribution of exoplanets and binaries is very similar, which is rather enigmatic, because planets and stars are supposed to have very different formation processes, and we expect that formation in a disk yields almost circular orbits. Therefore, other processes must be at play to strongly change the orbits of the planets.

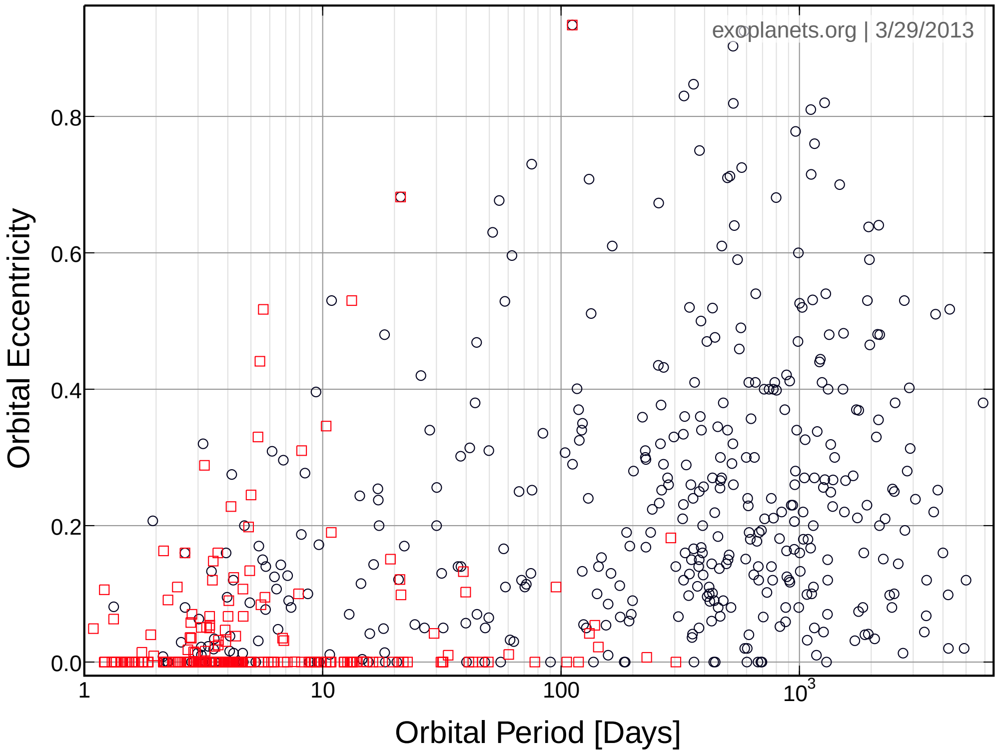

Figure B.7: Eccentricity-Period plot of exoplanets detected by transits (red open squares) and RV (black open circles). The black cross identify planets around a star in a multiple system. Plot made using `exoplanets.org` (Wright et al. 2012).

The diagram also shows other interesting features such as: the sub-group of long-period and low eccentricity, that correspond to orbits similar to the ones of the Giants of the Solar System; another group of planets with zero eccentricity and periods shorter than 6 days show evidence of orbital circularisation by tidal effects. Almost all planets in this region belong to this group.

The different eccentricities may be caused and maintained primarily by planet-planet scattering (e.g. Marzari et al. 2010). The scattering arises from a gravitationally unstable multiple system configuration which can result in the ejection of one planet (typically the lightest one), an increase in orbital separation between the different elements of the system, resulting in a usually more stable configuration, or in planet-planet/planet-star collisions. Scattering can also provoke effects, such as the Kozai Mechanism (e.g. Takeda & Rasio 2005; Moutou et al. 2009), that will enhance even more the eccentricity of one of the bodies. Other mechanisms that can also be at play are, for instance, the interaction with the disk itself (Goldreich & Sari 2003), the giant planets-planetesimals interactions (Levison et al. 1998; Murray et al. 1998), and the influence of a passing-by (e.g. Zakamska & Tremaine 2004) or bounded (e.g. Wu & Murray 2003) stellar companion.

Overall, the different sub-groups within Fig B.7, hint at different formation & evolution processes that may be often mixed in time, and are, therefore, hard to disentangle.

Appendix C

The Spectrograph

During the four years of my Ph.D. I made an extensive use of HARPS high-resolution spectra as well as participating in six observing missions with HARPS in La Silla. In this chapter I make a brief description of the working principles behind a spectrograph, as well as to depict the technical details, capabilities and limitations of the ESO HARPS spectrograph. For a detailed description of the basic physics, equations and tools behind the operation of a general spectrograph, the prospective reader can consult, for instance, chapter 3 of Gray (2005) or chapter 6 of Churchill (2010).

C.1 The basic principles of a spectrograph

A modern spectrograph is comprised of an entrance slit, a collimator, a grating, a camera, and a detector, as shown in Fig. C.1. The incident light that is originated in a source, a star in our case, enters the telescope and is reflected into the first component of the spectrograph, the slit, that is located in one of the focal planes of the telescope. The light that passes through the slit is diverging, and needs to be aligned with a collimator. The parallel light is then reflected by the collimator to the grating that disperses the light towards the camera that, in turn, will focus the light onto the detector.

The diffraction grating is the fundamental element of a spectrograph. A grating is characterised by having equal-spaced grooves in its surface. Fig. C.2 depicts a schematic of a reflection grating of length L, showing the individual grooves, with width s and distance d between each groove. The number of grooves N_g is given by the ratio between L and d. After the incident light, with angle α, is reflected by the grating, the light is diffracted at a wavelength dependent angle β.

The grating equation,

$$\frac{n\lambda}{d} = \sin\alpha + \sin\beta, \tag{C.1}$$

depicts the relation between diffraction angle and the wavelength, where n is the diffraction order, λ the wavelength of the incoming light, d the distance between grooves, α the incident angle of the incoming photons, and β is the angle of the diffracted light reflected from the grating. The angular

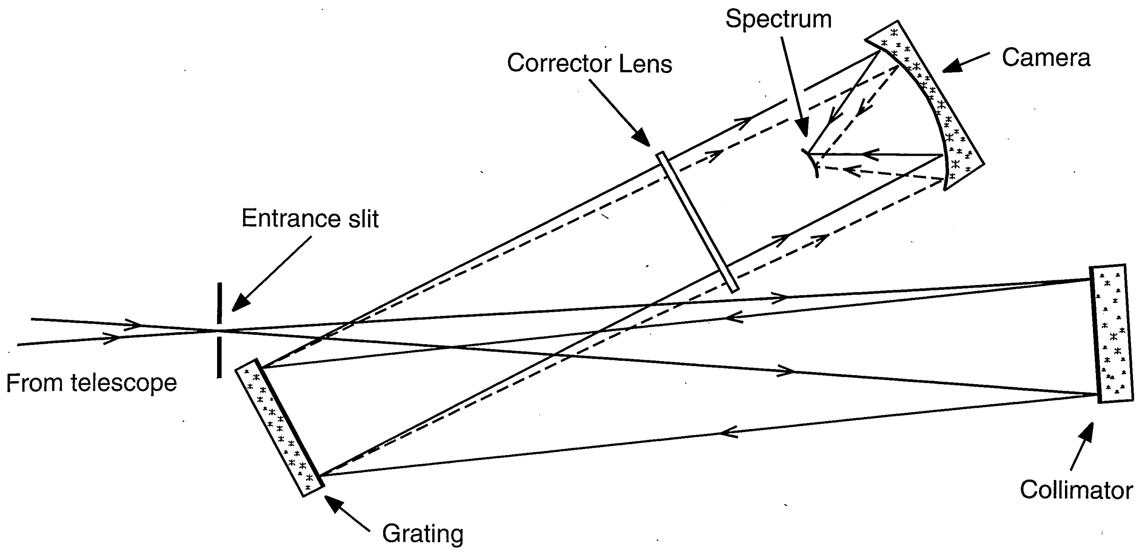

Figure C.1: Optical layout of a typical spectrograph. From Gray (2005).

dispersion as a function of wavelength can be obtained by differentiating Eq. C.1,

$$\frac{d\beta}{d\lambda} = \frac{n}{d\cos\beta} = \frac{\sin\alpha + \sin\beta}{\lambda\cos\beta}. \tag{C.2}$$

We can easily see that the angular dispersion increases with larger n and smaller d. From Eq. C.1 we can observe that we have multiple solutions of $n\lambda$ for a given β. We will thus obtain spacial overlap of different wavelengths in the recorded spectrum. To overcome this problem two solutions are possible. In the case of using a small order spectrograph, a blocking filter can be placed before the dispersion grating. For large n, as in the case of an echelle spectrograph, a cross-dispersing element (i.e. a grating or prism) is placed after the main grating.

In fact, what we really obtain is a continuum of centre-centre interference phases that are periodic over multiples of π. The general form of the interference phases is given by,

$$\phi_{cc} = n\pi = \frac{\pi d}{\lambda}(\sin\alpha + \sin\beta). \tag{C.3}$$

From here we can obtain the normalised intensity pattern as a function of ϕ_{cc},

$$I(\phi_{cc}) = \frac{\sin^2(N_g)\phi_{cc}}{\sin^2\phi_{cc}}, \tag{C.4}$$

called interference function, where $N_g = L/d$. For a fixed λ there is a range of maximum intensities for $\phi_{cc} = n\pi$ and zero intensities for $\phi_{cc} = (n/2)\pi$, as shown in Fig. C.3 a). As we can see, the diffraction pattern is periodic and symmetric for all n.

However, we also have to take into account the interference phases produced between the centre of each groove and its edge. Therefore, the centre-edge phase can be written as,

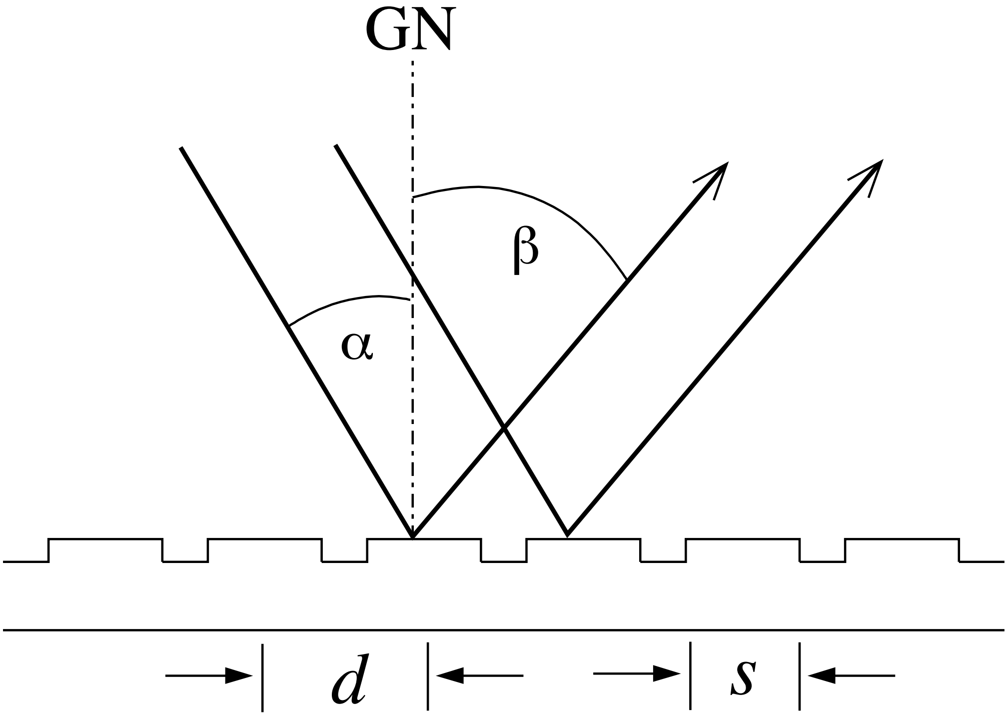

Figure C.2: A schematic of a reflection grating showing the individual grooves, where the *s* is the edge-to-edge length between grooves and *d* is the centre-to-centre separation. The incoming light has an angle of incidence α with respect to the grating normal. The interference of the reflected wave front has a diffraction angle β, which is function of the wavelength phase difference. From Churchill (2010).

$$\phi_{ce} = \frac{\pi s}{\lambda}(\sin\alpha + \sin\beta), \tag{C.5}$$

and the normalised intensity, called the blaze function, is

$$I_b(\phi_{ce}) = \frac{\sin^2\phi_{ce}}{\phi_{ce}^2}. \tag{C.6}$$

This function has its highest value when $\phi_{ce} = 0$, that occurs when the incident and refracted angle have the same value, meaning that $\alpha = -\beta$. The minima of this function are located at $n\pi$ intervals while $\Delta\phi_{ce} = \lambda/s$.

The resulting intensity function, shown in Fig. C.3 b) is

$$I(\lambda) = I(\phi_{cc}).I(\phi_{ce}) = \frac{\sin^2 N_g\phi_{cc}}{sin^2\phi_{cc}}.\frac{\sin^2\phi_{ce}}{\phi_{ce}^2}. \tag{C.7}$$

For a non-blazed grating, as the case in Fig. C.2, the peak of the intensity of this function is located when $n = 0$, where there is no dispersion. This dramatically reduces the throughput at higher orders. To solve this problem we need to shift the peak of the blaze function until it is centred at the order n we desire. To this end, the grooves of the grating must be tilted by an angle ϕ, as shown in Fig. C.4. This process is called blazing and it effectively allows a shift in the phase space. The intensity function will

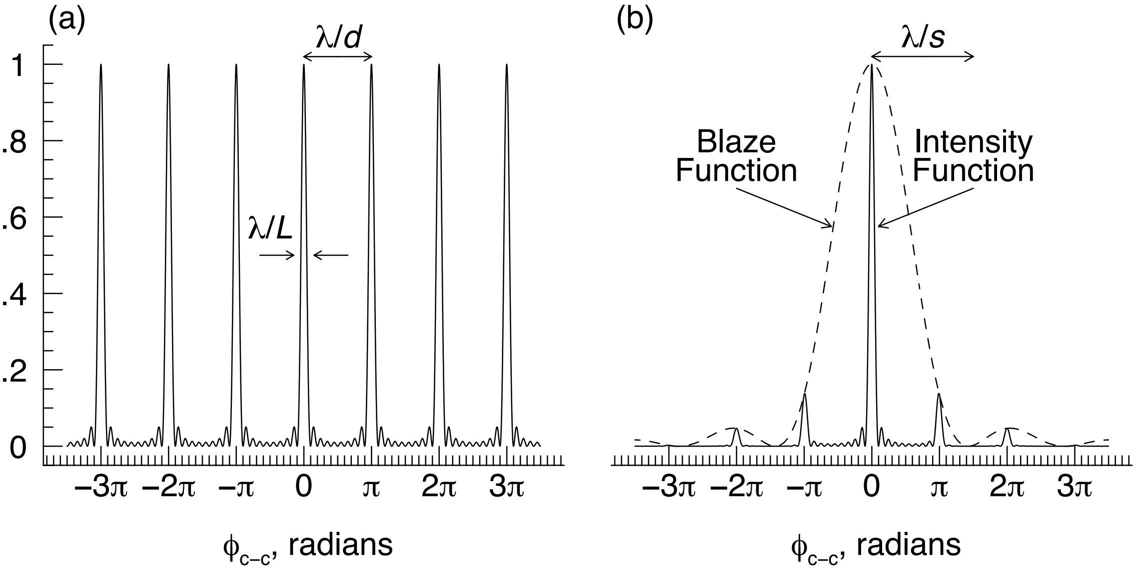

Figure C.3: a) Plot of the period interference function (Eq. C.4) as a function of the phase difference. b) The blaze function (Eq. C.6. From Churchill (2010).

now peak when $\bar{\beta} = -\bar{\alpha}$.

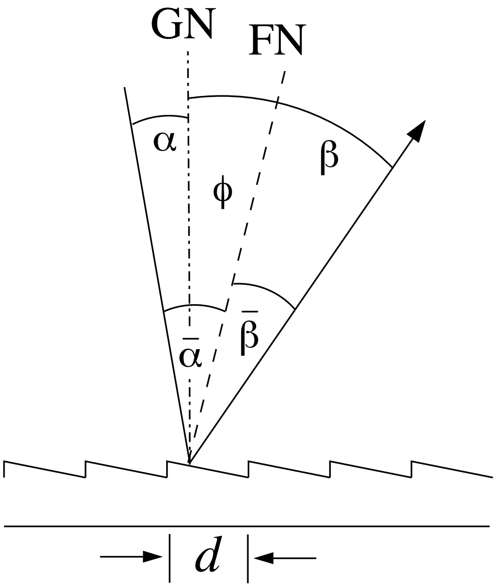

Figure C.4: In order to maximise the diffraction illumination pattern for $n > 0$, a phase shift is introduced to the centre-edge diffraction interference by grooving the facets at an angle ϕ, which also defines the facet normal, FN. The blaze function then peaks when $\bar{\beta} = -\bar{\alpha}$. From Churchill (2010).

Using the grating equation (Eq. C.1), we can write

$$\frac{n\lambda}{d} = \sin(\bar{\alpha} + \phi) + \sin(\bar{\beta} + \phi). \tag{C.8}$$

The blaze function maximises when $\alpha = -\beta$. Therefore,

$$\frac{n\lambda_b}{d} = 2\sin\phi\cos\bar{\alpha} + 2\sin(\phi\bar{\beta} + \phi), [check] \tag{C.9}$$

where λ_b is the blaze wavelength for order n.

In the design of a spectrograph, the n/d relationship is a critical choice. As n/d increases, the dispersion (and the resolution) also increases. Taking this into account the spectrographs either use low orders and low dispersions or high orders and high dispersions.

C.2 The echelle spectrograph

The echelle spectrograph has all the basic components of a spectrograph plus one extra constituent: the cross-disperser. This new element is placed forward of the grating element and allows the spatial separation of the echelle orders that are very close together, as shown in Fig. C.5. The cross disperser disperses the light at low orders, and is thus similar to a low order spectrograph grating.

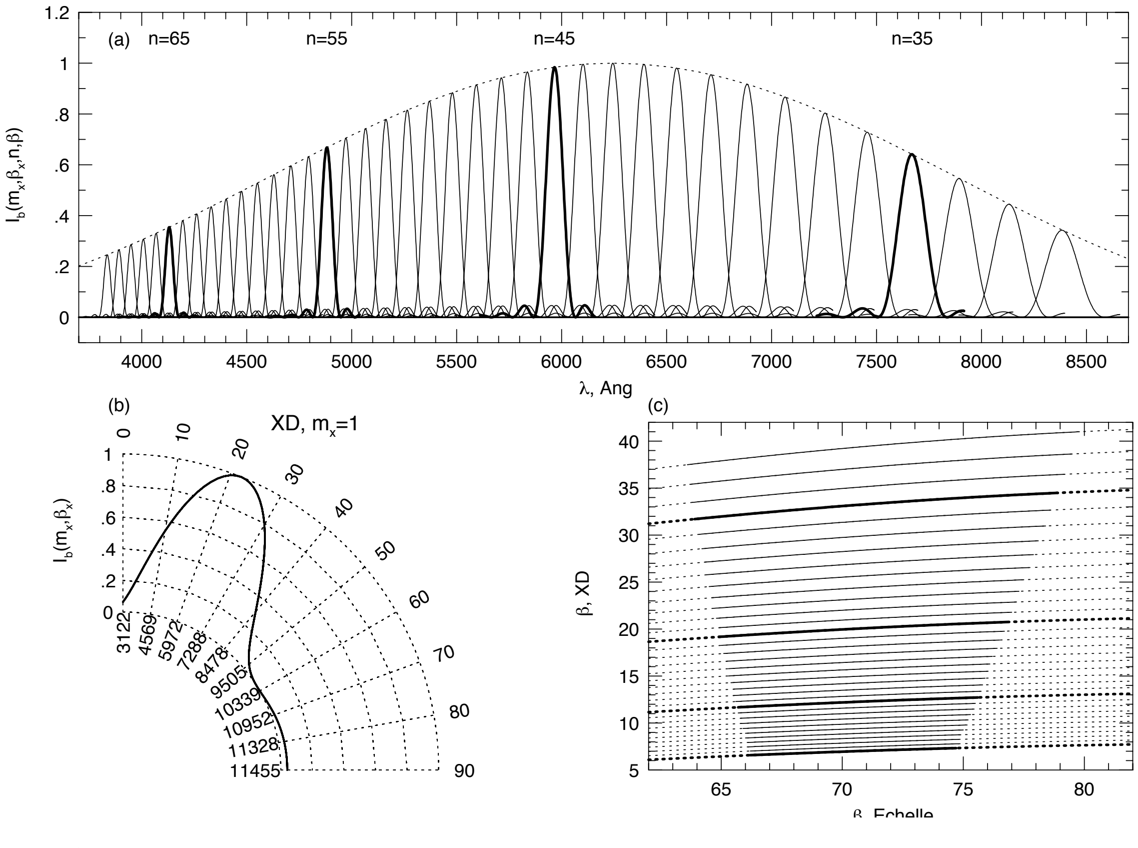

Figure C.5: a) Dependence of the echelle blaze functions on wavelength. The dotted curve is the cross-disperser blaze function; b) The cross disperser blaze function, shown in polar coordinate representation; c) The mapping of the echelle orders, n. The wavelength increases from the lower left to the upper right. The solid curve provides the free spectral range of each order. From Churchill (2010).

The main advantages of the echelle design over a low order spectrograph are high resolution (meaning high dispersion of the light) and a high wavelength coverage while minimising confusion between orders due to the use of the cross-disperser. The big disadvantage is the lower throughput (and thus signal to noise) due to the high-dispersion of light, implying the use of bigger telescopes or limiting the observations to brighter targets.

C.3 The HARPS Spectrograph

HARPS stands for **H**igh **A**ccuracy **R**adio **V**elocity **P**lanetary **S**earcher. This high-resolution spectrograph is an instrument designed to measure high precision and high resolution Radial Velocities (RV). Its main goal was to reach a radial velocity (RV) accuracy of 1 m/s for slowly rotating solar type stars ($v\sin i < 2km/s$). This never before reached precision enables the detection of low mass extra solar planets, with $msini$ lower than $10M_\oplus$ planets.

HARPS is a fibre-fed, cross-dispersed echelle spectrograph Mayor et al. (2003); Pepe et al. (2004). It has no moving parts and is located inside a vacuum vessel in a thermally stabilised enclosure. It operates at 17°C, constant within 0.005°C *rms*, with a pressure $< 10^{-2}$mbar. It is located in the Coudé floor of the 3.6m ESO telescope, at the ESO observatory of La Silla, Chile.

Two fibres, an object and a reference fibre, fed the spectrograph with light from the telescope and from the calibration lamps or sky. The light is re-imaged by the internal optics onto a mosaic of two 2k4 CCDs where two spectra of 72 orders are formed. The spectral region goes from 380 to 690nm. At the resolution of 115.000 each spectral element is sampled by 3.2 CCD pixels. The optics are mounted on a 2.5m optical bench made of plated steel.

The design of HARPS was based on previous planet-hunting spectrographs like ELODIE (Baranne et al. 1996) and CORALIE (Queloz et al. 2000b). The basic design of HARPS is very similar to these. The main advantages of HARPS are i) a greater instrument stability, as the spectrograph is installed in a sealed and evacuated enclosure with low temperature. This almost completely eliminates drifts in RV due to temperature, pressure or humidity variations; ii) higher S/N. The 3.6m ESA telescope on which HARPS is installed is bigger than its predecessors. Therefore, the S/N ratio is better. Moreover, the resolution of the CCD is increased by a factor of two and this also permits to reduce instrumental errors; iii) an improvement of online data reduction, that includes better corrections for instrumental effects and is faster.

HARPS is an ordinary echelle spectrograph. However, it distinguishes itself mainly by his incredible stability, not only by being intrinsically stable, that is temperature and pressure controlled, but also by using a ThAr reference lamp, thus being able to detect even the tiniest of instrumental drifts.

The spectrograph operates in low vacuum since pressure variations may produce huge drifts in the order of 100m/s per mbar. The pressure was put under 10^{-2} mbar so that the drifts do not exceed 1m/s per day. Temperature is also controlled. When the instrumental noise produced by the thermal dilatation of the CCDs due to tiny temperature variations is removed we get dispersion values consistent with photon noise of the ThAr reference lamp. This technique can track drift variations at 0.1 m/s. Factors like resolution, optical efficiency, size of instrument and telescope, fibre diameter, must be balanced in order to have the smallest instrumental errors.

After several tests, the attained value for the HARPS precision was well below 1 m/s. The best residuals obtained are as low as 0.2 m/s which indicates that with enough observations, it is possible to detect a 3 $M_{\oplus}$at 1 AU. At this precision level, we must count that one of the most probable sources of dispersion is the star itself (pulsations, activity, jitter). Disentangling noise and systematics from instrumental and stellar origin in not a trivial task. It needs time and lots of data. However, it is possible to average out most of the perturbing effects (stellar oscillations, activity jittering...). when observing in timescales compared to the periods of these effects (Dumusque et al. 2011b,a). The use of stellar noise removal techniques combined with a proper observation strategy led to the observation of the first earth-type planet using RV techniques (Dumusque et al. 2012). Efforts in the improvement of calibration with the ThAr lamps using a new HARPS made atlas with very high resolutions has enabled to reach new global uncertainties in the calibration (RV zero point) from 0.8 m/s to 0.2-0.4 m/s.

My second paper of the Ph.D. used HARPS M dwarf spectra to create a new calibration of M dwarfs using the photometric calibration of Neves et al. (2012) and the effective temperature calibration of Casagrande et al. (2008) as the metallicity and T_{eff} reference, respectively. Chapter 4 shows an in-depth analysis of this work.

Appendix D

Publications and communications related to this Thesis

Refereed papers

- SWEET-Cat: A catalogue of parameters for Stars With ExoplanETs I. New atmospheric parameters and masses for 48 stars with planets, Santos, N. C.; Sousa, S. G.; Mortier, A.; **Neves, V.**; Adibekyan, V.; Tsantaki, M.; Delgado Mena, E.; Bonfils, X.; Israelian, G.; Mayor, M.; Udry, S., 07/2013, A&A, accepted.
- The HARPS search for southern extra-solar planets. XXXIV. A planetary system around the nearby M dwarf GJ163, with a super-Earth possibly in the habitable zone, Bonfils, X.; Lo Curto, G.; Correia, A. C. M.; Laskar, J.; Udry, S.; Delfosse, X.; Forveille, T.; Astudillo-Defru, N.; Benz, W.; Bouchy, F.; Gillon, M.; Hbrard, G.; Lovis, C.; Mayor, M.; Moutou, C.; Naef, D.; **Neves, V.**; Pepe, F.; Perrier, C.; Queloz, D.; Santos, N. C.; Sgransan, D., 06/2013, A&A, accepted.
- Spitzer Observations of GJ3470b: a Very Low-density Neptune-size Planet Orbiting a Metal-rich M dwarf, Demory, Brice-Olivier; Torres, G.; **Neves, V.**; Rogers, L.; Gillon, M.; Horch, E.; Sullivan, P.; Bonfils, X.; Delfosse, X.; Forveille, T.; Lovis, C.; Mayor, M.; Santos, N.; Seager, S.; Smalley, B.; Udry, S., 01/2013, 2013, ApJ, 768, 154
- The HARPS search for southern extra-solar planets XXXIII. Super-Earths around the M-dwarf neighbors Gl433 and Gl667C, Delfosse, X.; Bonfils, X.; Forveille, T.; Udry, S.; Mayor, M.; Bouchy, F.; Gillon, M.; Lovis, C.; **Neves, V.**; Pepe, F.; Perrier, C.; Queloz, D.; Santos, N. C.; Ségransan, D., 02/2012, arXiv eprint: 1202.2467, 2013, A&A, 553, A8
- Metallicity of M dwarfs III. Planet-metallicity relationship on the HARPS GTO M dwarf sample, **Neves, V**.; Bonfils, X.; Santos, N. C.; Delfosse, X.; Forveille, T.; Allard, F.; Udry, S., 2013, A&A, 551, A36
- A hot Uranus transiting the nearby M dwarf GJ 3470. Detected with HARPS velocimetry. Captured in transit with TRAPPIST photometry, Bonfils, X.; Gillon, M.; Udry, S.; Armstrong, D.; Bouchy, F.; Delfosse, X.; Forveille, T.; Fumel, A.; Jehin, E.; Lendl, M.; Lovis, C.; Mayor, M.;

McCormac, J.; **Neves, V.**; Pepe, F.; Perrier, C.; Pollaco, D.; Queloz, D.; Santos, N. C., 2012, A&A, 546, A27

- Metallicity of M dwarfs. II. A comparative study of photometric metallicity scales, **Neves, V.**; Bonfils, X.; Santos, N. C.; Delfosse, X.; Forveille, T.; Allard, F.; Natário, C.; Fernandes, C. S.; Udry, S., 2012, A&A, 538, A25

- The HARPS search for southern extra-solar planets XXXII. Only 4 planets in the Gl-581 system, Forveille, T.; Bonfils, X.; Delfosse, X.; Alonso, R.; Udry, S.; Bouchy, F.; Gillon, M.; Lovis, C.; **Neves, V.**; Mayor, M.; Pepe, F.; Queloz, D.; Santos, N. C.; Segransan, D.; Almenara, J. M.; Deeg, H.; Rabus, M., 09/2011, arXiv eprint:1109.2505, submitted to A&A

- A short-period super-Earth orbiting the M2.5 dwarf GJ 3634. Detection with HARPS velocimetry and transit search with Spitzer photometry, Bonfils, X.; Gillon, M.; Forveille, T.; Delfosse, X.; Deming, D.; Demory, B.-O.; Lovis, C.; Mayor, M.; **Neves, V.**; Perrier, C.; Santos, N. C.; Seager, S.; Udry, S.; Boisse, I.; Bonnefoy, M., 2011, A&A, 528, A111.

Non refereed papers

- Prized results from HARPS. Low-mass/habitable/transiting planets orbiting M dwarfs. Authors: Bonfils, X., Bouchy, F., Delfosse, X., Forveille, T., Gillon, M., Lovis, C., Mayor, M., **Neves, V.**, Pepe, F., Queloz, D., Santos, N., Sgrasan, D., Udry. Hot Planets and Cool Stars, Garching, Germany, 12-16/10/2012. Edited by Roberto Saglia. European Physical Journal Web of Conferences, 47, 5004. Published: 04/2013.

- Metallicity of M-dwarfs: The link to exoplanets. Authors: **Neves, V.**, Bonfils, X., Santos, N. C. Proceedings of the IAU Symposium 276, 2011: The Astrophysics of Planetary Systems: Formation, Structure, and Dynamical Evolution, Torino, 11-15/10/2010, Volume 276, p. 443-444, Published: 11/2011.

Talks

- 2012/09: Oral talk at XXII ENAA (Portuguese National Encounter of Astronomy & Astrophysics), CAUP, Porto, Portugal. Title: A new visual spectroscopic metallicity scale for M dwarfs: the Śuper-Index' approach.

- 2012/07: Oral talk at PhD day, DFA, FCUP, Porto, Portugal. Title: Metallicity of M dwarfs: the link to exoplanets. 2012/06: Oral talk at Student's day @ CAUP, Porto, Portugal. Title: Metallicity/Stellar mass relationship with planets of the HARPS GTO M-dwarf sample.

- 2012/04: Oral talk at Journée des Thèses, IPAG, Grenoble, France Title: Towards a precise metallicity scale for M dwarfs.

- 2011/09: Oral talk at XXI ENAA (Portuguese National Encounter of Astronomy & Astrophysics), 7-10 September 2011, Coimbra, Portugal. Title: A comparative test of metallicity calibrations for M dwarfs.

- 2011/06: Oral talk during Students Day at CAUP. Title : Metallicity of M dwarfs: the link to exoplanets.
- 2011/01: Oral talk at IPAG Seminar. Title: Metallicity of M dwarfs: the link to exoplanets.
- 2010/04: Oral talk during PhD day at DFA, FCUP, Porto, Portugal. Title: M-dwarfs and exoplanets: perspectives and challenges of an exciting PhD project.

Poster communications

- 2012/06: A new visual spectroscopic metallicity scale for M dwarfs: the Śuper-Index' approach. Authors: **V. Neves**, X. Bonfils, N.C. Santos, X. Delfosse, T. Forveille, F. Allard, and S. Udry. Conference: Cool Stars 17 Ð 17th Cambridge Workshop on Cool Stars, Stellar Systems and the Sun, Barcelona, Spain.
- 2011/09: A Comparative Test of Metallicity Calibrations for M dwarfs'. Authors: V. Neves; X. Bonfils, N. C. Santos. Conference: Extreme Solar Systems II, Jackson Lake Lodge, Grand Teton National Park, Moran, Wyoming, USA.
- 2010/10: Metallicity of M dwarfs: the link to exoplanets. Authors: **V. Neves**, X. Bonfils, N. C. Santos. Conference: IAU Symposium 276, 2011: The Astrophysics of Planetary Systems: Formation, Structure, and Dynamical Evolution.
- 2010/08: Metallicity of M dwarfs: the link to exoplanets. Authors: **V. Neves**, X. Bonfils, N. C. Santos. Conference: Cool Stars 16 - 16th Cambridge workshop on cool stars, stellar systems, and the sun. Seattle, USA.

Outreach and public communications

- 2013/01: Public Talk. Title: Planetas habitáveis fora do sistema solar. Place: Caminha, Portugal. link: http://bibcouraminho.webnode.pt/.
- 2012/04: TV program interview. Title: Planetas semelhantes à terra povoam o universo - uma conversa informal tendo com base o ESO press release 1214. Programa 'Conta-me Histrias' no mbito do projecto Academia RTP. Gravado no Centro de Astrofsica da Universidade do Porto, Portugal.
- 2012/04: TV live interview. Title: Existem na nossa galáxia biliões de planetas rochosos na zona habitável de estrelas mais pequenas que o sol (related to the ESO press release 1214), Porto Canal, Porto, Portugal.
- 2012/03: Newspaper interviews (4). Title: Há milhares de milhes de 'Terras' na Via Láctea. Newspaper: Dirio de Notícias. Date: 29/03/2012; Title: Há muitas Super-Terras onde pode haver vida. Newspaper: Público. Date: 29/03/2012; Title: Planetas em zona habitável podem ser frequentes. Newspaper: tvnet.sapo.pt.Date: 29/03/2012; Title: Ciência: Mais um passo dado na busca de vida para além da Terra. Newspaper: Jornalismo porto net. Date: 29/03/2012. (all news are related to the ESO press release 1214).

- 2012/03: ESO press release 1214. Title: Many Billions of Rocky Planets in the Habitable Zones around Red Dwarfs in the Milky Way. Team: X. Bonfils, X. Delfosse, T. Forveille, M. Mayor, C. Perrier, F. Bouchy, M. Gillon, C. Lovis, F. Pepe, D. Queloz, N. C. Santos, D. Sgransan, J.-L. Bertaux, and **Vasco Neves**. link: `http://www.eso.org/public/news/eso1214/`

Observational experience, proposals & international collaborations

- Awarded ESO telescope time (P92) with the X-SHOOTER spectrograph @ VLT. Title: A spectroscopic metallicity scale for M dwarfs II. Authors: **Vasco Neves**; Xavier Bonfils; Nuno Santos; Xavier Delfosse; Thierry Forveille; France Allard. Time : 16.3h. Status: approved. Date: from 2013/10 to 2014/03.
- Awarded ESO telescope time (P88) with the X-SHOOTER spectrograph @ VLT. Title: A spectroscopic metallicity scale for M dwarfs. Authors: **Vasco Neves**; Xavier Bonfils; Nuno Santos; Xavier Delfosse; Thierry Forveille; Michael Gillon; France Allard. Time : 15h. Status: executed. Date: from 2011/10 to 2012/03.
- Awarded Hubble space telescope (HST) time with WFC3. Title: Investigating the nature of GJ 3470b, the missing link between super-Earths and Neptunes. Authors: David Ehrenreich; Xavier Bonfils; Michael Gillon; Stphane Udry; Michel Mayor; Xavier Delfosse; Thierry Forveille; Christophe Lovis; Nuno Santos; **Vasco Neves**. Status: Accepted. Execution Date: 2013/02.
- Awarded Spitzer Space Telescope Time with IRAC @ 4.5μm. Title: Characterization of a Low-density Transiting Exo-Neptune(GJ3470b). Authors: Brice Olivier-Demory; Michael Gillon; Xavier Bonfils; Xavier Delfosse; Thierry Forveille; Christophe Lovis; Michel Mayor; Stphane Udry; Nuno Santos;**Vasco Neves**. Status: Executed. Approval Date: 2012/06.
- Four observing missions with the HARPS spectrograph @ La Silla during 2010-2013: 8 nights @ May 2010; 11 nights @ May 2011; 10 nights @ March 2012, and 9 nights @ February 2013.
- Mission at the Observatoire d'Haute Provence (OHP - France), observing with the SOPHIE spectrograph for 7 nights at 2011/01.
- Member of the HARPS M dwarf group since 2010.
- Member of the EXO-Earths team since 2010. link: `http://www.astro.up.pt/exoearths/`